Microcantilever Biosensors

Lucy A. Williamson Hodge

A dissertation submitted for the degree of Doctor of Engineering

Heriot-Watt University

School of Engineering and Physical Sciences

September 2014

Abstract

The cross-sensitivity of microcantilever sensors presents a major obstacle in the development of a commercially viable microcantilever biosensor for point of care testing. This thesis concerns electrothermally actuated bi-material microcantilevers with piezoresistive read out, developed for use as a blood coagulometer. Thermal properties of the sensor environment including the heat capacity and thermal conductivity affect the 'thermal profile' onto which the higher frequency mechanical signal is superimposed. In addition, polymer microcantilevers are known to have cross-sensitivity to relative humidity due to moisture absorption in the beam. However it is not known whether any of these cross sensitivities have a significant impact on performance of the sensor during pulsed mode operation or following immersion into liquid. When analysing patient blood samples, any change in signal that is not caused by the change in blood viscosity during clotting could lead to a false result and consequently an incorrect dose of anticoagulants may be taken by the patient. In order to address these issues three aspects of the operation of polymer bi-material strip cantilevers has been researched and investigated: relative humidity; viscosity/density, and thermal conductivity of a liquid environment.

The relative humidity was not found to affect the resonant frequency of a microcantilever operated in air, or to affect the ability of the cantilever to measure clot times. However, a decrease in deflection with increasing relative humidity of the SmartStrip microcantilever beams is observed at 1.1 ± 0.4 μm per 1% RH, and is constant with temperature over the range 10 – 37 °C, which is an issue that should be considered in quality control. In this study, the SmartStrip was shown to have viscosity sensitivity of 2 cP within the range 0.7 – 15.2 cP, and it was also shown that the influence of inertial effects is negligible in comparison to the viscosity. To investigate cross-sensitivity to the thermal properties of the environment, the first demonstration of a cantilever designed specifically to observe the thermal background is presented. Characterisation experiments showed that the piezoresistive component of the signal was minimised to -0.8% ± 0.2% of the total signal by repositioning the read out tracks onto the neutral axis of the beam. Characterisations of the signal in a range of silicone oils with different thermal conductivities gave a resolution to thermal conductivity of

0.3 $Wm^{-1}K^{-1}$ and resulted in a suggestion for design improvements in the sensor: the time taken for the thermal background signal to reach a maximum can be increased by increasing the distance between the heater and sensor, thus lessening the impact of the thermal crosstalk within the cantilever beam. A preliminary investigation into thermal properties of clotting blood plasma showed that the sensor can distinguish the change between fresh and clotted plasma.

For my family

Acknowledgements

Firstly I would like to thank my supervisor Prof Ajoy Kar for granting me the opportunity to pursue this Engineering Doctorate at the IDC. His feedback on my thesis has been immensely helpful. I also acknowledge the financial support of the Engineering and Physical Sciences Research council for funding through the Engineering Doctorate Program. In addition I would like to thank both Prof Andy Harvey and Prof Derryck Reid for their management of the IDC and useful advice and assistance. Staying with Heriot Watt, I have also had useful technical discussions with Prof Marc Desmulliez. My thanks extend to my examiners Dr Joseph Ndieyira and Dr. Will Shu.

I am indebted to Dr Richard Dunn formerly of STFC and Microvisk who has provided the greatest technical assistance, advice and encouragement throughout and without whose support, know-how and management I would not now be approaching the end of this project. I also thank Mr Bob Ibbotson and Dr Slava Djakov for very thought provoking technical discussions on the long road to St Asaph. In addition, the technical advice and corrections provided by Dr Andreas Schneider of STFC were invaluable in completing *chapter 5*, and the second opinion of Dr Anke Lohmann was very useful in trying to troubleshoot the interference that has plagued the TD cantilever signal. Thanks also to Dr Simon Fairclough for providing feedback on *chapter 1*.

Finally and not least, I need to thank the good friends and relatives that have encouraged me along this road (with the best intentions) and given me the emotional strength to see it through. Specifically I would like to thank Dr Catherine Fitzpatrick and Dr Mhairi Martin for sharing this EngD journey with me and offering practical advice on many matters, but also good friends Mrs Joanna Priestley and Mrs Elisha Coutts, Mr Ian Tracey and of course Dr Jackson Smith and Mum and Dad who now all know considerably more than they ever wanted to about studying microcantilever sensors!

ACADEMIC REGISTRY
Research Thesis Submission

Name*:*	Lucy A. Williamson Hodge		
School/PGI:	Industrial Doctorate Centre		
Version: *(i.e. First, Resubmission, Final)*	First Submission	Degree Sought (Award **and** Subject area)	Engineering Doctorate (Physics)

Declaration

In accordance with the appropriate regulations I hereby submit my thesis and I declare that:

1) the thesis embodies the results of my own work and has been composed by myself
2) where appropriate, I have made acknowledgement of the work of others and have made reference to work carried out in collaboration with other persons
3) the thesis is the correct version of the thesis for submission and is the same version as any electronic versions submitted*.
4) my thesis for the award referred to, deposited in the Heriot-Watt University Library, should be made available for loan or photocopying and be available via the Institutional Repository, subject to such conditions as the Librarian may require
5) I understand that as a student of the University I am required to abide by the Regulations of the University and to conform to its discipline.

* *Please note that it is the responsibility of the candidate to ensure that the correct version of the thesis is submitted.*

Signature of Candidate*:*	Lucy A. Williamson Hodge	Date:	

Submission

Submitted By *(name in capitals):*	LUCY A. WILLIAMSON HODGE
Signature of Individual Submitting:	Lucy A. Williamson Hodge
Date Submitted:	

For Completion in Academic Registry

Received in the Academic Registry by *(name in capitals):*			
Method of Submission *(Handed in to Academic Registry; posted through internal/external mail):*			
E-thesis Submitted **(mandatory for final theses from January 2009)**			
Signature:		Date:	

Please note this form should bound into the submitted thesis.
Updated February 2008, November 2008, February 2009

List of Publications

Conference Papers

[1] Williamson Hodge, L.A.; Dunn, R.J.; Ibbotson, R.H.; Huq, S.E.; Kar, A.K.; , "Polymer microcantilevers for thermal sensing," Sensors, 2011 IEEE, 28-31 Oct. 2011, pp.671-674,

Acronyms

AC Alternating Current

AFM Atomic Force Microscopy: a technique that uses the interaction between a microcantilever and a surface to obtain information on the surface texture. It is typical to scan areas from a few μm to a few cm in length, and vertical resolution is from typically in Å or nm.

BNC Bayonet Neill–Concelman: connector for coaxial cable.

CAD Computer Aided Design. In this thesis the CAD software AutoCAD was used to design masks for photolithography.

CHE Coefficient of Humidity Expansion: A material property that describes the linear expansion of a material upon absorption of moisture from the atmosphere.

CTE Coefficient of Thermal Expansion: A material property that describes the linear expansion (positive CTE) or contraction (negative CTE, rare) of a material upon heating.

CWB Citrated whole blood.

DC Direct Current

FEM Finite Element Modelling

FDA Food and Drug Administration: Government agency in the United States of America. Remit includes licencing medical devices.

FPT Fractional Peak Time: signal characteristic used to characterise the TD microcantilever signal in response to actuation.

FPH Fractional Peak Height: signal characteristic used to characterise the TD microcantilever signal in response to actuation.

FTHWG Fractional Transient Hot Wire Gradient: signal characteristic used to characterise the TD microcantilever signal in response to actuation.

FTHWI Fractional Transient Hot Wire Intercept: signal characteristic used to characterise the TD microcantilever signal in response to actuation.

FFT Fast Fourier Transform

HPF High Pass Filter.

INR International Normalised Ratio: A standardised measure of blood clot time that accounts for variation in measurement techniques and reagent sensitivity.

INEX Semiconductor manufacturing foundry based in Newcastle, UK.

LOR Lift Off Resist: Type of resist used in a bi-layer lift off process in microfabrication

LPF Low Pass Filter

MD Mechanical Design: An early prototype of the Microvisk SmartStrip microcantilever, designed at STFC.

MEMS Micro-Electro-Mechanical Systems: Electrically powered moving components with length scales typically 1 μm to 1 mm.

MIP Molecular Imprinted Polymer

MNTC Micro and NanoTechnology Centre: A former department within the Science and Technology Facilities Council facility.

MV1, MV2, MV3 Design iterations of the Microvisk SmartStrip microcantilever.

NSB Non-specific binding.

OAT Oral anticoagulation Therapy: medication most commonly proscribed to lower risk of stroke. Common OATs include warfarin, acenocoumarol, phenindione,

PCB Printed circuit board

PI Polyimide: a range of polymers known for high thermal stability.

PT Prothrombin Time: time for a clot to be detected based on the instrument used and reagent sensitivity.

QC Quality Control

RBC Red Blood Cell

RF Radiofrequency.

SEM Scanning Electron Microscopy

SEMEFAB Semiconductor manufacturing foundry based in Glenrothes, Scotland, UK.

SHO Simple Harmonic Oscillator

SMR A microcantilever technique whereby a microfluidic channel is etched into microcantilever beam. Properties of interest in the liquid sample (e.g. concentration of analyte) may be determined from the resonance of the beam, without significant loss in Q-factor.

STFC Science and Technology Facilities Council: Provided funding and facilities towards the work documented in this thesis.

TCR Temperature Coefficient of Resistance

TD sensor Thermal Design sensor: A novel microcantilever sensor presented in Chapters 5 and 6 of this thesis.

TEG Thromobelastogram

UKAS United Kingdom Accreditation Service

VI Virtual Instrument:

ZIF Zero Insertion Force: A type of socket that does not require any force other than the weight of the component, to hold said component in place.

.

List of Symbols

Symbol	Description
c	Ratio of Young's modulus between layers of a bi-material strip
d	Ratio of thickness between layers of a bi-material strip
h	Heat transfer coefficient
k	Spring constant
l	Thickness of liquid cell in Fox-50 thermal conductivity meter
m	Mass (of beam)
n	Integer
p	Perimeter of beam segments
q_j	Power density
r	Radius, resistivity
t	Time
t_i	Thickness of layer in bi-material strip: *i* indicates layer index
t_b	Beam thickness (total all layers)
w	Width of beam
x	Distance along the length of the beam
z, $z_{autofocus}$, z_{actual}	Distance from beam to substrate
A_{Th}, A_{RH}, A	Structural parameter for bi-material strip equation
Bi	Biot Number
C	Specific heat capacity
D	Flexural rigidity
D_{Th}	Thermal diffusivity
E	Young's modulus
G, G^*, G', G''	Shear modulus
I	Moment of inertia
L	Length of beam,
N	Neutral axis
P	Power, Perimeter of beam leg
Q	Q-factor
R	Resistance
Re	Reynolds number
RH, RH_{local}, RH_{amb}	Relative Humidity
T, T_0, T_{amb}	Temperature
V	Voltage
Y	Modified Density Ratio
Z_{tip}	Distance from beam tip to substrate
α_{Th}	Coefficient of thermal expansion, CTE
α_{RH}	Coefficient of humidity induced expansion, CHE
β	Free convection coefficient
γ	Constant proportional to viscosity
δ	Phase angle between the shear stress and shear rate
ε	Emissivity
η, η^*, η', η''	Viscosity
κ_{eff}, κ_f, κ_{Th}, κ_{RH}, κ_h	Curvature
λ, λ_b, λ_{air}	Thermal conductivity
ρ_b	Density of the beam

ρ_f	Density of fluid
σ	Poisson Ratio
τ	Time constant
φ	Phase angle between the shear stress and shear strain
ψ_c, ψ_g	Thermal Resistance
χ	Temperature coefficient of resistance, TCR
ω, ω_0, ω_R	Angular frequency of beam

Table of Contents

Chapter 1

MEMS in Healthcare

1.1 Small Technology, Big Application

MicroElectroMechanical Systems (MEMS), is an interdisciplinary branch of applied physics that has become widely commercialised over the past three decades, and is now penetrating the healthcare industry where it is poised to have a significant impact. MEMS technology may also be known as 'microsystems' or 'micromachines' depending on the final application of the device. The field combines problems in electromagnetism, heat transport and elasticity, with chemistry and the scientific craft of microfabrication. In his now infamous 1959 talk entitled 'There's plenty of room at the bottom', Richard Feynman inspired a generation of MEMS developers and nanotechnologists with ideas of blood-circulating cell repair robots and atomic manipulation [1]. At the time of this talk, Feynman could only guess at the practical applications of his imagined micro-motors, but the first MEMS device, Nathanson's resonant gate transistor [2], was patented less than a decade later. MEMS technology is underpinned by microfabrication and employs many of the same processes that are used to manufacture modern computer transistors. The commercial success of microfabrication technology has inspired scientists and business leaders that the miniaturisation of common electromechanical components such as pumps, valves and sensors will usher in the next generation of portable, low cost and reliable products.

Global demand for healthcare is rising due to the increasing world population and longer life expectancy. Current rates of spending on healthcare are increasingly viewed as unsustainable [3]. One major challenge is to reduce the time each patient spends in hospital or at a clinic (the patient pathway) by increasing the speed and accuracy of diagnoses; detecting disease while it is preventable; and streamlining the management

the treatment of long term conditions. Miniaturised biosensor platforms that can be used by the patient at home have received a great amount of public funding and attention, and are presented as an enabling technology to deliver healthcare cost-effectively in the next century [4].

BioMEMS are a sub-category of biosensors, where MEMS components such as resonators, pumps and switches are used alongside microfluidics and biochemistry in the miniaturisation of analytical equipment. Such devices are also known as 'Lab-On-A-Chip' or 'micro-Total-Analysis-System'. BioMEMS, has inherent advantages over traditional technology: small sample and reagent volumes and short 'time to answer' increase rapid diagnosis and usability; low power consumption gives the option of single use batteries; high sensitivity increases the capacity for early diagnoses and can be used to increase the dynamic range; and highly parallel operation enables more robust diagnoses through detection of multiple biomarkers. In 2007, bioMEMS was hailed as 'the investment trend of the decade' by MoneyWeek [5] and as 'the largest and most diverse application of MEMS devices' by R&D Magazine [6]. In a 2008 survey of the US Food and Drugs Administration (FDA) managers as well as physicians, engineers, healthcare policymakers, manufacturers, futurists and technology analysts, MEMS was identified as one of 32 significantly innovative product groups likely to be in the US healthcare market by 2018 [7]. The two principle areas of application identified for this technology are in "invasiveness reducing technologies" (micro-surgery robotics) and in patient monitoring systems.

1.2 Commercialising MEMS for Healthcare

Whilst the healthcare industry seeks to benefit from new technology, it is notoriously conservative. Technology is advancing rapidly, but scandals such as the recent faults in Poly Implant Prothèse silicone gel breast implants [8], have reinforced the need for continued regulation, and agencies such as the FDA are cautious in approving new technology. Medical products therefore have long and expensive development times, typically 5 to 15 years. An approach taken by many companies to shorten the development cycle is to adapt existing technology that has already demonstrated a suitable level of performance in a different industry [9].

The first commercially successful mass produced MEMS device was the micromachined accelerometer, originally developed in 1979 at Stanford University, it was successfully scaled by Analog Devices in the early 1990's for use in automobile air bags, resulting in sales of 27 million units by 1998 [10]. The same technology was later adapted for use in modern pacemakers to detect the patients' activity level, and the action of heart-stimulating electrodes is modified accordingly [11]. Other applications of MEMS accelerometers and gyroscopes abound in the field of human motion analysis, which has a range of applications from evaluating the jitter caused by Parkinson's disease, to automatic notification of trips and falls [12].

The invention of scanning-tunnelling microscopy and later atomic force microscopy (AFM) in which the deflection of a microcantilever is measured optically for atomic scale surface metrology earned researchers from IBM and Stanford University the Nobel Prize in 1986 [13]. AFM is now a significant research tool in the biomedical sciences where it is used at different scales to study mechanical properties of individual molecules and cells [14]. There is also a growing body of research in label-free diagnostics using microcantilevers as signal transducers, much of which is conducted using 'off the shelf' AFM cantilevers [15].

Point of care diagnostics can reduce the patient pathway by combining: the sample, result and diagnosis into one consultation between the patient and healthcare professional. To do this, a point of care system must deliver results that match or exceed the current 'gold standard' laboratory tests in terms of accuracy, precision and robustness. In addition the equipment should be small (desktop or hand-held), ergonomic, easy to operate and display results in a format that can be understood by the physician and patient. The 'time to answer' should be no more than a few minutes. There are several biosensing technologies such as lateral flow, bioMEMS and electrochemical sensors that are commercialised for point of care diagnostics. BioMEMS offers the same advantages as competing biosensing technologies in terms of the small sample volume, short time to answer and the possibility for accurate results without pre-concentration of sample. BioMEMS offers additional advantages when the mechanical properties of the sample are indicative of disease state (e.g. blood clot measurements, sickle cell anaemia) or when there are difficulties obtaining results using electrochemical or optical techniques.

The total 'point of care' diagnostics market was estimated to be worth $US 15.4bn in 2010 [9], 85% of which is said to be from blood glucose testing for diabetics. This related electrochemical sensing technology provides a blueprint of how an ideal bioMEMS breakthrough product could emerge in medical diagnostics. Emerging markets within the home-use biosensor sector for which MEMS sensors have been demonstrated include HIV testing [16], hepatitis [17], and coagulation [18].

1.3 'Point of Care' Monitors for Coagulation

1.3.1 Coagulation Testing

In a healthy state, the coagulation cascade is activated to generate a blood clot around the site of damage to a blood vessel, and then return to the default, anticoagulant state. Oral Anticoagulation Therapies (OATs) such as warfarin and Coumadin are prescribed when the balance between clotting and anticoagulant mechanisms is tipped towards clotting, for example in people with mechanical heart valves, or those affected by atrial fibrillation or venous thromboembolism. The standard laboratory measure of clot time is the International Normalised Ratio (INR) test and this is traditionally performed in a haematology laboratory, away from the patient. Variation in the time taken for clotting to occur could be due to a single or multiple clotting factor differences within the clotting cascade *(figure 1.1)*: clot time is not a measure for a specific analyte but rather of the position of equilibrium of haemostasis [19]. The therapeutic window is narrow: INR of less than 2 indicates a risk of clotting; and greater than 4.5 indicates a risk of major bleeding [20]. The doctor or clinician will determine the ideal therapeutic window for each patient.

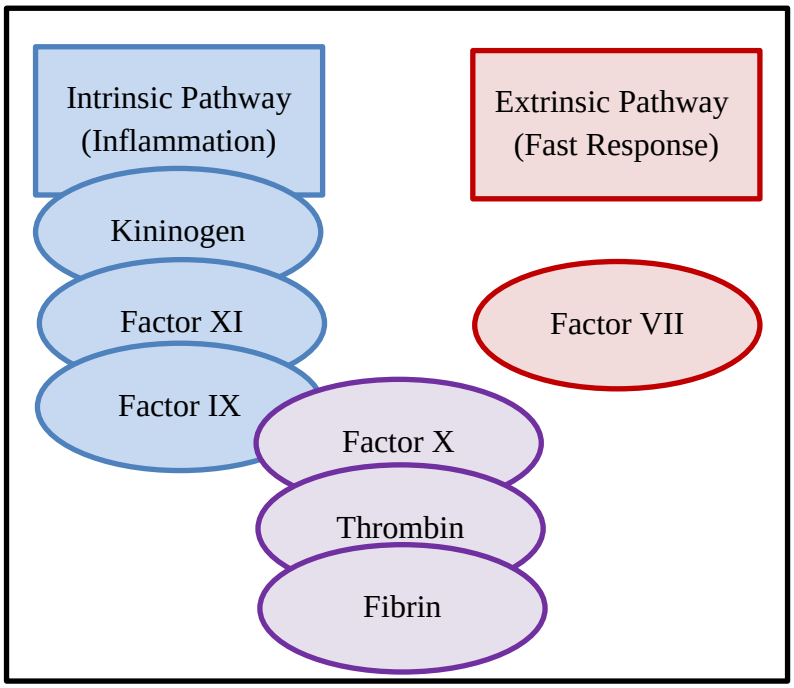

Figure 1.1: Schematic outlining the intrinsic and extrinsic pathways in the clotting cascade.

Traditional medical practice involves frequent clinic visits for sample collection and dose adjustment. Laboratory tests delay the time-to-answer, are costly and inconvenient for the patient and healthcare provider, and as such are performed less frequently than is optimal for patient care. Patient self-monitoring has been gaining popularity in the USA since it was first introduced in 1987 [21]. There is evidence from randomised controlled trials that self-management of coagulation therapy increases the proportion of time the patient INR is within the target window [22].

1.3.2 Current Point of Care Coagulation Test Technologies

Many 'clot time' tests are available within the haemostasis laboratory, but INR monitoring is the most frequently performed test and is widely used to monitor patient response to OAT. Patient self-testing is smallest but fastest growing area within INR monitoring. The market for patient self-test equipment bears some similarity with the glucose sensor market since disposable test strips are used frequently in conjunction with a portable interface. The INR self-test market is currently dominated by Roche Diagnostics Corporation, International Technidyne Corporation (ITC), Abbott Point of Care Inc. and Alere Inc. Various technologies are used to measure the clotting process. The technologies described in this section maintain an operating temperature of 37 ± 1

°C and use thromboplasin (rabbit brain or human recombinant) as an accelerator for the clotting reaction, giving ‘time to answer’ of a few minutes.

Electrochemical

Due to the position of thrombin near the bottom of the clotting cascade, an electrochemical assay of thrombin activity over time can be used to determine the Prothrombin Time (PT), from which the INR can be calculated. In the final stage of the clotting cascade, thrombin enables the conversion of fibrinogen to fibrin. In the patented amperometric technique from Roche [23], a dry reagent that may be specifically cleaved by thrombin to produce phenylenediamine which is oxidised to quinone diimine at the working electrode, generating increased current between the working and reference electrodes. The signal is increased by use of an enzyme such as glucose-dye-oxidoreductase (GlucDOR) and the natural glucose present in whole blood to continually regenerate the phenylenediamine. A measurement of the time from sample addition until the current between the electrodes exceeds a threshold value is converted to the PT value. A similar technique is used by Abbott (NJ, USA) in their i-STAT cartridges, however a different dry reagent is used [24]. Additional techniques used to determine blood clot times include electrical impedance (INRatio™ test strips, Alere, CA, USA) [25].

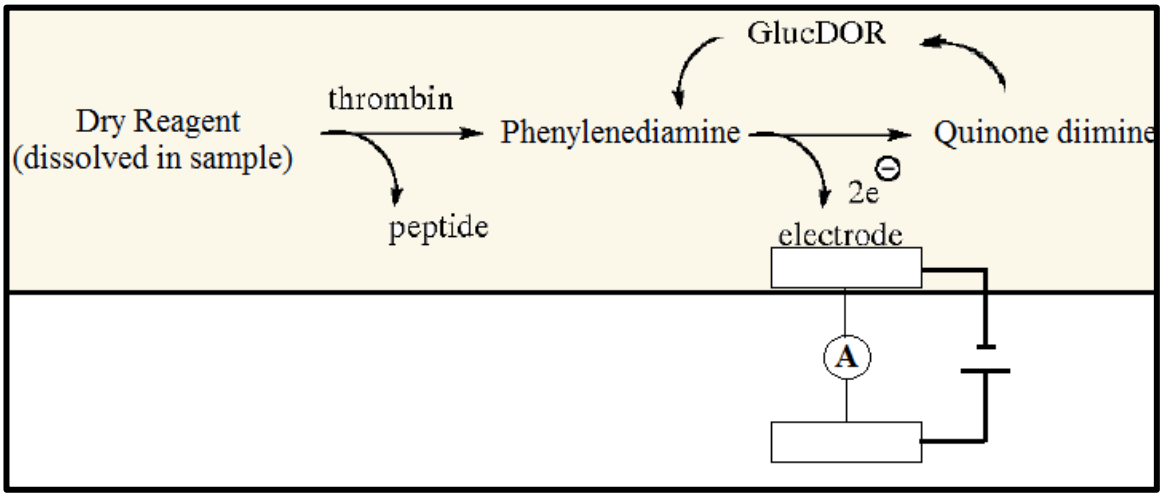

Figure 1.2: Schematic of the electrochemical clot measurement system. The current measured between the two electrodes varies according to the amount of thrombin in the sample. The measured PT occurs when the current exceeds a predetermined threshold.

An advantage of electrochemical methods is that they are relatively insensitive to motion of the sensor during measurement. The disadvantage of these methods is the susceptibility to interfering substances.

Optomechanical

The microfluidic optomechanical method is used by ITC in their Hemochron® Signature Elite measurement system and measures the clot time based on the change in physical properties of the sample [26]. The finger-stick sample (around 20 µl of whole blood) is introduced into the measurement cuvette and 15 µl of this is partitioned into the microfluidic test channel where it interacts with a clotting agent. The sample is mechanically moved back and forth within the channel (*figure 1.3*). Light emitting diodes are mounted in two positions along the sample window, and the optical absorption through the window is monitored as a measure of the speed at which the sample moves in the channel. Clot formation slows the sample motion, and the clot time is measured at the point at which the sample speed falls below a threshold value.

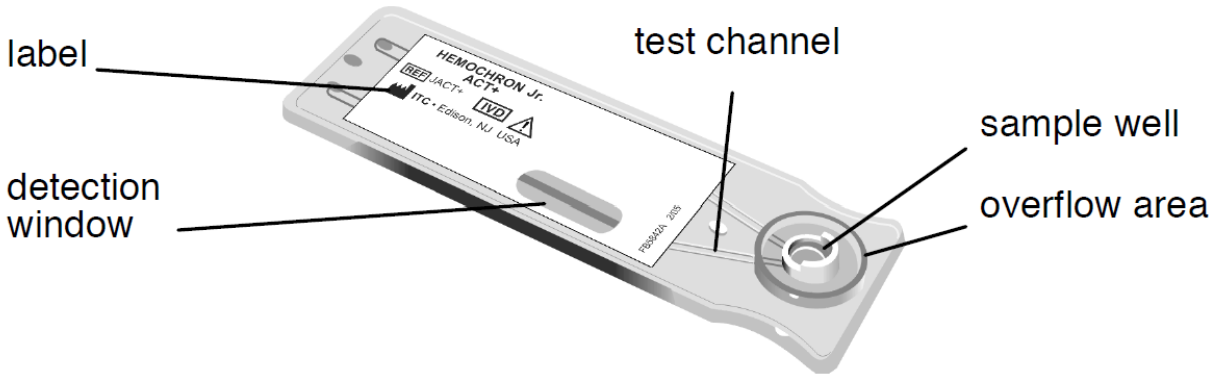

Figure 1.3: Cuvette used in Hemochron® Signature Elite for optomechanical detection of blood clotting. LED's against the detection window monitor slowing of the sample in the channel to determine clot time. Reproduced from [26].

The advantage of this test system is that it measures the physical change in the sample due to blood clotting (i.e. fibrin formation) for an accurate determination of the PT. The disadvantages are that it can be inadvertently affected by particulate contamination or air bubbles in the sample that may obstruct the channel or optical paths of the sensor.

The Hemochron series is primarily directed at bedside measurements performed by healthcare professionals rather than for home use.

Optomagnetic

Various optomagnetic techniques are used by Roche in their popular Coagucheck® product family [22], by Unipath Ltd. in their SmartCheck INR™ [27], and by Cardiovascular Diagnostics Inc. in the Thrombolytic Assessment System (TAS™ PT-One) [28] for citrated whole blood. The blood sample enters a channel in the test strip containing paramagnetic iron oxide particles or a small magnetic disk which becomes suspended in the sample. A magnetic field is used to oscillate the particles or disk, but as the clot progresses the motion of the particles becomes increasingly damped. Motion of the particles or disk is measured optically.

1.3.3 The Microvisk sensor

At the time of writing, Microvisk Limited are a venture funded small business operating in St Asaph, and Oxford, UK, employing around 40 people for the development and manufacture of a bioMEMS coagulometer. Founded in 2004 as a spin out company launched from the Science and Technology Facilities Council (STFC), they hold several patents in the field of fluid probes [29–31]. Microvisk Limited is developing the world's first polymer bioMEMS medical diagnostic device.

Microvisk products Coagmax and Coaglite are designed to help patients and healthcare professionals manage a program of oral anticoagulation therapy through self-monitoring of blood clot times. Unlike competing technologies, the microcantilever sensors *(figure 1.4)* within each SmartStrip respond to the physical properties of blood as a clot forms, and are unaffected by the optical properties of the sample. One disposable SmartStrip is used per test and the results are reported and tracked using the Microvisk CoagMax handset.

The cantilever beam is composed of three polymer layers, between which are two sets of metal tracks: gold for electrothermal actuation; and constantan for piezoresistive read out. The uppermost polymer layer has a higher coefficient of thermal expansion (CTE)

than the lower layers resulting in changes in the beam curvature with temperature on the same principle as the bimetallic strip. The reason that polymers are used as the structural layers is that the combination of large difference in CTE, of almost 60 ppm/°C, and low Young's moduli allow the beam to achieve deflection range on the scale of tens of microns. Such large deflection is readily detected by the integrated piezoresistive tracks without the need for precise optical instrumentation. The innovative use of polymers paved the way for increased portability, and hence, the commercial exploitation of the sensor. The foot-print of each sensor is reduced through the innovation of backside contacts to enable high density wafer fabrication.

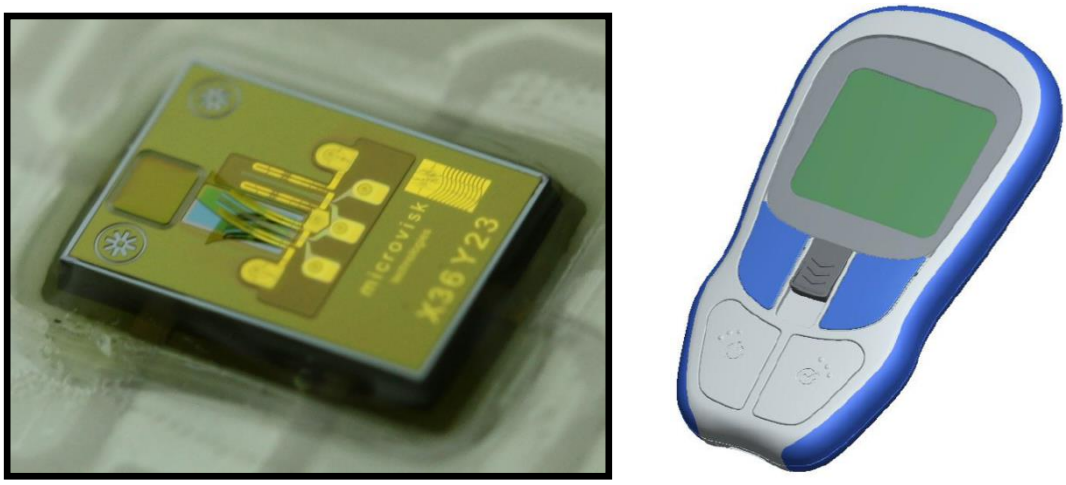

Figure 1.4: The MEMS sensor chip contained in each SmartStrip (left). The three-legged 'Epsilon design' of the released polymer microcantilever is visible protruding from the surface, with gold heater loops on the two outer legs and a constantan sensor in the centre. The reagent pad and contact vies are seen close to the tip and base of the beam respectively. The CoagMax handheld interface (right). Images courtesy of Microvisk Ltd.

The SmartStrip provides the interface between the patient and the sensor. A fluidic channel is used to wick a finger-prick of blood (less than 10 μl) towards the sensor by capillary action aided by the hydrophilic top sheet. As the blood passes over the reagent pad close to the tip of the microcantilever sensor, the dried thromboplastin clotting agent is re-dissolved and initiates the blood clot. The main components of the strip are shown in *figure 1.5*. Oscillations in the cantilever are induced by a voltage spike (0.5 ms, 6 V) delivered to the heater tracks. Motion is damped by the surrounding fluid. When a blood clot forms around the cantilever, the effect of the damping increases

sharply. A reference microcantilever (not released from the substrate) is used to remove some of the thermal background from the signal via arrangement in a Wheatstone bridge configuration.

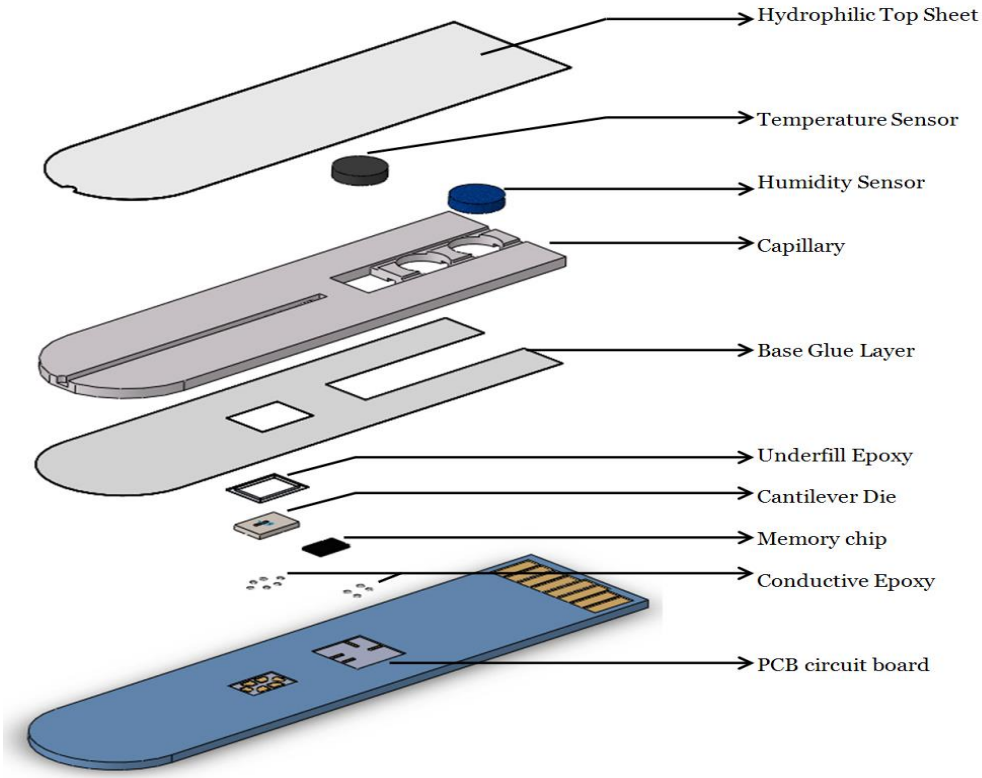

Figure 1.5: Exploded schematic view of the SmartStrip, courtesy of Microvisk Technologies Ltd.

Two sensors are included on each strip to measure temperature and humidity. Reactions in the clotting cascade are temperature dependent and proceed optimally at body temperature. Strips are supplied in sealed pouches with low moisture-vapour transfer rate containing a molecular sieve to preserve the low humidity environment of the assembly cleanroom. If the packaging becomes damaged and the strip is exposed to high humidity during transit, the strip may be damaged as detailed in Chapter 3 of this thesis, though the humidity sensor within the test strip will signal to the patient that a result cannot be obtained from a damaged strip, so the risk to the patient is minimised.

The CoagMax handset *(figure 1.4)* interprets the microcantilever sensor signal and presents it to the patient. This device contains the actuator driver, Wheatstone bridge supply and bridge completion resistors, high pass and low pass filters, amplifiers and

differentiator. Filtering is used to isolate the signal components in the low frequency region, which are the most affected by clot formation. Also contained within the handset are the heater used to keep the clotting reaction at 37 ± 0.5 °C throughout the test and an optical sensor to check that the strip has been inserted in the correct position. The test will not run unless the optical sensor response is satisfactory. The power supply (including re-chargeable battery, and mains charging adaptor) microcontroller, push-buttons and LCD display screen complete the device.

1.4 Scope and Structure of Thesis

This thesis concerns polymer microcantilever sensors with piezoresistive sensing and thermal actuation, with the specific example of the Microvisk SmartStrip sensor for measuring blood coagulation times. The work presented was conducted by the author between 2009 and 2011 at STFC, and between 2011 and 2012 at Microvisk Limited. The aim of the thesis is to investigate parasitic elements in the signal that may be due to moisture ingress in the polymer layers, sample density or the thermal properties of the sample.

In Chapter 2, a comprehensive survey on how the most basic MEMS structure, the microcantilever, can be used in a variety of sensing configurations for diagnostic sensors is presented. This chapter includes a critical examination of the relationship between beam design and function, and uniquely includes a review of 'pulsed actuation' methods as well as the more common static and resonant techniques. Once the techniques are introduced, the chapter looks at aspects of the design that might present problems for commercialisation. Chapters 3 and 4 are based on a series of experiments conducted at Microvisk, St Asaph, between January and June 2012. Chapter 3 discusses the impact of the ambient humidity on sensor yield and performance. Water sorption is a major implication of using a polymer material rather than silicon for the sensor beam. The investigation includes an expansion to the thermal bi-material actuator model to include the effect of ambient humidity. The model is then used to demonstrate how the deflection of the beam can vary significantly from its fabrication until it is used by the patient. Although the deflection sensitivity to moisture is comparable to the sensitivity to temperature, it was demonstrated that when the cantilever is operated by pulsed actuation, humidity does not impact device performance. In Chapter 4, the widely

reported idea that the clot sensing capability of the Microvisk sensor is due to the changing viscosity of the sample is re-examined. It is demonstrated that the sample viscosity has a much greater effect than sample density, though the contribution of mass loading remains an area for further investigation. The design, fabrication and characterisation of a new microcantilever sensor are presented in Chapters 5 and 6. The new sensor is an adaptation of the Microvisk sensor that it is 'blind' to the piezoresistive element of the sensor signal. The aim of doing so is to further investigate the thermal crosstalk in the signal and to determine whether it could have an effect on the measured clot time. Chapter 7 presents the main conclusions and an outline for further work resulting from this study.

Chapter 2
Literature Review of Microcantilever Biosensors

2.1 Introduction

Miniaturised handheld diagnostic devices are reducing the burden of regular testing on the healthcare industry and improving the quality of life for patients. A typical diagnostic will contain many of the following elements: sample inlet; sample preparation; reagent addition; reaction chamber; transducer and display. The role of the transducer is to convert a property of the sample, such as the presence of an antigen, the amount of glucose, or the coagulation status, into a signal that can be interfaced with the display module or be directly understood by the patient.

Different approaches to sample transduction in handheld diagnostic devices include optical techniques such as absorption, fluorescence and surface plasmon resonance; surface acoustic wave sensors; electrochemical cells and mechanical techniques such as the quartz crystal microbalance and the microcantilever. The transduction technique chosen depends greatly on the diagnostic application. For example, mechanical and fluidic techniques are both excellent methods to monitor blood clotting kinetics, where the rheology of the sample changes over time; whereas a labelled sandwich assay, such as the human chorionic gonadotropin assay in a pregnancy test, is transduced by optical

absorption methods, or visually by the patient. Microcantilevers require a two-part transduction stage: a property of the sample changes the mechanical properties of the beam; then a read-out system is used to monitor the beam and generate a signal.

It is beyond the scope of this review to detail and contrast all available transduction techniques. Within the field of microcantilever sensors, there is a wide variety of sensing modes and designs. A key requirement for a commercially viable sensor is that it should be specific to the target analyte or physical property change. This is often a problem for microcantilever sensors, as there are many possible sensing modes. The aim of this review is to give an overview of microcantilever biosensors developed in academic laboratories and discuss their potential for commercialisation. An emphasis is given to polymer microcantilevers.

In comparison to recent reviews on microcantilever sensors [32, 33], this review includes "ringing mode" operation of the cantilever, along with the more usual static and resonant modes of operation. Ringing mode operation is useful for applications that require low power to probe the bulk properties of the fluid, because actuations of the cantilevers are spaced at a lower frequency than the resonant frequency of the beam. The first part of this review details the techniques used in the state of the art microcantilever biosensors. The second part of this review uses a technical perspective to address the question 'why are there not more microcantilever biosensors being commercialised for consumer or point of care applications?'

Microcantilevers may be operated as static stress sensors, resonant mass sensors or in ringing mode and nearly all are coupled to a read out element that is either optical or electronic, to quantify changes in beam deflection. Sensors that use resonance or ringing mode also require an actuation mechanism. A chart summarising these design features as they are presented in this literature review is presented in *figure 2.1*. In the actual design of a sensor, these features are interdependent and the impact of each on the other should be considered.

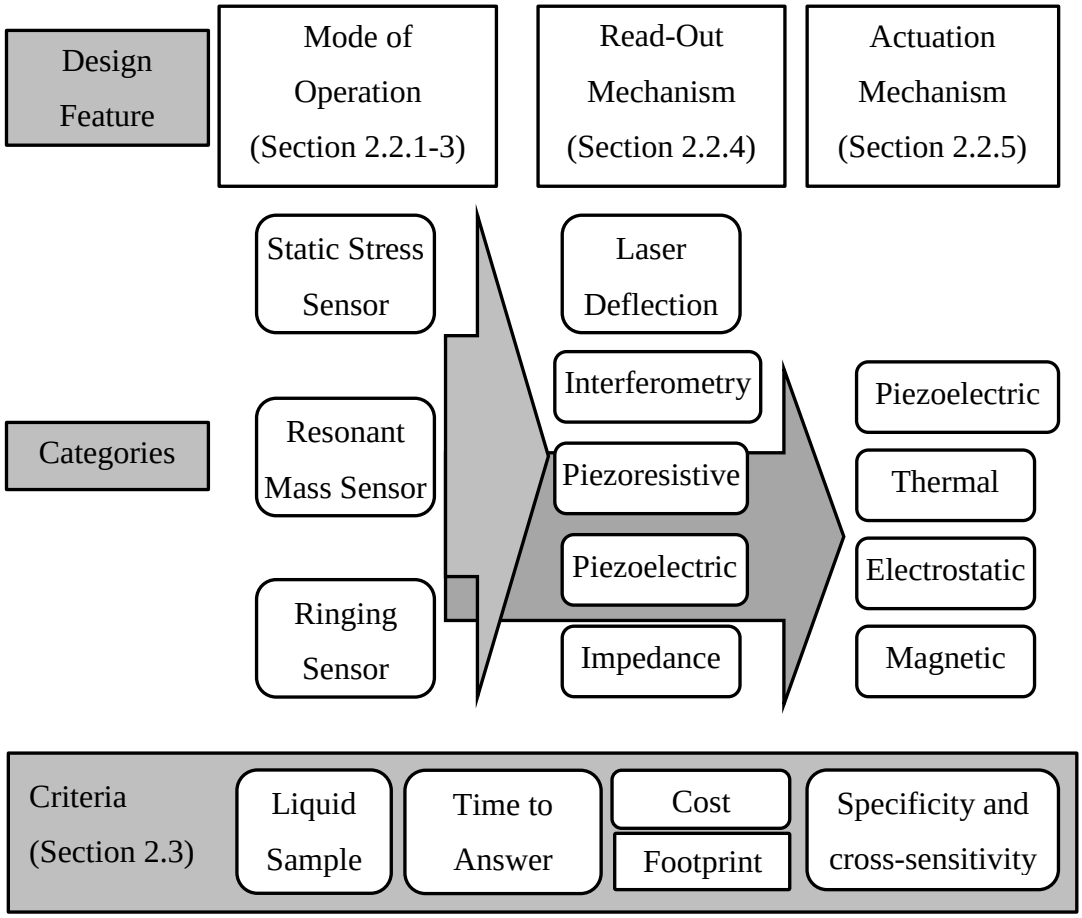

Figure 2.1: Summary of different microcantilever features and modes of operation.

2.2 State of the Art Microcantilever Sensing

2.2.1 Static Stress Sensors

Static stress sensors depend on the strain mismatch between two dissimilar layers causing a stress profile through the beam thickness that produces a bending moment on the beam. There are two categories of stress based sensor: surface stress and bi-material. Bi-material sensors have a film layer of a similar thickness to the beam. These sensors are most commonly attuned to physical properties such as temperature [34], [35, 36], water sorption [37], [38], [39] and also for chemical detection [40]. In each case the deflection is caused by swelling of the film layer relative to the beam substrate. When the film is very thin compared to the beam, the cause of generated stress is primarily lattice mismatch between the film and beam, and the device is known as a surface stress sensor. This type of sensor is well adapted for use as an affinity biosensor because molecular binding events occurring on the film alter the strain in the

film and cause a change in deflection. This concept was first demonstrated for the spontaneous absorption of alkanethiol monolayers onto a gold surface by the IBM research group in Switzerland [41]. The group have subsequently measured adsorption in liquids [42], DNA binding [43], and demonstrated an artificial nose that can measure several analytes simultaneously [40]. Other groups that have had notable success with surface stress sensors are Shu's group at Heriot Watt University, UK, who monitored yeast cell proliferation using a polymer cantilever [44], Dravid's group at North-western University, USA, who used surface stress changes to detect protein concentrations down to 100 fg/ml [45], and Chang's group from the National Taiwan University, Republic of China, who detected the hallucinogen MDMA over the range 5 – 50 μg/ml in buffer [46]. The relationship between surface stress and amount of target sample absorbed onto the cantilever surface is difficult to predict. An empirical calibration must be made in order to relate bending to analyte concentration. In addition, where non-specific binding occurs and the target species becomes interspaced with other species on the cantilever surface, the surface stress will be disrupted. Therefore it will be difficult to calibrate a surface stress based sensor to relate the stress induced deflection to the concentration of target analyte in solution in the presence of interfering substances, i.e. in a real sample of serum or urine, the composition of which will vary between patients. Investigations into the nature of surface stress by the McKendry group (UCL, London, UK) suggest that intermolecular bonds formed between adsorbed molecules on the surface affect the stress signal in addition to surface coverage of the capture molecule [47, 48].

The most appropriate read-out mechanism to use depends on the amount of bending expected. Where relatively stiff beams are used, deflections may be as small as a few nanometres and accurate optical techniques and vibration control are required. Larger stress induced deformations give more choice in sensing technique, but require careful calibration to compensate for the fact that tip deflection is increasingly non-linear.

2.2.2 Resonant Mass Sensor

Resonance frequency shift upon specific binding of a target analyte can be achieved via four different sensing modes: thin layer adsorption on the beam surface; point mass; the

inertia of swept liquid and mass added inside the cantilever in the technique known as Suspended Microchannel Resonance (SMR). These techniques are shown in *figure 2.2*.

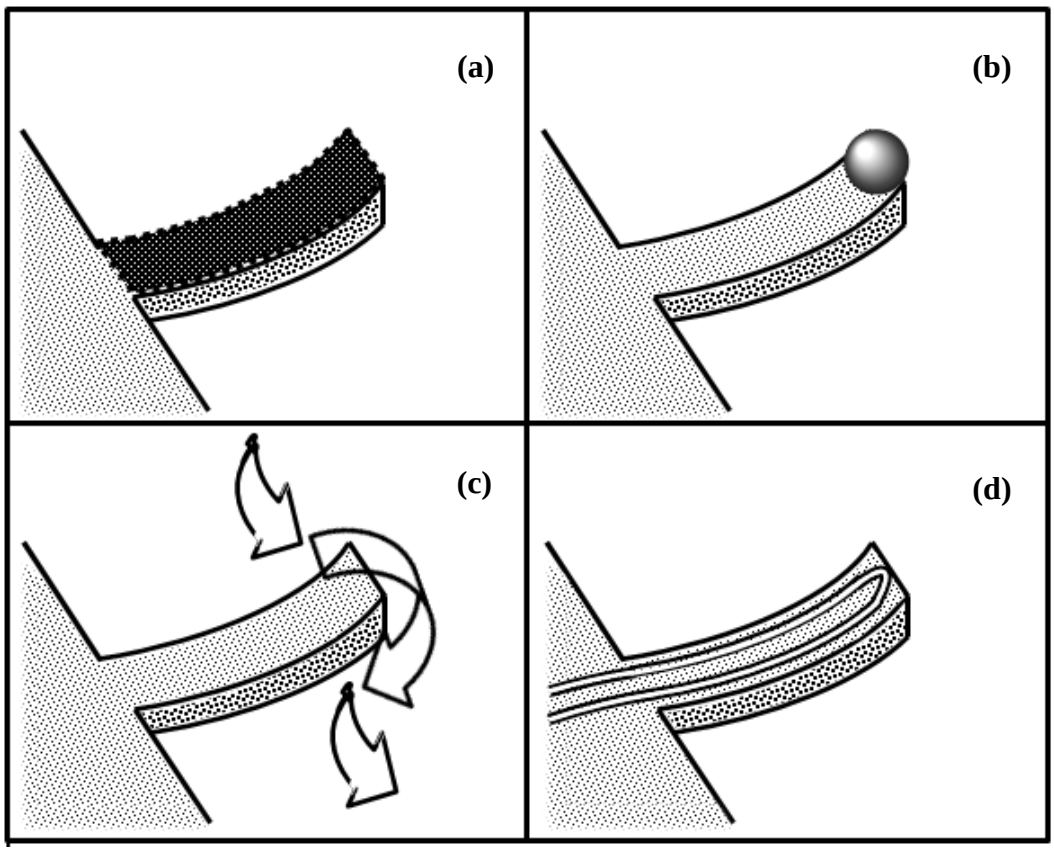

Figure 2.2 Sensing modes using resonating microcantilever sensors. Thin layer absorption (a); point mass attachment (b), liquid inertia (c) and suspended microchannel resonance (d).

Point mass addition *(figure 2.2b)* is the simplest technique and has been demonstrated for single cell detection [49] and bacterial cell detection at clinically relevant levels [50].

The shift in resonance frequency of a microcantilever upon adsorption of an analyte uniformly over the surface, for example in label-free immunoassay to ng/mL concentrations [51], involves consideration of the added mass of the analyte, its contribution to the stiffness of the beam and also the effect it has on the surface stress. A full treatment of these effects was considered by McFarland *et al* [52, 53]. The resonance increase due to adsorbate stiffness is thought to increase faster with adsorbed

layer thickness than the resonance decrease due to added mass [54]. If all of these effects are considered, it again becomes difficult to relate the concentration of a target analyte in a real sample to the shift in resonance frequency in a purely analytical way. Grüter and co-workers have recently made progress in teasing out these two effects by analysis of the quality factor and resonance frequency of silicon microcantilevers coated with copper film [55]. The film is known to form islands as the thin layer is slowly deposited by evaporation, before coalescing into a uniform layer. Thus the effects of mass alone were observed for small average thickness (3 nm) where the isolated island structure prevents stress in the layer from altering the flexural rigidity of the cantilever.

When a cantilever is oscillated in liquid, there is a shift in the resonance peak position caused by greater effective mass of the cantilever due to the inertia of liquid that is oscillated in phase with the beam, and an increase in the broadening of the resonant peak due to energy dissipation where fluid is out of phase with the beam [56]. The group led by Dufour, from Université Bordeaux in France have studied microcantilever rheometers extensively and have concentrated on semi-empirical derivation of analytical expressions to determine the fluid viscosity from the frequency spectrum [57]. Preliminary work on wire based sensors suggested that sensitivities of less than 1 cP are readily achievable [58].

Viscous liquid damping of the resonance signal is a problem when trying to measure the resonance shift due to analyte binding. Suspended microchannel resonance (SMR) is a technique developed by Manalis and co-workers at MIT, Massachusetts, US, to solve this problem and has recently gained much attention. The fluidics that carry the sample are contained within a microchannel embedded in the cantilever beam itself. The inside of the channel may be functionalised with specific binders for the target analyte [59], and when the target analyte accumulates in the channel, the resonance frequency shifts in correlation with the difference between the sample mass and the mass of the liquid volume displaced. When two beams are run in parallel with different density fluids in each, a measurement of the mass of binding analyte can be made. The technique has also been used in combination with cell trapping to weigh single cells [60]. However, it is sensitive to the viscosity and density [61] of the carrier liquid in a complicated way that depends upon the channel height and excitation frequency [62].

2.2.3 Ringing Viscosity Sensors

Relatively few studies exist looking at sensing applications of a microcantilever based on the mechanical response to a pulsed actuation. Using this technique, it should be possible to obtain information on the damping of the system (for example, the increasing viscosity of blood as a clot is formed) as well as frequency shifts due to added mass in the time domain and the thermal time constant of the system. This technique lends itself particularly well to thermal actuation because it is possible to obtain high thermal gradients local to the beam without significantly heating the bulk of the sample.

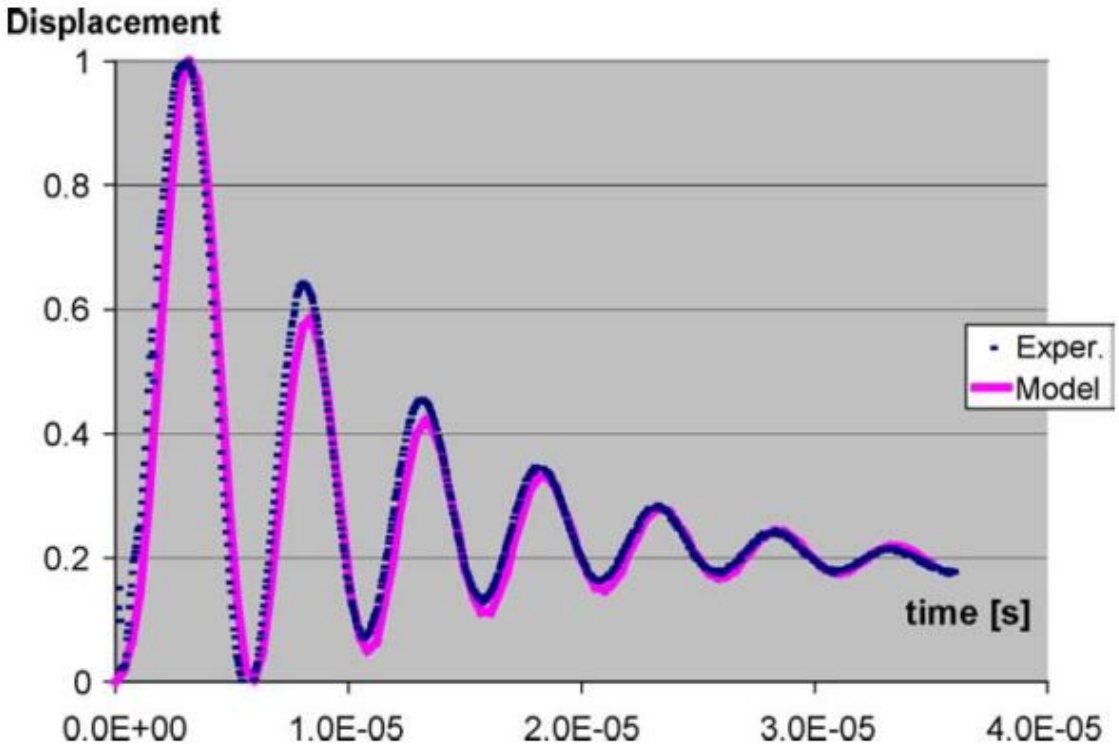

Figure 2.3 Example of a microcantilever tip motion following pulsed actuation in a liquid sample. The displacement is normalised. Reproduced from [63] *with permission.*

The frequency response of a simple microcantilever beam to an impulse load in damped media can be simulated [63] using the equation of motion in (2.1). The temporal profile of a 1D beam, $z(x)$ is a function of the beam thickness, t_b, Young's modulus, E and Poisson ratio, σ. The surrounding fluid can have two effects on the motion of the beam: inertia of fluid pushed by the beam $n\rho_f t_b$; and the effect of viscous drag ($\gamma\, \partial y/\partial t$ where γ is proportional to viscosity):

$$\left(\rho_b + n\rho_f\right)t_b \frac{\partial^2 z(x)}{\partial t^2} + \gamma \frac{\partial z(x)}{\partial t} + \frac{E{t_b}^3}{12(1-\sigma^2)} \frac{\partial^4 z(x)}{\partial t^4} = 0 \quad (2.1)$$

In equation (2.1), ρ_b is the density of the cantilever, and ρ_f is the density of the fluid. Equation (2.1) may be solved with the boundary conditions that the beam is initially flat and still, remains anchored at all times and undergoing only lateral bending modes. Numerical solution of this equation was performed by Cabal and co-workers simulating a 1.5 µs pulse delivered by thermal actuation to a silicon nitride / titanium alloy cantilever as part of an inkjet dispenser. The simulations compared well with experimental results for the beam tip deflection in air and ethanol for optimised *n* (multiple of the beam volume that indicates how much fluid is moved by the beam) and γ *(figure 2.3)*. The frequency response matched well to solutions of the Euler-Bernoulli equation, though the full simulation is required to predict the damping. In equation 2.2, the general form of solutions to equation (2.1) is shown for the resonant frequency ω where *D* is the flexural rigidity of the beam and ω_0 the first eigenvalue solution.

$$\omega = \frac{1}{2\pi}\frac{\omega_0^2}{L^2}\sqrt{\frac{D}{(\rho_b+\eta\rho_f)t_b}}\sqrt{1-\frac{\gamma^2 L^4}{4\omega_0^4 D\,(\rho_b+\eta\rho_f)t_b}} \quad (2.2)$$

A similar study was conducted by Han and Chen of the University of Texas, Austin, US, who constructed a numerical solution for the case of thermally induced bending of a bi-material beam in gold and polysilicon subject to a 12 ns laser pulse. The group used an energetic approach to formulate the Lagrangian and solved the Euler-Lagrange equation of motion numerically. They also found that eigenmode frequencies are similar to that obtained from the solution of the Euler-Bernoulli equation [64]. Earlier numerical studies on macro-scaled steel rods showed the influence of pulse length, and the position along the beam at which the pulse is applied. For a cantilever actuated at the tip, shorter pulse lengths increase the predominance of higher order deflection modes. However, the higher deflection modes are preferentially damped when the viscosity of the environment increases. For highly damped systems, only the fundamental mode is excited [65]. In contrast, Moulin and co-workers found that for chevron shaped cantilever beams, ringing was not observed when the beam was heated at the tip, but was observed when the whole beam was heated [66]. This is because the

thermal conduction down the cantilever length is slow compared to the ringing. The greater the thermal isolation, the higher the ringing amplitude as the beam retains more energy from the pulse in the form of elastic energy.

In 2004, the group at Rutherford Appleton Laboratory looked at pulsed actuation of polymer-metal thermal bi-material strips with a view to biosensing applications. They used very high power pulses and obtained large, reversible deflections [67], however it should be noted that too high a thermal shock can permanently deform the cantilever if it is taken beyond the elastic limit of the materials [68].

There is greater propensity for higher order modes to exist in the beam stress than in the tip deflection following application of a short pulse. This may discourage use of piezoresistive stress sensing for impulse-response study of the beam because the superposition of modes will result in a signal that requires greater processing. In comparison, optically monitoring the tip deflection, where the fundamental mode is predominant mode should give a smooth signal in the time domain. When the beam is heavily damped however, the contribution of the higher modes in the stress signal is preferentially diminished compared to the fundamental mode, indicating that it should also be possible to obtain a smooth signal using a piezoresistive sensor in liquids [65].

2.2.4 Read-Out Mechanisms

Sensing mechanisms to read-out the mechanical changes in the microcantilever beam can be broadly categorised as either optical or electronic. A simpler beam design can be used with the optical techniques reducing cost and cross-sensitivity on the beam, but increasing the cost and complexity of the sensor housing. The most widely established read-out method is the optical lever, where a laser beam is deflected from the tip of the microcantilever onto a position sensitive detector. Distance between the cantilever and the detector magnifies the deflection, allowing detection of sub-nanometre changes in the beam deflection [69], [66]. When this detection method is used for static mode stress sensors, increasing the length of the beam enhances sensitivity because small beam deflections scale quadratically with length [70]. For resonance measurements, the beam length should not be increased because this will decrease the resonant frequency relative to the thermal noise. Other techniques, e.g. perforated beams may be used to

increase the sensitivity [71]. Also attracting attention for use with microcantilever arrays are interferometric techniques [72], and the use of the cantilever as a waveguide [73], whereby deflection of the cantilever reduces coupling of the incident light path.

The most common form of electrical read-out is the piezoresistive sensor. A serpentine track [74], [75] is embedded within the cantilever. Sensitivity is enhanced when the piezoresistor is close to the top surface, but the resistor itself needs to be encapsulated from electrolyte samples posing limitations on the cantilever thickness and introducing complexity. Optimisation of a piezoresistive cantilever may vary, depending on whether point loading or distributed load causes the beam deflection, according to an experimental study of quasi-static beam deflection by Loui and co-workers. For tip loading the beam should be long and narrow and for surface stress sensing it should be shorter and wider [76]. Alternatives to the piezoresistors for electronic sensing are capacitive sensors [77] and piezoelectric sensors, where measurements are taken in resonance mode, and impedance measurements provide on-chip means with which to both drive and also record the frequency of oscillation [78].

2.2.5 Actuation Mechanisms

Actuation is usually required whenever resonance or pulsed mode operation is used. Oscillations from ambient thermal excitation are only sufficient for identification of resonant frequency shifts at the cost of long measurement times [49], [79]. When microcantilever sensors are made by customising a commercial AFM set up, the actuation mechanism is usually a piezoelectric oscillator proximal to the beam. In this method the whole experimental set up (except optical components) is vibrated. In this section, integrated actuation mechanisms including optothermal, electrothermal, electromagnetic and piezoelectric actuation are briefly described.

In optothermal actuation, a laser beam is focused onto the cantilever tip, causing localised heating, and the resulting deflection of the cantilever is linear with irradiation power [80], [81]. Pulsed laser sources may also be used to excite resonance [64].

There are two categories of thermally actuated microcantilever, both of which are referred to in the literature as thermal bimorphs. For clarity, the term 'bi-material strip' here refers to the vertically actuated thermal bimorph actuator where the motion is due to unequal coefficients of thermal expansion of two thin layers, and 'lateral thermal actuator' to describe single layer structures where two conductive cantilevered beams are joined at the apex. In such structures, one of the beam legs is made thinner than the other and so will incur more resistive heating and hence undergo greater thermal expansion upon actuation making the beam bend [82]. In both cases, actuation frequency is limited by the thermal time constant of the beam.

The electromagnetic technique can be up to two orders of magnitude more efficient than electrothermal actuation, and the correspondingly low heat dissipation upon exciting the cantilever to resonance improves the sensitivity [83], and has been demonstrated in liquid environments [84].

The principle of operation of piezoelectric actuation stems from its crystalline structure: the application of an electric field along a crystal plane enhances the electrostatic interaction between anion and cation already present, causing expansion and contraction and associated strain in the material. Piezoelectric materials are capable of operating at high frequencies, even on the macro scale [85], [86], and although sometimes limited in amplitude, this limitation can be overcome through design concepts such as multi-layered alternately poled structures. The drawback is that this layering induces additional complexity into the fabrication of the beam. There is ongoing research to develop new crystals with ever higher strain-to-applied field ratios in order to overcome this limitation.

2.2.6 Polymer Microcantilevers

Polymer cantilevers have been developed by several research groups due to their low Young's modulus compared to traditional silicon-based cantilever materials, which means that large displacements can be achieved with relatively low power. Typical Poisson's ratios for polymers are 0.3 to 0.5, compared to 0.2 for silicon derivatives, but this is more than compensated for by the difference in Young's modulus. *Table 2.1*

details the material properties of polymer cantilevers used for biosensors through the mechanism of surface stress, with traditional materials shown also for comparison.

Polymer	Thickness (μm)	Dimensions (μm)	Young's Modulus (GPa)	Notes	Ref.
SU-8	2	75 x 200	2 – 3	10μg/ml C-reactive protein (13mN/m)	[73]
SU-8	3	120 x 250	2 - 3	4.1mN/m	[87]
Polyimide PI 2562	7	100 x 400	1.8	0.21mN/m	[88]
Cyclic Olefin Copolymer	-	-	3	Proposed material for injection moulded cantilevers	[89] [90]
Polypropylene	-	-	1.3-1.9		[90]
Polyvinylidenfluoride	30	-	6.7		[90]
polyoxymethylene copolymers	-	-	6.7		[90]
Polyimide PI 2610	-	-	8.5	-	[91]
Traditional Materials					
Si_3N_4	-	-	190	-	[73]
Polycrystalline silicon	-	-	165	-	[70]

Table 2.1 Material properties of some polymers and their use in microcantilever surface stress sensors.

An additional advantage for polymer microcantilevers is that it is possible to modify the surface properties of the polymer in order to promote direct functionalization (of an antibody for example) to the surface [73, 92–94]. This is a preferable alternative to the gold-thiol linkages commonly used on silicon substrates as it avoids unwanted deformations based on mismatched thermal expansion between the surface and the bulk of the beam. When surface modification is achieved using a directional method such as chemical vapour deposition [87], this reduces the amount of unintentional binding to the backside of the beam, which would otherwise reduce the sensitivity. In addition, the reported sensitivity to pH for an SU-8 microcantilever is reduced compared to gold coated silicon nitride.

The drawback to using polymer cantilevers is that at present, insufficient research has been done to address the problem of integration of the electronic components (particularly when using piezoresistive methods for measurement of deformation). The

problem is exacerbated when making highly multiplexed arrays, therefore silicon remains a promising stress sensing material for commercial sensor development despite its limitations to stress sensitivity [74].

2.3 Towards Commercial Biosensors

Point of care or home use biosensor devices might look and operate rather like a 'chip and pin' credit card machine, with the sensor being the 'card' and the transducer and user interface being provided by a separate 'reader'. The sensor should be disposable in order to contain potentially biohazardous patient specimens. The reader should also be small and ideally handheld if it is used for a consumer application. It should require only simple user inputs and display an unequivocal and correct result within a few minutes. In the previous section we reviewed the main techniques that are used for microcantilever sensing. In this section, we evaluate how those techniques have been selected and modified to move towards clinically useful sensing.

2.3.1 Time to answer

The factors that determine the response time of a typical microcantilever affinity biosensor (i.e. a sensor that detects formation of an analyte layer on the surface) include: concentration of target analyte; size of the cantilever, size of the flow cell, binding affinity and reversibility, deflection, stress or resonance sensitivity and detection mechanism. In addition, there is often drift in the beam deflection upon the addition of liquid, which may take hours, or days to settle [95]. The drift is often attributed to thermal equilibration or the effect of water on the beam surface [96]. Unless this can be wholly avoided, for example by using a reference beam for differential sensing, practical applications will be limited to resonant or pulsed mode applications. In addition, the long data collection times required for weak resonance signals limit the use of non-driven resonance measurements.

Figure 2.4 shows the binding of e-coli to a functionalised millimetre long piezoelectric cantilever in a liquid flow cell [85]. In this case it seems that the availability of binding sites limits the time to answer at high bacterial concentrations. In a consumer or

commercial setting (e.g. for performing spot-checks on food and beverages), a time to answer of 20 minutes would be too long. However for such an application it would not be necessary to know whether you have 1000 or 10,000 EC/mL, just that a significant level of contamination is present. Therefore the answer could be based on a cut-off of a few minutes.

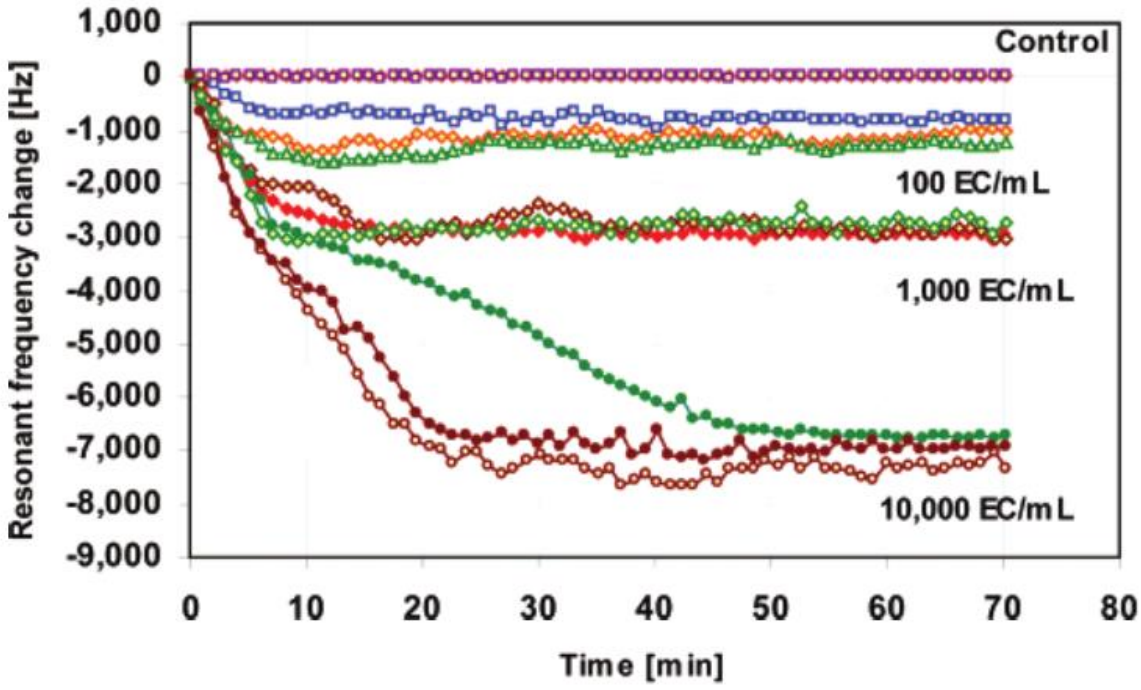

Figure 2.4 Real-time measurements of the binding of e-coli (EC) to a functionalised millimetre long piezoelectric cantilever in a liquid flow cell at 1ml/min. There are three measurement traces at each of the three concentrations. The control lines are for 0 EC/mL in buffer. Reproduced with permission from [85]

The binding affinity and 'on rate' are specific to the analyte/antibody combination under study; high affinity antibodies are not available for every analyte. Many biosensors use the biotin-streptavidin reaction for proof of concept, due to the exceptionally strong binding affinity (10^{-15} M) of this reaction [45, 97–100]. Typical binding affinities are at least a factor of 3 lower than this [101] and some, such as the aggregation of the protein α-synuclein are so low that they would not be suitable for commercialisation in a biosensor format [48]. Assay kinetics may be optimised through temperature and pH regulation. To optimise the binding kinetics through sensor design it is ideal to

minimise the size of the liquid cell with respect to the cantilever surface, thus limiting the distance that an analyte must diffuse to reach the beam [102].

Analysis of the time to answer in the SMR configuration was considered as a sensitivity limiting parameter by Arlett and Roukes *(figure 2.5)* [103]. High sensitivity is achieved by scaling down the mass of the beam. However this also constrains the dimensions of the embedded fluidic channel and hence the liquid volume that can interact with the functionalised inner channel walls per second. Assuming that the reaction is fast and irreversible, this places a limit on the device sensitivity, because the liquid cannot be made to flow in the channel at arbitrarily fast speed due to the pressure that would be generated. However due to the high sensitivity of this mode of operation, it is still possible to achieve pico-molar limits of detection for proteins within a few minutes.

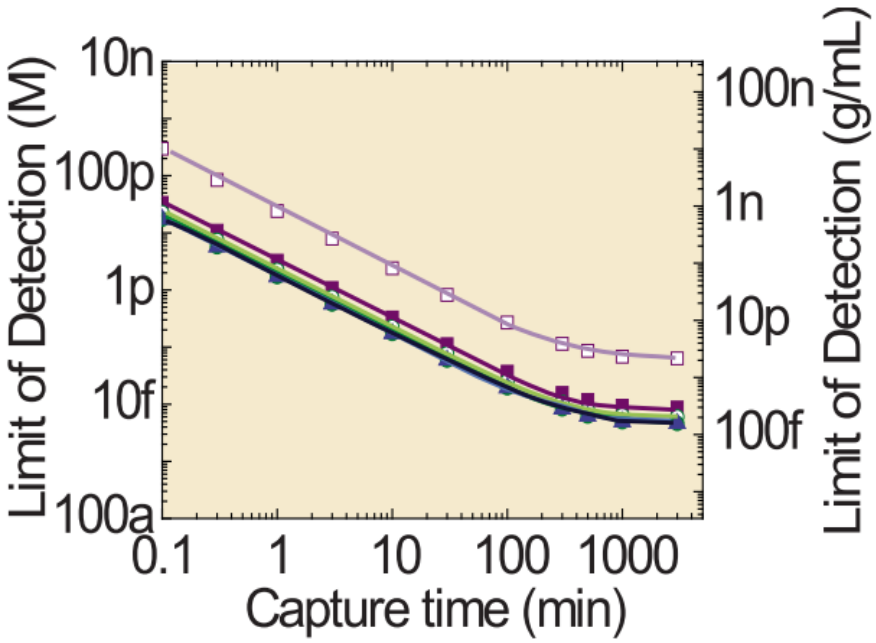

Figure 2.5 Analysis of how the resolution of a suspended microchannel resonator (20 × 4 × 0.7 µm) must be compromised in order to achieve a reasonable time to answer. The analyte in this example is prostate specific antigen. Reproduced with permission from [103].

2.3.2 Cost of Manufacture

The inherently small size of microcantilever sensors suggests low cost per sensor both for device fabrication and for any specific coatings, such as antibodies, used as sensing layers, which are often expensive and limited in supply. Three approaches may be taken to keep the manufacturing cost per device low: make the sensor chip as small as possible to maximise the number of sensors per wafer; use established semiconductor processing protocols such as the Multi-User MEMS Process [64, 104, 105], Complementary metal–oxide–semiconductor [56, 74] or silicon on insulator [106]; or move away from silicon processing towards reel-to-reel manufacture. With established techniques, not only can development and infrastructure costs be reduced through outsourced manufacture, but some or all electronics can be integrated onto the same chip. Microfabrication of polymer devices is inexpensive compared to silicon micromachining when performed at the batch scale. Further research is underway to drive costs down by fabricating sensors using ultra low cost injection moulding techniques [107–109], though use of this technique may limit the complexity of design.

The infrastructure and running costs required to support MEMS fabrication and assembly are significant, but falling. There are also several foundries in the UK [e.g. INEX, SEMEFAB] currently offering design development and fabrication of MEMS components which can help reduce the sensor development costs. A more prohibitive cost may be the level of development still required to automate the assembly and packaging processes [110], as this topic is not well addressed in the literature.

Another significant barrier to commercialising some of the work reviewed thus far is that almost all of the sensing platforms have been prepared for a specific application, for example to detect prostate specific antigen. Individual applications may not alone justify the development cost of the sensor. What is needed is a generic platform that can be used to test for any number of different disease biomarkers, which may have a wide range of clinically relevant concentrations and have differing binding affinities. This has not, specifically, been demonstrated in the literature, although some of the most established research groups in the field have continually adapted the same core technology for a number of different applications. An example of this is Manalis and

co-workers with SMR. With a multi-application sensing platform, the economies of scale could be met.

2.3.3 Stability, reproducibility and life-cycle

Limited research has thus far been performed and reported into the storage stability of microcantilever biosensors. The McKendry group report storage stability of two weeks for functionalised microcantilevers in deionised water [48]. Dry storage is preferable, and methods for deposition and drying of antibody for storage of up to several years are available provided the packaging is opaque, sealed, and has low moisture vapour transfer rate. It is now possible to use synthetic polymers that are engineered with binding sites, as an alternative to biomolecules. Molecular imprinted polymers (MIPs) have been developed towards applications in biosensing and chromatography over the past 15 years, offering an attractive route to biosensing over the 'wet biochemistry' techniques discussed previously in this chapter because the active polymer layers are long lasting on a substrate (more than 4 months with no loss in sensitivity for atrazine detection reported by Piletsky and co-workers in 1995 [111]). Once the optimum target, monomers and copolymer have been identified, it is possible to apply a thin layer to a surface by grafting, sandwich casting, spin coating or electro-polymerisation. Alternatively the MIP may be synthesized in bulk, ground to a fine powder and then 'set' on a surface by spin coated PVC. However the technique suffers from low binding affinities and specificity, since the compound used for synthesis of the MIP (the quasi-target) is not the same as the intended target molecule for detection, but an analogue of similar molecular geometry. The majority of MIPs have been tailored for relatively small, rigid, organic molecules such as active pharmaceutical compounds.

An issue often related to storage conditions is reproducibility. There are few studies in the literature that specifically address this issue, but it is evident from *figure 2.4* that there is one trace out of 10 that does not fit with the observed trends in resonance frequency shift over time. One approach to dealing with anomalous results such as this is use highly multiplexed arrays as the Boisen group from Denmark have done, to gain greater confidence in the results [112].

Many research groups have developed cleaning protocols for re-use of their microcantilever biosensors [113] that would not be appropriate in a commercial biosensor. Safe disposal of the test chip is a greater concern. This means that the patient sample should remain encased within the chip as far as possible, particularly when the sensor is to be used in a non-clinical setting; the power generation for actuated chips should be external so that battery disposal is not required; and the sensors themselves should not contain toxic degradants [114].

2.3.4 Small footprint

The actuation and read out mechanisms make a large difference to the size of the device, and where an attempt has been made to miniaturise the whole platform, piezoresistive read out and thermal [115] or magnetic [58, 84, 116] actuation are preferred. The optical lever technique is inherently bulky, since the sensitivity is dependent on the distance between the cantilever tip and the detector. The impracticality of the optical lever technique increases with multiplexing, and interferometric read out is proposed as an alternative for miniaturisation [117]. So far, much progress has been made on individual components (power supply, sample pre-treatment, fluidic handling and data analysis [118]) but very few researchers pull these together [119], because the challenge in doing so is perceived as an engineering rather than scientific research problem. The majority of progress has been made with electrochemical sensors, possibly because the precedent has been set by commercially available glucose monitors. The recent commercialisation of a handheld atomic force microscope [120] as well as the Microvisk CoagMax sensor platform show that small, integrated microcantilever sensors are possible [30].

2.3.5 Blood sweat and tears: challenges of the biological sample matrix

Liquid handling

Possibly the most challenging aspect of realising a commercial biosensor is the sample matrix. As noted, damping of oscillations can limit the resonance mode sensitivity by reducing the Q-factor from up to 10000 - 100000 in a vacuum to just 1 - 10 in water. When static mode cantilevers are used, the Q-factor problem is avoided, but instead the effect of liquid flow becomes a problem. Sensitivity of the static mode cantilever is enhanced for beams with low stiffness, but this makes the sensor vulnerable to

variations in flow rate for example due to pump cycles or to creeping flow in capillary systems [121].

Various approaches have been used to work around the low Q-factor problem. Use of an integrated electronic feedback system to amplify the response from either piezoelectric [83] or optical [122] detection and modulate an electromagnetic driving voltage has been demonstrated to increase the Q-factor in water by three orders of magnitude. Another technique is to avoid oscillations in liquid altogether by keeping the beam unactuated while it is exposed to the sample and employing a drying protocol prior to actuation in a vacuum [123] but this technique incurs the risk of incomplete drying and additional stresses forming on the beam during the dehydration protocol.

Additional complications of operation in liquid are the variable refractive index and opacity of the sample, which have led many researchers to disregard optical sensing techniques in favour of piezoresistive sensors. SMR has already been discussed as a technique that can be used to avoid damping due to a liquid sample, and has been demonstrated with piezoresistive as well as optical techniques [103]. Q factors in SMR vary with design, but are typically in the range 5000 - 15000.

Biochemical Specificity

Functionalization of the microcantilever with capture molecules (e.g. antibodies) can pose a significant challenge, and is usually performed post-manufacture. Bio-specific layers do not spontaneously form on silicon, so either silicon oxide-silane chemistry [124, 125], gold-thiol chemistry [41], or grafted polymer layers [126] are used. The process is relatively simple in resonance mode cantilevers, where immersion can be used to coat the whole surface of the beam simultaneously. For stress sensors only one side of the beam should be coated with the stress-inducing layer. This is usually achieved by coating the upper surface of the beam with gold, then using thiol-linkage chemistry to bind the antibody to the gold. The disadvantage of this technique is that it necessitates making the cantilever into a bi-material structure even before the sensitive layer is added, increasing the cross sensitivity to temperature. Tightly controlled gold deposition conditions are required if the surface stress of the functionalised cantilevers is to be reproducible from batch to batch [127]. In addition, the quality of the

functionalised layer depends on the protocol used to add the layer. Ionic strength during functionalization [128] and the time allowed for capture molecule immobilisation are key factors that determine the packing density of the molecules on the surface, which in turn impacts the attainable signal to noise ratio [129].

A technique to coat different specific layers to each side of the cantilever was demonstrated by Raiteri and co-workers [99]. Such a technique can be used to passivate one face of the cantilever beam in order to prevent physisorption occurring there which would reduce the sensitivity to the target binding on the opposite side. Non-specific binding *(NSB, figure 2.6)* poses a significant challenge for all types of biosensor [129]. Often, the high sensitivity biosensor is designed to detect molecules at low concentrations: for example, prostate specific antigen is present at around 4 ng/ml in men who may have increased likelihood of developing prostate cancer [130], but the total protein concentration in blood is around 70 mg/ml. Therefore the receptor needs to have a binding affinity for the target that is 60 million times stronger than for the average protein molecule just to get a signal 3× baseline noise, assuming all attachments are non-reversible. It is possible to estimate a 'biological noise floor' i.e. the minimum concentration of analyte that must be present to obtain a signal to noise ratio greater than three using the ratio of available binding sites for specific and non-specific binding, the concentration of parasitic molecules and the ratio of binding affinities of the specific and non-specific interactions with the capture molecule [131].

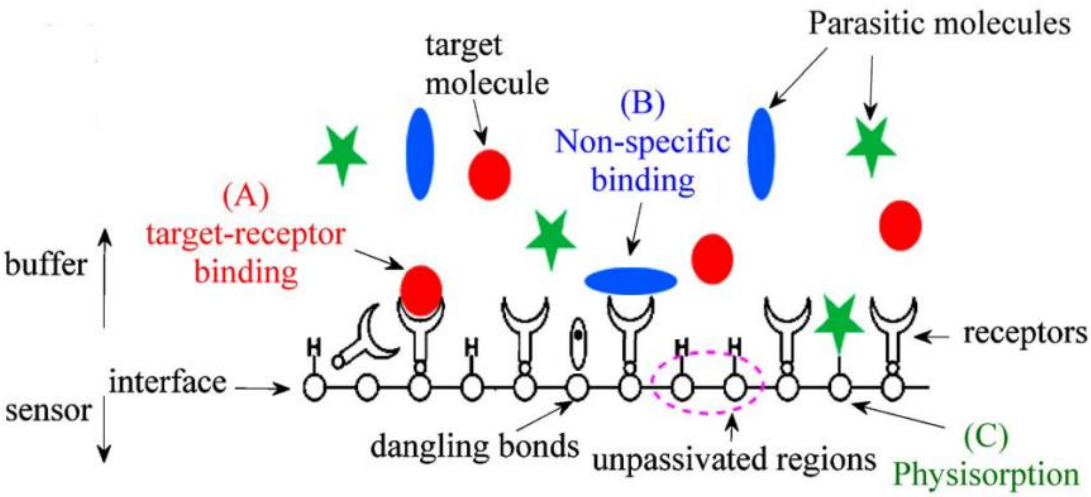

Figure 2.6 Target-capture binding (A), non-specific binding (B) and physisorption (C) on a functionalised cantilever surface. Adapted from [129].

The specificity problem is much more troublesome in label free biosensors than in traditional sandwich assay based methods because in the latter the non-specific binding must occur with both the immobilised antibody and the label for the NSB to contribute to a false positive signal. It is much more probable that the parasitic molecule will bind to either the label or the immobilized antigen, either of which will reduce the sensitivity of the test, which remains undesirable, but has a lower impact on the result as long as sufficient target analyte binding occurs. Steps that can be taken to reduce the impact of NSB include backfilling the surface with an inert layer, also known as passivation and therefore prevent physisorption occurring at the surface. Polyethylene glycol (PEG) is often chosen as a passivation layer because the molecule is relatively small and so can fill up the smallest gaps between capture molecules on the surface [129]. The use of a reference beam can also compensate to some extent for NSB [132], and this technique applied equally to optical detection methods [98] as well as being used with a Wheatstone bridge configuration in piezoresistive sensing [133].

When hydrophilic polymer layers were used to functionalise a silicon surface, such as the co-polymeric thin coating based on N,N-dimethylacrylamide with silanating moieties detailed in reference [126], no additional passivation/backfilling were required, because the hydrophilic surface of the polymer completely covers the silicon [134].

Demonstrations of microcantilever operation in clinical samples

Table 2.2 shows how the techniques discussed in this review have been applied in the relatively few research articles that have demonstrated their sensors in a real patient sample, be it whole blood, blood serum, plasma, saliva or another fluid.

Ref.	Analyte	Matrix	LOD	Mode	Specific Binding	Time to answer	Notes
Shu 2008 [132]	CDK2 protein	Cell lysate	80 nM	Surface stress with optical lever detection	Aptamer; with backside passivation and infilling	Not given	Constant flow 200µl/min 25±0.2°C
Cha 2009 [135]	Hepatitis B Virus DNA	Undiluted Blood Serum	23 pM	Resonance mode with self-sensing piezoelectric actuation	Complimentary strand 23-mer DNA	>2 hours, plus ~100 minutes for sample PCR	Amplification via 140nm silica nanoparticles
Hwang 2009 [136]	Prostate Specific Antigen	Undiluted blood serum	10 pM	Resonance (90kHz) mode with self-sensing piezoelectric actuation	Antibody binding with dip and dry protocol, backfilled using BSA	>1 hour	Temperature and humidity control
von Muhlen 2010 [137]	ALCAM (cancer biomarker)	Undiluted blood serum	0.1 pM	SMR (200kHz) with electrostatic actuation and optical lever detection	Novel polymeric zwitterion functionalization chemistry and reference beam	Not stated	Actuated in a vacuum.
Capobianco 2011 [138]	HER2 (cancer biomarker)	Diluted blood serum	0.6 nM	Longitudinal extension resonance mode with piezoelectric self-sensing actuation	Antibody binding	Not stated	Q-factor serum = 15
Loo 2011 [139]	HER2 (cancer biomarker)	Diluted blood serum	0.6 nM	Longitudinal extension resonance mode with piezoelectric self-sensing actuation	Antibody binding	100 minutes	7 patients, 3 healthy controls, blind tests in triplicate
Timurdogan 2011 [17]	Hepatitis A and C protein biomarkers	Undiluted blood serum	1.66pM	Feedback enhanced resonant array with electromagnetic actuation and interferometric	DSP linker on Au sensor surface	Not stated	-

Ref.	Analyte	Matrix	LOD	Mode	Specific Binding	Time to answer	Notes
				sensing.			
Calimak 2013 [117]	Absolute viscosity of sample	Undiluted blood serum	0.04 cP	Resonance with electromagnetic actuation and interferometric sensing.	N/A	Not stated	-
Microvisk and this work (2004-2014)	Change in viscosity upon clotting	Undiluted whole blood	2-3 cP	Pulsed mode with electrothermal actuation and piezoresistive sensing	No binding, but thromboplastin used to accelerate clotting	~2 minutes	-

Table 2.2 Microcantilever sensor operation in clinical sample matrices.

2.3.6 Cross-sensitivity

With so many possible sensing modes and applications, it is not surprising that microcantilever biosensors are prone to high levels of cross sensitivity, i.e. sensitivity to changes other than the change intended to be measured. In some cases, cross-sensitivity is a consequence of incomplete knowledge of the binding mechanism, for example, the fact that the contributions of mass, beam stiffness and stress to changes in the resonance frequency upon analyte binding still have not been resolved completely [140]. Careful study of these examples will increase understanding and allow the design of better sensors. However, cross sensitivity to external parameters such as temperature and humidity must be carefully controlled.

Cross-sensitivity to temperature

There are several ways that changes in temperature can degrade the performance of a biosensor. Firstly, for any bi-material or multi material sensor, a small temperature change can result in unequal thermal expansion between the layers and therefore lead to stress throughout the device, which will change the deflection [141]. Secondly, most affinity reactions have temperature sensitive kinetics and work optimally at body temperature (37 °C). Thirdly, temperature can also adversely affect monolithic resonance mode cantilevers due to thermal noise setting a minimum sensitivity via statistical mechanical thermal fluctuations, which is a concern for nano-scale sensors [142]. The viscosity and density of most fluids are highly temperature dependent, which means that temperature must be controlled in SMR measurements [143].

Optothermal and electrothermal actuation obviously lead to temperature fluctuations, but care must be taken to ensure that the average temperature does not drift over the course of the measurement, particularly over the course of binding reactions. Other less obvious routes to unintended temperature changes are self-heating of piezoresistive or piezoelectric sensor read out components and optical heating when using the optical lever or interferometry techniques. A low power probe is therefore desirable, but heat build-up may be avoided by pausing the data collection intermittently [17].

Thermal drift in surface stress cantilevers can be minimised by coating the backside of the beam with an identical gold layer to the one used to functionalise the binding

surface [144]. However, this technique will only work if the backside is also passivized as it would otherwise incur high levels of NSB. An alternative approach is to avoid the use of gold-thiol chemistry in the functionalization process. Calleja and co-workers have used silanization methods to functionalize an SU-8 polymer microcantilever, with fluorocarbon passivation on the backside to effectively prevent NSB, and found a 10 fold reduction in temperature sensitivity compared to similar beams made of silicon nitride and gold [145].

Cross-sensitivity to humidity (Swelling)

When porous materials such as polymers are used in the microcantilever structure, the cantilever becomes sensitive to humidity. Boisen and co-workers found that the static response of layered silicon/silicon oxide beams coated with 10 μm of photoresist was non-linear to the humidity measured in an environmental chamber. Saturation occurred at ~58% humidity and was thought to be due to plastic deformation of the resist [80]. With 'in-liquid' applications, the major concern of this porosity is that the cantilever deflection experiences drift for some time after being immersed in the liquid, and as discussed this increases the time to answer. When using the 'dip and dry' method for resonance sensing, it is important to control the humidity during actuation of the beam [136].

Multi-parameter sensors

For most applications it will be sufficient to use a miniature temperature modulation unit, probably located within the permanent part of the sensor unit to control the temperature during experiment. If a disposable device is required, or if the device is used for inline monitoring, integrated compensation of the temperature and humidity are required for cross-sensitivity analysis [146, 147].

2.4 Chapter Conclusions

Advances in microcantilever biosensing have been reviewed with a view to determining the limiting factors to commercialisation of this technology. The extensive literature generated in this field over the past 15 years as well as the wide range of operational

modes and applications illustrates the huge amount of opportunity for research in this field. A cursory analysis of the literature statistics provided by Google Scholar indicates that progress within this field has slowed very recently. The number of published research articles found for the search terms 'Microcantilever' and 'Biosensor' together are expressed per year as a fraction of the number found with the search term 'Biosensor' in *figure 2.7*. The fall in output after 2010 indicates that the major proof of concept objectives in this field have been largely achieved and indeed this review has identified several demonstrations of microcantilever sensors operating with sensitivity in the nanomolar to femtomolar range with specificity appropriate to blood plasma samples. However, only one study has been identified that confirms equivalence of the microcantilever sensor to a gold standard technique with multiple patient samples [139], which must be the ultimate aim in assessing whether the technology is ready to transfer from a research to a commercial environment.

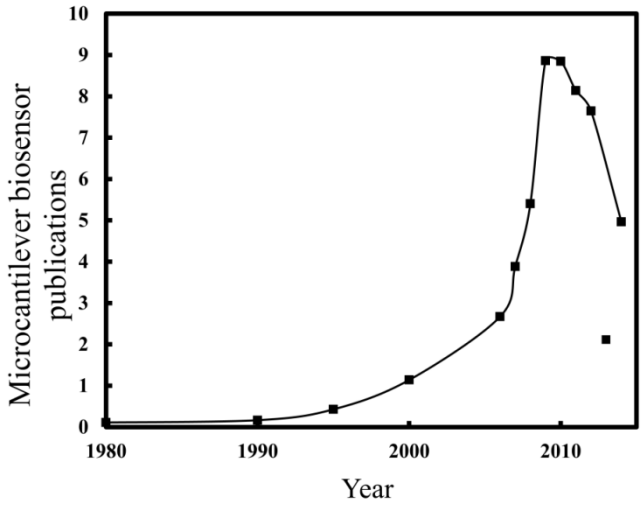

Figure 2.7 Number of publications found in a search for 'Microcantilever', 'Biosensor' expressed as a percentage of the number of publications found in a similar search for 'Biosensor' on Google Scholar by year.

This review has specifically addressed the technical challenges that must either be met in the academic environment or at least show feasibility for the concept to be appropriate to commercialisation. These challenges in cost reduction, platform miniaturisation, time to answer, sensitivity and specificity and elimination of cross sensitivity. Affinity microcantilever biosensors are the most widely studied class of sensor. Great strides have been made in each of these areas, but for affinity based

sensing the challenge in combining is significant: of all the affinity sensors documented in *table 2.2*, none of them have analysis times of less than one hour. As we have seen, the time to answer is part of a trade-off also involving sample volume, deflection or resonance sensitivity, target concentration and binding affinity of the target analyte compared to interfering substances in the matrix.

Within this review, microcantilever based viscosity biosensors have been identified as a specific area of application in which it is possible to achieve high sensitivity with small sample volumes in a compact sensor within a few minutes. These sensors do not encounter the problems associated with specific binding that plague the majority of microcantilever biosensors, and which is the primary reason why microcantilever based viscosity biosensors are the first type of microcantilever biosensor to be commercialised. The largest technical challenge that remains in this field is eliminating cross-sensitivity. The work presented in this thesis looks at three aspects of the cross sensitivity of the Microvisk microcantilever biosensor, currently under development for determination of blood clotting INR: sensitivity to humidity by polymer absorption; mass sensitivity by the inertia for swept fluid; and sensitivity to the thermal properties of a liquid sample. These topics are dealt with in Chapters 3, 4 and 5-6 respectively.

Chapter 3

Effect of Humidity on a Polymer Microcantilever Biosensor

3.1 Introduction

The absorption of moisture in polymer thin films is known to cause swelling and changes in the polymer mechanical properties. However these findings are rarely taken into account by groups that have designed polymer microcantilever sensors [148] and actuators [149, 150] for operation in air or water. Notable exceptions are Urbiztondo *et al* [151], who use a degassing procedure to rid their zeolite and polymer coated cantilevers of water in order to increase the sensitivity to organic vapour absorption, and Keller *et al* who perform their measurements under vacuum [152]. Another common approach is to incubate polymer cantilevers in water for up to 10 hours before measurements are made [44, 96]. Such approaches limit the usefulness of the cantilever sensors for real-world sensing applications. This chapter presents experimental results describing the effect of humidity on the beam deflection, and on the performance of the Microvisk SmartStrip sensor. Full details of the Microvisk Smartstrip cantilever sensor design are not presented here as they are a trade secret; however the design of a similar cantilever (designed and fabricated by the Author) is detailed in Chapter 5, and the basic layout of the cantilever within the SmartStrip is pictured in *figures 1.4 and 1.5* of Chapter 1.

The investigations presented were conducted in response to a period where the batch yield of Microvisk SmartStrips was intermittently low (at worst, down to 50%), and was also driven by unexplained results for the deflection as a function of temperature observed in previous research at STFC [18]. The beam tip deflection was investigated as a function of temperature and humidity over values typically encountered during the product life-cycle: from clean-room assembly (20 °C, 10% relative humidity) to transportation and storage (5 °C, variable humidity) and finally to conditions immediately pre-use, at 37 °C.

The goal of the present study is to describe and explain the deflection of a typical beam between 5 and 40 °C and from 0 to 100% RH (relative humidity). The first key metric to be examined is the cantilever tip height. The SmartStrip design restricts the tolerance limits for the tip height; beams with deflection greater than 380 μm will be damaged by surface adhesion to a hydrophilic carrier tape used to seal the test strip. The SmartStrip dimensions were defined by the requirement for capillary flow up the channel to the sensor, therefore the channel depth could not be increased to give more tolerance on the cantilever deflection as this would also have the effect of diluting the clotting reagent and would increase the measured clot time. It was important to understand the root cause of variability in beam deflection: did it relate to the manufacture of the cantilever dies or was it an artifact of the strip build process? In addition to the work reported here, other investigations into the fabrication and assembly were conducted by Microvisk staff. Both damage caused by the pick and place assembly equipment, and issues with static in the strip assembly clean room were found to be the major root causes of the low yield, with the variation in beam height with atmospheric conditions a contributing factor.

This chapter begins by exploring the theoretical tip deflection of a bi-material microcantilever beam. The major works of the theory on thermal bi-material cantilever deflection had considered only metals or silicon. For beams made from polymer, or other porous material, the theory is incomplete, and the atmospheric humidity must be accounted for, unless the device is intended for use in a low humidity environment or in a vacuum. Experimental results of the tip deflection at varying humidity and temperatures are used to construct an empirical model to predict the tip deflection. Since the humidity affects the deflection of the beam when static, it may also impact the

performance of the actuated sensor. The study was therefore extended to include the impact of atmospheric conditions on the beam stiffness and the sensor signal drift during a clotting reaction.

3.2 Beam Deflection

Polymer swelling due to moisture absorption is well known, however because the majority of bi-material strip cantilevers have been developed using silicon and metals for use as temperature sensors, the change in curvature due to moisture absorption in a bi-material microcantilever has rarely been explicitly considered. A notable exception is Sager and co-workers [153], who studied various polyimide combinations for use as bi-material microcantilever humidity sensors. However, the combined effects of temperature and humidity on a bi-material microcantilever have not previously been presented as an analytical model. This section begins by outlining the main theory for temperature and humidity induced changes in deflection and then goes on to demonstrate results from the analytical model that combines the two effects, as developed in this work.

3.2.1 Analytical model of beam deflection

The model presented in this section is based on a simple approximation to the SmartStrip microcantilever sensor: a rectangular bi-material strip where both layers are the same length and width but may have unequal thicknesses; henceforth referred to a simple bi-material strip. In the Microvisk cantilever, the three-legged 'epsilon' design and integrated serpentine metal heater and sensor tracks are deviations from this ideal. The metal tracks for the heater and sensor significantly increase the flexural rigidity of the beam above that generated by the polymer layers alone. The assumptions in the model are that both materials are isotropic; the temperature of the beam is uniform; and that each layer has a uniform thickness throughout the length of the beam.

In this model and the subsequent experimental validation, we shall consider the deflection of a bi-material strip in two situations: (1) at ambient temperature and relative humidity, and (2) when the cantilever is heated relative to the surrounding environment, for example, by placing the sensor chip on a hot surface. The *Biot* number *(Bi)* is a ratio

of rate of heat transfer into and out of the beam and can be used to gauge whether the assumption of uniform temperature throughout the beam is valid when the cantilever is heated relative to the surrounding environment.

$$Bi = \frac{hL}{\lambda} \tag{3.1}$$

In equation (3.1), h is the convective heat transfer coefficient (film coefficient) between the polyimide and the surrounding fluid, L is the beam length, and λ the effective thermal conductivity of the beam. When *Bi* is less than 0.1, the temperature distribution of the beam can be neglected. The heat transfer coefficient between an SU-8 microcantilever and air was found to be approximately 1000 $Wm^{-2}K^{-1}$ [82]; so one would expect a similar value between polyimide and air. The thermal conductivity of the Microvisk SmartStrip beam is dominated by the metal tracks (approximately 320 $Wm^{-1}K^{-1}$ for gold and 20 $Wm^{-1}K^{-1}$ for constantan). The calculated *Biot* number is therefore ~10^{-3} so the temperature can be considered to be uniform along the whole length when heated at one end, as would be the case if it was on a heated substrate. Note that even if a purely polymer beam is considered, the calculated *Biot* number increases to ~10^{-2}, due to the lower thermal conductivity of the polymer, but we would still expect an even temperature distribution in the beam.

Curvature

Curvature of a beam is the result of a non-linear stress profile throughout its thickness. For a bi-material polymer microcantilever such as the SmartStrip coagulation sensor, the main sources of stress are: the residual thin film stress; the stress induced from thermal strain mismatch; and the stress resulting from strain mismatch due to moisture absorption. The sensor may incur additional stresses during normal use, due to plastic deformation (e.g. if the beam is squashed) or by water damage. It has been shown that the curvature resulting from these different stresses is additive [154], therefore the total curvature κ_{eff} is the sum of the "thin film curvature", κ_f, the "thermally induced curvature change", κ_{Th}, the "humidity induced curvature change", κ_{RH}, and the "historical curvature change", κ_h:

$$\kappa_{eff} = \kappa_f + \kappa_{Th} + \kappa_{RH} + \kappa_h \tag{3.2}$$

Temperature-induced curvature

The first prominent application of the thermal bi-material strip structure was as a bimetallic strip temperature sensor with high rigidity and chemical insensitivity. Timoshenko first derived how the curvature of a bi-material strip changes with temperature for a uniformly heated beam [155], but was later corrected by Chu *et al* [156] who considered both the resultant force and bending moment on the beam in the static situation. Peng [70] successfully applied this theory to MEMS cantilevers of polysilicon and aluminium, and simplified the formula for the temperature dependent contribution to the curvature κ_{Th} to:

$$\frac{d\kappa_{Th}}{dT} = A_{Th}\Delta\alpha_{Th} \tag{3.3a}$$

The 'structural constant' A_{Th}, is derived for a simple bi-material strip as:

$$A_{Th} = \frac{cd(1+d)^2}{c^2d^4+4cd^3+6cd^2+4cd+1} \cdot \frac{1}{(t_1+t_2)} \tag{3.3b}$$

In equation (3.3b), $c = E_2/E_1$ is the ratio of the elastic moduli of the two materials and $d = t_2/t_1$ is the thickness ratio of the two layers; $\Delta\alpha_{Th}$ is the difference in CTE of the two materials and T denotes temperature. Using the same approach as Chu, Bühler *et al* developed a generalised equation [157] for the curvature of multimorphs of n layers, and Garcia *et al* [158] obtained a similar equation by considering iteratively the effect of each additional layer on the resultant structure. For the purposes of this work, we need only consider that the change in beam curvature with temperature has a structural component, $A_{Th,}$ and the thermal mismatch component $\Delta\alpha_{Th.}$

Humidity-induced curvature

Change in curvature due to moisture absorption is the result of one layer swelling more than the other and hence having greater humidity induced strain. In [153], Sager and

co-workers suggested that an equation for the change in curvature of a bi-material strip in response to the change in relative humidity may be derived by analogy to the well-defined equation for the change in curvature due to temperature induced strain mismatch. This derivation has been performed by the author and is presented in equation (3.4).

$$\frac{d\kappa_{RH}}{dRH} = A_{RH}\Delta\alpha_{RH} \tag{3.4}$$

The terms of equation (3.4) are partitioned into a separate structural component and a component that describes the differing response of the two layers to relative humidity. A_{RH} is a structural term that is equal to the term A_T. From now on, both shall be known as A. In addition to the assumptions noted above, the following assumptions are implicit in equation (3.4):

1. The relative humidity of the surroundings does not vary over the dimensions of the cantilever beam.
2. The cantilever is 'open' to the atmosphere such that the absorption of moisture into the cantilever beam does not significantly reduce the humidity of the surroundings.
3. Both layers of the beam are sufficiently thin that any moisture absorbed by a layer of the beam is uniformly distributed throughout that layer.
4. The equilibrium amount of water vapour absorbed into the beam at a given humidity is independent of temperature.
5. There is a linear relationship between the relative humidity and the length expansion in each polymer layer such that the coefficient of humidity expansion, α_{RH}, may be expressed as a number in units of ppm/%RH or equivalent. This is the case when both polymer layers exhibit absorption isotherms that follow Henry's law, and show linear axial expansion per unit of absorbed moisture.
6. The structural component A is not affected by temperature or moisture absorption.

Assumptions 1 and 2 are entirely justified for the microcantilevers considered in this thesis due to their small size and the fact that they have not been packaged in a hermetically sealed cell. If a thin sheet of dry polymer is suddenly exposed to a moist atmosphere, a concentration gradient would be set up with maximum (ambient) moisture concentration at the surfaces, and minimum (zero) moisture concentration in the center. Over time, the gradient would decrease as more water diffuses into the polymer. The diffusion coefficient of polyimide is approximately 2.5 x 10^{-12} m^2/s [159], which over a 10 minute period gives a diffusion length of 7.8 µm. It is therefore reasonable to expect that assumption 3 is also true to a first approximation because the polyimide layers used are typically 2 - 4 µm thick [160]. Although some studies have shown absorption behavior in polyimides that does not follow Henry's law [153], Buchhold and co-workers found that the linear assumption is correct to within 10% [161]. Therefore, assumption 5 of this model may be considered to be valid to a first approximation. It is not known to what extent the absorbed moisture affects the physical properties of the beam (Young's modulus of the polymer layers, thermal conductivity and thermal expansion coefficients). However, a study by Lahokallio and co-workers [162] found that the elastic modulus of polyimide was unaffected by 85% relative humidity during an accelerated aging study, therefore it is considered likely that the layer swelling and subsequent bending of the beam are the primary effect of water ingress and therefore assumption 6 is also reasonable to a first approximation.

.

Thin film curvature

The curvature due to thin film stresses is closely linked to the microfabrication techniques used to make the cantilevers, for example, the cure temperature of the polyimide and whether it was deposited by spin coating or by spray coating techniques. When fabricating the SmartStrip microcantilevers, the polymer layers are applied to a wafer as a liquid monomer solution, and a thermal cure at approximately 350 °C is required to form the polymers and completely remove the solvent. Adhesion between two polymer layers must therefore occur during the cure cycle of the upper of those layers, under conditions of minimum strain. The thin film curvature takes a similar form to the thermal curvature equation (3.3) when the temperature difference considered is between the 'adhesion' temperature and the ambient temperature. Defects encapsulated within the polymer during fabrication, also contribute to the thin film stress.

Historical curvature

The final term contributing to the polymer beam curvature is the "historical curvature change". It has been observed that after actuation, the microcantilever has lower curvature than before actuation. Washing and drying the microcantilevers (for re-use in the laboratory) can also change the curvature: if the drying is performed using an air-jet, care must be taken to ensure that plastic deformations do not occur as a result of the force of the jet; and if drying is performed by heating to evaporate a solvent, the curvature can increase at the base of the beam if a small amount of solvent becomes trapped there and the escaping gas pushes the beam upwards. Microcantilever re-use is therefore avoided whenever possible.

Deflection

To a first approximation, there is a linear relationship between the total curvature of the beam and the deflection at the tip, Z_{tip}, that may be obtained trigonometrically [70]. For a beam of length L, the deflection is given by:

$$Z_{tip} = \frac{L^2}{2}\kappa_{eff} \tag{3.5}$$

The linear approximation becomes increasingly inaccurate for large deflections. Alternatives to the linear approximation include the commonly used circular approximation [163], where the beam co-ordinates are modelled on the arc of a circle. For a beam where L = 750 μm and κ_{eff} = 1000 m^{-1}, the linear approximation gives deflection of 281 μm, compared to 268 μm for the circular approximation. For the purpose of this model, it is sufficient to use the simpler linear approximation because the error in the method (13 μm for the typical tip deflection of a SmartStrip cantilever under ambient conditions) is approximately the same as the variability between different Microvisk SmartStrip beams measured under the same conditions.

The analytical model of a bi-material microcantilever that takes into account the effect of humidity as well as temperature on the beam is now presented. The deflection will change with temperature and humidity according to the following relationships:

$$\frac{dZ_{tip}}{dT} = \frac{AL^2}{2}\Delta\alpha_{Th} \qquad \frac{dZ_{tip}}{dRH} = \frac{AL^2}{2}\Delta\alpha_{RH} \tag{3.6}$$

For the simple case of a bi-material cantilever strip, the constant *A* can be calculated using equation (3.3b). *Figure 3.1* shows the model developed by the author of how the temperature and humidity affect the beam deflection for different values of Young's Modulus ratio *(c)*, different layer thickness ratio's *(d)* and different total beam thicknesses. For more complex designs, such as in the Microvisk SmartStrip, *A* must be determined empirically.

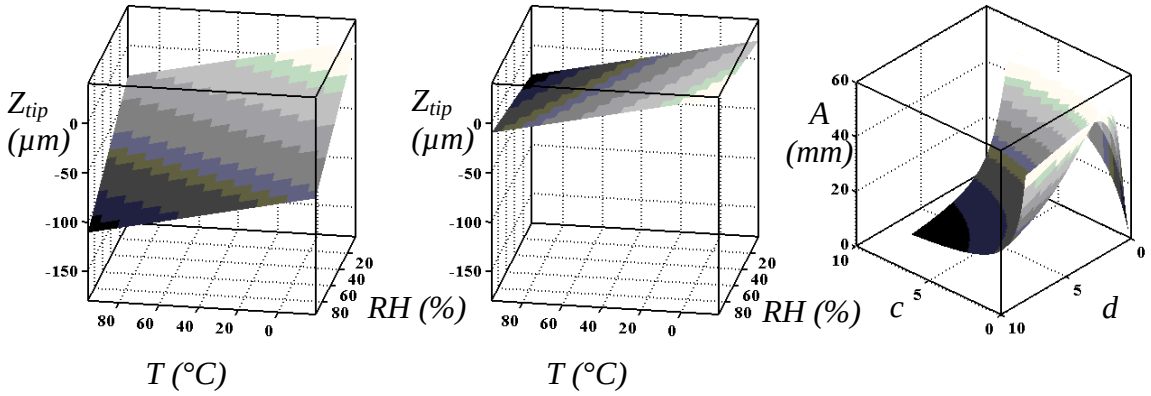

Figure 3.1 Left and Centre: Tip deflection versus temperature and relative humidity of a bi-material microcantilever. Ratio of Young's Modulus, c, and ratio of layer thicknesses, d, both equal to 1. Beam length L = 750 μm thickness t, = 10 μm. In the left hand graph, ΔαTh = 60 ppm/°C and ΔαRH = 120 ppm/%RH. In the central graph, ΔαTh = 60 ppm/°C and ΔαRH = 30 ppm/%RH acting in the opposite direction. Right: variation in the structural parameter A with c and d. Diagrams produced by the author using Matlab.

It is important to distinguish between the ambient relative humidity in the room and the relative humidity local to the beam if it is heated, for example, by placement on a hot surface, or by actuation. The relative humidity as a function of temperature, assuming that atmospheric pressure and total water content remain constant, is given by the Buck equation [164].

$$RH_{local} = RH_{amb}\, e^{\left(\frac{4217.46(T_{amb}-T)}{(240.97+T_{amb})(240.97+T)}\right)} \tag{3.7}$$

When the beam has been heated to temperature *T*, above the ambient temperature in the room T_{amb}, the relative humidity local to the beam $(RH_{local}\ (T))$ will be modified compared to the ambient relative humidity in the room (RH_{amb}). A good approximation is to say that the relative humidity halves as the temperature increases by 10 ºC. Equation (3.7) can be used as a correction factor in experimental results where the cantilever beam is heated above the ambient room temperature.

Figure 3.2 shows how relative humidity of the atmosphere affects the beam deflection when the sensor is heated locally. As the ambient relative humidity tends to zero, the plot of temperature versus tip deflection becomes straight, but as the relative humidity increases, the temperature versus humidity curve becomes increasingly non-linear. In *figure 3.2*, $c = 0.2$, $d = 0.4$ and $\Delta\alpha_{Th} = \Delta\alpha_{RH} = 60$ *ppm* per unit temperature or RH. As the ratio of $(\Delta\alpha_{Th} / \Delta\alpha_{RH})$ increases, the maximum deflection at 100% ambient humidity is achieved at a lower set temperature.

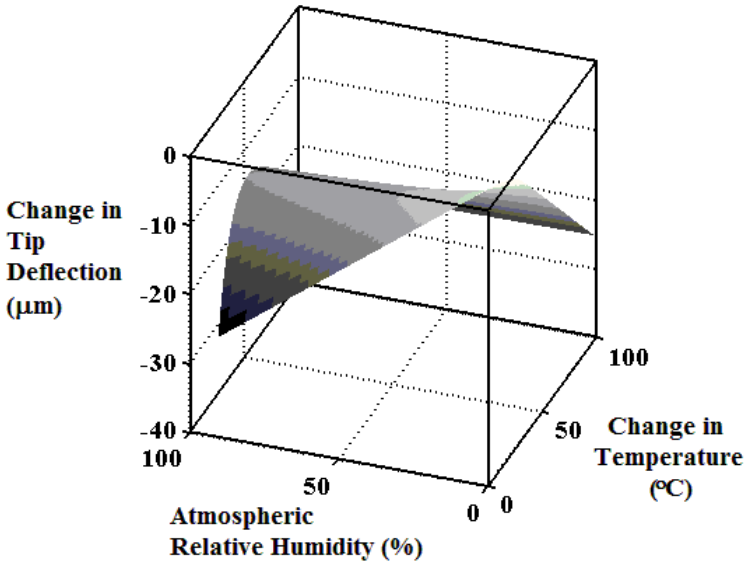

Figure 3.2 Change in tip deflection of a bi-material microcantilever when heated locally (e.g. by hotplate or actuation) at ambient humidity. For the simulation shown, c = 0.2, d = 0.4, t = 5µm, $\Delta\alpha_{Th}$ = 60 ppm/°C and $\Delta\alpha_{RH}$ = 60 ppm/%RH. Diagram produced by the author using Matlab.

Finite element modelling

Finite element techniques enable the researcher to integrate computer aided design (CAD) and modelling to better understand how the materials and design of their device

will affect the sensor performance. For example it allows numerical solutions of the heating and bending of a microcantilever subject to electrothermal actuation to be obtained by using an approximation to the governing differential equation (heat equation) over small subdomains of the structure to find an approximate solution. Despite often long computation times, it offers a distinct advantage over analytical modelling in cases of complex geometry. Many researchers working in the field of polymer microcantilevers either confine their simulations to the use of commercially available finite element models such as ANSYS or COMSOL [70], or else focus on a purely experimental approach.

Finite element modelling (FEM) of the SmartStrip cantilevers was beyond the scope of this thesis. However it has been attempted in prior studies at Microvisk and STFC [18]. An analysis conducted on the first design of the cantilever sensor, MV1, a Π shaped cantilever composed of two polyimide layers with gold heater and sensor tracks confirmed that the linear relationship between temperature and deflection, as described using equations (3.2), (3.3) and (3.5), should be valid in a polymer thermal bi-material strip in the limit of low relative humidity. The FEM did not take account of moisture absorption in any way.

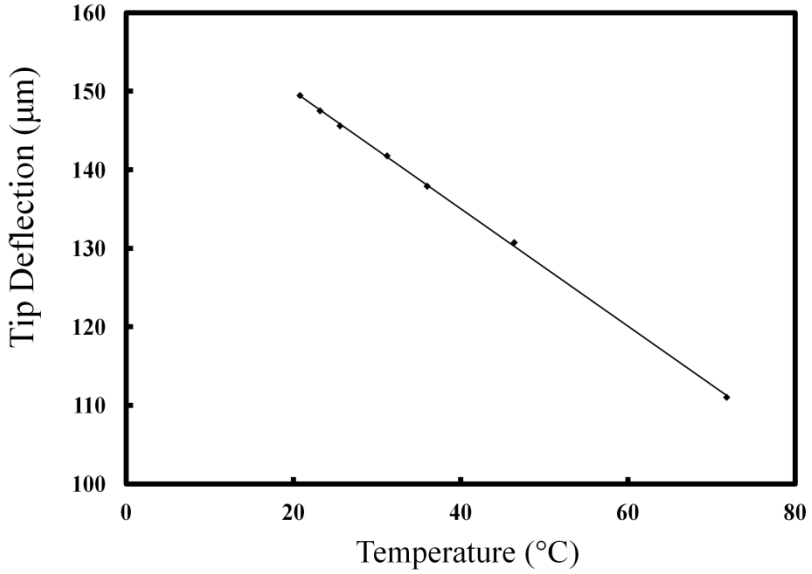

Figure 3.3 FEM simulation of temperature versus deflection for MV1, a Π shaped cantilever composed of two polyimide layers with gold heater and sensor tracks, with a length of 600 µm. Figure adapted from [18].

Figure 3.3 combines the results of two sets of simulations: tip deflection versus actuation power and actuation power versus temperature. As the Biot number is less than 0.1, the temperature of the beam should be uniform whether the beam is heated from the substrate or by electrothermal actuation via the heater tracks. The linear relationship between temperature and tip deflection obtained using FEM is what would be expected from the analytical model if $\Delta\alpha_{RH}$ is small compared to $\Delta\alpha_{Th}$ or if the relative humidity was close to zero. However, the experimental results obtained in the previous study were qualitatively different from the FEM simulations, with a maximum deflection at 50 °C. At that time, relative humidity was not considered as a possible cause of the discrepancy, which was attributed to temperature gradients throughout the thickness of the beam and the low thermal expansion of nickel-chromium and gold microstructures (4.9 ppm.K^{-1} and 14.2 ppm.K^{-1} respectively) limiting the expansion of the high CTE polyimide layer (60 ppm.K^{-1}). The analytical model developed in this section shows that moisture absorbed from the atmosphere and then expelled, as the beam is heated locally during the experiment, can explain the qualitative differences between simulation and experiment observed previously.

3.2.2 Measuring the deflection of a microcantilever beam

A measurement technique that is independent of the piezoresistive signal is required to determine the deflection of an un-actuated cantilever so that the profile can be measured at a range of atmospheric conditions. Direct optical microscopy of the beam profile is difficult because the distance between the beam and the edge of the chip is about the same length as the working distance of the microscope lens, less the lens protector (2 mm). Electron microscopy has also been used [163], but requires vacuum conditions; also polymers are difficult to image unless platinum-coated because they become excessively charged by the electron beam, and may become damaged. Stylus based techniques such as AFM or profilometry have also been used [165], but there is a trade-off between the dynamic range required for highly deflected beams and the stylus weight, which makes them unsuitable for accurate measurement of a beam with high deflection and low Young's modulus. This sub section presents the experimental set up developed and used for measurements of the microcantilever tip deflection at STFC and Microvisk.

An optical system was designed to measure the deflection of the cantilever directly *(figure 3.4)* [13]. The cantilever chip was mounted on a z-stepper platform (Thorlabs APT Precision motion controller), calibrated with a minimum step size of 75 nm. A camera (Canon S515, 8.0 megapixels) was mounted to a 10× microscope lens (Nikon Metaphot) so that the whole cantilever could be imaged. A microscope piece (MM99-58, Martin Instruments) was used to prevent vignetting. The autofocus function on the camera was turned off, so that the focal point remained a constant distance below the microscope lens. The stage on which the cantilevers were mounted was stepped so that the focus progressed down the cantilever beam. At each 5 μm step an image was acquired.

We developed software that can scan the same area of each image acquired by the camera, and assign a value for the focus of that area based on the contrast and sharpness. The focal point was found from the maximum focus score from all the images. Selecting areas at the tip of the cantilever and at the substrate enables the calculation of the deflection. Measurements were taken stepping both upwards and downwards to capture any systematic error from the stepper. Interfering vibrations

were minimized by performing the experiment on an anti-vibration bench (Halcyonics Micro-40).

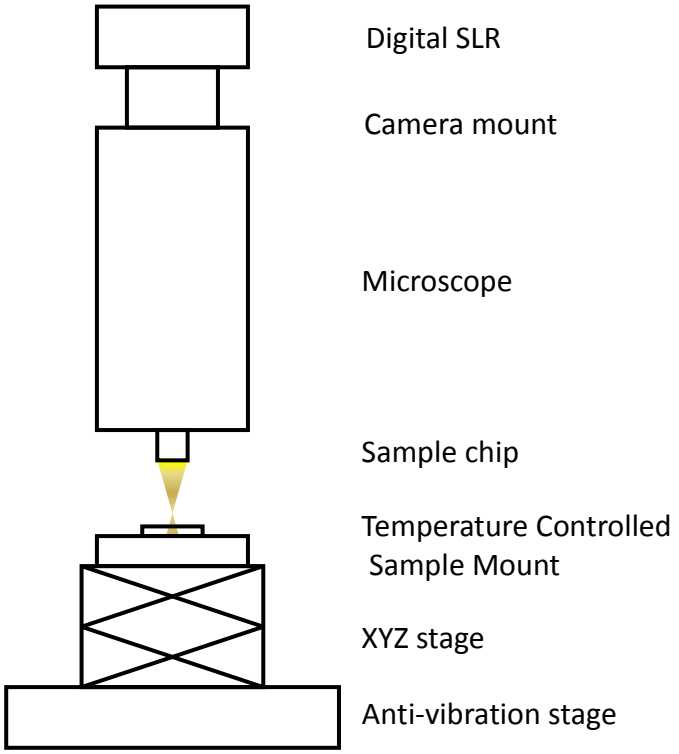

Figure 3.4 Autofocus experimental lay out for data capture. The xyz stage is used to move the sample vertically through the fixed distance focus of the digital SLR camera, with images taken at increments. Data is subsequently analysed using LabView software to determine the relative height of different features on the sample chip.

Experimental Considerations

Sample placement: Double sided sticky pads were used to fix the sample mount to the microscope stage. When the mount is first pressed onto the sticky pad there is a small amount of compression that releases over time. Therefore the chip was fixed in place at least 10 minutes prior to the first image capture.

Movement in the *xy* plane: Images were acquired at sufficient magnification to just show the whole cantilever; therefore no intentional movement in the *xy* plane was needed. Small rotations in the *xy* plane were noticed when the material was stepped in the *z* direction when the *z*-stepper was close to the limits of the motor range. All

measurements were made close to the centre of the *z*-stepper range to mitigate the problem. The residual error is captured in the linearity verification as detailed below.

Lighting: To ensure that any sources of light remained fixed during data collection, experiments were performed without natural lighting.

Microscope apertures and filters: Images with no filters or apertures were compared to phase contrast imaging (used in conjunction with a green filter for greater clarity). Although the phase contrast gave autofocus profiles with a sharper peak, it also had the most unstable baseline, and that introduced errors in the peak fitting; therefore phase contrast was not used.

Digital zoom: The digital zoom was kept fixed for each data set collection but was not replicated exactly between experiments as it could only be set on the camera using an unlabelled slider. High digital zoom leads to increased pixilation that adversely affects the sharpness of the Autofocus peak score.

***z*-stepper calibration:** To verify that there was no systematic measurement error in the calibration of the z-stepper, several data sets were obtained with the microscope moving both upwards and downwards and no difference in the results was found.

Data Analysis Considerations

Autofocus fit function: This is the function used to rate how 'in-focus' each image is. Three different functions were considered: Normalised Variance, Square Gradient and Laplace. A comprehensive review of different Autofocus functions has been conducted by Groen [166]. The autofocus equations were compared based on peak sharpness and signal to noise ratio, and their insensitivity to small variations in location of the analysis window (robustness).

Location of analysis windows: For each degree that the microcantilever chip is tilted with respect to the microscope lens, an error of up to 4% could be introduced to the beam height measurements if the tip and substrate analysis windows are separated by

the length of the beam. Therefore the substrate analysis window is located as close to the tip as possible. Twenty measurements analysis windows are used in total: ten across the tip of the beam and five on the substrate at either side of the tip of the beam. It has been noted that some of the experimental error reported here can actually be attributed to sag at the centre of the beam tip caused by the fact that the heater tracks (which run close to the sides of the beam) extend further down the length of the beam than does the sensor track, decreasing the rigidity in the centre of then beam-tip relative to the sides of the beam-tip.

Size of analysis windows: The optimal size for the analysis window is sufficient to capture a single feature that is of high contrast when the image is in focus. For the size and zoom of the images collected, an analysis window of 20 x 30 pixels was found to be optimal for substrate and tip measurements. Due to the small inconsistencies in the digital zoom on the camera, the information content per analysis window varies slightly between measurement sets, contributing to the variation in error in the different measurements.

Determining focal point: Once each image was assigned an autofocus score, the *z*-position corresponding to the focal point for each window could be determined. The fit to the autofocus score was found to be of Gaussian form, as expected, since a number of pixels contribute to the score at each microscope step, and the focus of the microscope is at the waist of a Gaussian beam. Matlab was used to make a Gaussian fit to autofocus score *vs. z* for each analysis window.

Linearity verification

A linearity check was performed using metrology primary standards. These are Tungsten Carbide gauge blocks of various thicknesses, each independently certified to within 100 nm (UKAS accredited). The height range of interest was 0 to 400 µm to cover the tip deflection of the microcantilever. Appropriate step heights were constructed by placing three such gauge blocks of different heights next to one another underneath the autofocus microscope such that an image could be captured containing three different height levels. An optical flat was used to support the gauge blocks and ensure that they were all on the same level. Due to the smoothness of the polished

gauge blocks, it was difficult to find any features that the autofocus software could use for analysis of the images. Two methods were investigated to artificially 'add' features to the blocks without damaging them. These were (1) dusting the blocks with a fine light reflecting powder before image collection; and (2) deliberately transferring fingerprints to the blocks. The fingerprint method was discarded as it did not create features of sufficient size or contrast to obtain sharp autofocus peaks. The temperature during the linearity check was 19 to 24 °C and since the CTE of the gauge blocks is 5 ppm/°C, temperature has a negligible effect on the results.

A step distance of 0.005 mm was used (since this is a practical step size for measuring the deflection of a cantilever beam), at 10× optical magnification. Three standards were used together because that is the maximum number that could fit on the optical flat without overlapping the edge and it is crucial for this experiment that all the gauges are flat on the surface; overhang could tilt one of the gauges and thus increase the error in the experiment.

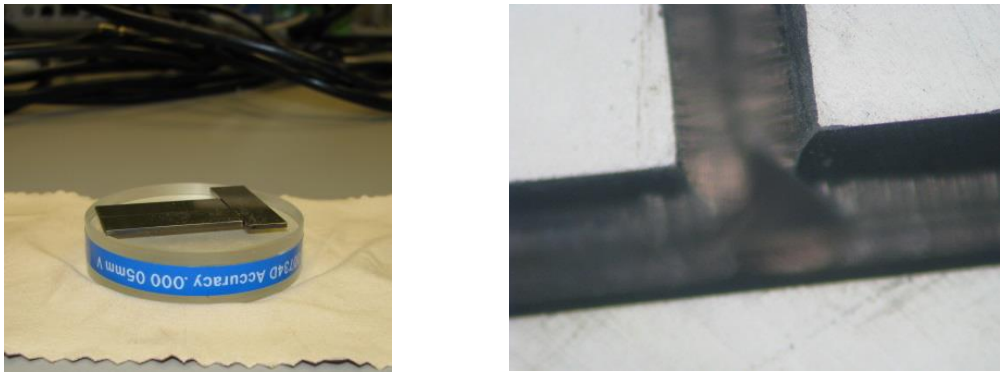

Figure 3.5 Metrology primary standards on an optical flat as used for the linearity calibration of the autofocus experiment (left). Example autofocus image for the standard trio showing the top right slab in focus (right).

The use of dust to create features for the autofocus program is a source of error, since the dust particles add an unknown height to each measurement point. Therefore the average of 10 points was used to define each level. It was assumed that the size distribution of dust particles on each block is the same, therefore when looking at the height difference between the blocks, the error from the variable particle size should diminish with increasing *n*. The standard sets used are detailed in *table 3.1:*

Set Number	Gauge block thicknesses (mm)	Target height differences (μm)	Height differences determined by autofocus (μm)	Autofocus error (μm)
1	1.49 1.10 1.09	400.0 ± 0.1 390 ± 0.1 10 ± 0.1	437 ± 2 414 ± 3 23 ± 3	+ 37 + 24 + 13
2	1.49 1.21 1.19	300 ± 0.1 280 ± 0.1 20 ± 0.1	305 ± 5 282 ± 2 23 ± 3	+ 5 + 2 + 3
3	1.49 1.34 1.29	200 ± 0.1 150 ± 0.1 50 ± 0.1	233 ± 2 174 ± 2 59 ± 2	+ 33 + 24 + 9

Table 3.1 Linearity standard calibration results grouped by measurement set.

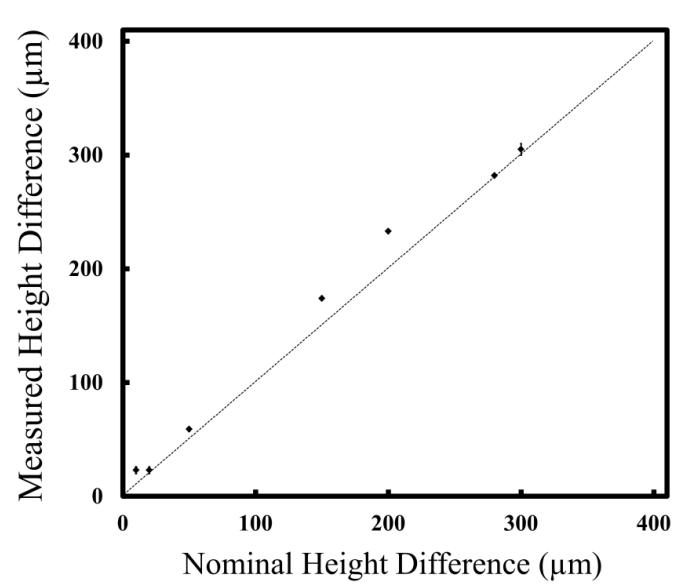

Figure 3.6 Linearity verification for the Autofocus experiment. The experimental (diamond points, with error bars) results are shown in comparison to an ideal linearity line (y=x).

The autofocus technique was found to overestimate height difference between calibration levels. If this was due to systematic error in the *z*-stepper increment, the deviation from linearity would increase linearly with target height difference, which is not found to be the case. The size of the offset varies with the set number (e.g. all the results for set #2 are very close to the true values). The most likely cause is very slight tilting/misplacement on the optical flat which can happen when the standards are pushed together in order to efficiently capture as much of each surface as possible.

Therefore, the best set of measurements (set 2) has been used for linearity verification, which gives a linearity equation of:

$$z_{autofocus} = 1.0025\, z_{actual} + 2.8415 \qquad (3.8)$$

To measure the deflection of a microcantilever beam at fixed temperature, the sensor chip was mounted atop a calibrated ceramic micro-heater (RS DN505-05) and the temperature adjusted via an external resistor. An equilibration time of 6 minutes was established by monitoring the sensor resistance.

3.2.3 Results and analysis: Measured deflection as a function of temperature and humidity

Temperature versus deflection

Measurements of the tip deflection for different temperatures were performed in a low humidity environment (2 - 4% RH at 20ºC) using a calibrated Nikon iNEXIV VMA-2520 optical profilometer, a commercial version of the autofocus experiment described in *section 3.2.2*, accurate to within 10 µm for microcantilever tip height. The Nikon profilometer is much faster and less labor intensive than the home built Autofocus, but was not available for use outside the Microvisk QC laboratory. The stepper motor and camera functions are automated and inertial motion of the sample is avoided by moving the camera lens rather than the sample.

The results, with error bars based on 10 measurements of each of 5 cantilever beams, show good repeatability between the SmartStrip cantilevers, and are linear with temperature as predicted in the earlier theoretical work (*section 3.2.1*). The experimentally determined deflection versus temperature gradient is similar to that obtained by the finite element simulations *(figure 3.3)*: experimental dZ_{tip}/dT = -0.91 ± 0.03 µm / °C; theoretical dZ_{tip}/dT = -0.75 µm / °C.

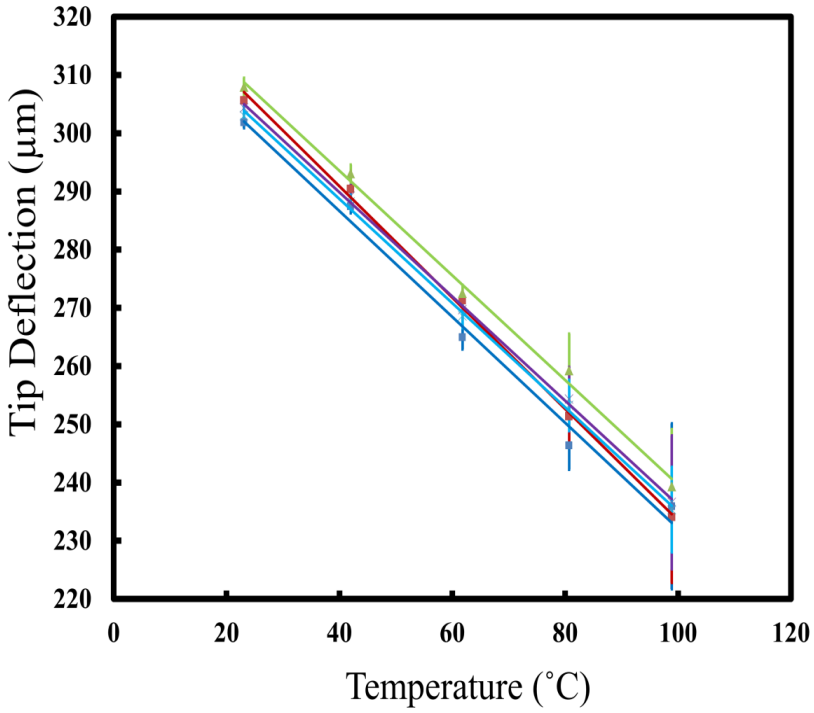

Figure 3.7 Temperature vs. tip deflection for five SmartStrip dies performed at 2–4% relative humidity.

An approximate value for $\Delta\alpha_{Th}$ of 57 ppm/°C is obtained for the SmartStrip microcantilever beams from the data sheets for the two polyimide formulations used, yielding the structural constant $A = 16.0 \pm 0.4mm$. According to the analysis of Peng [70], the maximum value of A for a beam of this length is 60 mm, which corresponds to the greatest deflection sensitivity to temperature. The discrepancy is unlikely to be due to poor optimisation of the Microvisk beam, which was done experimentally, but rather due to the simplifications inherent in the Peng model, in particular the addition of metal tracks that stiffen the beam.

If we assume that the relative ambient humidity in the experiment is sufficiently low to have a negligible effect on the beam deflection, and that there is no historical component to the curvature (a fair assumption as the beams had not been actuated or washed, had been stored in a cool, dry environment and transferred into the dry cleanroom overnight before the measurements were taken), the deflection equation may be formulated as shown in equation (3.9).

$$Z_{tip}(T, RH = 0, \kappa_h = 0) = \frac{L^2}{2}\kappa_{eff} = \frac{L^2}{2}\left(\frac{d\kappa_T}{dT}.(T_0 - T) + \kappa_f\right) \tag{3.9}$$

In equation (3.9), T_0 is the ambient temperature during the experiment, in this case T_0 = 22.5 ± 0.1 °C. The intercept can be used to calculate a thin film curvature of 1.233 ± 0.001 mm^{-1}. If the curvature is assumed to be purely due to the thermal cure process, we can use it to estimate an annealing temperature of *358 ± 9 °C*, which implies that adhesion between the layers occurs at the peak of the thermal cure temperature cycle (350 °C) close to the glass transition temperature of the films.

Humidity versus deflection

A second experiment determined whether the variation of tip deflection with humidity was linear under conditions of constant temperature. The experiment was performed within a small laboratory room at Microvisk, St Asaph, which contained thermostatically controlled chiller and heater units to control the temperature and a humidity control unit with wall-mounted fan. Set points for the temperature were chosen to be 5 ºC, 20 ºC and 37 ºC, as these are typical temperatures for refrigeration, ambient storage and use of the strips respectively. The relative humidity was varied between 10% and 50% at each temperature set point. Ideally the maximum relative humidity would have been 100%, but as the humidity increases, the chance of condensation causing damage to the cantilever chip or to the optical equipment increases, therefore 50% relative humidity was chosen as a practical upper limit. The same five beams were tested in each condition. Because the temperature and humidity were being controlled by the air conditioning unit during the 5 ºC and 20 ºC testing, there was no need to incorporate *equation (3.7)* into the calculation when evaluating the results; values were read directly from the thermohygrometer (calibrated Rotronix HygroPalm23-A) placed next to the experiment. A similar range of ambient humidity was tested at 37 °C. However, since this temperature was obtained using a sub-miniature ceramic heater under the chip, the actual humidity local to the chip is modified according to *equation (3.7)*, making the humidity range tested smaller than intended. In practice, the set temperature of 5 ºC was both difficult to work in and the air conditioning unit struggled to maintain humidity, so the average temperature recorded for these experiments is 10 ± 2 ºC.

Results for the tip deflection versus relative humidity local to the beam have been averaged over all five SmartStrip microcantilevers and are presented in *figure 3.8.* Error bars for humidity are the average standard deviation of the before-test and after-test measurements of all five strips. Where the humidity set point is higher than the ambient humidity outside the room, the air conditioning unit periodically releases a fine spray of water into the room, to be circulated by the fan; therefore errors in the relative humidity are noticeably larger at high humidity.

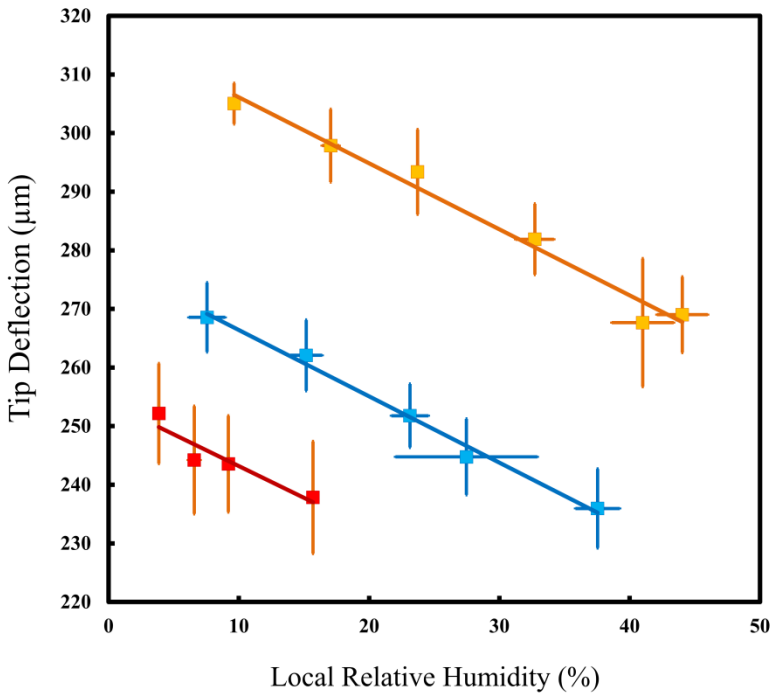

Figure 3.8 Tip deflection of a SmartStrip Microcantilever as a function of relative humidity local to the beam. Top data obtained at 19.8 ± 0.8 °C, orange; Middle data obtained at 10 ± 2 °C, blue; Bottom data obtained at 37 ± 0.5 °C, red. The bottom set of data was collected using a heater placed directly under the chip to control the temperature. Lines shown are linear best fits to each data set and each has $R^2 \geq 0.9$.

The gradients of the three plots in *figure 3.8* are -1.1 ± 0.4 µm/%RH, -1.1 ± 0.2 µm/%RH, and -1.1 ± 0.1 µm/%RH for the data obtained at 37 °C, 20 °C and 10°C respectively. The fact that the gradients of these measurement sets are the same to within experimental error helps to verify the assumption in the analytical model *(section*

3.2.1) that the equilibrium amount of absorption of moisture by the beam is independent of temperature. The structural parameter *A*, determined from the "temperature *versus* deflection" experiment can now be used to determine the difference in coefficient of humidity expansion ($\Delta\alpha_{RH}$) for the polyimide layers in the SmartStrip. $\Delta\alpha_{RH}$ is found to be 70 ± 10 ppm/%RH, which is comparable to the difference in coefficient of thermal expansion in the same materials (53 ppm/°C).

The significant offset between the "deflection *versus* humidity" plots recorded at different temperature set points should now be noted. The intercept values of the three plots in *figure 3.8* are 254 ± 10 µm, 317 ± 10 µm, and 277 ± 10 µm for the data obtained at 37 °C, 20 °C and 10 °C respectively. The deflection at the intercept is due to the remaining curvature components: temperature induced; thin-film curvature and historical changes to curvature. *Figure 3.7* shows that as the relative humidity tends to zero; the tip deflection of the beam should decrease with increasing temperature, but in *figure 3.8* it is the middle temperature (20 °C) that has the highest deflection at 0% relative humidity. Temperature versus deflection *(figure 3.7)* was not recorded below 20 °C in figure 3.7. It is possible that changes to the structural constant *(A)* occur as the beam is cooled further.

The thin-film curvature is due to the stress induced in the polymer layers through the microfabrication process, and should therefore remain constant throughout the experiments. *Figure 3.9* shows the effect on the total beam tip deflection if the contributions from the thin film stress and the temperature induced stress are subtracted from the measured deflection.

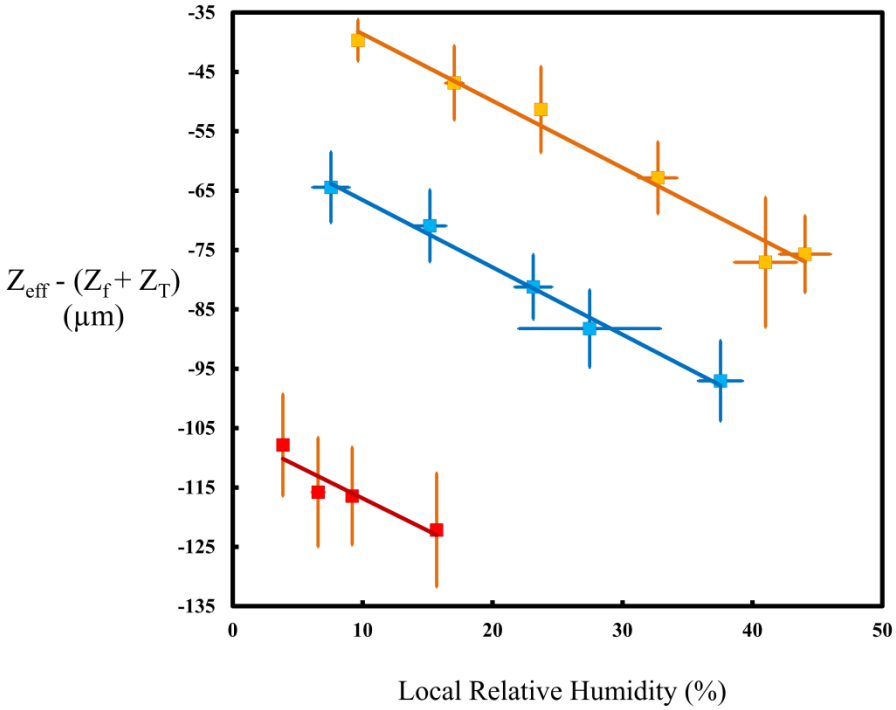

Figure 3.9 Tip deflection of a SmartStrip Microcantilever as a function of relative humidity local to the beam less the thermal and thin film contributions to the deflection. Top data obtained at 19.8 ± 0.8 °C, orange; Middle data obtained at 10 ± 2 °C, blue; Bottom data obtained at 37 ± 0.5 °C, red. The bottom set of data was collected using a heater placed directly under the chip to control the temperature. Lines shown are linear best fits to each data set and each has $R^2 \geq 0.9$.

The intercept values are now -106 ± 10 µm, -27 ± 10 µm, and -55 ± 10 µm for the data obtained at 37 °C, 20 °C and 10 °C respectively. If there was no additional source of stress in the beam other than the thin-film temperature and humidity induced stresses these intercepts would all be zero. It must therefore be concluded that the historical curvature component must have changed over the course of these experiments.

3.2.4 Discussion

The data presented in *figures 3.8* and *3.9* shows considerably more variability than the data obtained from the Nikon iNEXIV VMA-2520 optical profilometer *(figure 3.7)*. The precision of the home built autofocus measurements could be improved by changes to the experimental set up. Simple and relatively inexpensive improvements to the

Autofocus experiment include the use of a camera with programmable interface so that (1) the experiment could be automated; i.e. the z-step and image capture could be alternated within a "for loop", (2) the digital zoom could be specified exactly to obtain consistency between measurement sets. A higher optical zoom could be used to obtain narrower depth of field and thereby increase the precision of the measurements. Setting the digital zoom to zero for each measurement set would reduce variations in precision between the sets. Performing the experiment with higher optical zoom and no digital zoom would only capture the tip of the cantilever in the images, not the whole beam. The reason that the data reported here is based on images of the whole beam is that at the time of data collection the most accurate position for the substrate measurement had not been determined. An additional source of error in the measurements is the air conditioning unit used for the measurements of "humidity *versus* deflection" reported in *figure 3.8*. The unit uses a fan to distribute the temperature and humidity throughout the room. It was necessary to protect the beams from the resulting air currents by constructing a paper enclosure around the autofocus to protect the beams from draughts.

Temperature versus deflection

From measurements of temperature versus deflection at low humidity it is possible to demonstrate that the FEM simulations performed previously *(figure 3.3)* were qualitatively correct: the deflection of the SmartStrip microcantilever decreases linearly with temperature, with a gradient of $dZ_{tip}/dT = -0.91 \pm 0.03$ µm / °C. By assuming that the data-sheet values for the thermal expansion coefficients are correct, and accurate to the quoted level of significant figures, a value for the structural constant (*$A = 16.0 \pm 0.4$ mm)* was determined for the SmartStrip beam that encompasses the contribution to the stiffness of the beam made by the serpentine heater and sensor channels as well as the polymer layers. It was also possible to estimate the thin-film curvature and to find the annealing temperature of the beam if the historical contribution to curvature is assumed to be negligible. The drawback to this approach is the reliance on the data-sheet values for the CTE of the polyimide layers, and the assumption that the metal layers do not affect the stress profile within the beam when the temperature is changed but only contribute to the stiffness of the beam.

Humidity versus deflection

It was found that the decrease in deflection with increasing relative humidity of the SmartStrip microcantilever beams is 1.1 ± 0.4 µm per 1% RH, and is constant with temperature over the range 10 – 37 °C. An additional study performed at Microvisk by Mr Ibbotson, used data generated at Semefab foundry (where the sensor chips are made) and the goods-inward QC facility at Microvisk to estimate the effect of humidity. At Semefab, the tip deflection of 85 microcantilevers, from 15 wafer batches was measured at approximately 45% RH and 22 - 23 °C. The same cantilevers were measured upon arrival at Microvisk, where the temperature is the same, but the humidity is reduced to 10% RH. Both sites use Nikon iNEXIV to measure tip deflection. The calculated variation with humidity was 1.4 ± 0.2 µm per 1% RH.

Using the assumption that the value of "*A"* calculated from the temperature versus deflection data is correct, a value for the difference in CHE of the two polymer layers was determined to be 70 ± 10 ppm per 1% RH over the temperature range 10 – 37 °C. Bhargava and co-workers also found that equilibrium water absorption was independent of temperature in polyimide HFPE-II-52 [159]. An experimental value for α_{RH} of an individual polyimide was determined by Gerlach *et al* [167] using x-ray curvature measurements. The polymer studied by Gerlach was Pyralin-2722 (from HD Micro), which has a similar structure to PI-2562, one of the polymers used for the SmartStrip cantilever beam (both BTDA-ODA polymers). Gerlach determined α_{RH} = 60 - 75 ppm/%RH, which is comparable to the thermal expansion for the same polymer.

At 20 °C, the absolute values for tip deflection at the lowest relative humidity are in good agreement with the values recorded in the "temperature *versus* deflection" measurements. This gives additional assurance (above the calibration checks) that the home built autofocus is as accurate as the Nikon iNEXIV VMA-2520 optical profilometer, even though the latter method is more precise. Measurements made using the home built autofocus at 10 °C and 37 °C both yielded lower than expected tip deflection, and it is proposed that there is a "historical" element to the curvature that has changed between the measurement-sets. The experiments had been conducted in the following order "temperature versus deflection at low relative humidity", "relative humidity versus deflection at 20 °C", "relative humidity versus deflection at 37 °C" and finally "relative humidity versus deflection at 10 °C". The possibility that the deflection

is simply decreasing over time as the thin films "relax" is discounted because the measurements were all acquired within one week, and if such a large variation was routine, it would have already been noticed in variations in QC data. After the final measurement at 37 °C / 50% RH was made, the air-conditioning unit was set to 10 °C, 2% RH, ready for the low temperature measurement set. A possible cause for the lower than expected deflection at 10 °C is that the temperature fell too quickly, while there was still a high amount of water vapour in the air, and relative humidity may have approached or crossed the dew point as the room was equilibrating. This could have resulted in condensation forming on the cantilever beam, which would result in stiction, providing extra force to pull the cantilever towards the substrate permanently. It would have been ideal to verify this hypothesis by observing the effect of the cooling process on new SmartStrip microcantilever dies and monitoring, even very crudely (for example with a micro-video camera with 10 × magnification) the profile of the beam as the temperature and humidity change over time. The test could then be repeated, but this time reducing the humidity as much as possible before starting to decrease the temperature. Unfortunately, only limited access to the Microvisk temperature controlled facility was available at the time this work was performed as the room was required for storing shelf-life stability trial samples, so these checks could not be performed. Similarly, it is possible that in the high temperature measurements, the moisture that has 'sweated' out of the beam has not evaporated from the interface between the beam and the substrate and is also causing stiction. This would explain why both sets of results have lower deflections than would otherwise be expected.

Temperature versus deflection with uncontrolled humidity

It was attempted to use the model developed in *section 3.2.1* along with the empirical values for A, $\Delta\alpha_{Th}$, and $\Delta\alpha_{RH}$ to explain some "temperature *versus* deflection" data obtained from microcantilever beams from the MD design, an early prototype of the current SmartStrip sensor that is made with NiChrome sensor tracks instead of Constantan. The data-set was acquired using the autofocus experiment prior to investigations into relative humidity in the beam, and as such was not performed in a controlled humidity environment, though the ambient relative humidity was recorded along with the ambient temperature. Temperature of the chip was varied using the sub-miniature heater placed below the chip. What was not realised at the time was that the

local humidity was also being varied in accordance with *equation (3.7)*. The data and model are shown in *figure 3.10.*

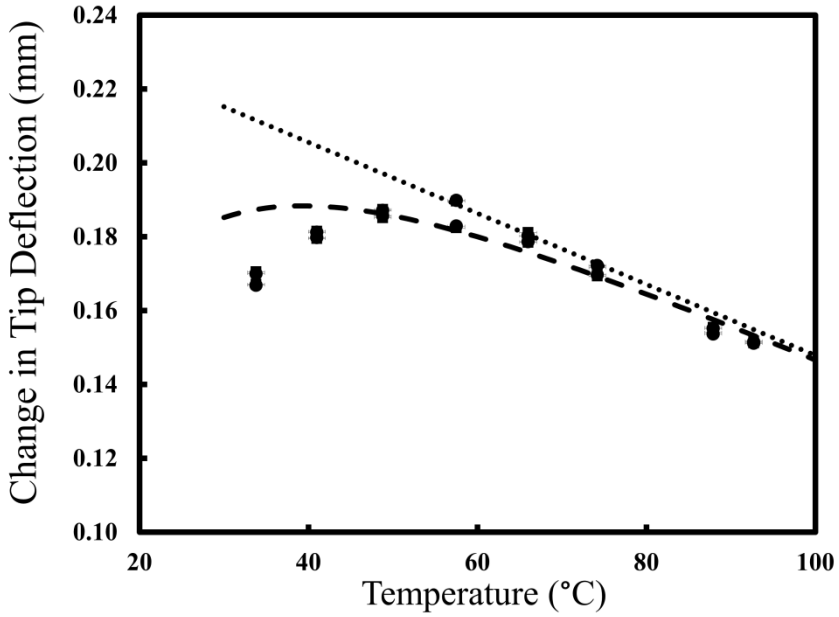

Figure 3.10 Experimental measurements of tip deflection vs temperature for two different beams (dots) under ambient laboratory conditions: average relative humidity during measurement was 34%. Theoretical predictions based on temperature alone (dotted line), and the combined effect of temperature and relative humidity (dashed line) are plotted here for comparison. Values used in the simulation are A = 60 (mm)$^{-1}$, $\Delta\alpha_{Th}$ = 57ppm / °C, and $\Delta\alpha_{RH}$ = 70 ppm /%RH.

It was necessary to adjust "*A"* in the model to be 60 mm^{-1}, however as the metal tracks in the MV3 design are somewhat different to those in the current SmartStrip design, this was expected. However, because both designs use the same polymers, we should expect to have similar values for $\Delta\alpha_{Th}$ and $\Delta\alpha_{RH}$. Incorporation of the change in relative humidity local to the beam into the theoretical prediction greatly improves the agreement between theory and experiment but does not explain it fully. The theoretical tip deflection that accounts for both temperature and local relative humidity (dashed line in *figure 3.10*) is still a little greater than the experimental result at the lowest temperatures measured, indicating that the relative humidity is having a stronger effect on the beam deflection than observed in section 3.2.3. Both the temperature on the chip and the relative humidity were measured using calibrated sensors; however it is possible that the calculation of the local relative humidity underestimates the humidity local to

the beam because the heated, dried air is not prevented from mixing with the rest of the air in the room.

The results presented throughout this section show that the non-linear relationship between temperature and deflection of the microcantilever beams when measured under ambient laboratory conditions can be attributed at least in part to the influence of absorbed water vapour within the beam. This conclusion is in agreement with a recent study by Larsen *et al* [34], who also obtained a curved deflection profile (using ceramic-polymer bi-material cantilevers) which they attributed to moisture ingress, though they did not perform further characterization experiments (to find the CHE for example). The Larsen study addresses an omission in the work reported here, in that they looked at both directions of temperature sweep, and they reported the same trend in each. In their study, the maximum deflection is obtained at a lower temperature of 35 °C, compared to the present study where the maximum deflection was obtained close to 60 °C. The difference in maxima could be due a lower value of 'ambient' humidity in the laboratory of Larsen (it is not reported), or it could be that the relative size of the opposing bending moments due to absorbed moisture and temperature is tipped further in the direction of temperature for the Larsen study than in the present work.

3.3 Resonance measurements

In the model presented in *section 3.2*, it was assumed that the composite structural parameter *A* is invariant with temperature and humidity. If moisture ingress is affecting the flexural rigidity of the beam, this could be observed as shift in the resonance frequency of the beam. The ringing response to a short pulse, in air, was tested at different relative humidity to find out whether the resonance frequency changes. As Tsilingiris showed [168], the variation in the viscosity of air with relative humidity at 20 ^{o}C is negligible, so changes in the signal response will reflect changes that the water vapor causes to the beam rather than to the air.

The response from sixteen SmartStrips was measured at nominal relative humidity of 5%, 50% and 80%. The temperature was fixed at 20 °C during all measurements, and

the cantilevers equilibrated for at least two hours at each of the relative humidities before testing. The excitation pulse used was 0.1 ms, 6 V, 10 Hz, as this has been shown to produce a clear 'ringing' response when actuated in air, such as the example shown in *figure 3.11* which was obtained at a relative humidity of 5%.

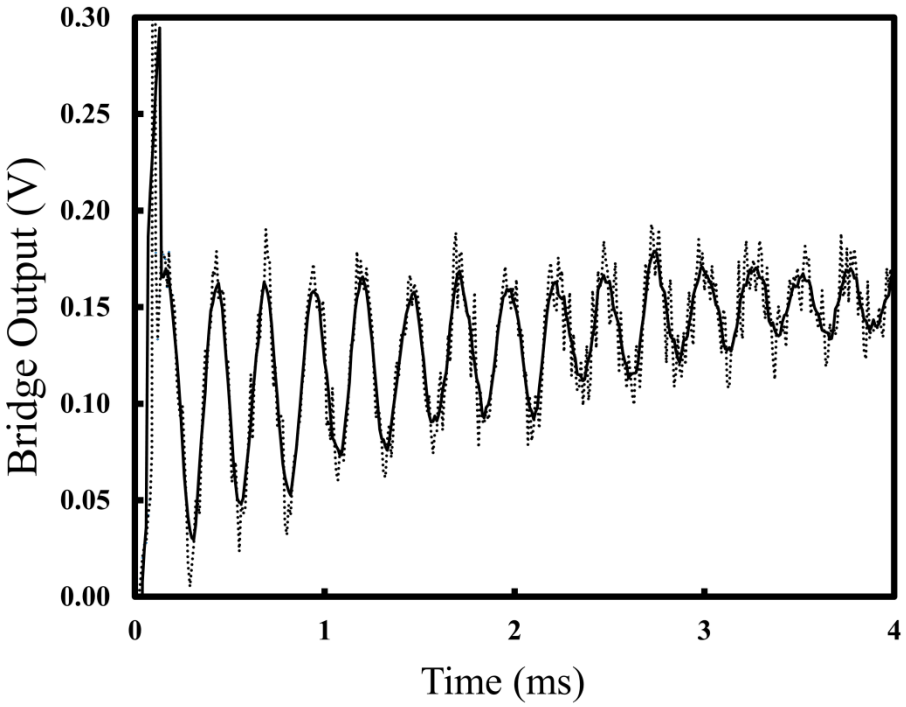

Figure 3.11 Sensor signal from a 10 µs actuation pulse from strip 51-577 at 5% RH, 20 ºC. Dotted line = raw data, solid line = 8 point rolling average. The damped oscillations are clearly visible over the gently curved background.

The resonant frequency was determined directly from the averaged raw data (peak to peak). It was expected that at higher relative humidity, the beam would absorb more water and the increase in total weight of the beam would reduce the resonance frequency. This is not observed to a significant extent in the results obtained in *figure 3.12*, possibly because of the relatively high error in resonance frequency measurement which is mostly due to variation between individual strips. The low pass filter output from the processed SmartStrip signal was also collected.

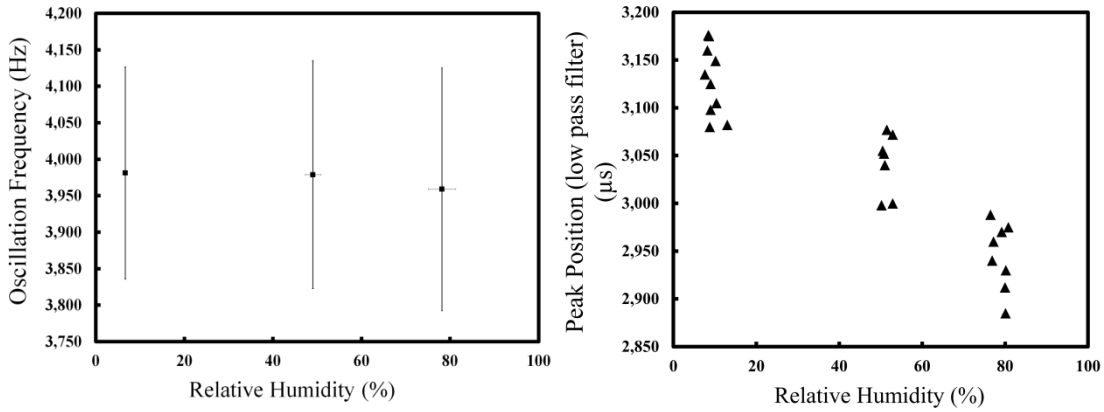

Figure 3.12 Measurement of resonant frequency of the SmartStrip microcantilever at different humidity. Error bars show standard deviation based on 16 different strips (left). Low pass filter peak position signal for SmartStrip sensors as measured using the CoagMax handset at different relative humidity.

Comparing the two sets of results shows that although there is not a statistical difference in resonance in air when the relative humidity is changed by 30 - 40%, there is a difference in the filtered signal that is used in clot time measurements.

3.4 Impact of humidity on whole blood measurements

To conclude this study on the effect of moisture absorption on the sensor, it was necessary to determine whether there is any impact on the sensor operation in whole blood, as used by the patient. The test algorithm within the current generation of Microvisk CoagMax reader uses changes in the peak position of the output voltage after the low pass filter to determine the prothrombin time.

3.4.1 The Bias

The initial peak position is measured (point A) and a cut-off value calculated as 105% of this value. When the signal exceeds this cut off; the experiment stops (point B). The clot time is calculated as the maximum difference between the signal and the straight line from A to B.

If there is drift in the signal, particularly at the start of the experiment, the elbow that defines the clot time is too shallow for the time to be accurately determined. In extreme cases, the drift may be so severe that the cut off value is exceeded before the clot has occurred, in which case an error occurs on the test and no result is obtained.

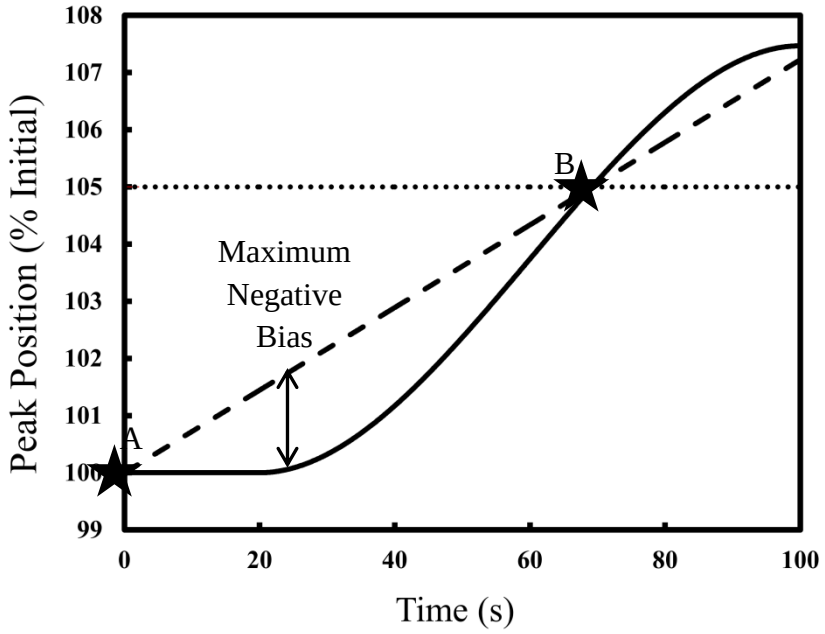

Figure 3.13 Theoretical clot curve showing how the CoagMax algorithm calculates the clot time based on the maximum negative bias between the start-value (point A) and where the signal crosses the cut-off value (point B).

3.4.2 Data collection and analysis

To study the impact of ambient relative humidity on the background signal in a typical patient sample, ten SmartStrip sensors were tested using a CoagMax reader under each of three humidity conditions: 10%, 50% and 80% relative humidity. Citrated whole blood (CWB) was used as the analyte; the purpose of the citrate is to inhibit clot formation so that the background signal within the sample matrix can be seen clearly. Data was collected from the low pass filter (LPF) of the reader. The sensor was actuated for 30 seconds before the addition of the sample as would be the case during use by the patient. All testing was performed at the ambient laboratory temperature of 20 – 25 ºC.

The data were post-processed to identify the correct start time for the test. This is the time at which the liquid first contacts the sensor and can be found from the signal data by subtracting the time at which the greatest drop in peak position signal is detected. An example of typical signal data is shown in *figure 3.14*.

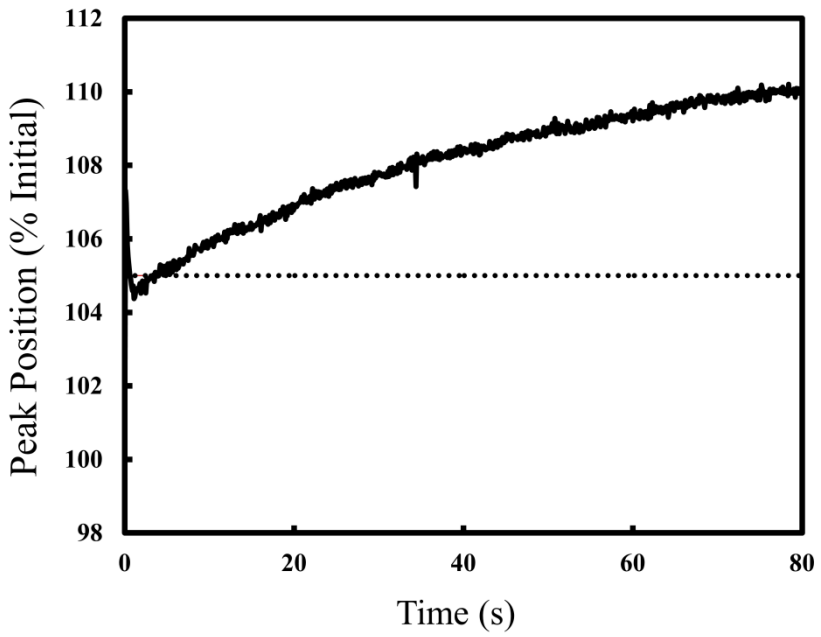

Figure 3.14 Typical data showing how the peak position increases over time in citrated whole blood. In this example (strip G51547, measurement taken at 50% humidity) the cut off threshold is exceeded twice: once at the 2nd data point due to the initial data disturbance and again after approximately 5 seconds due to sample drift.

There are two artifacts in the data that could lead to an error being recorded on the CoagMax: the disruption in the signal immediately after the liquid makes contact with the sensor; and the initial drift in the signal. The combination of these two artifacts gives rise to 4 observed failure modes:

1. Signal exceeds 105% of initial signal within the first 30 seconds due to the initial disruption. It then returns to a value close to its initial value and does not drift above 105%.
2. Signal exceeds 105% of the initial signal within the 30 seconds due to the initial disruption but does not return below 105%.

3. Signal exceeds 105% of initial signal within the first 30 seconds due to the initial disruption. It then returns to a value less than 105%, but drifts out of this range again during the test.
4. The initial disruption does not cause the signal to exceed the cut off value within the first 30 seconds, but drift in the signal over time results in the signal going above 105% during the test.

A summary of the frequency of these different failure modes encountered is given in *table 3.2*, below.

Failure Mode	Number of Failures		
	10% Humidity	50% Humidity	80% Humidity
1	1 of 1 0	0 of 7	0 of 8
2	2 of 10	2 of 7	3 of 8
3	3 of 10	1 of 7	1 of 8
4	0 of 10	1 of 7	0 of 8

Table 3.2: Summary of failure modes in citrated whole blood tests. Note that the data is not smoothed for this analysis, which gives a slightly higher error rate.

To separate these two effects, the signal gradient is calculated between 1 and 5 seconds to measure drift, and the time to cross threshold is calculated assuming a straight line from the initial time point. Note that the CoagMax has a secondary cut-off time at 60 seconds; therefore the calculated time to threshold has been capped at this value. To measure the effect of the initial signal disruption on the time to cross threshold, the average peak position for the first second is calculated and an average gradient is used to calculate the time to threshold.

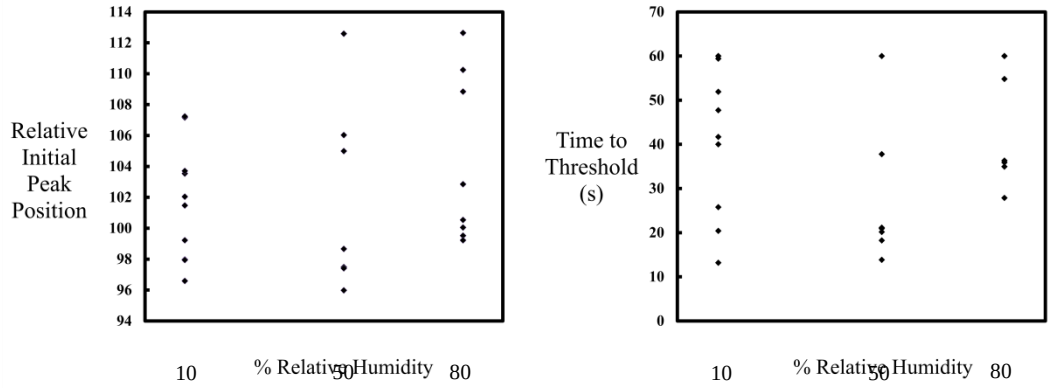

Figure 3.15 Individual value plots showing how the disruption at the initial time point varies with relative humidity (left); and how the gradient of the low pass filter peak position signal at 1 to 5 seconds changes with relative humidity (right).

3.4.3 Discussion

Neither of the two artifacts in the signal data that can result in errors from the CoagMax algorithm are highly correlated with relative humidity. The disruption noted at the start of the signal is the most significant effect and is thought to be due to the force of surface tension acting on the cantilever as the meniscus of the sample front envelops the vibrating beam. Efforts have been made to ensure that the flow to the beam is reproducible: the inside of the fluidic channel from sample inlet to sensor has been plasma-surface treated in order to create a hydrophilic channel to encourage fast fluid flow. If the channel is not sufficiently hydrophilic then creeping flow results and can increase the time required for the meniscus to cross the sensor. Another pragmatic and immediate solution would be to set point A to be one second after the sample registers on the sensor, as at this point any disruption has passed. The signal gradient within the first 5 seconds of exposure to the sample is more likely to lead to a false result (early clot detection) than to an error, and therefore has potentially greater consequences for the validation of the sensor. The cause of this gradient is not known, though it is not highly correlated with the initial peak position ($R^2 < 0.01$). One possible explanation is the time taken for the sensor and sample to thermally equilibrate: however since the sample was pre-warmed to body temperature (37 °C, the same temperature as the sensor operates) so it seems unlikely that it is the cause of the drift in this instance.

3.5 Conclusions: Effect of Relative Humidity on the SmartStrip Sensor

Figure 3.16 shows how the deflection of a typical SmartStrip microcantilever sensor may vary over various stages between manufacture and use, from the empirical model developed in *section 3.4*. Variation of over 100 µm is possible, though this is due in part to the unknown temperature reached during transportation (temperatures in the midst of cargo shipping vessels have been recorded in excess of 50 °C). Without humidity control in the form of packaging with zeolite the situation would be much worse.

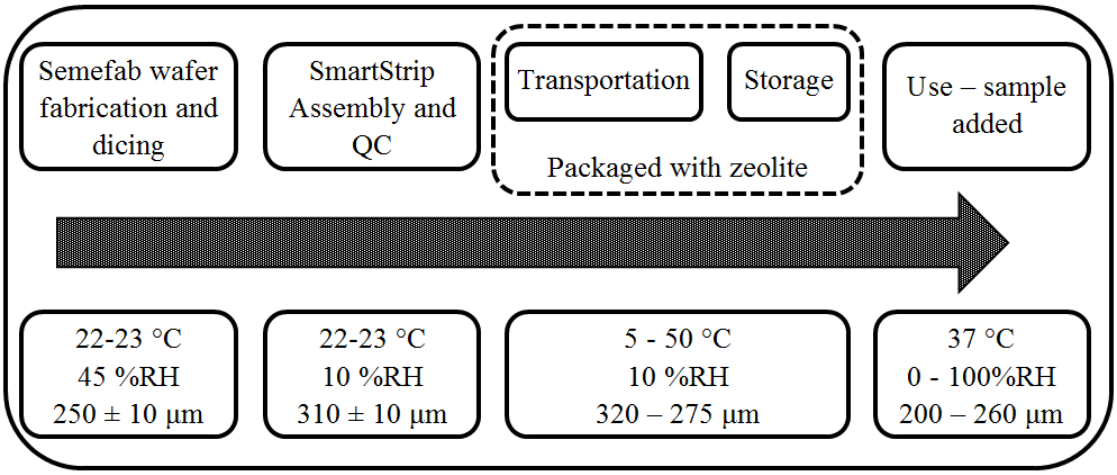

Figure 3.16: Flow diagram illustrating the range of ambient conditions encountered from fabrication to use of a SmartStrip microcantilever sensor with calculated tip height. The impact of 'historical' deflection change on the microcantilever is not considered here.

Fortunately, the impact of the variation in temperature and humidity is limited to its effect on the deflection of the beam. The impact on the flexural rigidity of the beam and its operation in whole blood has been shown in this chapter to be negligible. The experiments performed on citrated whole blood lead to the suggestion that the way that the fluid meniscus disrupts the signal from the sensor as it flows over the cantilever beam may result in errors within the clot detection algorithm. To check this hypothesis, further testing might include using a detergent such as Triton X added in small amounts to progressively lower the surface tension of an aqueous sample. The amount of signal disruption could be qualitatively and quantitatively monitored against the amount of

surfactant added, and the contact angle of the test liquid could be measured in the Microvisk laboratory.

An additional topic for investigation within this subject is the performance of the microcantilever during and after freezing. The low deflection observed for the humidity study at 10 °C suggests that sub-zero degree Centigrade temperatures may not lead to greater deflection of the beam via the CTE as previously thought. Comparison of changes in the beam height when the temperature is lowered under conditions of zero humidity (e.g. in a nitrogen chamber) and in the presence of moisture could be used to investigate the hypothesis put forward in the discussion that the low deflection at 10 °C was caused by condensation on the beam leading to irreversible stiction.

To conclude, the SmartStrip microcantilever sensor is not cross-sensitive to relative humidity and there is no impact in use by the patient. However the variation in microcantilever tip height with relative humidity shows that polymer microcantilevers such as the SmartStrip microcantilevers would be cross sensitive to relative humidity if they were used in static mode.

Chapter 4
Viscosity Calibrations

4.1 Motivation

Self-actuated microcantilever sensors for viscosity measurement is an active area for research, with several new studies reported in the past 3 years [57, 117, 169, 170]. The advantages over traditional methods (e.g. Ubbelohde viscometer that measures the flow velocity through a capillary to determine viscosity) are the low sample volumes required, remote operation, and low cost of manufacture, leading to the potential for disposable viscosity sensors that are apt for medical diagnostic applications.

For blood clot testing, the microcantilever sensor should be able to accurately determine the time when nature of the sample changes. The 'before clot' and 'after clot' measurements are therefore obtained on a single sensor chip and a small offset between the individual results on individual chips (i.e. chip-to-chip variability) is inconsequential to the measurement. However, in order to use the sensor in an application where comparative measurements would not be made using the same sensor, for example, in the quality control of a shampoo where different batches are compared over a long period of time, there would need to be good agreement between different chips. To the best knowledge of the author, this study presents the first consideration of chip-to-chip variability in a microcantilever viscosity sensor. Although much of the commercial literature concerning Microvisk CoagMax states that the product works by detecting the change in viscosity during clot formation, the sensor design and data processing algorithm have changed significantly in recent years. It was therefore appropriate to re-evaluate the effect of fluid viscosity on the cantilever signal for the current version of the sensor. The specific aims were:

1. Understand the effect of fluid viscosity on the CoagMax signal.
2. Determine whether the change in blood viscosity upon clot formation is sufficient to explain the change in signal on the CoagMax that is used to determine the clot time.
3. Explain how the CoagMax signal relates to fluid viscosity in terms of the mechanical motion of the beam.
4. Determine the sensitivity of the Microvisk SmartStrips to viscosity.

4.2 Introduction to Microcantilever Rheology

4.2.1 Viscosity and Rheology

The rheological properties of a fluid describe the extent to which it has solid like elastic properties and liquid like dissipative (viscous) properties. The complex viscosity η*, or alternatively the complex shear modulus G* are used to describe the viscoelasticity of the fluid:

$$\eta * = \frac{shear\ stress}{strain\ rate} = \eta' - i\eta'' \qquad G * = \frac{shear\ stress}{shear\ strain} = G' + iG'' \tag{4.1}$$

Under small perturbations, the deformation is proportional to the shear stress and the viscoelastic properties are independent of the applied force and $\eta'' = 0$. When the deformation is sufficiently large, the sample microstructure of a non-Newtonian fluid changes in response to the applied force (for example, red blood cells concentrating in the centre of a micro-capillary channel where the flow is fastest) which leads to the viscoelastic properties being dependent on both the magnitude and frequency of the applied force. The relaxation time is a measure of the time required for the energy stored via the elastic characteristic of the fluid to be dissipated via the viscous characteristic and is given by:

$$relaxation\ time = {}^{\eta''}/_{\omega\eta'} \tag{4.2}$$

So for deformations that occur at a faster rate than the relaxation time, the substance behaves like a solid, and for slower deformations it behaves as a liquid.

Damping of an oscillator in a viscoelastic fluid can be used to find the properties of that fluid. The simplest model is a damped simple harmonic oscillator (SHO). The phase shift between the viscous and elastic components of either η* or G* can be found from the Q-factor:

$$Q = \frac{\eta''}{\eta'} = \frac{G\prime}{G\prime\prime} = \tan\varphi = \frac{1}{\tan\delta} \tag{4.3}$$

where φ and δ are the phase angles between the shear stress and shear strain and the shear stress and shear rate respectively.

4.2.2 Viscoelastic properties of Whole Blood

Whole blood is a complex fluid consisting of plasma (an aqueous solution of proteins and salts), red blood cells (RBCs, biconcave discoid cells approximately 2 μm deep by 8μm diameter), white blood cells (typically larger than RBCs) and platelets. It can be modelled either as a solid-liquid suspension or as a liquid-liquid emulsion. There are multiple interrelated factors which contribute to the viscosity profile which is non-Newtonian [171]. These are described below and depicted in *figure 4.1*.

Plasma viscosity: plasma is a Newtonian liquid with typical viscosity range of 1.1 - 1.35 cP at 37 °C. Plasma viscosity is proportional to the concentration of protein and may be elevated in patients with tissue injury or in various disease states.

Haematocrit: this is the volume fraction of RBCs in whole blood and is typically 40-45%. For a given shear rate, viscosity increases with haematocrit since RBCs disrupt laminar flow lines. RBCs are the primary cause of the non-Newtonian nature of whole blood due to their shape: as the shear rate increases, they have greater tendency to orient in the plane of fluid flow thus minimising resistance to that flow making whole blood a 'shear thinning' fluid.

Mechanical properties of RBCs: red blood cells are highly deformable due to elastic properties of the membrane cytoskeleton. The mechanical behaviour is dependent on the haemoglobin concentration and cell hydration. RBCs have been observed to behave somewhat like oil droplets when studied in micro-capillaries and for this reason the emulsion model of blood is valid.

Rouleaux: the reversible formation of chains of RBCs under conditions of low shear stress has the effect of changing the effective particle size distribution and increasing the viscosity under low shear. The size of aggregates depends on the plasma protein composition and on the surface properties of the cells and is inversely proportional to the shear force.

Temperature: Affects the viscosity of almost all fluids via the inter-particle collision rate. The majority of experimental research on blood rheology is conducted at 37°C.

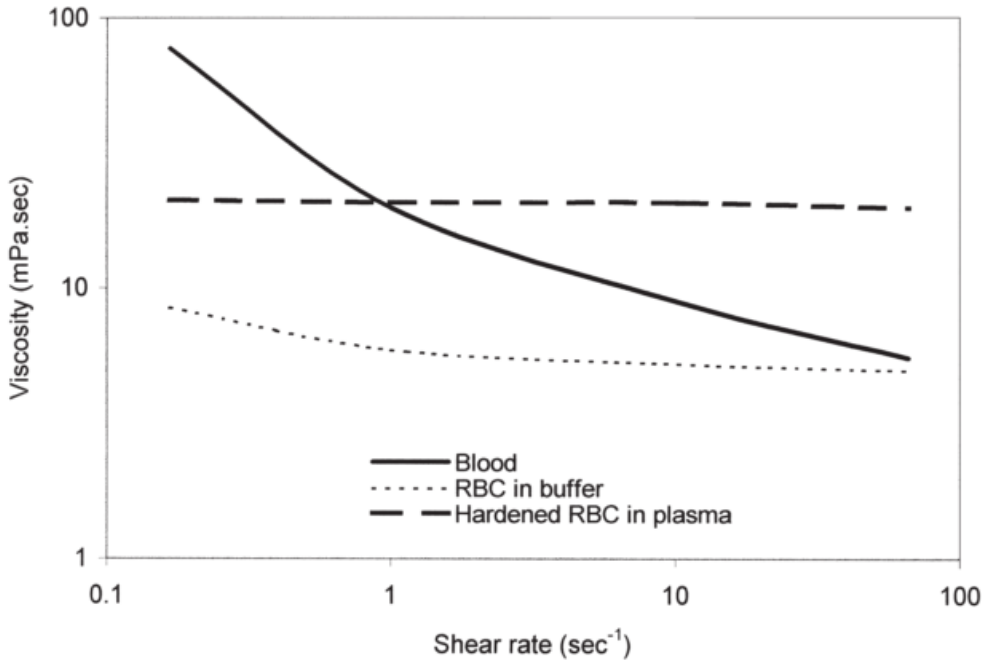

Figure 4.1: Illustration of the non-Newtonian character of whole blood due to the orientation of RBC. Reproduced from 'Blood rheology and hemodynamics', Baskurt et al *(2003)* [171].

An order of magnitude calculation for the shear rate of liquid moving around the microcantilever upon actuation can be estimated by considering the linear velocity of the tip of the beam (0.067 m/s as measured using a high speed camera during pulse actuation) divided by the beam width. This estimation is based on the assumption that the deformation of flow lines at the edge of the beam is negligible. The calculation reveals maximal shear rates to be in the order of 200 s^{-1} at the tip of the beam. Shear rates closer to the anchor are considerably less both because the linear speed of the beam is lower and because the holes in the beam decrease the effective width. However, since the motion of the beam is constrained by the part of the beam that encounters the highest force and torque, fluid rheological properties in that region will define the measurement. From *figure 4.1* we can correlate the shear rate of 200 s^{-1} with the lowest viscosity range of whole blood, where it is not heavily influenced by RBCs. Indeed during careful observations of the microcantilevers operating in whole blood, clearing of the liquid in the region of the cantilever can be observed with the aid of 10× optical magnifier, indicating that the RBCs are being batted away from the beam and it is mainly the plasma viscosity being measured.

The biochemical clotting cascade causes physical changes in the structure of blood as platelets aggregate and fibrin networks develop during clot formation. Typically clot time measurements are made using PT techniques such as capillary inversion and clinicians are more concerned with the clot time than with the 'absolute viscosity' values. However there have been some studies on the viscosity of blood. Of particular interest is the work of Dintenfass [172] who showed how the viscosity of whole fresh and clotted blood was affected by the shear rate of the measurement technique. The data in *table 4.1* show that the trend for fresh blood is consistent with *figure 4.1*. However the measured blood clot viscosity falls off much more sharply when the shear is increased, until at 400 s^{-1} it is the same as for un-clotted blood. This means that the viscometer (a variable frequency thromboelastometer) was effectively vibrating the clot apart. However there was also evidence that rates of shear up to around 40 s^{-1} are conducive to faster clotting times.

Shear Rate (s^{-1})	Fresh blood viscosity (cP)	Blood clot viscosity (cP)
1.8	70	12500
9.4	20	2000
44	8	300
400	4	4

Table 4.1: Viscous properties of whole blood. Values reproduced from [172].

The viscoelastic properties of fresh and clotted blood both have a complex relationship with the shear rate, therefore absolute values for "the viscosity change during blood clotting" are difficult to obtain as they depend on the measurement technique used, clotting chemistries employed and variability in the patient samples. *Table 4.1* shows how high shear rates can disintegrate the clot and reduce the measured viscosity. Values for clot viscosity at a shear rate of 28,000 s^{-1} (c.a. 70cP) may also be extrapolated from data obtained by an ultrasonic technique employed by Yesner in the 1950's [173], however it may be that in this case, the amplitude of oscillation of the vibrating probe (less than 1 μm) was insufficient to adequately shear the fluid. In terms of viscosity sensitivity, the SmartStrip cantilevers must be able to operate comfortably over the range 1 – 70 cP.

Other well established methods for monitoring clot time such as the thromboelastogram (TEG) report the system response to the properties of the sample, rather than the properties themselves and determine CT based on changes in response relative to a given threshold. From the example TEG given in [174] we see that this maximum signal of clotted blood is approximately 22 times greater than the signal at 'R-time' which is used to determine the onset of clot formation. To an order of magnitude we need to have a viscosity sensitivity of around 3 cP to measure blood clotting as accurately as the TEG. This simplification ignores the contribution of elastic effects in both the TEG and microcantilever measurements, and is meant only as a guide.

Modern methods in microrheology [175] and its application to prothrombin time measurement [174, 176] are reviewed extensively elsewhere.

4.2.3 Rheology using microcantilevers

One of the most widely cited theoretical works on microcantilever beam oscillations in viscous media is by Sader [177]. He showed that the SHO approach is only valid at the limit of vanishing viscosity, *i.e.* with a very low damping coefficient. When the oscillations are significantly damped, they become coupled and the solutions are no longer simple. Sader derived the frequency spectrum in the case where there is small but finite dissipation for arbitrary driving forces and, specifically for the uniform heating of a rectangular beam and its surrounding environment. However we see from *figure 4.2*, that the main differences in the frequency spectrum occur away from the resonant peak.

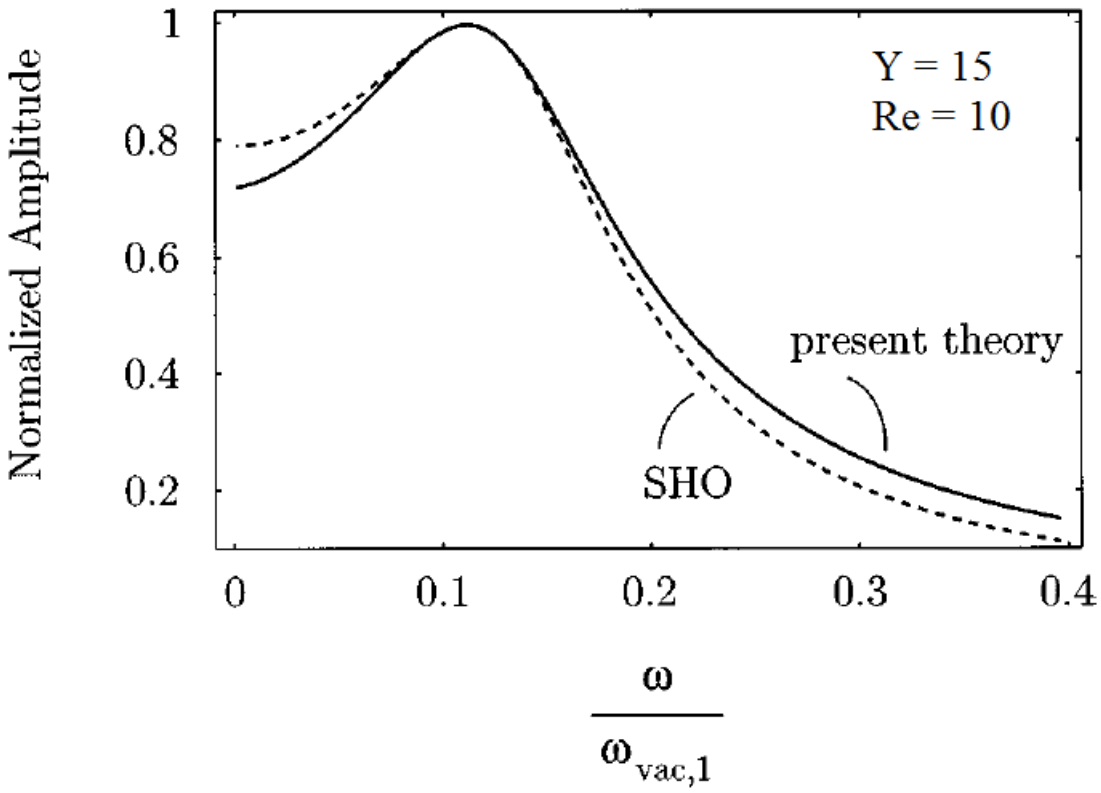

Figure 4.2: Comparison of the normalised frequency spectrum for SHO model (dashed line) and the hydrodynamic equations derived by Sader (solid line). Adapted from [177].

The model is based on four key assumptions: the beam is isotropic and of uniform cross section; the length is much greater than width and the amplitude of oscillation is small compared to the beam geometry. The last condition is particularly important as it

allows the model to neglect non-linear convective forces in the liquid that would arise from oscillation. For the case of the MV3 cantilever not one of these conditions is met, therefore quantitative agreement between the results obtained by the author and the theoretical description by Sader is not probable. However we can make use of the qualitative aspects and scaling parameters to understand the results obtained using the MV3 microcantilevers. Two important scaling factors are the Reynolds number *Re*, and the modified density ratio *Y*.

$$Re = \frac{\rho_f \omega_{vac} w^2}{4\eta_f} \qquad Y = \frac{\rho_f w}{\rho_c t_b} \tag{4.4}$$

From *Re* we see that the viscous forces become more important as the dimensionality of the beam (width *w*) is reduced; *Y* describes the effective inertial load added to the beam as it sweeps through the fluid. Sader then goes on to define an empirical model of the hydrodynamic function describing the inertial and viscous forces exerted on the beam by the fluid. The model predicts that the resonant frequency in fluid should tend towards the un-damped resonant frequency (ω_0) as the modified Reynolds number tends to infinity. A log-log plot of *Re vs.* ω_R (resonant frequency in the liquid) should be approximately linear in the region $Re \in [0.1, 1]$, with ω decreasing with *Y*. The Q-factor should be linear with *Re* on a log-log scale and increase with decreasing *Y*. For 'short pulse' actuation of the MV3 beams (w = 300 µm, frequency f = 2000 Hz) in water (viscosity η = 0.001 Pa s, density ρ_f = 1 kg/m^3), the Reynolds number is estimated to be approximately 1, meaning that the viscous forces are equal to the inertial force, however this does not allow for the large holes along the length of the beam. A more realistic estimate of 0.08 may be calculated if the effective width is considered to be 80 µm, the width of one leg of the beam.

Another significant work which shows parallels with the present study is the Hennemeyer's work on the rheology of sugar solutions [178]. As in the previous work, passive beam excitation due to Brownian motion of the fluid was used and a frequency spectrum for the beam obtained with Q factors greater than 1. From the frequency spectrum and known viscosity and density of pure water they were able to calibrate the un-damped resonant frequency ω_0 and mass per unit length µ by using the

hydrodynamic function $\Gamma = \Gamma_{Re} + i\Gamma_{Im}$, previously derived by Sader, using the following coupled equations:

$$\omega_R = \frac{\omega_{vac}}{\sqrt{1+\frac{L\pi\rho_f w^2}{4m\Gamma_{Re}(\omega_R)}}} \tag{4.5}$$

$$Q = \frac{\frac{4m}{\pi L\rho_f w^2}+\Gamma_{Re}(\omega_R)}{\Gamma_{Im}(\omega_R)} \tag{4.6}$$

In equations (4.5) and (4.6), m is the mass of the cantilever beam. Note that equation 4.5 is identical to the earlier result of Chu *et al* when the real component of the hydrodynamic function is equal to 1. They then went on to predict frequency profiles for various solutions of fructose and sucrose, finding good agreement with experiment for the resonant frequency, but not for the Q factor, which deviated to a greater extent as the viscosity increased. Hennemeyer *et al* did not relate the results back to either the complex viscosity or elastic modulus of the liquids.

4.3 Materials and Methods

4.3.1 Calibration fluid

The choice of calibration liquid was based on the following criteria:

1. Fluid must be in liquid phase (same as whole blood and plasma).
2. Calibration fluids should cover the range of 1 - 10 cP.
3. There is some literature available for viscosity of different solutions.

Table 4.2 shows data from the glycerol supplier (P&G chemicals) for the dynamic viscosity of aqueous solutions of glycerol at various concentrations.

Glycerol Concentration (% w/w)	Dynamic Viscosity (cP) Temperature (˚C)					
	20.00	30.00	40.00	50.00	60.00	70.00
0.00	1.01	0.80	0.66	0.55	0.47	0.41
10.00	1.31	1.03	0.83	0.68	0.58	0.50
20.00	1.76	1.35	1.07	0.88	0.73	0.64
30.00	2.50	1.87	1.46	1.16	0.96	0.82
40.00	3.72	2.72	2.07	1.62	1.30	1.09
50.00	6.00	4.21	3.10	2.37	1.86	1.53
60.00	10.80	7.19	5.08	3.76	2.85	2.29
65.00	15.20	9.85	6.80	4.89	3.66	2.91
67.00	17.70	11.30	7.73	5.50	4.09	3.23
70.00	22.50	14.10	9.40	6.61	4.86	3.78
75.00	35.50	21.20	13.60	9.25	6.61	5.01
80.00	60.10	33.90	20.80	13.60	9.42	6.94
85.00	109.00	58.00	33.50	21.20	14.20	10.00
90.00	219.00	109.00	60.00	35.50	22.50	15.50

Table 4.2 Glycerol viscosity at various temperatures. Data supplied by P&G chemicals.

There are a few drawbacks to using glycerol solutions as viscosity standards. The first is that above 85% w/w glycerol, the mixture is hygroscopic (takes in water) whereas below this concentration, the mixture gives up water [179]. From the table above, it is clear that there is no need to use solutions above 85%, so care should be taken to avoid water being lost from the sample. The second drawback of this system is the necessity to use a surfactant to enhance mixing of the two liquids. This means that on the nanoscale, the solution is not uniform, but consists of micelles. It was noted during the experiments that mixtures containing 65, 70 and 75% w/w glycerol appeared milky, and slightly blue tinged, indicative of the aggregate formation. An alternative calibration fluid system, silicone oils, was not considered at the time of testing.

4.3.2 Temperature Control

A calibrated dry-bath (Grant Instruments) was used to maintain a constant test temperature throughout the experiment to ensure that the drift in laboratory temperature throughout the day did not affect the viscosity of the solutions. In choosing the set temperature the following factors were considered:

1. The viscosity of glycerol solutions is most temperature sensitive at low temperatures.
2. The optimum operating temperature of the dry-bath is 37°C. At this temperature it is stable to within 1°C.

3. Evaporation of the solutions will increase with temperature and this will reduce the water content.
4. The sensor chips were designed to operate at 37°C. Operation has been characterised at this temperature and at room temperature only. In order to evaluate how the test signal changes in response to viscosity we should test within the same temperature range.

After weighing these factors, it was decided to use a test set temperature of 30 °C. Test tubes were filled with glycerol solution and equilibrated before testing. A thermometer was used to record the temperature throughout the experiment. All tubes were covered with foil when not in use for testing to minimise evaporation.

4.3.3 Preparation of Standard Solutions

Glycerol solutions were prepared by weight as indicated in the manufacturers' datasheet and in the literature. A four point balance was used to record the weights. The surfactant Triton-X was used at a concentration of 0.5% in each solution (even 100% water). The table below shows the concentrations and corresponding viscosities (interpolated from the data sheet) prepared.

Weight of Glycerol (± 0.0001 g)	Weight of Water (+/- 0.0001 g)	Percentage Glycerol (%w/w)	Viscosity at 30±1˚C (cP)
0	16.95015	0 ± 0	0.800 ± 0.001
3.4023	15.3204	18.17 ± 0.02	1.204 ± 0.001
5.0806	13.5303	27.30 ± 0.03	1.777 ± 0.001
6.7874	11.8311	36.46 ± 0.03	2.307 ± 0.003
7.6362	11.324	40.27 ± 0.04	2.695 ± 0.005
8.4696	10.2401	45.27 ± 0.04	3.40 ± 0.01
9.3208	9.321	50.00 ± 0.05	4.27 ± 0.01
10.1651	8.496	54.47 ± 0.05	5.32 ± 0.01
11.0223	7.6941	58.89 ± 0.05	6.72 ± 0.02
11.8775	6.792	63.62 ± 0.06	8.95 ± 0.04
12.7156	5.9496	68.12 ± 0.06	12.25 ± 0.05
13.5478	5.5601	70.90 ± 0.06	15.16 ± 0.07

Table 4.3: Preparation of glycerol solutions

4.4 Experiment #1: The CoagMax

4.4.1 Experimental Set-Up

Partially assembled SmartStrips composed of only the cantilever die and supporting PCB were used in this experiment. Additional components such as the reagent and capillary would add unnecessary complexity. Each strip was mounted onto an extension PCB so that the cantilever die could be inserted into the liquid without wetting the inside of the CoagMax. This extra set of contacts increased the electrical spikes due to vibration in the signal but could not be avoided. A clamp was used to hold the CoagMax steady and thus minimise noise.

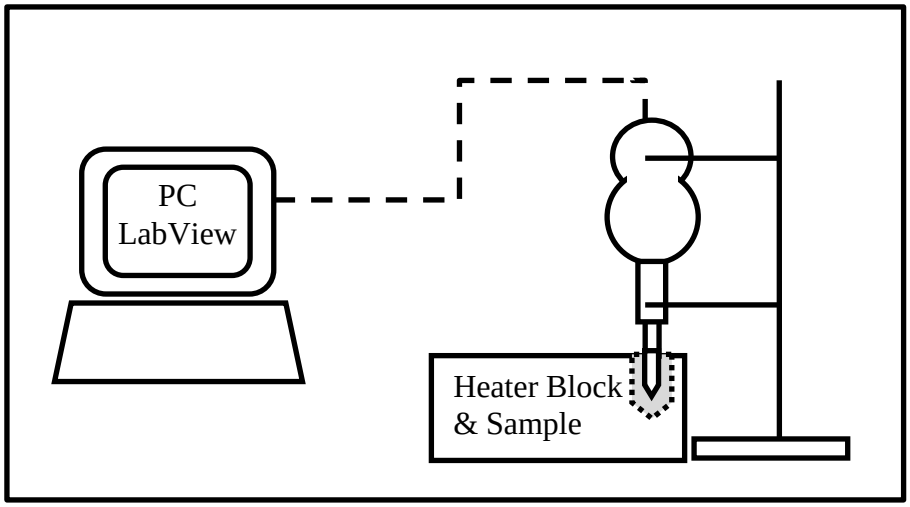

Figure 4.3: Diagram of apparatus for CoagMax signal measurements in glycerol solutions.

The actuation pulse used was a 6 volt, 0.5ms square wave at 10Hz. Data was collected in two channels simultaneously (42 Hz high pass and 150 Hz low pass filter outputs) at a rate of 100,000 sample points per second for 0.01 seconds per pulse. A 30 second reference signal was recorded for each strip in air to check that the strip was functioning correctly, and then the strip was immersed into the glycerol solution. Ten strips were tested for each glycerol solution and all strips used were from the same manufacturing batch.

4.4.2 Data Analysis Methods

There are three key features that can be used to evaluate the collected signals: the peak height; peak position and valley position. Therefore, when we consider both the high pass and low pass signals, we need to look at six dependent variables. A LabView data analysis program was written by Dr Richard Dunn to find the peak position and height, and valley position for each pulse. A schematic of the output signal showing the key signal parameters is given in *figure 4.4,* below.

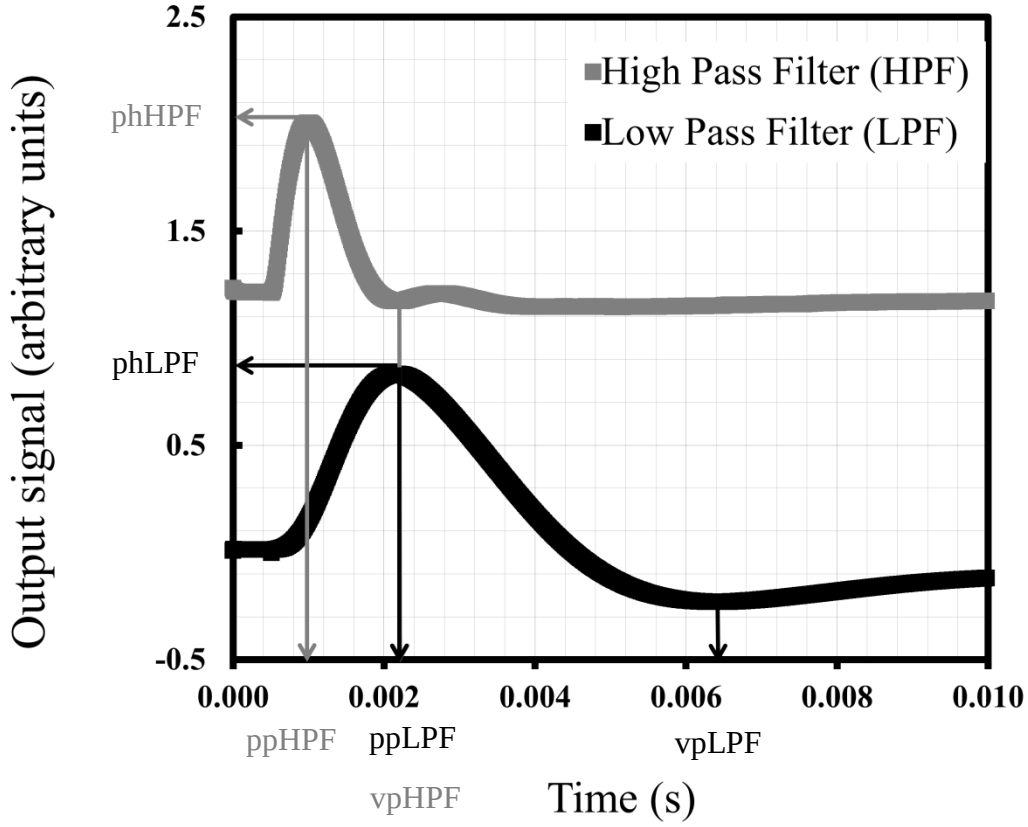

Figure 4.4 Schematic showing the form of the output from high pass and low pass filters (HPF and LPF respectively) of the SmartStrip sensor. Key signal parameters are indicated on their axes and are the peak height (phLPF and phHPF), peak position (ppLPF and ppHPF) and valley position (vpLPF and vpHPF).

The output from the LabView data analysis program shows how the six dependent variables vary over the duration of each test. For the purpose of evaluating the sensor response in different viscosity fluids, an equilibrium value for each of the six parameters from each SmartStrip using Matlab (The MathWorks Inc.) was calculated. After the strip has equilibrated to the liquid temperature of 30 °C, the filtered response curves should keep to a constant form. A linear fit, excluding outliers due to electrical spikes or samples where there was unexpected drift, was made to each dependent variable collected over the final 30 seconds of signal collection in the liquid. Data was only accepted for samples where more than 95% of the data points were within 5% of the intercept value of this best fit. This means that samples which have the occasional electrical spike will be accepted, but samples that have a best fit gradient of more than *intercept*·× 5.3%, i.e., samples that have not equilibrated normally, will be rejected. Electrical spikes in the data are much more common when the extension PCB is used. Drift in the signal can occur when the Wheatstone bridge does not balance correctly, or

if the cantilever is damaged. The equilibrium value is taken to be the best fit value at t - 30 seconds, where t is the total length of time that the signal was recorded. Note that the frequency at which read errors occurred on the strip increased with the viscosity of the test liquid, so fewer than 10 strips results are presented for each condition. An individual value plot was created for each data parameter so that any outlier strips could be visually identified. These are shown in *figure 4.5*, below.

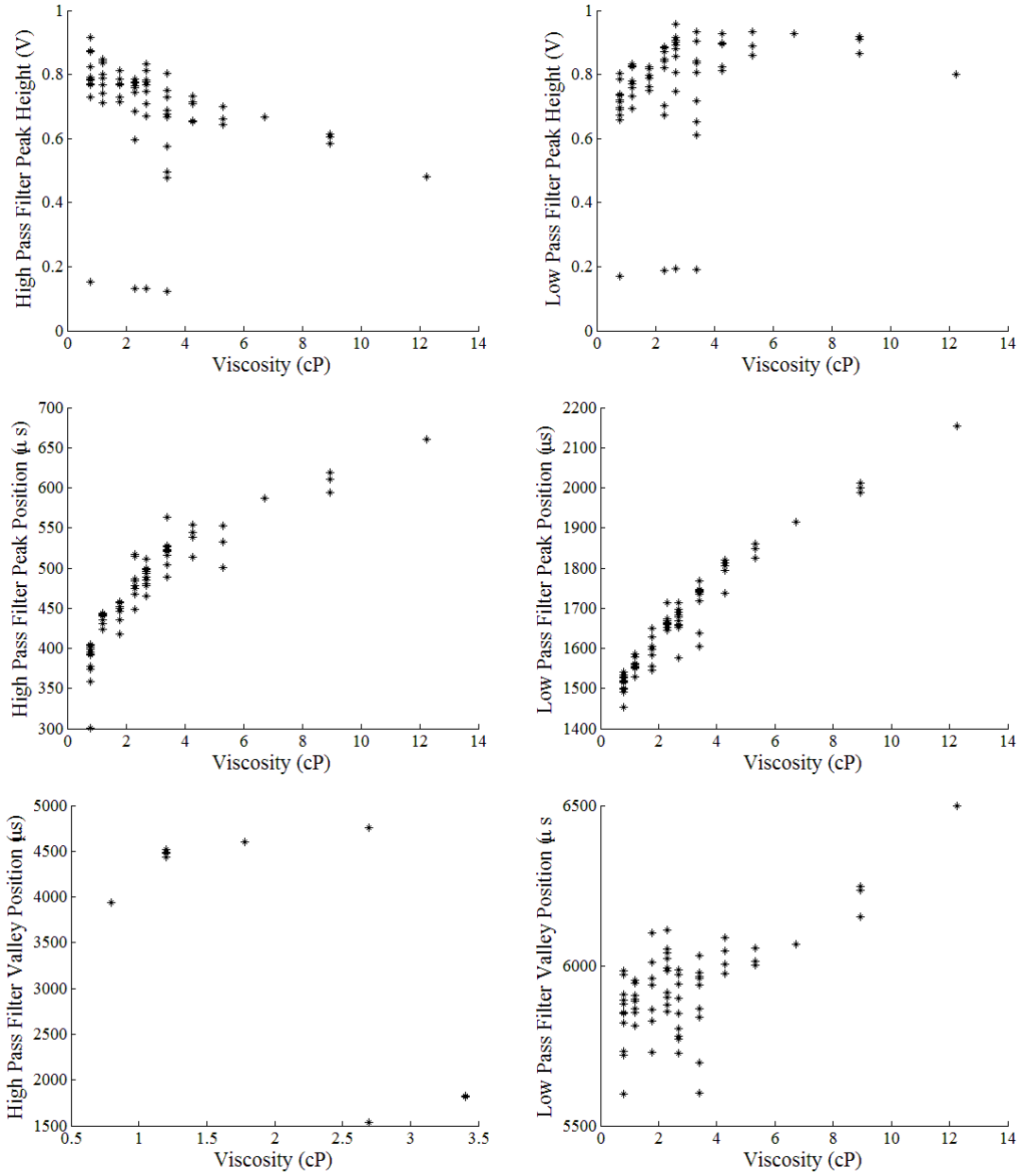

Figure 4.5: Individual value plots showing the six key signal parameters: Low Pass Filter, right; High Pass Filter, left; peak height, peak position and valley position at top, middle and bottom respectively. Individual Strip names have been removed from the diagrams for clarity.

The highest degree of correlation (c = correlation coefficient for x vs. y) between viscosity and the dependent variables is observed for the low pass filter peak position (c = 0.9554), closely followed by the high pass filter peak position (c = 0.8758). The peak heights for low pass and high pass filter outputs have low correlation (c = 0.2689 and -0.3046 respectively) due to the presence of several low-outlying results. Double checking against the raw data confirmed that these average values reflect the genuine results and that the peak heights are particularly low for these strips. The valley positions also have low correlation coefficients of 0.6862 and -0.7537 for the low pass and high pass filter results respectively. Very few results are recorded for the high pass filter valley position indicating that this parameter changes over time. Possible causes of the variability of the results were investigated. A correlation between the signal parameters and time would indicate that the sample composition was changing over the duration of the tests, but has not been observed. Differences in the cantilever layer thicknesses or heater or sensor resistances are unlikely to cause variations in the signal, as these would result in differences in the baseline of the signal (i.e. the 'zero' Wheatstone balance level), which are normalised by the low pass and high pass filters.

4.4.3 Results and Discussion

Figure 4.5 shows how each of the signal parameters from the CoagMax varies with liquid viscosity. The most discriminatory parameter based on linearity and standard error was found to be peak position of the low pass filter. This confirms that the parameter used in clot diagnosis is the best choice for the sensor. The absolute viscosity resolution within the range 0.7 – 15.2 cP was found to be 2 cP based on the range of responses from the different strips.

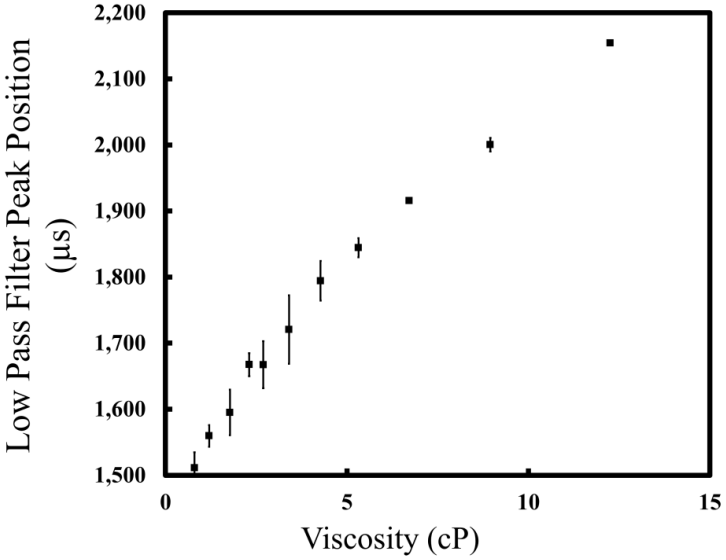

Figure 4.6: Variation of peak position of the low pass filter signal with viscosity. The mean response is plotted and error bars are 1 standard error.

The first and second aims listed in *section 4.1* cover how the CoagMax signal relates to viscosity and this was analysed using the same metrics as for blood clot detection, *i.e.* monitoring the position of the peak from the low pass filter (ppLPF). Possible sources of variability were considered:

1. Variations between strips
2. Variations in the fluid temperature. This will have greatest impact on the solutions where the water content is high.
3. Concentration of water in the liquid decreasing over time.

The magnitude of (1) and (2) combined can be estimated from the pure water sample tests and appear to be the dominant errors, however due to the low number of results obtained at higher viscosities it is difficult to make a statistical comparison.

4.5 Experiment #2: The Microsystems Electronics

Evaluating the microcantilever signal from the CoagMax as a function of viscosity is useful for understanding product performance, but offers limited insight into the physics, since information about the motion of the beam is lost in the filtering. As identified by other researchers including Dunn and co-workers [180], it is very difficult

to resolve thermal and mechanical aspects of the microcantilever signal, especially since the two sets of properties cannot be varied independently within a liquid sample, making even empirical signal analysis difficult. Therefore viscosity calibrations were repeated using bespoke electronics from Microsystems, (Mikrosistemi Ltd., Varna, Bulgaria).

4.5.1 The AC signal for mechanical motion

Experiments were performed at Microvisk in 2009 (by Dr Richard Dunn and Dr Vladislav Djakov) using a high speed video camera to record the profile of the cantilever beam as it was actuated. The microsystems electronics hardware was used to record the electrical signal simultaneously. *Figure 4.7* shows how the AC Wheatstone bridge output follows the beam tip deflection in real time.

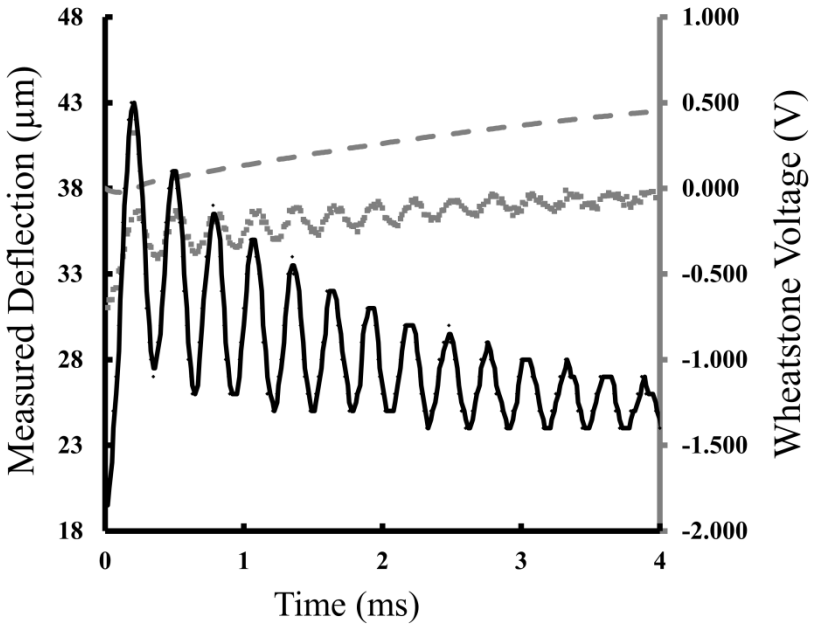

Figure 4.7: Comparison of analysed high speed video frames capturing cantilever tip deflection (black, plotted with 2 point moving average), DC signal (grey, dashed) and AC signal (grey, dotted) from the Microsystems electronics. Responses follow 200 µs actuation pulse delivered to the cantilever in air.

The AC signal from the microsystems electronics clearly captures the decaying oscillations of the cantilever beam, whereas the DC signal does not. In the following experiment the AC signal was used to get information on the motion of the beam.

4.5.2 Experimental Set-Up

The experimental set up used to obtain AC signal response is shown in *Figure 4.8*. LabView (Version 8, National Instruments) was used to control signal generation (*via* Agilent function generator, 33220A) and data acquisition (*via* data acquisition card NI USB-6251, and Microsystems bespoke electronics comprising amplifier and switchboard). The amplifier gain was set to ×390 throughout.

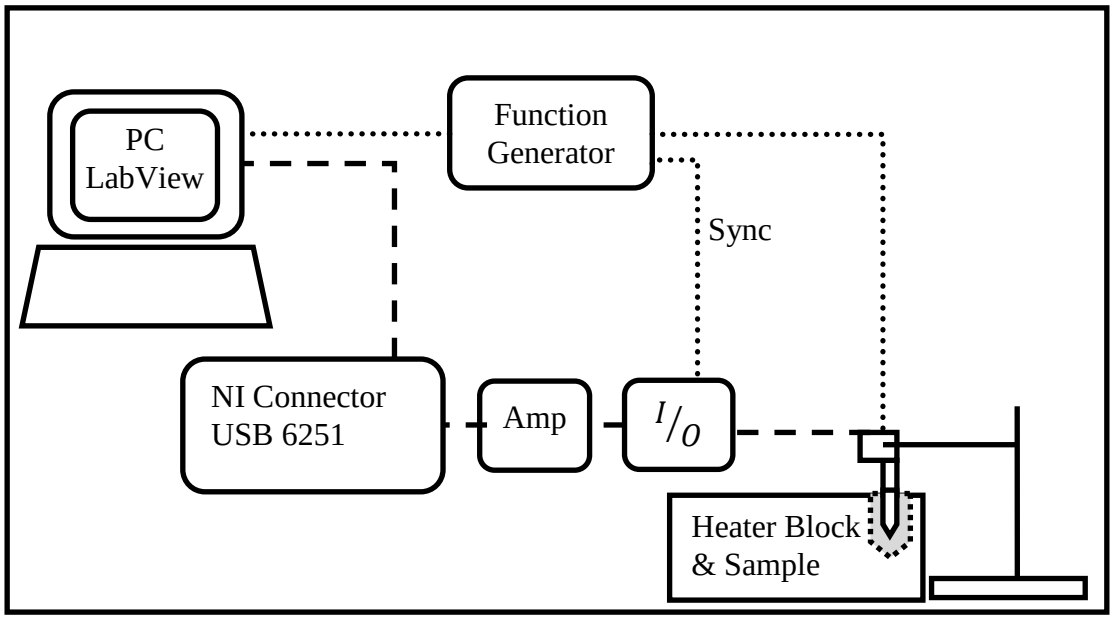

Figure 4.8: Block diagram of microsystems set up: dotted lines are for actuation, dashed lines for sensing.

As with the previous testing using the CoagMax, partially assembled SmartStrips, composed of only the cantilever die and supporting PCB, were used in this experiment in conjunction with an extension PCB so that the strip can be immersed into the glycerol solution. Solutions used are the same as previous. Output from each test is stored automatically as *LabView measurement files* (".lvm") and subsequent data processing was done using Matlab. Details for the experiment were recorded automatically in a notepad file.

4.5.3 Characterisation of the electronics

Information about the components of the Microsystems electronics (*i.e.* a circuit diagram) was not available, so a full characterisation of the electronics was done including checking for linear output from the function generator, linear gain and frequency dependence of the measured signals.

Actuation: The function generator actuation voltage supplied to the SmartStrip ($V_{applied}$) was found to be linear with the LabView input (V_{input}). Over a 360 Ω resistor (the closest available on the day to 80 Ω heater resistance) the values could be converted using the following formula: $V_{applied} = 1.9209V_{input} - 0.1756$.

Gain: The gain was measured for an input at 200 Hz. The gain setting of ×390 used in experiments was found to correspond with an amplification of 70.671 times over the range 0 to 0.08 V.

Frequency Dependence: The Wheatstone bridge excitation voltage (V_{in}) is DC. The damped oscillation of the cantilever means that V_{out} has a component that is rapidly changing. In the electronics, this is isolated using a high pass filter. The electronics has been designed so that the AC signal is always amplified to the same level, and therefore DC signal is attenuated in comparison.

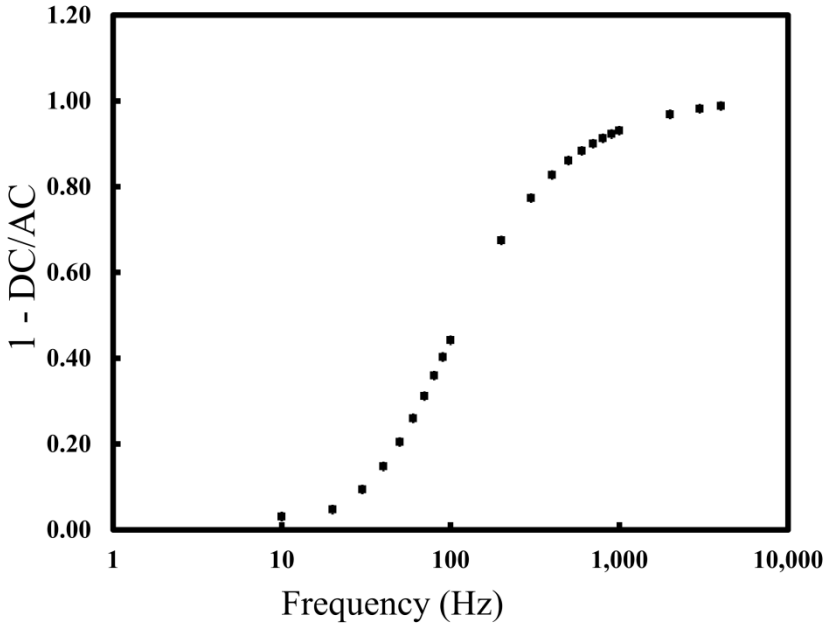

Figure 4.9: Frequency dependence of the Microsystems Electronics. Frequency cut off in the AC signal is below 1000Hz.

The anticipated resonance frequency is approximately 4 kHz, so the signal from the electronics should not be significantly attenuated.

4.5.4 Pulse Selection

Data were collected on two types of pulse. The first condition is set to be as close as possible to the actuation and data collection in the CoagMax: each 6.0 V pulse is 0.5 ms long and delivered at a frequency of 10 Hz. Data is recorded over 1000 points per pulse at an acquisition rate of 100 kS/s. The second pulse used was the same as the first, but had a pulse width of 1.0 ms. This was used so that enough energy could be delivered to the beam to set up a full oscillation in the liquid samples. The experimental data acquisition process is shown in *figure 4.*10

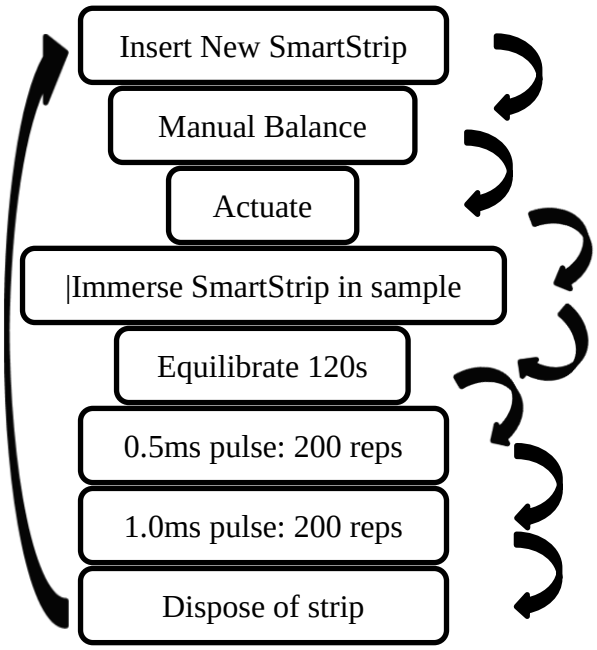

Figure 4.10: Actuation sequence employed during Microsystems viscosity tests. Each strip is tested with two different pulses in one glycerol solution.

Unfortunately there was an error in the LabView data collection program, which was written on a different version (different laptop) of LabView to the one that was used for data collection. The program worked as intended on the original laptop, but when transferred to the new machine, the program appeared to function correctly, but it was later found that instead of recording 200 pulses, it only recorded data from one pulse of each condition. This was because the terminals to the 'write data' sub-VI differ in position in the two different versions of LabView. Because operation of the VI had been checked on the original machine, the error was not identified until data analysis and there was no time to repeat the experiment correctly.

4.5.6 Data Analysis – AC data

Example raw data results from the 0% glycerol and 60% glycerol solutions are shown on the following panel grouped by test liquid. The data have been normalised by subtraction of the final value of each plot. Due to the electrical spike in each signal at the time of the heater being turned on and off, normalising to the initial value is not appropriate for these results.

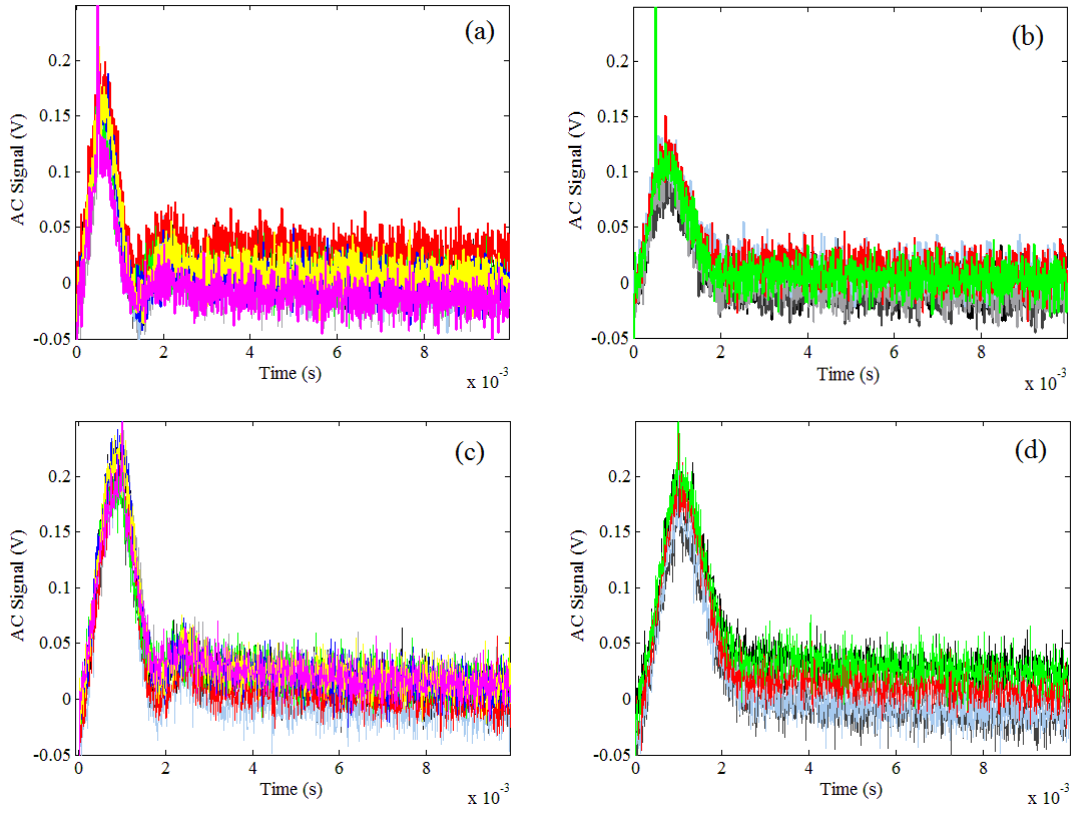

Figure 4.11: Normalised raw data showing good agreement between individual strip responses for the 0.5ms AC signal in (a) pure water and (b) 60% glycerol solution and for the 1ms AC signal in the same liquids (c and d respectively). Traces from several strips are shown in each figure plotted in different colours.

Although the error in the data collection *VI* means that it is not possible to average out the noise for individual strips, the similarity in response of all strips tested in the same liquid, once normalised, means that it is possible to use an inter-strip average to reduce the effect of the noise before using a fast Fourier transform to identify the oscillation frequency distribution *(Figure 4.11)* of the beams in each liquid.

The data processing was carried out according to the following method:

1. Average the signal from all strips tested at each glycerol concentration.
2. Because the pre-amplification AC signal is not completely attenuated at 100 Hz (corresponding to the length of data set), there is a small amount of drift in the data that arises from the thermal profile seen clearly in the DC data. This is observed in the averaged data by the fact that the oscillations do not occur around zero, they are on a very slight slope. To get an improved frequency

spectrum, the linear background (as fitted to the data after 0.005s) was subtracted from the averaged AC data at each glycerol concentration, as an approximation to the subtraction of a low frequency oscillation. Although this is not an ideal way to process the data, it is acceptable because the gradient is very shallow and the quality of the data is already limited for the reasons discussed above.

3. Fast Fourier transform was performed. Since we want to find the natural oscillation frequency of the beam under different viscosities, data acquired during the pulse was discarded from the Fourier analysis.

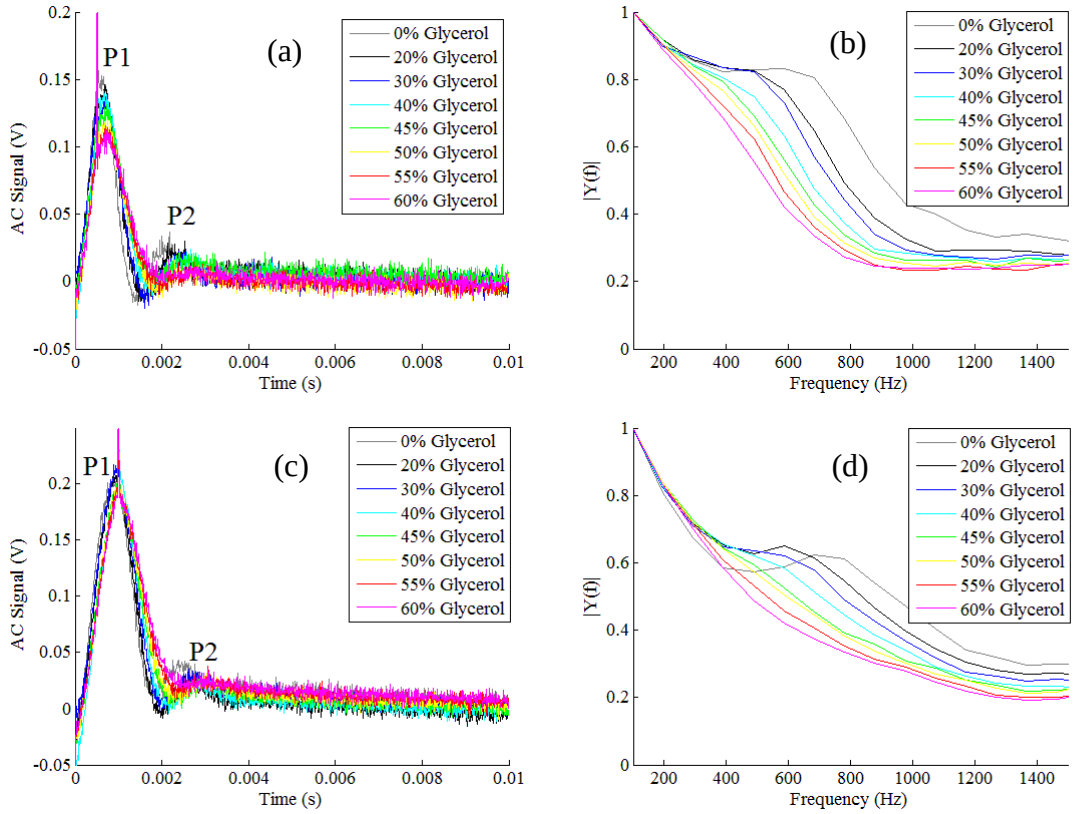

Figure 4.12: Mean signal at each glycerol concentration (a and c) and FFT (normalised to the highest value) of the average signal (b and d) for 0.5 and 1ms pulses (top and bottom respectively).

From observation of *figure 4.12* we see that the cantilever response is under-damped, tending towards critical damping at high viscosity. The sloped profile of the FFT makes the beam oscillation frequency difficult to identify, though it is similar in form to the profiles obtained by Agoston *et al* [181] for magnetically actuated cantilevers undergoing forced oscillations in a variety of engine oils. As can be seen from *figure*

4.12, the 1.0 ms pulse saturates the deflection of the cantilever in solutions containing 40% glycerol or less, but the 0.5 ms pulse does not. Frequency components at less than 400 Hz are due to the tail (i.e. the gradient between 0.004 s and 0.01 s) of each peak and limited sample size. A sharper frequency spectrum could have been obtained if (1) a continuum of pulses were captured in each data set, with shorter spaces between pulses (e.g. pulse frequency = 200 Hz) to increase the proportion of the signal that is oscillating, (2) a longer signal was collected to increase the frequency resolution, and (3) the signal-to-noise ratio was increased, e.g. by averaging over a larger number of samples. A 'ball-park' estimation of the natural frequency of the beams can be found from observation of the FFT as c.a. 800 Hz in pure water, reducing to c.a. 400 Hz in 60% glycerol for the 0.5 ms pulse. In the 1 ms pulse, the system is very close to the critical damping point in the 60% glycerol solution and no resonance peak can be seen in the frequency spectrum. Various methods for extracting the resonant frequency and Q-factor from data in the time and frequency domains:

Method 1: Estimation from time domain data. In the 0.5 ms pulse, there is an overshoot after the pulse has finished and there are two 'natural' peaks in the data (amplitudes P1 and P2 shown in *figure 4.12*) from which the resonant frequency and logarithmic decrement can be estimated and the Q-factor calculated as:

$$Q = \frac{\sqrt{2\pi^2 + \left(\ln\left(\frac{P1}{P2}\right)\right)^2}}{2\ln\left(\frac{P1}{P2}\right)} \tag{4.7}$$

Method 2: Fit to the forced SHO model in the frequency domain. No satisfactory fits to the fast Fourier transform frequency spectrum *(figures 4.12b and 4.12d)* were obtained using the well-known SHO frequency spectrum equation for a forced harmonic oscillator:

$$A(\omega) = \frac{A_0 \omega_R^2}{\sqrt{\left(\omega^2 - \omega_R^2\right)^2 + \left(\frac{\omega \omega_R}{Q}\right)^2}} \tag{4.8}$$

The FFT obtained from the raw data had a large component at zero frequency due to the sampling conditions that was not resolved from the peak of interest (as can be seen in the top panel of *figure 4.13)* making direct application of the SHO equation difficult. It is noted that when the 60% glycerol solution is used, barely any resonance is observed. Therefore subtraction of the FFT from the 60% glycerol data from the FFT of the other solution data (0%, 20% glycerol etc.) gives an indication of what the FFT would look like without the background slope arising from the zero frequency component. An estimation of the resonant frequency has been made using this approach and is depicted for the 0%, 20% and 30% glycerol solutions in *figure 4.13.*

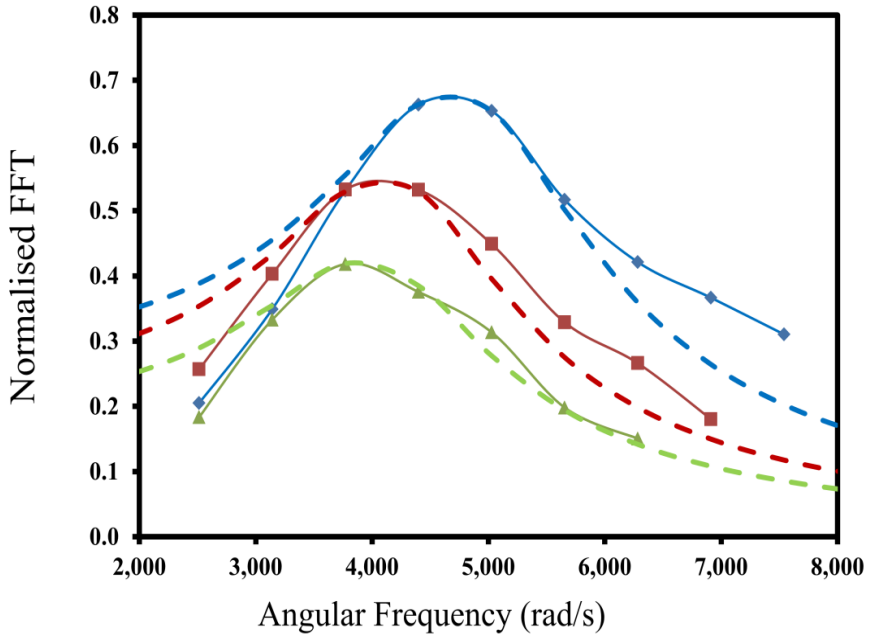

Figure 4.13: Frequency spectrum of 0.5 ms pulse response in 0%, 20% and 30% glycerol solutions (blue, red and green respectively) normalised against the frequency spectrum from 60% glycerol. A weighted best fit of the data to equation 4.8 is plotted in dashed lines.

Method 3: Estimation of resonant frequency from the gradient of the phase shift. This was the approach taken by Agoston *et al* who, in a cantilever study of the viscosity of various engine oils produced a similar frequency distribution to the data here presented (though in their study the Q factor was not calculated). Comparison of the phase and FFT spectra shows the validity of this approach. Here we use the value of the most negative phase as a measure of Q factor.

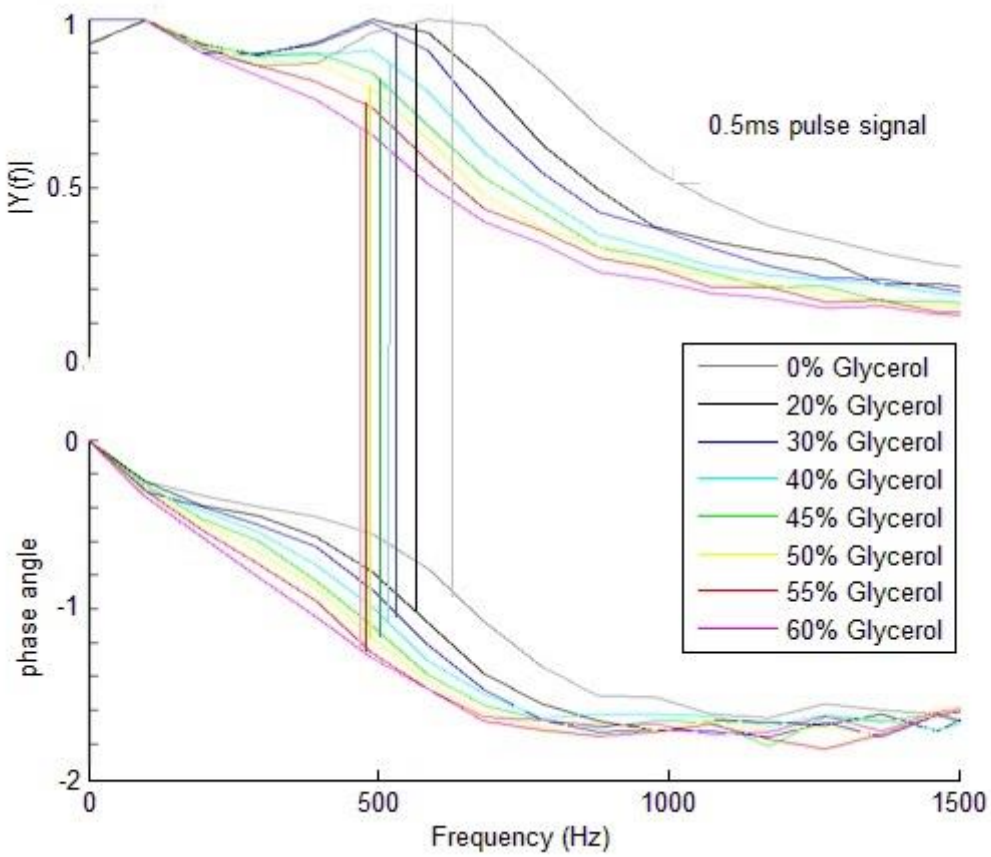

Figure 4.14: Relationship between phase angle spectrum (lower plots) and frequency spectrum. Resonance can be found from the most negative phase gradient.

The different methods to calculate ω_R and Q are compared in *figure 4.15;* further calculations are based on the average and standard deviation of these results.

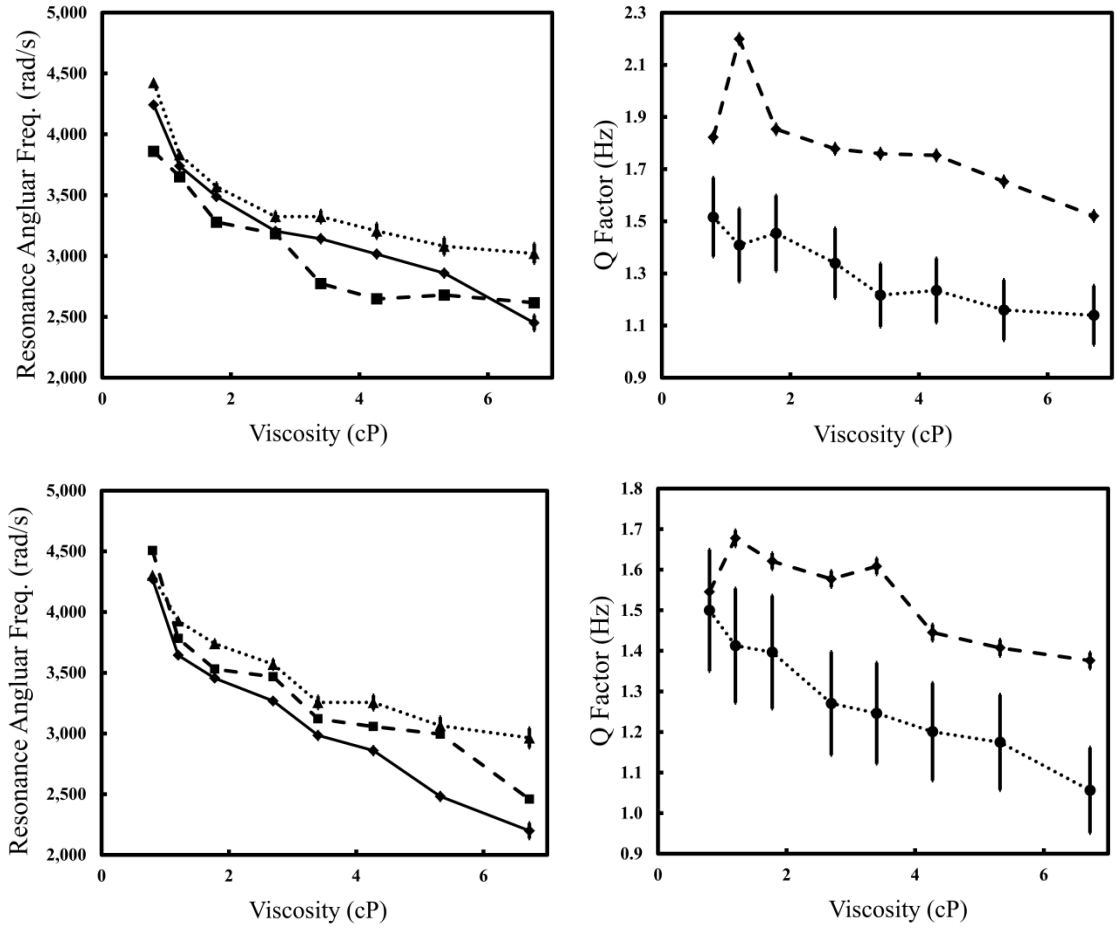

Figure 4.15: Comparison of resonance frequency (left) *and Q factor* (right) *using different calculation methods (phase gradient ♦, fast Fourier transform ■, time domain estimate ▲ and logarithmic decrement ●) for data collected from 0.5 ms actuation pulse* (top) *and 1.0 ms actuation pulse* (bottom).

Figure 4.15 shows that the three methods used to calculate the resonance frequency of the beam are broadly in agreement. The error bars shown for each technique represent uncertainty in the data analysis technique: statistical analysis of the errors was not possible because it was necessary to use the averaged data to reduce the effect of noise in the signal. As the viscosity of the test liquid increases, the difference in the calculated resonance frequency from each of the three techniques increases, reflecting the fact that the cantilever is tending towards critical damping.

4.5.7 Results and Discussion

Using the dimensionless parameters *Re* and *Y* defined in *section 4.2.3*, we find that ln(Re) is linear with the natural log of the measured resonant frequency and Q-factor, indicating that the hydrodynamic function of the beam is indeed of the same form as defined by Sader in [177].

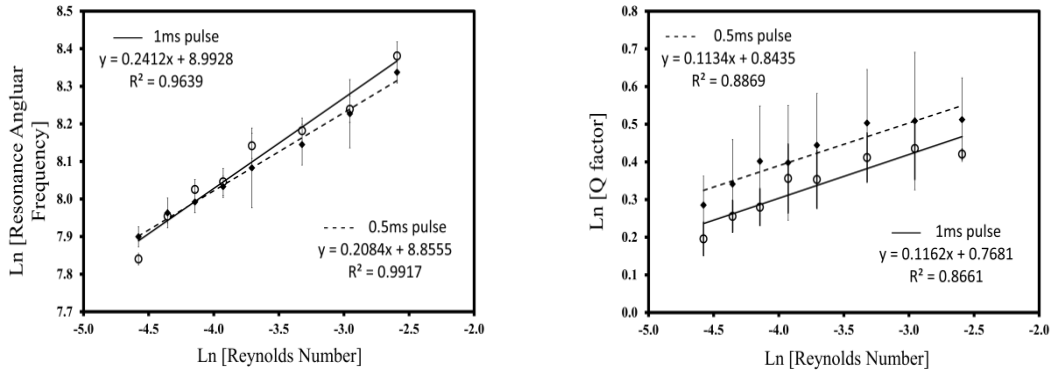

Figure 4.16 Linear response of the resonance frequency (left) in and Q-factor (right) in different liquids as a function of the Reynolds Number plotted on a log-log scale.

The resonant angular frequency of the beam in a vacuum was calculated from the mechanical properties of the beam, $\omega_0 = \sqrt{(k/m)} = 6.8$ krad/s, assuming the beam behaves as a simple harmonic oscillator with a solid uniform rectangular cross section. The spring constant $k = 3EI/L^3$ where E is the composite Young's modulus (a volume average of the Young's moduli of the individual layers), I is the moment of inertia of the beam $(I = wt^3/12)$, and the beam has dimensions: length *L*, width *w* and thickness *t*.

The experimental values can now be compared with Chu's model accounting for density only *(figure 4.15)* where we see that the fluid density does not give rise to the change in frequency of the beam in different fluids.

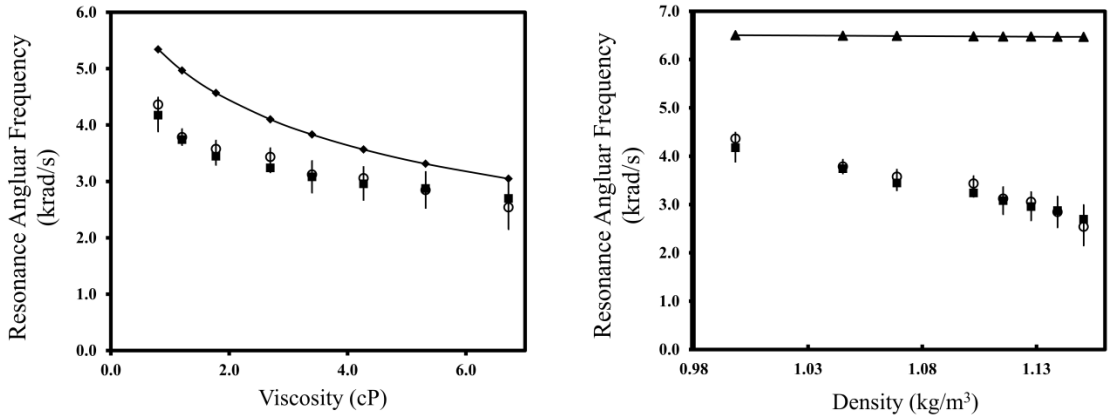

*Figure 4.17 Comparison of theoretical results based on Sader's hydrodynamic constants with ω_0 calculated from the dimensions of the beam (♦) with experimental results from 0.5 ms (■) and 1 ms (**O**) pulse, showing the variation of resonance frequency with test liquid viscosity (left). Chu's analysis of the effect of density on the resonant frequency with ω_0 calculated from the dimensions of the beam (▲) and the experimentally determined resonant frequencies in liquids of various density (right).*

When ω_0 is used to predict the resonance in glycerol solutions ω_R, calculated values according to Sader's hydrodynamic constants follow the same trend as the experimental data but are offset by approximately 1 krad/s. This is most likely to be due to uncertainty in the mechanical properties of the materials in the beam, which were found in the literature [91, 182, 183]. The full width of the beam of 280 µm was used in calculations. Because the cantilever beam has three legs, each 66 µm wide, the smaller width was considered for use with these equations and would be more appropriate than the full width *if* the liquid flows through the holes as the beam moves through the fluid. From [184] we know that the thickness of the fluid moved vertically by the cantilever is given by the fluid viscosity η_f and density ρ_f and is found by equation (4.9) to be at least 700 µm for all fluids tested. Although less fluid than this will move at the sides of the beam, the fact that δ is an at least 17.5 times as great as the holes size gives confidence that there is negligible flow through the holes in the beam during oscillations.

$$\delta = \sqrt{\frac{2\eta_f}{\rho_f \omega}} \tag{4.9}$$

4.7 Conclusions

This chapter began with the following aims:

Effect of fluid viscosity on the CoagMax signal: The peak position is the parameter that is most sensitive to viscosity and that it is linear with viscosity within the range 0 – 10 cP, showing a sensitivity of 2 cP.

Change in blood viscosity upon clot formation: A literature review revealed that a change in viscosity of 3 cP would be sufficient to trigger a TEG measurement of prothrombin time. Therefore the cantilever sensitivity to viscosity alone is sufficient to explain the change in signal as blood begins to clot.

Relationship between mechanical motion of the beam and fluid viscosity: Using the AC signal from the microsystems electronics, it was shown that the effect of fluid density on the beam deflection following a short actuation pulse is negligible compared to the effect of the viscosity. The use of a 1 ms pulse to generate responses of higher amplitude did not raise the Q-factor as desired: instead the Q factor is lower than that observed for the 1 ms pulse. This is because with the longer pulse, the cantilever is on the verge of being 'over driven'.

In this chapter the SmartStrip microcantilever sensor response to viscosity is characterised and it is shown that changes in this parameter alone are sufficient for the detection of blood clotting in the clinical trials. The sensitivity of this commercial system (2 cP) is not as high as for another system recently reported recently in the literature (0.04 cP) [117], but is sufficient for the application, with the advantage that this is a fully developed, packaged system and that the result encompasses chip-to-chip variability unlike previously published work. This study would be improved further by additional testing using a calibrated viscometer to verify the viscosities of the prepared test liquids.

Chapter 5
Design and Microfabrication of a Thermal Sensor

5.1 Introduction and Background

Microcantilevers designed for measurement of thermal conductivity or measurement of topography using the thermal properties of surfaces have been reported by several research groups, most notably by King *et al* of the University of Illinois, USA [115, 185, 186], and also by Rangelow *et al* [187] and Haeberle [188]. The principle used in each case is to scan a surface in a similar manner to AFM, using a cantilever with a heated element at the tip to produce a constant heat source, and a thermal sensor such as a platinum thermocouple integrated into the beam design close by. As the cantilever scans the surface, heat is conducted away from the beam by the substrate; hence the temperature recorded at the thermocouple corresponds with the thermal conductivity of the substrate and distance of the tip from the substrate. This scanning approach is therefore limited to solid samples, with the most accurate results being obtained under vacuum.

To the best knowledge of the author, no microcantilever sensor has been demonstrated for measurement of the thermal conductivity of liquid samples. In addition, in published studies where a different fluid property such as viscosity has been measured, the influence of the thermal conductivity of the liquid has not been evaluated. The major challenge involved in such an undertaking (when done experimentally) is the difficulty in uncoupling the mechanical and thermal components of the signal. In addition, it is difficult to resolve thermal and mass transport effects within the fluid.

Resonance measurement of microcantilever sensors driven by thermal actuation are usually made in the high frequency domain because of the dominance of thermal effects in the low frequency or direct current modes [189]. The SmartStrip sensor uses the peak position from its low pass filter output to determine the clot time. It is therefore possible that there is a cross sensitivity to the thermal properties of the surrounding environment of the beam that could affect the performance of the sensor.

In this chapter, the design for a microcantilever sensor to investigate the thermal properties of a liquid environment is presented. There are differing accounts in the literature of whether a thermally actuated microcantilever with piezoresistive read-out mechanism could be expected to show significant sensitivity to the thermal conductivity of a liquid sample, and these are discussed further in this section *(section 5.1)*. A novel design for the cantilever is presented in *section 5.2*, the key feature of which is positioning the read-out piezoresistor in the neutral axis of the beam to uncouple the mechanical aspect of the signal. Details of the microfabrication and characterisation of the sensor batch are then presented in *section 5.3* with chapter conclusions in *section 5.4.*

5.1.1 Research at STFC and Microvisk

Research into thermal bi-material microcantilever sensors at STFC began in 2003 with polyimide and gold as the bi-material layers, a chromium heater and no sensor [163], and the company Microvisk Ltd. was spun-out shortly afterwards. Early research focussed on optimising the radius of curvature through variation of the layer thicknesses. Applications in x-ray focusing were realised [190, 191], introducing a sensor element; and the group took part in a European project, PRONANO, to develop highly multiplexed polymer cantilever scanners for metrology applications [192, 193]. Operation as a surface stress sensor was also investigated [88] using an encapsulated gold layer as a piezoresistor. The sensor developed in this work also uses encapsulated gold sensors, but the placement of these sensors within the layer structure has been modified to decrease stress sensitivity and isolate the thermal signal.

Research at Microvisk Technologies Ltd. focussed on cantilever design and signal processing [30, 31, 194]. *Figure 5.1*, below, shows a comparison between solid and

epsilon shaped beams via the dc signal component. As shown in *Chapter 4*, the oscillatory component of the signal is most closely related to the viscoelastic properties of the fluid sample, and it is thought that the overall rate of decay of the sensor response is due to heat transfer from the beam to the fluid.

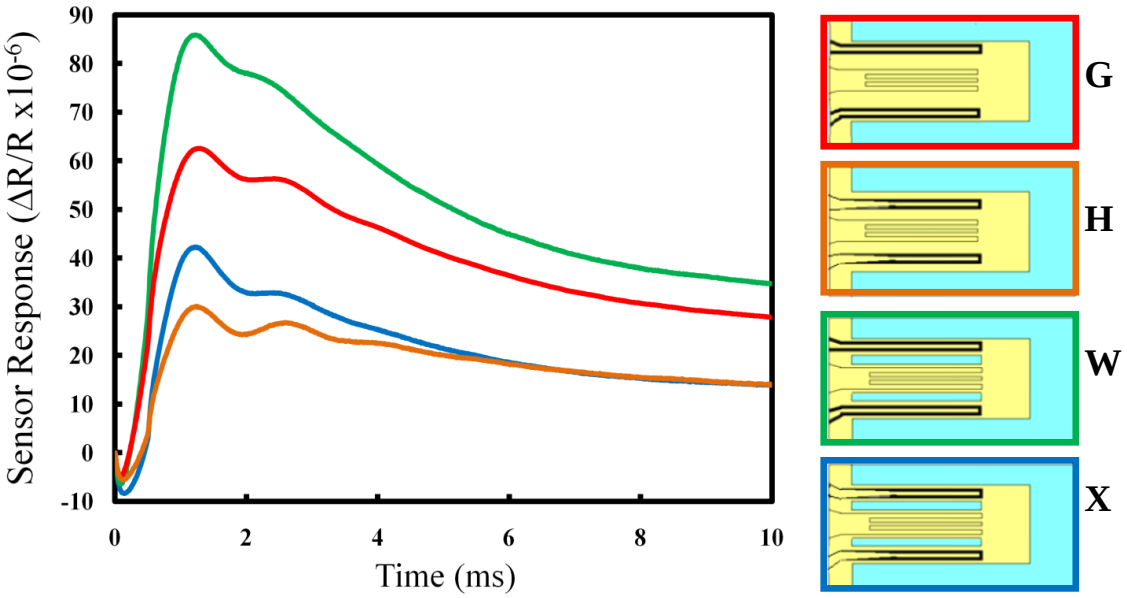

Figure 5.1 Single microcantilever response of MV2 W (green), MV2 G (red), MV2 X (blue), and MV2 H (orange) in water using a short (0.5 ms) actuation pulse. The power of the actuation pulse is 300 mW for MV2 W, 270 mW for G, 181 mW for X, and 179 mW for H. Reproduced with permission, from [18]. *Schematic illustrations of each design are shown to the right.*

It is interesting to note then that the company preferred to develop the epsilon design over the solid design for the pragmatic reason that the oscillations are increasingly difficult to detect as the damping increases, in comparison with the shift of the pronounced first peak that is observed on the signals from the epsilon shaped devices. Since holes in the beam (i.e. gaps in the epsilon design) decrease the resistance to fluid flow, we would expect them to decrease the sensitivity of the mechanical signal as well as decreasing heat conduction between heater and sensor read-out tracks.

5.1.2 Electrothermal dynamics in the microcantilever

The theory of heat distribution in a microcantilever with epsilon design is examined in detail in the work of Li and Uttamchandani [195]. Details of their design differ from the thermally actuated bi-material cantilevers presented in this work: for instance, deflection in their polysilicon unilayer structure is driven by difference in expansion between the outer 'hot arms' and the inner 'cold arm', rather than bi-material deflection (i.e. a lateral thermal bimorph). Such an effect is likely to contribute to the deflection of cantilevers presented in the current work as well, and presents an avenue for further research.

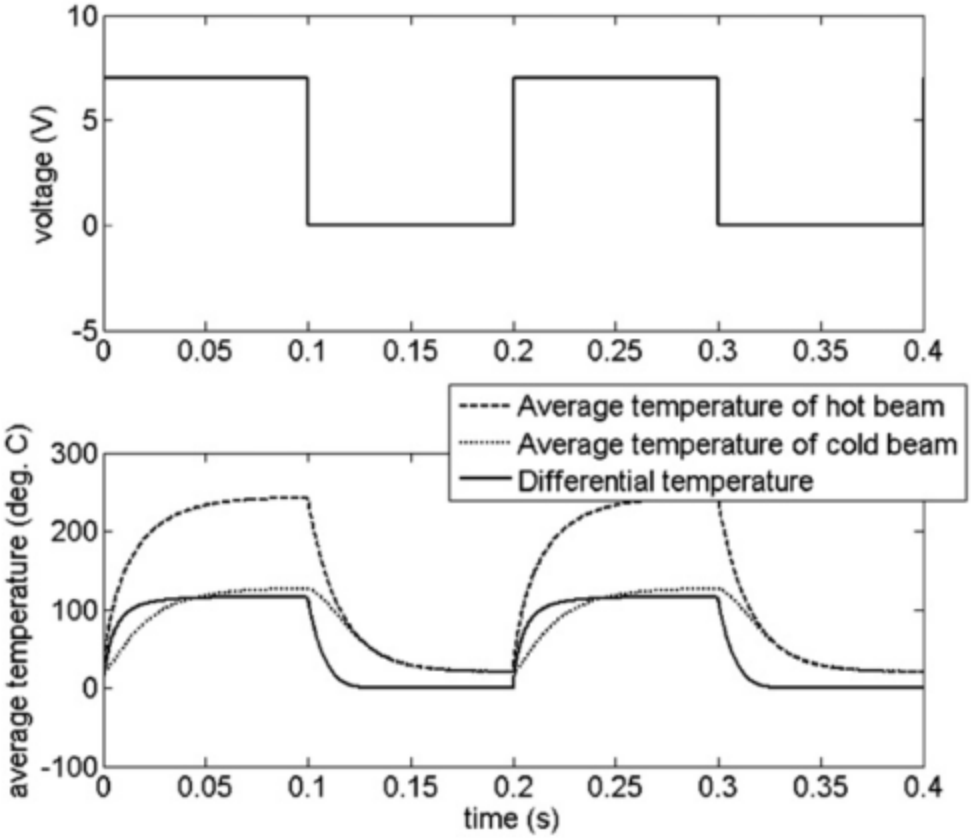

Figure 5.2 Temperature profile of the beam (lower) modelled from a square wave actuation (upper). Reproduced with permission [195].

Temperature distribution throughout the beam was obtained numerically by solution of the following coupled heat equations for the 'hot' and 'cold' beams (represented by subscripts 1 and 2) respectively:

$$C\rho w t_b \frac{\partial T_1(x_1,t)}{\partial t} = \lambda_b\big(T_1(x_1,t)\big)\, w t_b \frac{\partial^2 T_1(x_1,t)}{\partial x_1^2} - \frac{\lambda_{air} P}{\Delta z}\ (T_1(x_1,t) - T_0) - P\beta(T_1(x_1,t) - T_0) - P\varepsilon\sigma_0(T_1(x_1,t))^4 + \frac{w t_b V(t)^2}{r_h(T_1(x_1,t))L_h^2} \quad (5.1)$$

$$C\rho w t_b \frac{\partial T_2(x_2,t)}{\partial t} = \lambda_b(T_2(x_2,t)) w t_b \frac{\partial^2 T_2(x_2,t)}{\partial x_2^2} + - \frac{\lambda_{air} P}{\Delta z}\ (T_2(x_2,t) - T_0) - P\beta(T_2(x_2,t) - T_0) - P\varepsilon\sigma_0(T_1(x_1,t))^4 \quad (5.2)$$

In each case, the term on the left hand side of each equation describes the rate of temperature change in each part of the beam, and the terms on the right show the conduction through the beam to the substrate, heat lost by conduction to the immediate surrounding air, heat lost by convection and by radiation. The final term in equation (5.1) describes the energy source of the system: the voltage *V(t)* dissipated in the heater arm. Material parameters for the heat capacity, *C*, the density, ρ, thermal conductivity, λ_b *(T)*, resistivity, r_h, emissivity, ε of the beam, as well as critical dimensions are shown in *table 5.1* and compared with values for the TD design presented in this chapter, either obtained by measurement or experiment, or from the literature.

Parameter	Symbol	Units	Value for silicon	Value for td cantilever	References and notes
Specific heat	C	$J\ kg^{-1}\ K^{-1}$	740	1150	Area average for Au and polyimide.
Density (beam)	ρ	$kg\ m^{-3}$	2300	1484	
Thermal Conductivity (beam)	λ_b	$W\ m^{-1}\ K^{-1}$	$2\times10^{5}T^{-1.27}$	$3e^{0.004T}$	[196]
	Thermal conductivity dominated by polymer if considered as parallel thermal circuit due to the comparatively small cross sectional area of the gold tracks.				
Resistivity of actuator	r_h	Ω m	$r_{h0}(1+\zeta T)$	$r_{h0}(1+\zeta T)$	Values are given in the rows below
Resistivity at ambient (r_{h0})	r_{h0}	Ω m	5.6×10^{-5}	7.3×0^{-8}	TD values based on measurements in *chapter 6.*
Temperature Coefficient of Resistance	Z	K^{-1}	3	3.4×10^{-3}	
Thermal conductivity of air	λ_{air}	$W\ m^{-1}\ K^{-1}$	0.026	0.026	
Emissivity	E		0.6	0.95	Value for polyimide
Air free convection coefficient	B	$W\ m^{-2}\ K^{-1}$	10	10	
Distance from beam to substrate	Δz	M	200×10^{-6}	200×10^{-6}	Weighted average for curved beam
Length "unfolded" hot beam	L_h	M	3950×10^{-6}	1850×10^{-6}	From final design
Perimeter of beam segments	P	M	120×10^{-6} (estimate each beam segment is 59×1μm)	Hot Beam: 60×7 μm Cold Beam: 100×7 μm	Typical beam design

Table 5.1 Comparison of thermo-mechanical design properties of the Thermal Design (TD) Microcantilever with a silicon microcantilever modelled by Li & Uttamchandani [195].

Although the product Cρ is approximately equal for the two beams (silicon *vs.* TD – polyimide and gold), the greater thickness of the polyimide beam means that at least 3.6 times more energy is required to heat the TD beam than the silicon design. The thermal conductivity in the polyimide-gold beam is two orders of magnitude smaller than in polysilicon beam, even when the gold tracks are taken into account, so we should expect the TD sensor to retain the heat from the actuation pulse for longer. Given the differing beam dimensions and that the resistivity of the TD actuator tracks close to ambient temperatures is three orders of magnitude lower than for the polysilicon beam, the TD heater resistance is approximately 7 times lower than the silicon design. Therefore a given actuation voltage should result in 7 times more Joule heating in the TD beam. The combination of these three factors should mean that the thermal rise time of the TD beams would be faster than the polysilicon beam, but the thermal decay would be slower. In the simulations and experimental results of Li and Uttamchandani they observe a thermal rise time of 17 ms for the whole beam, therefore it might reasonably be expected to observe sub-millisecond thermal rise time in the TD design beams operated in air.

Theoretical examination of the thermal pathways in a polysilicon microcantilever was also studied by King *et al* [185]. Using finite element simulations, they were able to compare the magnitude of the different heat dissipation mechanisms in a microcantilever beam where the heater, made from doped silicon, was located at the very tip of the beam as shown in *figure 5.3.*

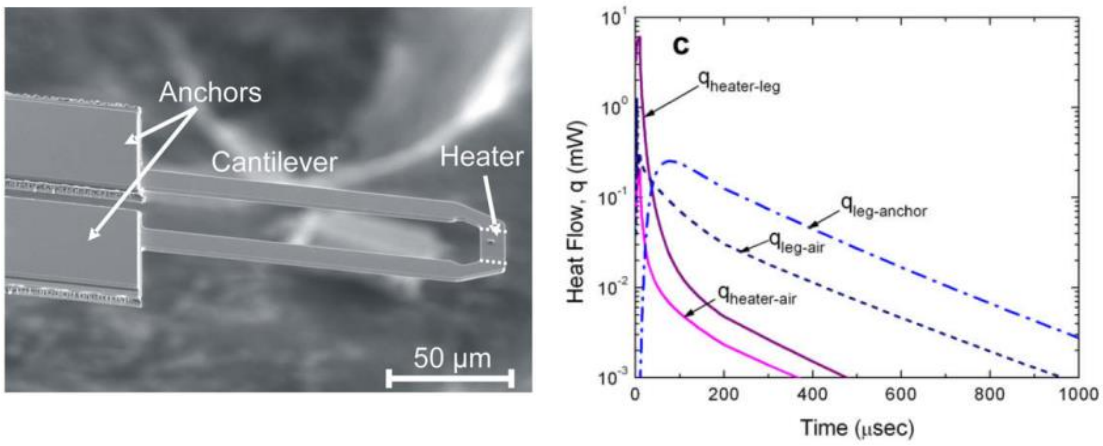

Figure 5.3 Heated tip microcantilever sensor by King et al (left). *FEM comparison of heat lost through various physical pathways following a 10µs pulse (right). Reproduced with permission* [185].

They found that thermal convection was the primary mechanism (20% in the heated tip of the beam, plus 40% in the unheated legs) due to the high surface area to volume ratio in the MEMS device. Conduction through the legs (40%) was limited by the finite size of the anchors: *figure 5.3(b)* shows that heat loss through the legs lags the heat pulse by about 50 µs. This would not be the case in the TD device, as the effective heat sink is the gold and polyimide on the surface of the chip, measuring a total of 7 mm × 4 mm and so relatively much larger. Radiative heat loss was negligible, even at T > 500 °C due to the combination of small surface area and the small value of $\sigma_{0,}$ and we should expect the same from the TD device despite the slightly higher emissivity of polyimide (0.95) compared to polysilicon (0.8).

5.1.3 Thermal Conductivity Sensing

The key properties of a fluid that relate to conductive heat transport are its thermal conductivity (λ), isobaric heat capacity (*C*) and density (ρ) which together define the thermal diffusivity (D_{Th}); the propagation velocity of an isothermal surface spreading outwards from a source of heat:

$$D_{Th} = \frac{\lambda}{\rho C} \tag{5.3}$$

The most widely used experimental technique for measuring the thermal conductivity of a fluid is the 'hot wire' method. A long fine wire, typically 10 μm in diameter is suspended concentrically within a much larger diameter cylinder that is filled with the test fluid. The wire is thermally isolated from the top and bottom of the cylinder using ceramic mounts. A constant power per unit length (q) is supplied to the wire and simultaneously its resistance is measured. The temperature of the wire is monitored over time, and from this profile thermal information about the fluid is extracted. Two different techniques may be employed: steady state and transient.

In the steady state hot wire method the temperature of the wire is measured *at equilibrium* both before *(T_1)* and after *(T_2)* the central wire is powered on:

$$\lambda = \frac{q \ln\left(\frac{r_2}{r_1}\right)}{2\pi(T_1 - T_2)} \tag{5.4}$$

The accuracy to which the thermal conductivity can be calculated depends upon having precise values for the inside of the cylinder and wire radii (r1 and r2), as well as the temperature values. It is also important that convection cells are not generated within the fluid, thus low power must be used, which limits the sensitivity of the technique.

The transient hot wire method uses the temperature profile of the wire prior to the re-establishment of thermal equilibrium to simultaneously determine the thermal conductivity and thermal diffusivity of the fluid. An ideal plot of ln(time) against $\Delta T_{WIRE} = (T_1 - T_2)$ contains a linear region where the temperature rise is dependent on the fluid thus:

$$\Delta T_{WIRE} = \frac{q}{4\pi\lambda}\left[\ln(t) + ln\left(\frac{4D_{Th}}{r_2^2 c}\right)\right] \tag{5.5}$$

The model is based on an infinitely long string of point sources of heat each conducted into an infinite medium at constant pressure. Corrections may therefore be applied to the model to account for the finite dimensions of the wire (in practice a second, short hot wire is often incorporated to correct for the finite length) and cylinder diameter, for

compression within the fluid, convection and thermal radiation. A further discussion of the technique can be obtained from the papers of Roder and Perkins at the National Institute of Standards and Technology [197, 198]. The principles of this technique have been adapted to various geometries such as the parallel plate method, but it is not known whether the temperature profile of an actuated microcantilever would be significantly affected by the thermal conductivity of the surrounding fluid.

5.1.4 Thermal measurements with Microcantilevers

Steady State measurements

Consideration of the power transferred to a cantilever beam by uniform internal electrothermal heating, in balance with the heat loss mechanisms of conduction, convection and radiation led Peng [199] to derive the following expression for the steady-state temperature distribution along the length of the beam, *T(x)*:

$$T(x) = T_f + \frac{q_j}{2h}\left[1 - \frac{\cosh\left(\sqrt{\frac{2h}{\lambda_b t_b}}(L-x)\right)}{cosh\left(\sqrt{\frac{2\alpha}{\lambda_b t_b}}L\right)}\right] \tag{5.6}$$

The following parameter values for the TD sensor were substituted into equation (5.6):

- Power delivered to the beam per unit cross sectional area q_j 26700 W/m^2
- Thermal conductivity of the beam (average) λ_b 9.9 W/mK
- Length of the beam L 7.5×10^{-4} m
- Total thickness of the beam t_b 7×10^{-6} m
- Temperature of the surrounding fluid T_f 298 K
- Heat transfer coefficient (beam to fluid) h $38500.\lambda_{fluid}$ W/m^{2}K

The heat transfer coefficient was estimated from the value used previously (section 3.2.1, [82]) for a microcantilever operating in air, and multiplied by ratio of thermal conductivity of air to fluid, in this case it is the thermal conductivity of silicone test liquids, which range from 0.1008 to 0.1554 W/mK. Using these values, a prediction of the difference in beam temperature for the TD beam when immersed in liquids of varying thermal conductivity was made, *figure 5.4*.

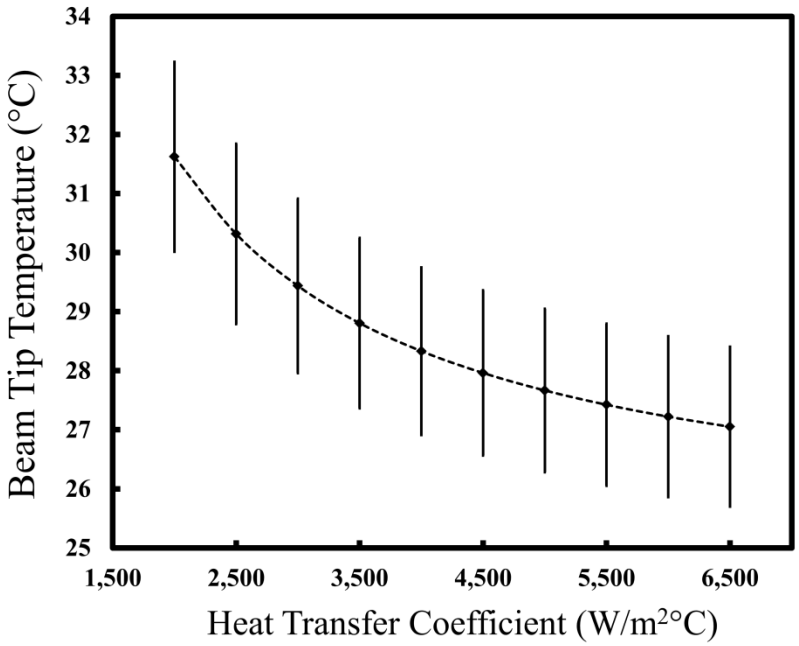

Figure 5.4 Predicted behaviour of the tip temperature for 5mW dc heating in fluids of different thermal conductivity. Error bars are calculated compound error based on 5% uncertainty in power, 10% uncertainty in beam thermal conductivity, 5 µm uncertainty in beam length, and 0.5 µm uncertainty in beam thickness.

The simulations do not predict large differences in steady state response with thermal conductivity of the environment. Peng postulated that this was because the thermal conduction to the substrate is much higher than the losses through convection or conduction to the fluid (radiative losses were found to be negligible compared to both). It is reasoned that the small thermal differences will not result in sufficiently large change in signal to be measurable.

In a later study by Puente *et al* [200], a microsensor consisting of two doubly clamped beams, each containing a thermistor, was able to detect changes in the thermal conductivity of natural gas with a sensitivity of 9.3V/(W/mK), again, using a steady state method. The set-up used by Puente is shown below:

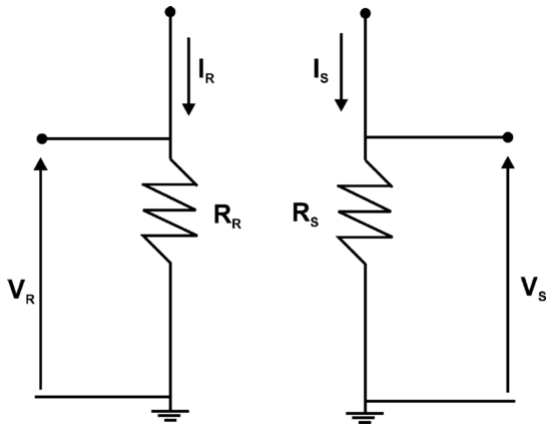

Figure 5.5 Microsensor for measuring thermal conductivity, reproduced with permission from [25]. The reference resistor R_R is supplied with low current I_R and is used for temperature sensing. The sensing resistor R_S is supplied with high current I_S and is used for thermal conductivity measurements.

According to the calibrations performed by Puente, the voltage change between 100 mW/mK and 155 mW/mK (the range covered by the calibrations done on the TD sensor in *chapter 6*) would be 511 mV, assuming linearity over this range. This study gives reason to doubt the earlier findings from the Peng simulation, and consider a microcantilever for measurements of the thermal properties of fluids. The width of the doubly clamped bridges was found experimentally not to affect the sensitivity of the conductivity measurements, which again contrasts the assertion by Peng that conduction to the substrate reduces fluid sensing capacity, since a wider beam would be expected to conduct away more heat. The temperature coefficient of resistance of the gold TD cantilever sensor is 1100 ppm per °C as found in *chapter 6*. The TCR of the platinum resistors used in the Puente study is 1545 ppm per °C; therefore we should expect a corresponding drop in sensitivity. Because a cantilever has only one point of contact with the surface, it may be that a cantilever design works even more efficiently that Puente's microbridges.

5.2 Theory and Design

5.2.1 Design Specification

The microcantilever sensor for measuring thermal properties of fluids was designed with the following objectives in mind: (1) reduce the effect of fluid viscosity on the signal; (2) integrate with existing electronics platform, and (3) maintain the large beam deflection when the beam is released from the substrate in order to minimise heat lost to the substrate. For ease of applying the results directly to the current Microvisk cantilever design (MV3), as well as to mitigate risk of failure in the microfabrication output, it was necessary to keep the basic shape of the cantilever beam similar to the MV beams used in *Chapters 3* and *4*. Note that the interaction we wish to measure is the heat flow out of the beam, which for a given cantilever and pulse profile is governed by the temperature, heat capacity and thermal conductivity of the surrounding fluid.

Figure 5.6 Schematic of Thermal Design (TD) microcantilever beam requirements. Outer dimensions are length = 750 μm; *width = 280 μm*; *thickness less than 10 μm.*

5.2.2 Neutral Axis Theory

Sensor layer position: In order to minimise sensitivity to the motion of the beam (without inhibiting the motion itself), the sensor read-out tracks should be at the neutral axis of the cantilever. The position of the neutral axis *(N)* in a two layer structure can

be calculated from the Young's modulus *(E)*, width *(w)* and thickness *(t)* of the layers using beam theory as:

$$N = \frac{E_1 w_1 \frac{t_1^2}{2} + E_2 w_2 \frac{t_2^2}{2} + E_2 w_2 t_1 t_2}{E_1 w_1 t_1 + E_2 w_2 t_2} \tag{5.7}$$

This equation is the key to making a thermal sensor that moves through the liquid, as it enables suppression of the mechanical component of the signal. For a fixed beam length and spring constant *(k)*, layer thicknesses that ensure the neutral axis lies on their interface were calculated using equation (5.8).

$$t_1 = \left[\frac{kL^3}{E_1 w_1 + (E_1 w_1)^{\frac{3}{2}} (E_2 w_2)^{-\frac{1}{2}}}\right]^{\frac{1}{3}} \quad and \quad t_2 = \left[\frac{E_1 w_1}{E_2 w_2}\right]^{\frac{1}{2}} \tag{5.8}$$

5.2.3 Key design decisions

Beam stiffness: The restoring force must be sufficient to return the beam to its equilibrium position after actuation, whilst achieving the highest possible actuation efficiency. The beam stiffness at the tip is given by the force constant *k* and the suggested target was 0.2 N/m based on previous work within the group at MNTC which had indicated that 0.2 N/m was a suitable value to enable large deflections in liquid whilst providing sufficient restoring force for oscillations to occur. This value was used in the layer thickness calculations described in equation (5.8).

Un-actuated deflection: Thermal isolation of the cantilever from the substrate will be enhanced for beams that have high deflection because of minimised thermal contact between the beam and the substrate. Equilibrium deflection was discussed in *chapter 3;* the theory developed by Timoshenko, Peng and others can be used to optimise the thermal bi-material cantilever for maximum deflection [154]:

$$E_1 t_1^{\,2} = E_2 t_2^{\,2} \tag{5.9}$$

Selection of sensor material: Metals available for use within the MNTC cleanroom facility include Gold, Titanium, Aluminium and Chrome. Gold was chosen as the sensor material because of its chemical inertness and the capacity within the STFC facility to create uniform layer at the microscale through controlled evaporative deposition. Gold also has a relatively high temperature coefficient of resistance, which will enhance thermal sensing. In addition, the fabrication cost is reduced and the process is simplified by having the heater and sensor on the same photomask.

Selection of heater material: The use of gold for the heater tracks was chosen for similarity with the previous work. In addition, gold was used for both heater and sensor tracks because it has relatively high temperature coefficient of resistance compared to the other available metals, and an ultimate tensile strength of 100 MPa, whereas the ultimate tensile strength of aluminium is 70 MPa.

Metal	Temperature Coefficient of Resistance at 20 °C ($°C^{-1}$)	Young's Modulus (GPa)	Electrical Resistivity ($\times 10^{-8}$ Ωm)	References
Gold	0.0025 (thin film); 0.0034 (bulk)	78	2.35	[199, 201]
Titanium	0.0007 (thin film); 0.0054 (bulk)	116	42.0	[199, 201]
Aluminium	0.0028 (thin film); 0.0043 (bulk)	70	12.9	[199, 201]
Chrome	0.0006 (thin film); 0.002	248	2.66	[199, 201, 202]
NiChrome	0.0015 (thin film)	-	-	[203]

Table 5.2 Comparison of the TCR of various metals available within the MNTC for fabrication of the metal tracks in the proposed microcantilever design.

Selection of thermal actuator materials: various polymers were considered for use in the bi-material cantilever layers; *table 5.3* summarises the material properties. Actuation efficiency is the amount of deflection of the beam per unit of actuation power, which in this case is related to the temperature of the beam. High actuation efficiency is desired because although in this study the motion of the beam will not be measured by the sensor, it is still desirable that the beam should move through the liquid

in order to capture any effect this may have on the beam temperature. For high actuation efficiency a high difference in CTE was sought, resulting in the selection of PI-2562 and PI-2610 as thermal actuator layers.

Material	Coefficient of Thermal Expansion (ppm/°C)	Young's Modulus (GPa)	Ref.
PI-2610 Film	3	8.5	[91]
PI-5878 Film	20	2.3	[91]
PI-2525 Film	40	2.5	[91]
PI-2562 Film	60	1.8	[182]
HD-4100	35	3.4	[204]
HD-7010	50 – 90	2.5 - 2.9	[205]

Table 5.3 Comparison of cured film properties for various formulations of polyimide. Note that HD-4100 and HD-7010 are negative Photodefinable films, and the range of values for HD-7010 is dependent on the cure conditions.

Sensor Design: Lee *et al* conducted an experimental study of how the beam design of electrothermal microcantilevers affected the thermal profile [206]. The designs considered and a comparison between the thermal rise and cooling times are presented in f*igure 5.7*. The design of the TD microcantilever sensor developed by the author is most similar to design F, which has the longest cooling to heating time ratio.

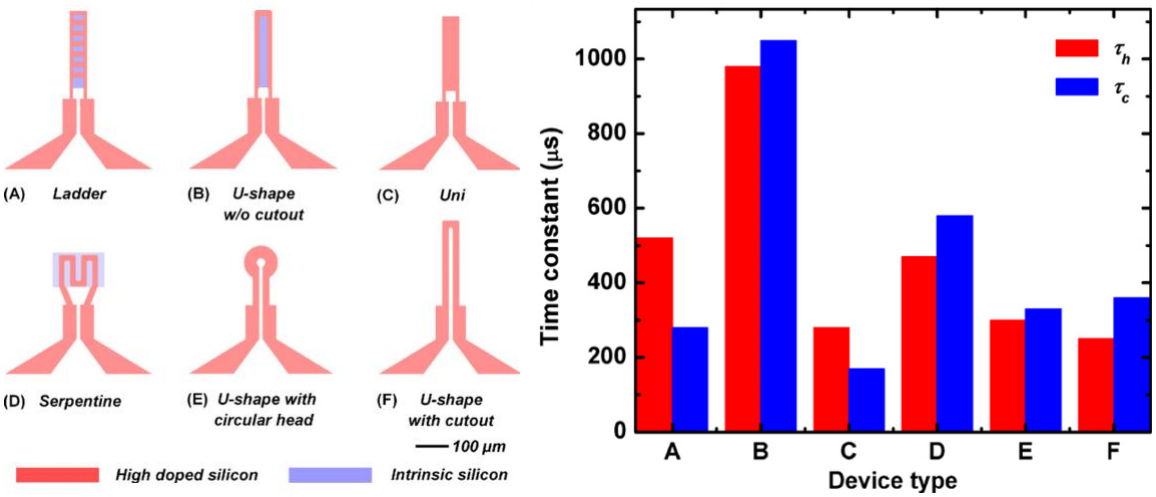

Figure 5.7 Shape effects in the thermal profile of an electrothermal microcantilever hotplate developed by Lee et al. *The design produced in this thesis is most similar to 'F', so we should expect a longer cooling constant than heating constant from the current work. Reproduced with permission* [206].

Previous studies at MNTC had shown that a serpentine sensor read-out track design results in high sensitivity to deflection through increasing the magnitude of the resistance change when the beam is bent. Although it is not the aim of this study to make a strain gauge, it was decided to stay with the existing sensor design plan to reduce the risk of fabrication failure.

Hole dimensions: The size of holes within the beam are a design parameter that had not previously been investigated in detail, therefore it was decided to vary this design on the wafer. Previous work at Microvisk and at MNTC used widths of 40µm. In this study the wafer included variations at 20, 30, 40, 50 and 60 µm, as well as some designs with elongated holes. The distance between the metal tracks and the edge of the polyimide were kept constant to mitigate the risk of the tracks being exposed upon etching the cantilever shapes.

Temperature drift compensation: In order to compensate signals caused by a drift in the absolute temperature of the liquid during measurements, an unactuated reference cantilever was used. The aim is to measure the change in temperature from the heat leaving the actuated cantilever, rather than from heat in the sample, in order to sense the

thermal properties of the sample. Therefore it was decided to have two released beams per sensor and to connect them in a Wheatstone half bridge. The reference cantilever was used to compensate for the thermal drift and is un-actuated, while the active cantilever probes the thermal interaction with the fluid.

Release Layer: An effective release layer can have a huge impact on the fabrication yield. Incomplete release can shorten the effective beam length leading to lower actuation efficiency. Previous methods employed at MNTC and elsewhere ranged from multiple metal layers [88] to Teflon [207]. Crucial to the selection is the need of the release layer to be deposited first and then to withstand all subsequent fabrication steps, particularly high temperature curing, and plasma etching of the polyimide layers, and then to be removed without damage to the polymers. In this case, it was found that a chrome release layer would be ideal since it can be selectively etched with Chrome Etch Melange, to which both PI2652 and PI2610 are chemically resistant.

5.2.4 Final beam design

The final microcantilever sensor design is pictured in *figure 5.8*. Dimensions shown on the figure are common to all design variations, except for width of the beam (given for the 40 μm hole variation) and the dimensions of the holes in the beam, which are summarised in *table 5.4*. In the 'EH' (elongated holes) design variation, the holes extend further back into the body of the chip.

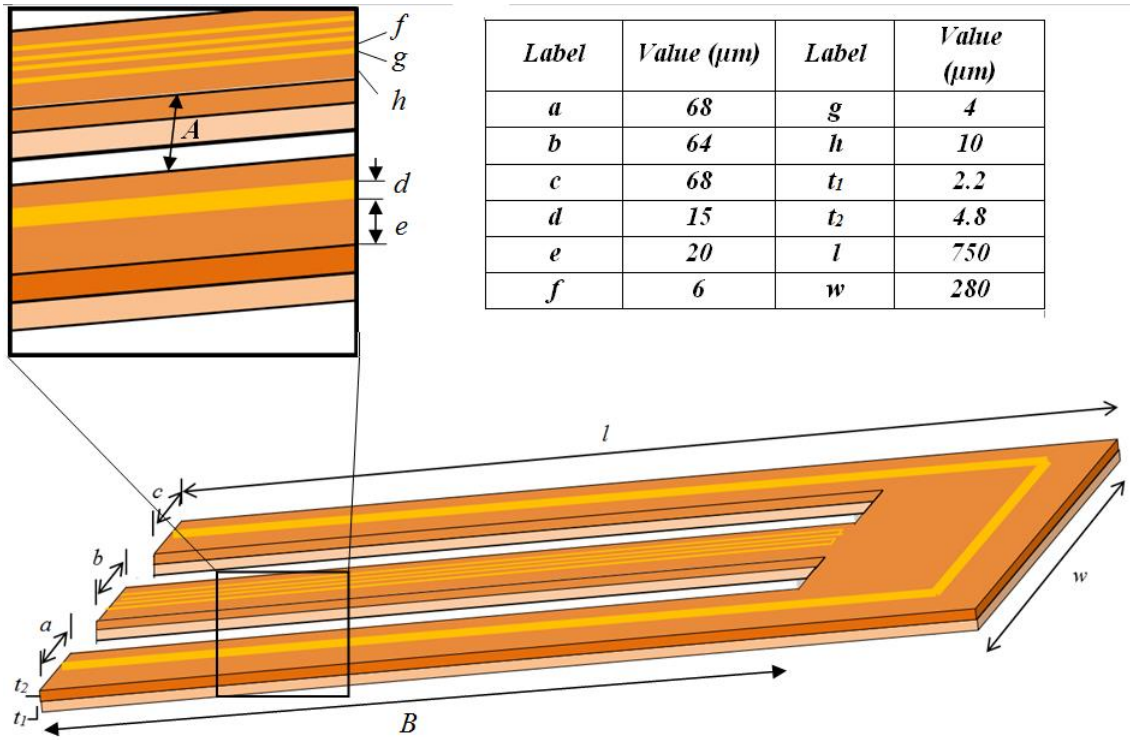

Label	Value (μm)	Label	Value (μm)
a	68	*g*	4
b	64	*h*	10
c	68	t_1	2.2
d	15	t_2	4.8
e	20	*l*	750
f	6	*w*	280

Figure 5.8 Microcantilever Sensor Thermal Design (TD).

Design Permutation Shorthand	A (μm)	B (μm)
20	20	610
30	30	610
40	40	610
50	50	610
60	60	610
EH	40	735

Table 5.4 Dimensions specific to design variations for the Thermal Design microcantilever sensors.

5.2.5 Wafer design

Having decided on the microcantilever beam design variations, materials and release mechanism the next step was to fabricate devices on a single wafer. For compatibility with experiment set-ups used with previous chip designs, die dimensions of 4 mm x 7 mm were used and the format of contact pads for both heater and sensor was maintained from the previous version. A four mask optical lithography process was used, as will be

discussed in detail in *Section 5.3*. The individual masks are used to pattern the following features:

- Release Pads — Positive resist / Brightfield
- Heaters and Sensors — Positive resist / Darkfield
- Contact Pads — Positive resist / Darkfield
- Cantilever Beams and Dicing Tracks — Positive resist / Darkfield

The mask designs were designed by the author using AutoCAD design software. Brightfield lithography was chosen for the release pads, as it does not matter if these are a little smaller than the specified lateral dimension. Darkfield lithography was required for the heater and sensor tracks to obtain the required 4 μm track width. All corners were rounded to reduce stress. They were fabricated by Deltamask (*Enschede, The Neatherlands*) using laser patterning to create a chrome pattern on high quality soda-lime glass plates. All masks were 5 inch square, as compatible with fabrication on 4 inch diameter wafers. The mask designs are presented in *figure 5.9.*

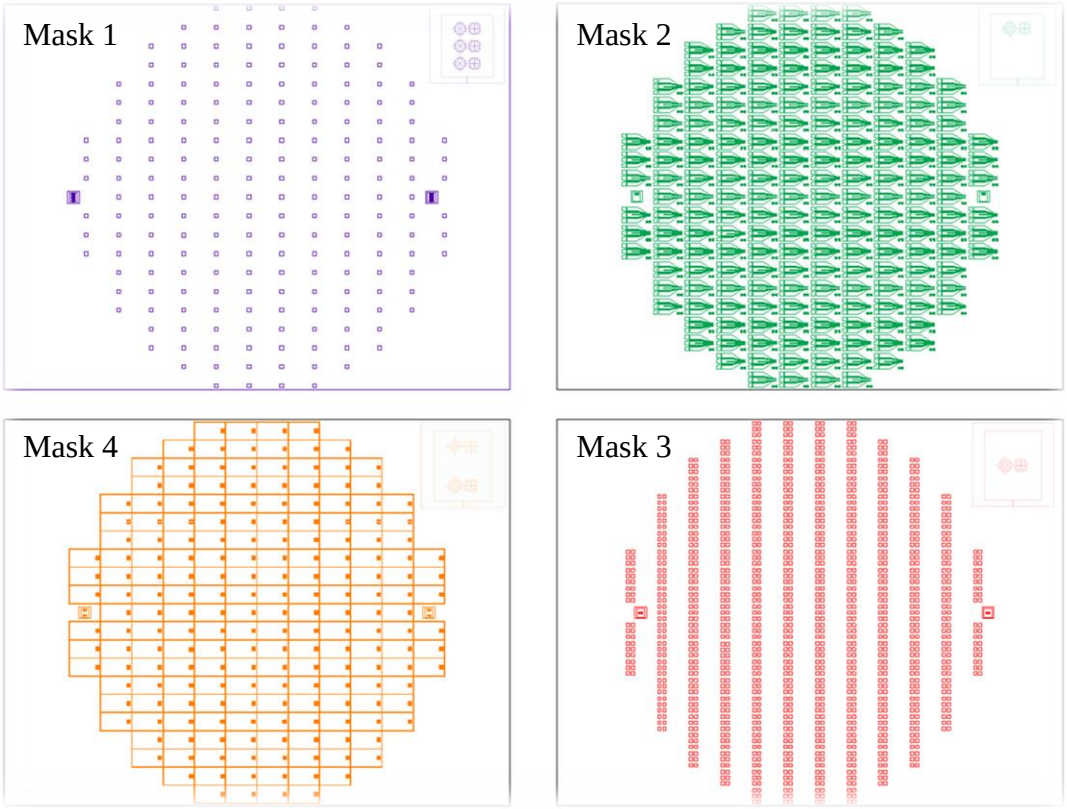

Figure 5.9 AutoCAD images of mask designs for thermal conductivity cantilever sensors. The alignment marks are shown as a top-right inset in each picture. Clockwise from top-left: Mask 1 (release pads); Mask 2 (heaters and sensors); Mask 3 (contact pads); and Mask 4 (cantilever beams).

5.3 Microfabrication

5.3.1 Process flow for chosen design

Two wafers, each with a set of cantilevers, were fabricated in the cleanrooms at MNTC. The process is described in detail in the following sections, and summarised in *figure 5.10.* Briefly, the wafer is oxidised, before patterning the chrome release pads; the first polyimide layer (PI-2610) is applied and then the gold heater and sensor tracks are patterned; additional gold is deposited to build up the contact pads, then the second polyimide layer (PI-2562) is applied and etched back to reveal the contacts; finally the shape of the cantilever beam is etched through the polyimide layers and they are ready to be released.

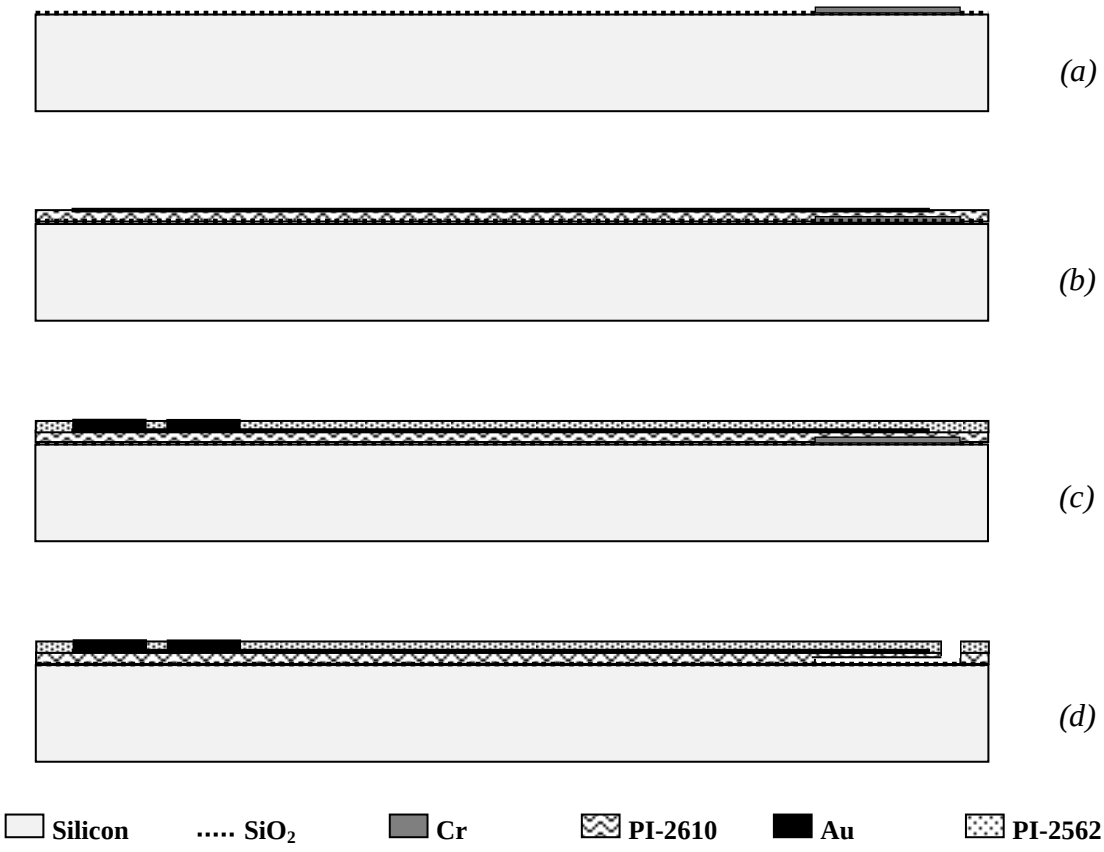

Figure 5.10 Process flow for Thermal Design (TD) microcantilever sensor chip: (a) Oxidation of silicon wafer and release layer patterning; (b) PI-2610 and heater/sensor layer in gold; (c) PI-2562 and contact pads; (d) Cr etch to release the beam.

5.3.2 Microfabrication Steps

Wafer Preparation

Si(100) wafers were partially oxidised by a wet oxidation furnace process creating a silicon oxide layer 0.4 – 0.7 μm deep. This involved controlled heating of the wafers to 1050 °C in air followed by exposure to water vapour at this temperature using oxygen gas that has 'bubbled' through a water bath (outside the furnace at a temperature of ~95 °C). This process allows water molecules to reach the silicon surface at a steady rate whereupon the following reaction occurs: $Si + 2H_2O \dashrightarrow SiO_2 + 2H_2$. The reaction occurs at the upmost surface layer first, after which the water molecules must penetrate the newly formed SiO_2 to react with the Si (diffusion limited reaction). The solubility of water molecules in silicon is four times greater than that of oxygen [208] and it is for this reason that the wet oxidation process is preferred over dry oxidation for thick (over

100 nm) oxide layers. Whilst the processing time is therefore reduced for wet oxidation, the drawback is a reduction in uniformity over the wafer thickness compared to dry oxidation. However, in this case the purpose of the oxide layer is to provide additional isolation of the devices, so variation in the oxide thickness is tolerable.

Release Layer

The first structures constructed on the wafer were the chrome release pads. These were fabricated by first evaporating chrome onto the wafer with using a V2000 deposition system (Surface Vacuum Systems). The layer was approximately 80 nm thick. Wafers were rotated above a crucible in which the chrome is evaporated using a focussed electron beam. The chrome was deposited at a rate of 0.5 Å/s. It is difficult to achieve higher deposition rates, or thicker layers with this metal, as the high melting point and granular nature means that a liquid melt is not formed in the crucible. If the chrome layer is too thin, Van der Waals interactions between the cantilever and the substrate may prevent the cantilever curling up on release, a phenomenon known as stiction. If the chrome is too thick, the yield of the cantilever devices will be reduced, due to the prolonged chrome etch during cantilever release which can also damage the gold contact pads and their adhesion to the device.

The chrome was patterned by photolithography. A positive photoresist *(JSR Corporation, Japan)* was spin coated *(Laurelle 300 mm spin coater used throughout, Laurelle Technologies Corporation, PA, USA)* onto the chrome covered wafer. A mask aligner (MA6, Karl Zuss) was used to expose the wafer to approximately 10 mW/cm^2 broadband UV light for 7 seconds through mask 1 *(figure 5.9)*. The wafer was developed in TMA238-WA (tetramethyl ammonium hydroxide, supplied by Clariant) before being immersed into chrome etch melange (OM Group Ultra-Pure Chemicals Ltd). The etch time depends upon the chrome thickness and was determined by eye after about 50 seconds. Oxygen plasma treatment for removal of residual resist was performed both after development and again after etching to ensure complete removal of outlying resist and chrome respectively in order to minimise defects. This was performed with a System 90 (Plasmalab, Oxford Instruments) using 50sccm of oxygen gas at 200 mT and 100 W RF power for approximately 1 minute. Once satisfactory patterning was obtained, the developed resist was removed using acetone to leave the metal pattern.

Polyimide PI 2610 Layer

Chrome quickly oxidises in air, so it was imperative that the first polyimide layer was applied without undue delay. Polyimide 2610 (HC Microsystems) was spun onto the patterned wafer using the following parameters in order to obtain a layer approximately 5 μm thick:

Step	Detail	Explanation
Pre-bake	150 °C for ~10 mins	Drives off surface moisture
Spin 0.1% v/v VM610	6000 rpm @ 1000 rpm/s for 30s	Adhesion layer. Near monolayer thickness on the wafer.
Static dispense PI2610	4.5 ml by auto-pipette	Large volume required because the high viscosity of PI2610 slows spreading. It is dispensed in such a way as to cover ~80% of the wafer before spinning commences.
Initial ramp-up	500 rpm @ 100 rpm/s for 10s	Ensures that the resist is distributed towards the edges of the wafer
Final spin speed	2250 rpm @ 1000 rpm/s for 45s	2.2μm layer thickness determined by spin-speed curve (generated by the author). Longer spinning duration reduces the layer thickness but improves uniformity.

Table 5.5 Spin Parameters for PI-2610.

A softbake of 90 seconds at 90 °C followed by 90 seconds at 150 °C was performed using two hotplates. This was followed by a full oven cure under nitrogen. During the cure, the temperature was ramped from room temperature to 350 °C over a period of 83 minutes; it was then held constant for 30 minutes before being cooled to room temperature over a period of 8 hours.

Metal Tracks

The heater and sensor designs were integrated into a single mask, since they are both fabricated in gold. The relative thicknesses of the polyimide layers are chosen such that the interface of the two polyimides is along the neutral axis of the beam and fabrication of the heaters and sensors is performed directly on the first polyimide layer. The minimum feature size to be made is 4 μm, the width of the sensor tracks. Parts of the serpentine sensor tracks are just 6 μm apart. There is, therefore, a danger of under-etching and removing the features altogether if a direct pattern transfer, like the chrome

patterning is used. The preferred method of patterning for these features is a positive resist bi-layer lift off. This involves spin deposition of a non-photosensitive LOR (lift-off resist) layer and then depositing a positive photoresist on top. The LOR is soluble in the same developer as the positive resist and to a greater degree, resulting in an undercut pattern *(figure 5.11).*

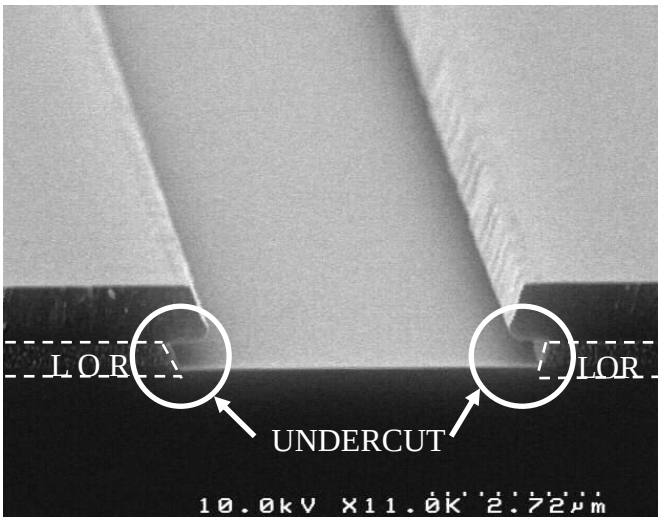

Figure 5.11 SEM of lift off profile obtained by the author, showing the clear undercut needed for successful deposition of the metal tracks. When the thin metal layer is deposited, the undercut regions remain clear of metal and the LOR layer (outlined in white dashed lines for clarity) is attacked by the developing solution.

The choice of LOR depends on the required thickness of the metal pattern. The LOR layer needed to be at least one and a half times as thick as the metal layer so that the solvent has space to get around the metal to remove the LOR. As a metal thickness of 150 nm was desired for the heater and sensor tracks, LOR 5A was chosen for the lift off resist (supplied by MicroChem Corp., USA). The 'A' indicates the nature of developing solution that can be used, in this case MF (metal free) CD26, an alkaline corrosive developer (Rohm and Haas Electronic Materials LLC, USA). This works well with positive photoresists such as Megaposit SPR350 (Rohm and Haas Electronic Materials LLC, USA). The alternative 'B' series of LOR resists is developed in organic solvents and works well with photoresists such as JSR positive resist.

The etch rate of the LOR can be varied through the process parameters, primarily the soft-bake temperature of the resist. Experimentation found that a soft-bake temperature of 155 °C was required in order to obtain sufficient undercutting in the time it takes to develop the SPR layer fully. An SEM of the resist profile is shown in *figure 5.11*. The LOR thickness was measured to be 450 nm, the SPR was 850 nm and the undercut was approximately 450 nm deep.

In order to verify that an undercut has been obtained without cutting the wafer to obtain an SEM profile, it is possible to view the layers under a microscope. If the undercut is present, there will be two lines at each edge of the structure that come into focus at different distances *(figure 5.12).*

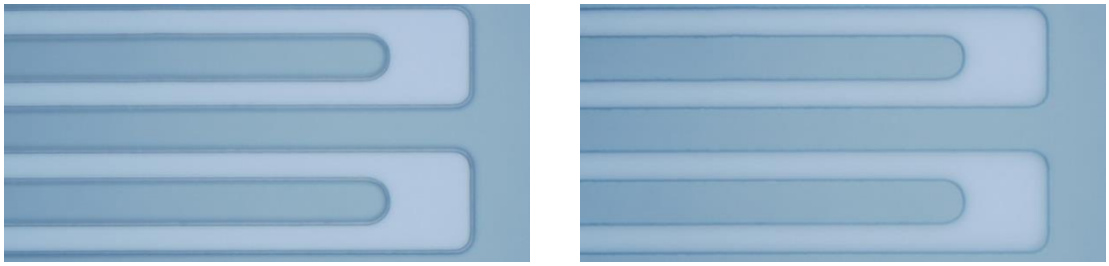

Figure 5.12 Optical micrographs (x150 magnification) showing the resist/LOR pattern for part of the sensor structure. The same area is recorded at two different focus points indicating that there is an undercut in the LOR layer.

Once a satisfactory lift off profile was obtained, the V2000 evaporation depositor was used to coat the wafer with 150 nm of gold. Unlike chrome, gold forms a melt inside the crucible making it easier to evaporate large amounts in a uniform manner. To promote adhesion to the polyimide coated surface, a seed layer of 10 nm of chrome is first deposited. This has little effect on the electrical properties of the heater/sensor. Gold on top of the LOR/SPR structures is removed when the wafer is soaked in MF CD26 to dissolve the remaining LOR, revealing the heater and sensor structures on the wafer surface.

Polyimide PI2562: Deposition and Etch

The second polyimide layer was then spun onto the wafer. This material (PI-2562) has a higher coefficient of thermal expansion than the preceding PI-2610 layer and therefore when the cantilevers are released they will bend upwards. Spin curves for PI-2652 were also determined. The target thickness was 4.8 µm, which is outside the thickness range given in the manufacturers process guidelines. Therefore, as well as trying very low spin rates, a two layer spin (spin-softbake-spin-softbake-cure) was also investigated. It was thought that this technique might result in greater uniformity for the thick layers, but as the results show *(figure 5.13)*, this proved not to be the case. A single layer spun at 500 rpm for 5 seconds, and then 800 rpm for 45 seconds was used for fabrication of the sensors. A softbake at 120 °C for 300 seconds immediately followed the spin.

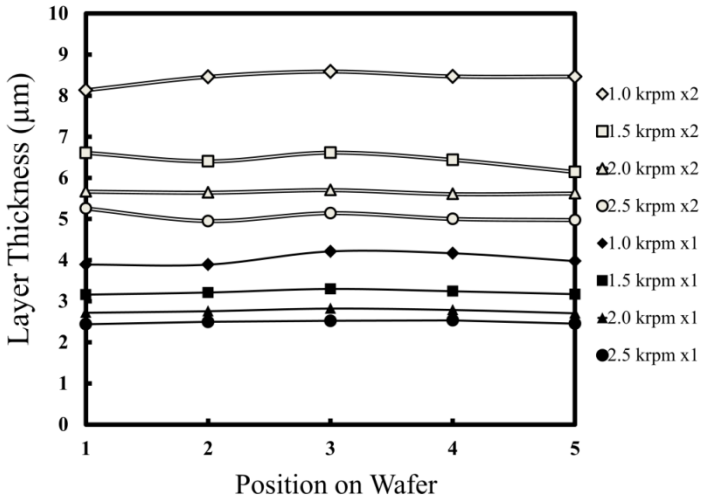

Figure 5.13 Profile of polyimide thickness over the width of the wafer. Positions 1 and 5 are approximately 1 cm from the wafer edge, position 3 is at the centre and positions 2 and 4 are in between. Greater variability over the wafer is seen when using double layers of polyimide (double lines) than with single layers (single lines).

The recommended curing sequence is similar to that used for the previous polyimide, with the maximum temperature again 350 °C maintained for 1 hour. An additional hold time at 200 °C for 30 minutes was also incorporated in the ramp-up as per the manufacturer's process guidelines.

Contact Pads

At this stage, the heaters and sensors are fully encased between the polymer layers. Space for the contact points was etched into the top layer. This is achieved by patterning with a thick positive resist using contact optical lithography and Mask 3 *(figure 5.9)*. AZ9260 (MicroChemicals GmBH, Germany) was spun onto the wafer at 2250 rpm to obtain a layer approximately 10 μm thick. This needs to be well in excess of the polyimide thickness to be etched, as it is removed faster than the polyimide layer by the etching process. It should be noted that this resist absorbs moisture from the atmosphere once applied and that the best processing conditions are obtained when the resist is kept in the dark for up to 2 hours (this time is dependent on thickness) after the soft-bake (105 °C, 120 seconds) but before exposure (25 seconds) and subsequent development in AZ400K developer (AZ Electronic Materials USA Corp) diluted 1:4 by volume with deionised water. Oxygen plasma etching (30sccm, 100mT, 200W) was performed in the Plasmalab System 90.

Three methods were used to verify that the plasma etch was complete. Firstly a visual inspection of the surface of the pad bases for the 'rainbow' effect of interference that would be observed if a thin film was present. Secondly, measurements were made using a Nanometrics Nanospec Film Thickness System set to a 'photoresist on gold' method. Thirdly measurements were made of the resistance of the heater and sensor using a Karl Zuss probe station. Typical values of 70 Ω for the heater and 300 Ω for the sensor were noted, and these are in agreement with results obtained for similar devices in the laboratory. Once it was verified that etching was complete, a lift-off process (using mask 3, *figure 5.9*) with the same parameters as described above was used to pattern the contact pads with gold. In this case 200 nm gold was applied at a rate of 0.5Å/s.

Cantilever Shape

The final patterning stage of the process is to create the cantilever structures and dicing tracks. These are both achieved with a single mask (mask 4, *figure 5.9*). The latter are used to ensure that when the wafer is diced into chips, the blade does not contact any polyimide where it might stress or crack the material. The pattern was made using a very thick layer of AZ9260 positive photoresist and photolithography on the MA6 mask

aligner (as before). The polyimide is then exposed (no longer covered in resist) only on the release area and dicing tracks, and is dry etched using the System 90 (as before).

Because (a) the polyimide is ~7 µm thick, and (b) the selectivity between etching polyimide and AZ9260 is poor under the etch parameters used (100mT, 200W, 30sccm oxygen plasma), the AZ9260 needs to be very thick. Etch tests prior to full wafer processing revealed that the etch rate of polyimide PI-2610 was 0.081 ± 0.030 µm/min, and the etch rate of AZ9260 was 0.138 ± 0.012 µm/min. A colleague, Dr Andreas Schneider, performed similar measurements to obtain an etch rate of 0.107 ± 0.002 µm/min for polyimide PI-2562. Measurements were taken using the Tencor profilometer (Kia) for etch depths up to 5 µm. It was noted that the polyimide etch rate decreased with thickness etched, making it very difficult to remove the final traces of this polymer. Therefore, the target thickness for the AZ9260 layer was set to be 15 µm in order that it should mask the polyimide until it had been etched back to the silicon oxide/chromium layer. The spin parameters used to obtain this thickness were: 750 rpm; soft-bake for 120 seconds at 120 °C; 3 hours hold time; 69 seconds exposure at 10 mW/cm^2 (Karl Zuss MA6 mask aligner) through mask 4; 8.33 minutes development in 1:4 AZ400K developer: water. At this point the wafer is completed *(figure 5.14).*

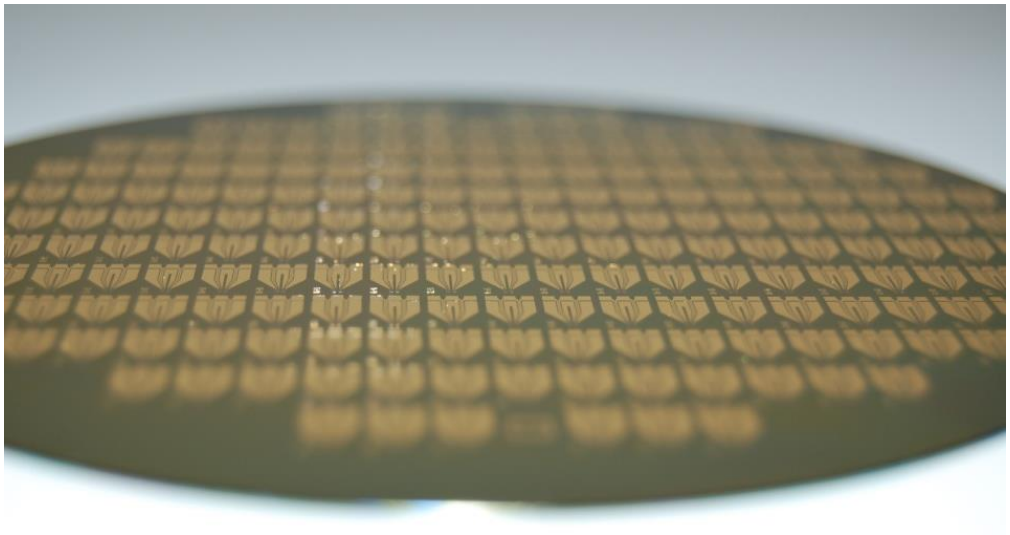

Figure 5.14 Photograph showing a completed wafer before dicing.

Chip Production

The completed wafers were sent for dicing by Qudos Technology Ltd., UK. Note that there was still a layer of AZ9260 resist covering the wafers at this stage in order to prevent any dust or debris from the dicing process damaging the devices. Before use, each device chip was immersed in acetone to remove the resist layer, followed by immersion in chrome etch melange to release the cantilever from the substrate. A common failure mode for MEMS structures is stiction; the unwanted adhesion to the surface of a microstructure. This happens when the rigidity of the structure is insufficient to overcome intermolecular forces such as Van der Waals forces between the structure and the surface. Stiction is made worse by the presence of moisture and therefore a wash with a volatile solvent (acetone) was performed immediately before drying. An investigation using the autofocus experiment detailed in *Chapter 3* found no difference in beam deflection with drying temperatures between 30 – 70 °C.

5.3.3 Results – metrology of chips – and suggestions for improvements.

Yields of over 70% for the first wafer and over 80% for the second wafer were obtained from the fabrication process. Losses were due to incomplete lift off of gold during patterning of the heater and sensor tracks, and a fabrication error where the wafer was allowed to dry out during the development of the JSR resist prior to etching the beam shape in the 2nd wafer.

It would have been desirable to cut through the beam structure to see clearly the placement of the neutral axis within the layer structure. This should have been possible to view using SEM, despite the inherent difficulty in obtaining high resolution images of polymers, or using energy dispersive X-ray analysis to identify the gold layer. However I did not want to risk shattering the wafer by trying to cleave it; and attempts to get a clean section through an individual chip were not successful.

Scaled microscope images were used to measure the actual width of the heater and sensor tracks and the width of the holes for a series of microcantilevers. A graticule (Pyser-SG1, 50×2µm rulings) was used to scale the images collected using 50× and 100× objective lenses. Two measurements were made for each dimension over three

different beams. The measurement error was 0.3 µm which was mainly the result of imperfect focusing of the camera during image capture.

Sensor Design	Width of heater tracks (µm)	Width of sensor tracks (µm)	Width of holes (µm)
EH	19.3 ± 0.3	4.5 ± 0.3	43.9 ± 0.4
20	18.7 ± 0.4	4.3 ± 0.3	23.8 ± 0.3
30	19.5 ± 0.2	4.6 ± 0.2	33.1 ± 0.3
40	19.0 ± 0.3	4.5 ±0.3	44.8 ± 0.3
50	18.9 ± 0.4	4.5 ± 0.2	54.4 ± 0.2
60	19.5 ± 0.1	4.7 ± 0.1	65.0 ± 0.1

Table 5.6 Metrology results of Thermal Design (TD) microcantilever chips fabricated by the author at the MNTC cleanroom.

5.3.4 Interface with Electronics

Previous experiments performed using microcantilever chips at the MNTC had involved using a wire bonding technique to electrically connect the chip to a ceramic mount which was interfaced with the experiment electronics (Wheatstone bridge circuit and actuation voltage source) via a ZIF connector. These experiments were characterised by high levels of interference at harmonics of 50 − 60 Hz and it was thought that the source was external power supplies in the vicinity that were being picked up by the cantilever sensor, since this is the part of the experiment with least shielding.

A new connection system using spring-mounted contact pins positioned using a two axis micropositioning stage was designed by Mr Robert Ibbotson, fabricated externally and assembled at the MNTC *(figure 5.15)*. The outer casing was metallic and lidded with the aim of providing shielding for the sensor. In addition, shielded cables were used throughout (coaxial cable for the actuation voltage, 9-core mesh insulated cable for the sensor circuit). Cable lengths were reduced as far as practical (all less than 0.5 m) and the shielding was verified to have been grounded. It was found that these

precautions did not significantly reduce the interference in the experiments, which may be an inherent problem with the sensor design, although crosstalk between the actuation and sensing circuits can be ruled out because the noise occurs even when the beams are not being actuated.

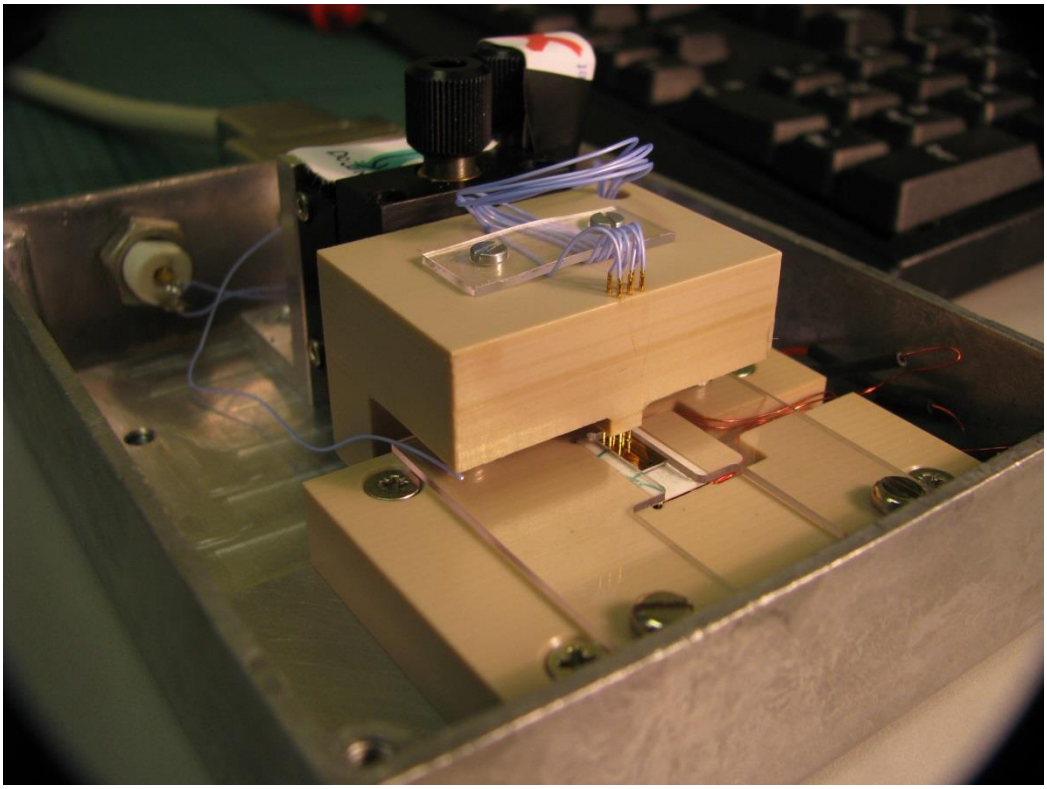

Figure 5.15 Thermal Design (TD) microcantilever chip mounted within the new test platform for interfacing with the experiment electronics. The ceramic sub-miniature heater is clearly visible (white) beneath the chip, and the shielded BNC interconnect for the actuator circuit is visible at the upper left of the photo. The 9-core cable connect (upper right) is partially obscured by the micro-position mount for the spring loaded contact pins.

The use of the pin-pad system enabled us to forgo the expensive and time consuming wire bonding process, greatly reducing the cost of the project. A cavity was positioned underneath the sensor to contain a sub-miniature heater for temperature control during experiments.

5.4 Conclusions

In this chapter, the first study of a microcantilever designed to sense the thermal conductivity of liquids is presented. The work can be used to analyse whether any change in sample thermal conductivity would affect the signal in the Microvisk sensor (i.e. are the sample thermal properties a source of cross sensitivity in a viscosity measurement) or to determine whether there is any potential for the microcantilever to be used as a thermal conductivity sensor. The component of the DC microcantilever signal arising from changing heat flux within the beam following a thermal actuation pulse has been discussed. Factors in the design of a microcantilever with suppressed piezoresistive signal have been assessed, with the principle novel design feature being the placement of the sensor resistor tracks close to the neutral axis of the beam.

In lieu of a simulation of the proposed design, comparisons have been made with the literature. The sensitivity to thermal properties of the fluid will depend on the proportion of heat lost to the fluid compared to the proportion lost to the substrate by conduction through the cantilever arms. The substrate area of each chip acts as a large heat sink, but the fact that the cantilever deflection is made to be high and the beam is designed to move through the fluid should increase the proportion of the heat lost to the fluid. The predictions made for the proposed design are that the thermal rise time would be shorter than 17 ms, and shorter than the thermal decay time.

Sensors were successfully fabricated in polyimides and gold using a four-mask photolithography process with an overall yield of 75%. Gold sensor tracks were 0.5 µm wider than intended, heater tracks were around 4.5 µm wider than intended and holes in the beam were 3-5 µm wider than intended, probably due to the long etch time required.

The requirement for narrow heaters and sensors (minimum feature size 4 µm) meant that glass plate photolithography was the most reliable method of fabrication. The high cost of the mask plates resulted in very conservative designs. For future research, it might be better to use a rapid-prototyping technique to experiment with more radical design variations to aid in design selection. In this well established method [209], a high resolution commercial printer is used to transfer the mask design onto a laminate which is then used as a photolithography mask. Resolution of structures is limited by

the printer and is typically 20 microns, which would be sufficient to investigate different cantilever beam shapes (though not sensor operation) or release techniques for robustness with low risk to the project. One alternative design involved joining the passive and actuated cantilevers so that the Wheatstone bridge could cancel out some of the piezoresistive signal, but this was dismissed due to the possibility of twisting the whole structure upon actuation. Other alternative designs involved inverting the position of the heater and sensor tracks so that the heater was on the inside of the sensor, or constricting the polymer channel that links the central part of the beam with the outside of the beam for greater thermal isolation of the sensor from the heater.

Details of the methodology used by the author to fabricate the sensor were also presented. Ideally several wafers would have been fabricated using different layer thickness ratios in order to show how the properties of the read out sensor change with its position within the layer structure of the beam. In particular it would be interesting to repeat the fabrication process but using PI2562 for both layers. The work by Li and Uttamchandani [195] indicates that due to the Epsilon shape of the beam, thermal gradients between the heater and sensor arms are sufficient to cause deflection of the beam, and since PI2562 has the highest coefficient of thermal expansion, it might be possible to realise the cantilever using a single polymer. *Chapter 6* will present the results of characterisation experiments performed on the fabricated sensor chips.

Chapter 6
Characterisation and Clinical Evaluation of a Thermal Sensor

6.1 Introduction

In this chapter, the thermal and mechanical properties of the thermal design (TD) sensor are characterised and it is shown that the sensor is responds differently to fluids with different thermal properties. The TD design presented in *chapter 5* is reliant on correct placement of the sensor tracks at the neutral axis of the beam to eliminate bending stresses and return a pure thermal signal. There are several difficulties in the approach taken: calculation of the neutral axis position is based on material properties of the polyimide films supplied by the manufacturer without explicit statement of measurement tolerance, making it difficult to estimate the true error in the calculation; there is an additional error in the deposition calibration curves for the polyimide layers (i.e. spin speed *vs.* layer thickness) as there are small non-uniformities in layer thickness associated with spin deposition. To gain confidence that the sensor position is sufficiently close to the neutral axis to significantly reduce the bending strain, a series of characterisation experiments were performed *(section 6.2)*. For comparison, some microcantilevers of very similar design, but with sensors fabricated using NiChrome (nickel-chromium alloy in the ratio 80:20) were also analysed. Position of the sensor in the comparator beams (known henceforth as MD for Mechanical Design) was close to the upper surface. Note that at the time these characterisation experiments were performed, the collaboration with Microvisk Ltd. had not been established; therefore SmartStrip microcantilever sensors were not available for use as comparators. The MD cantilevers were designed by Dr Richard Dunn at STFC and fabricated at the INEX

foundry, Newcastle, UK with STFC central funding. Characterisations in air are reported in *section 6.3.* In order to determine whether the low frequency components of the microcantilever sensor signal are cross-sensitive to the thermal conductivity and heat capacity of the test liquid, tests using silicone oils were performed and are detailed in *section 6.4.* In *section 6.5*, the study is completed with an evaluation in blood plasma to see whether the clotting process affects the thermal properties of the sample.

6.2 Characterising the TD microcantilevers: A Comparative study

6.2.1 Temperature vs. Resistance

The temperature coefficient of resistance (TCR) for the sensor can be estimated from the fit to R_S/R_0 versus chip temperature where $R_S(T)$ is the sensor resistance and R_0 is resistance at room temperature (20 °C). This measurement is not exact in a released cantilever because it will also include the piezoresistive component due to the change in beam curvature. Unreleased cantilevers were therefore also measured to assess the relative contribution of the mechanical effect to the overall signal. Measurements were made using a ceramic micro-heater placed underneath the chip. The temperature was verified using a calibrated thermocouple micro-sensor (RS components) with a precision of 0.1 °C. The resistance was monitored in real-time using a 6 ½ digit digital multimeter (2100 6 ½ Digit USB Digital Multimeter, Keithley). The heater initially over-shoots when the set temperature is increased, but then regains equilibrium within 10 minutes due to the low thermal inertia of the system, at which point the resistance is recorded. Example results obtained for the both sets of cantilevers are shown in *figure 6.1*, and comparison between the released and unreleased cantilevers is made in *table 6.1*. For the TD cantilevers, TCR = 0.11% per °C, and the released and un-released beams have similar profiles. The temperature *vs.* resistance for the MD cantilevers is affected greatly by releasing the beam, reflecting the increased mechanical sensitivity of the MD cantilevers relative to the TD cantilevers. The thermal sensitivity of the MD cantilevers (including the thermo-mechanical effect) is dR/R = 0.016% per °C. The measurements were made within the metal box test platform: enclosing the beam to shield from draft.

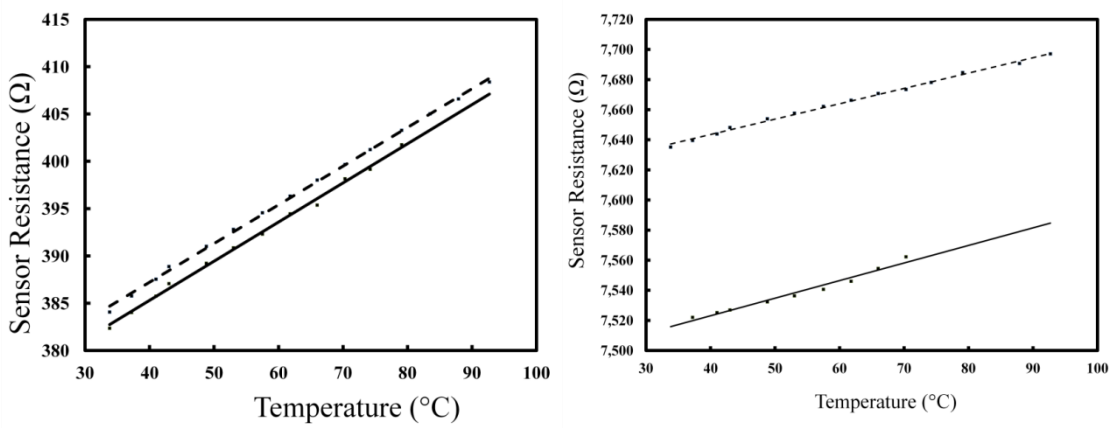

Figure 6.1 Resistance versus temperature relationship for TD (left) and MD (right) cantilevers; both released (solid) and non-released (dashed).

Design	Est. TCR for released beam (% per ^{o}C)	TCR for un-released beam (% per ^{o}C)	Mechanical contribution to signal (%)
TD (Gold)	0.108 ± 0.006	0.107 ± 0.006	0.4 ± 8.5
MD (NiCr)	0.0156 ± 0.0004	0.0136 ± 0.0004	13 ± 3

Table 6.1 Comparison of TCR for different cantilever designs.

6.2.2 Temperature vs. Deflection

Measurements of the microcantilever tip deflection at different temperatures were made using the home built autofocus system described in *section 3.2.2* and in [75]. The results show that the TD microcantilevers have greater deflection (approximately 340 µm) compared with that of the MD cantilevers (approximately 180 µm), and that the relationship between temperature and displacement in each is non-linear with a maximum deflection between 50 °C and 60 °C. At the time these experiments were conducted, high humidity during the measurements was not known to be the cause of the non-linear result, but as a result of the analysis in *Chapter 3*, it is now known that the true temperature *vs*. deflection relationship can only be found in the region of the graph where virtually all the moisture has all evaporated; i.e. the linear region between 80-115°C.

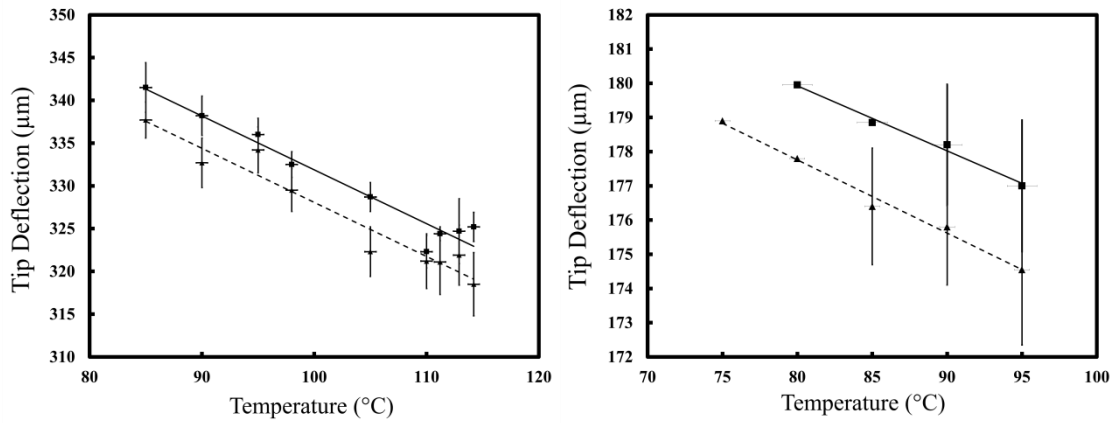

Figure 6.2 Microcantilever tip deflection versus temperature. Left: Two results from cantilevers fabricated within MNTC to Thermal Design (TD). Right: Comparator cantilevers fabricated at the INEX foundry to the Mechanical Design (MD).

In the linear region, the deflection decreases by 0.631 ± 0.002 µm per °C for the TD beams and 0.16 ± 0.04 µm per °C for the MD beams, which is in concord with the idea that the TD thermal actuator beams should move upon actuation just like the MV and INEX beams, but in the case of the TD, we should not be able to sense that movement using the integrated sensor. The larger deflection observed for the TD beams is a consequence of having the heater and sensor tracks in a single layer in the TD sensor and thus reducing the stiffness of the beam.

6.2.3 Deflection vs. Resistance

Method

The gauge factor for the sensors was determined by pushing the cantilever tip down using a fine pin whilst simultaneously recording the sensor resistance. The experimental set up was similar to that used by Ibbotson *et al* [88] and is pictured in *figure 6.3*. Chips were wire bonded into ceramic holders so that electrical contact could be made via a ZIF holder to leave easier access for the pin above the beam. An *xy* stage was used to position the chip underneath the pin, which was lowered in increments of 10 microns using a piezo-stepper motor with PC interface. The sensor resistance was recorded using a 6 ½ digit digital multimeter (2100 6 ½ Digit USB Digital Multimeter, Keithley) connected via the contact pins in the ZIF holder. A telescope was used to view the pin as it pushed down on the microcantilever tip in order to make sure that it

was in the same position relative to the end of the beam throughout the test. Once the pin had been lowered to the point that the resistance stopped changing with pin height, the direction was reversed until the original deflection was recovered. The up-down process was repeated twice more to determine whether hysteresis was present in the system. The experiment was performed in the MNTC clean room to ensure that the temperature and humidity remained constant throughout the test. Conditions of constant temperature and humidity were verified using a thermohygrometer placed next to the test set up and also a smaller 'local' thermometer placed close to the microcantilever chip. Bright lighting was necessary to view the chip through the telescope and the temperature was noted to increase slightly if the experiment took a long time. Readings were only taken when the 'local' temperature was stable, and within 1°C of the ambient temperature.

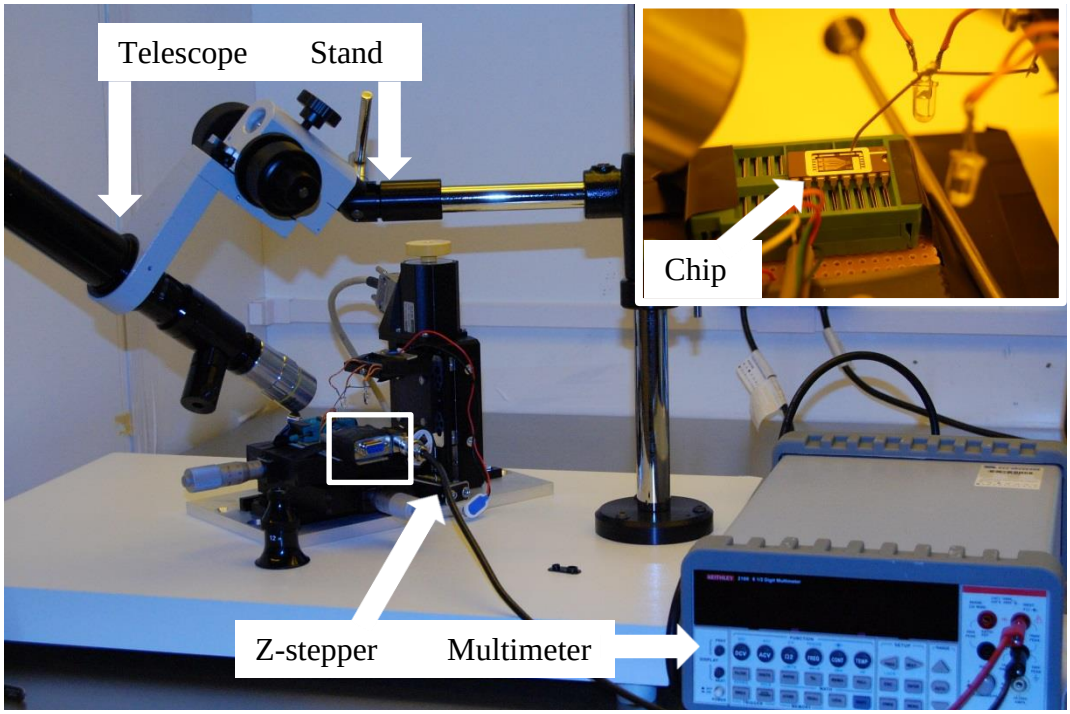

Figure 6.3 Experimental set up for the gauge factor experiment showing telescope, xy stage, z-stepper (PC control not seen) and digital multimeter. Inset shows a TD microcantilever chip mounted in ceramic casing held within a ZIF socket. The local temperature probe can also be seen.

Results and Discussion

Even using the telescope it was difficult to accurately judge the position at which the cantilever tip 'just' contacted the substrate. The data have been scaled to fit the 'zero deflection' point to where changes in the resistance had reached a minimum and the beam appears to be straight. Therefore there may be a systematic error in *z* of no more than 20 microns (2 data points) in each set of data. *Figure 6.4* shows example raw data from a TD and an MD chip to illustrate hysteresis and imprecision in the measurement. Note that vertical error bars are plotted on both graphs that represent the error in the resistance read out, but due to the high sensor resistance in the MD devices, they are too small to see.

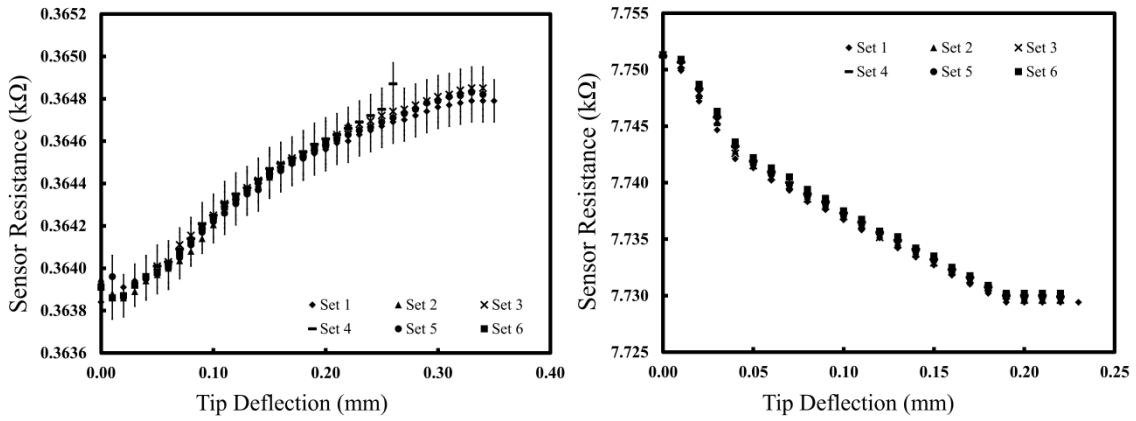

Figure 6.4 Raw data from the deflection vs. resistance experiment. TD 11-50 (left), and MD 11-02 (right). In Sets 1, 3, and 5 the pin is moved in the direction of decreasing microcantilever deflection, and sets 2, 4 and 6 the pin is moved in the direction of increasing microcantilever deflection.

A possible cause of the small amount of hysteresis in this experiment is the small variation in the pin position relative to the tip of the microcantilever which needs to be monitored closely and adjusted periodically. The effect of pin misalignment is seen in *figure 6.4a* for measurement set 4 of the TD sensor, taken in the upward direction. At *z* = 0.27 mm, the pin slipped off the edge of the beam, and it is possible to see in the previous few readings how the measured resistance has increased deviation from the other measurements at that height.

Averaged results for the four sensors of each design type that were tested are presented in *figure 6.5*. The resistance of the TD cantilevers increases with increasing tip deflection (i.e. increasing curvature of the beam), therefore the sensor read-out tracks are undergoing positive strain (tension) which means they must be below the neutral axis. Conversely, in the MD the sensor read-out track is above the neutral axis and therefore being compressed upon deflection (resistance decreases with increasing deflection).

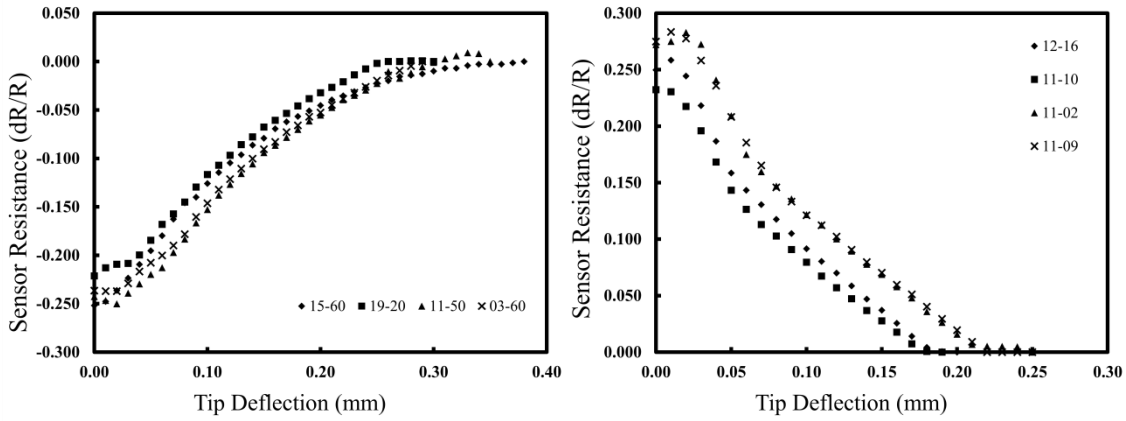

Figure 6.5 Deflection sensitivity of cantilevers from four individual chips. The chip identification is displayed in the figure legends. The left hand graph shows the results from Thermal Design cantilevers, the right hand graph shows the results from the comparator MD design.

Each type of beam has four distinct phases of resistance sensitivity. This is intuitive based on the design of the chips: as the tip is lowered from its maximum deflection, the first part of the beam to straighten out is the base, where there are only two passes of the sensor track and they are made slightly wider than in the main part of the sensor; next the tracks narrow and the sensitivity increases; then there is a region of higher sensitivity, where there are four passes of the narrow sensor and finally a region of low sensitivity where most of the movement of the pin goes into pushing down the polyimide and heater tracks at the very end of the beam. The region of maximum sensitivity, where the tip deflection is between 80 - 140 µm is of interest here. The maximum sensitivity is dR/R = 16 ppm/µm for the thermal design, and dR/R = -27 ppm/µm for the mechanical design.

6.2.4 Discussion of the characterization results

The TD microcantilever beams have been characterised in order to determine to what extent the integrated sensor is functioning as a thermistor and to what extent it is functioning as a piezoresistor, using a previous design of microcantilever sensor (MD) as comparator. Temperature *versus* resistance traces of released and unreleased beams *(section 6.2.1)* indicate that the contribution of the mechanical component to the resistance change with temperature in the thermal beams is 0.4% ± 8.5%, i.e. is zero within the margin of error, and in the mechanical design beams is 13% ± 3%.

By observing the equilibrium beam tip position at different temperatures it can be determined that in the absence of moisture, the deflection of the TD beam decreases by 0.631 ± 0.002 µm per °C, and the deflection of the MD beams decreases by 0.16 ± 0.04 µm per °C. The deflection sensitivity was found to be 16 ± 4 ppm per µm for the TD beams and -27 ± 15 ppm per µm for the MD beams, with the resistance change in the case of the TD sensors being opposite in sign to the change due to heating. Combining the deflection sensitivity with the deflection change upon heating gives the piezoresistive contribution to the signal when the beam is heated of 8 ± 2 ppm per °C for the TD beams (against the thermal signal) and 4 ± 3 ppm per °C for the MD beams (reinforcing the thermal signal). Comparison with the total resistance change of the released beam upon heating gives an alternative estimate of the mechanical contribution to the signal of -0.8% ± 0.2% for the TD beams and 2.8% ± 1.7% for the MD beams.

Both methods used to estimate the mechanical contribution to the signal have flaws that contribute to their large relative errors and, in the case of the MD beams, their disagreement with one another. However it is clear that the piezoresistive signal *is* minimized in the thermal design cantilevers relative to the mechanical design in conditions of steady state heating. In the comparison of released and unreleased beams, it was not the same chips used both before and after release, so most of the difference in relative resistance change is due to chip-to-chip variability. In the deflection sensitivity measurements it is assumed that the beam profile changes are the same when the beam is pushed down by the tip (force concentrated on the end of the beam acting downwards) and when the beam is thermally actuated (force acts through the length of the beam). The analysis is concentrated on the most sensitive part of the deflection-

resistance curve, whereas the resistance *versus* temperature relationship has different deflections at each temperature. In addition, the need to have some chips wire-bonded for the deflection sensitivity measurements meant that it was necessary to use different chips in the different experiments increasing the disparity between the results. Finally, the piezoresistive constants of gold and NiChrome vary with temperature as shown by Angadi and Whiting [210]. Previous work on sputtered NiChrome strain gauges by Kazi and coworkers also showed that the TCR is increasingly temperature dependent at high temperatures [206, 207], in contrast to the linear result observed in *section 6.2.1*. Both the present and previous works are affected by additional stress due to the bi-material effect between the strain gauge and substrate, even when the substrate is fixed.

6.3 The Thermal Design Microcantilever Signal

6.3.1 Thermal Imaging

In order to make a suitable choice for the actuation pulse for the "Thermal Design" cantilever sensor, some preliminary measurements were made using a thermal imaging camera to determine the temperature reached by the beam during various actuation pulses. The advantages of using a non-contact technique to compliment the signal from the integrated sensor are that the cantilever beams are neither damaged (when operated in air) nor hindered in their motion during the measurements. The specific aims of the thermal imaging measurements were:

- To ensure pulse energy is sufficiently low to avoid excessive heating and subsequent denaturation of sample in a biological application of the sensor.
- To understand whether the reference beam is being heated and if so, what is the impact?
- To understand how the introduction of liquid affects the temperature of the beam
- To determine whether the temperature is building between consecutive pulses.

Measurements were conducted using a Micro-Epsilon (Ortenburg, Germany) infra-red camera at the Microvisk manufacturing facility. The camera was sensitive to wavelengths between 9 µm and 14 µm and gave a spatial resolution of 10 µm and temporal resolution of 10 µs.

Experimental Set Up

A narrow angle (9°) lens was used for measurements because this allowed for the greatest spatial magnification. A calibration of the cantilever sensor at known temperatures was required. For calibration measurements, an electrically isolated TD chip was placed on top of a calibrated sub-miniature ceramic heater on a platform beneath the thermal imaging camera. Thermal videos were recorded as the heater was stepped from room temperature to 100 °C and analysed over representative sections of the chip. It was possible to adjust the focus of the lens to maximise the contrast between areas of different emissivity (e.g. on the boarder of one of the contact pads) to minimise noise. It was assumed that after 10 minutes the whole chip was in equilibrium with the heater as had been found previously *(section 6.2.1).* To take measurements of cantilevers undergoing electrical actuation, the chips were wire bonded to a ceramic holder and connected to a function generator using a ZIF connector *(figure 6.6).* Thermal imaging measurements were performed behind a black-out screen to reduce the thermal background from lighting in the laboratory.

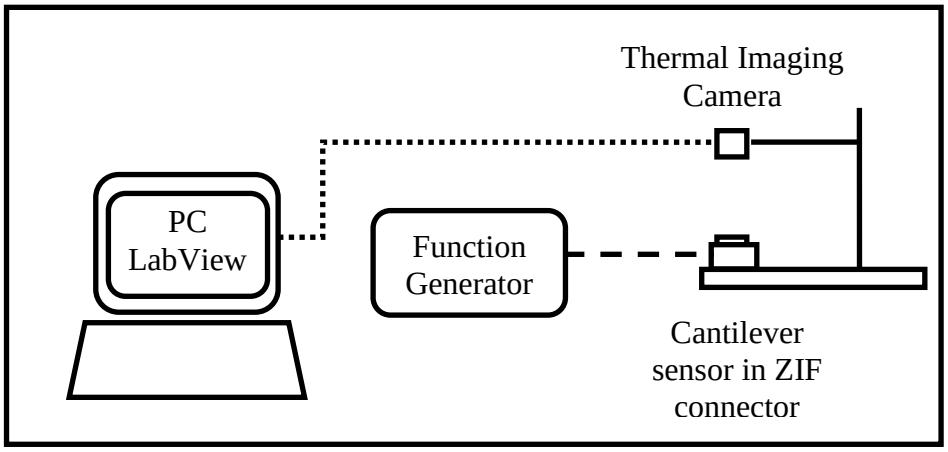

Figure 6.6 Schematic of experimental set up used to take thermal video recordings of microcantilevers during actuation.

Measurements were taken for six TD microcantilevers. Two sets of measurements were taken using square wave pulses occurring at a frequency of 1 Hz. The first measurement set used pulse duration of 400 ms and varied the applied voltage between 0 mV and 800 mV (pulse power measurements). In the second set of measurements, the voltage was fixed at 500 mV and the pulse duration was varied between 10 ms and 990 ms (pulse duration measurements). A thermal imaging video of the microcantilever was recorded for a period of at least 30 seconds for each combination of pulse duration and

voltage used to actuate the microcantilever. A still from one of the thermal imaging videos is presented in *figure 6.7.*

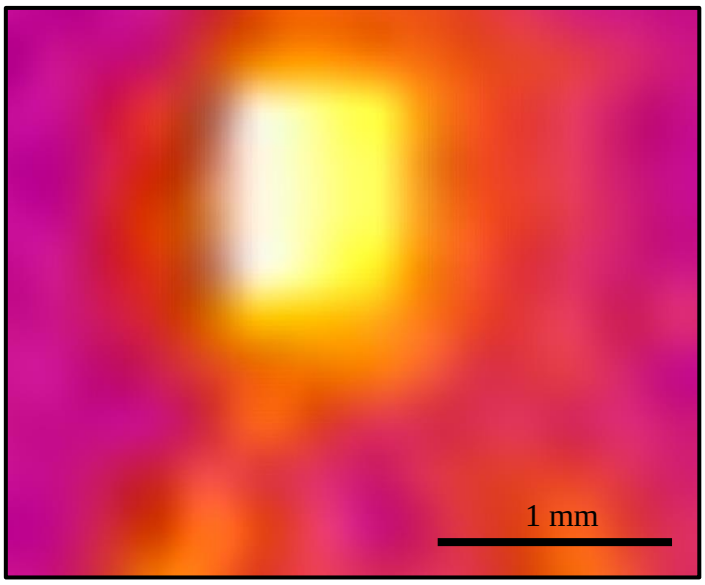

Figure 6.7 Still from a thermal imaging video. The colour-scale is mapped to the range of temperatures in the image, with white the hottest and purple the coldest. The white area is a microcantilever during actuation at 800 mV.

Data Processing

A *9-by-7* grid (each square 220 ± 50 µm in length) was superimposed on the thermal video from which the greyscale values for different parts of the microcantilevers could be extracted. Subsequent data analysis was performed using Matlab R2012a (Student Edition) and is outlined in *figure 6.8*. It was noted that there are periodic 'blinks' in the signal, where a shutter closes for a fraction of a second in order to recalibrate the microbolometer which heats up during use. The reported data during these 'blinks' were removed from the analysis. The change in signal before versus after a blink corresponds to a temperature of 1 °C; this is the measurement error of the camera.

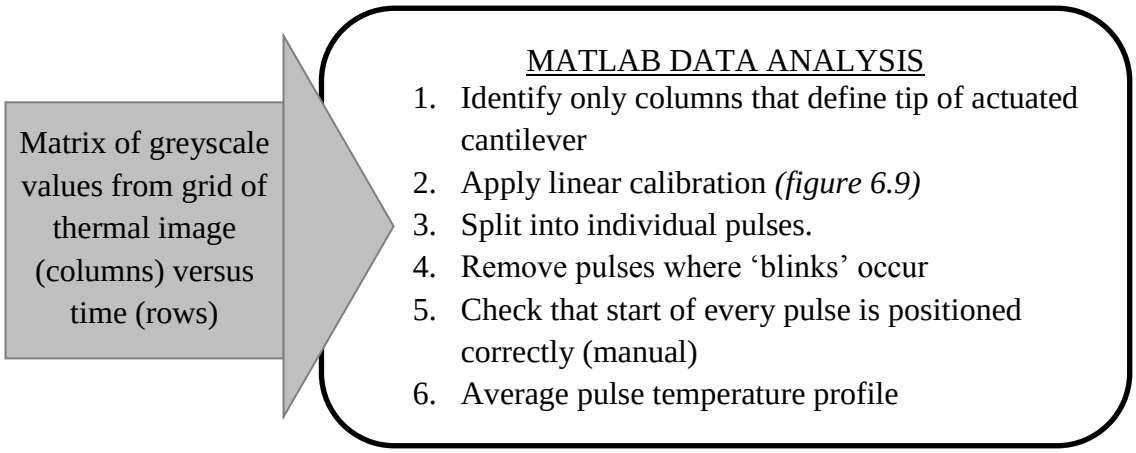

Figure 6.8 Outline of Matlab data analysis program for converting raw data from the thermal imaging camera into the temperature profile of the cantilever tip over the course of an actuation cycle.

To account for differences in reflectivity between a beam that is flat and one that is released (with the tip angled away from the camera), calibrations were performed using released and un-released beams. Three different areas on the chip surface were also calibrated for reference. These were the release pad, embedded gold tracks (Au substrate) and polyimide on the substrate. An example is shown below in *figure 6.9.*

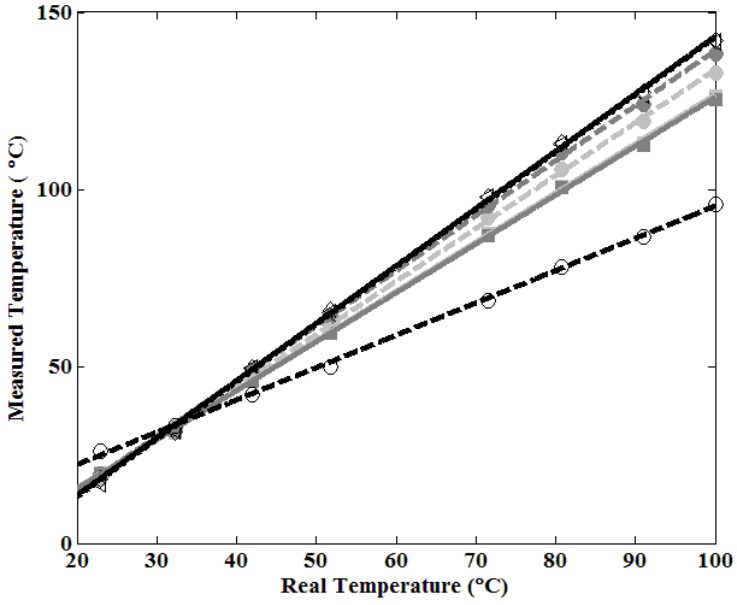

Figure 6.9 Thermal image temperature calibrations from a single TD chip: tip of the beam (filled circles); base of the beam (filled squares). Dark grey = beam with greatest deflection, light grey = less deflected beam. Parts of the substrate were also measured (black traces: dashed line = sensor tracks; solid line = release pad; dotted line = polyimide substrate).

Analysis was conducted to determine the temperature at the tip of the beam during a pulse. The area analysed contains the portion of the sensor that is subject to greatest heating. The thermal video recording could not be synchronised with the output from the function generator in the time available to set up and run the experiments. A Matlab script was written to identify the start of each pulse semi-autonomously by searching for a sudden increase in the signal-to-noise ratio within a range dictated by the pulse parameters that were used. The temperature increase for each pulse was determined from the height of each peak in temperature relative to the next trough and there was no drift in the ambient temperature signal between pulses that could be due to heat building up around the beam over the course of many actuations or due to a drift in the ambient temperature.

Results and Discussion

Pulse Power

The heating of the beam in air during a 400 ms pulse is pronounced and the maximum temperature reached at the tip of the beam scales linearly with the power supplied in the actuation pulse as shown in *figure 6.10.* The change in tip temperature with actuation power is 1.7 ± 0.5 °C/mW for the cantilevers tested. The large relative uncertainty arises from the variation between the different microcantilevers. The standard deviation of the recorded temperature reached by the beam for different pulses in a single pulse train is typically less than 1 °C.

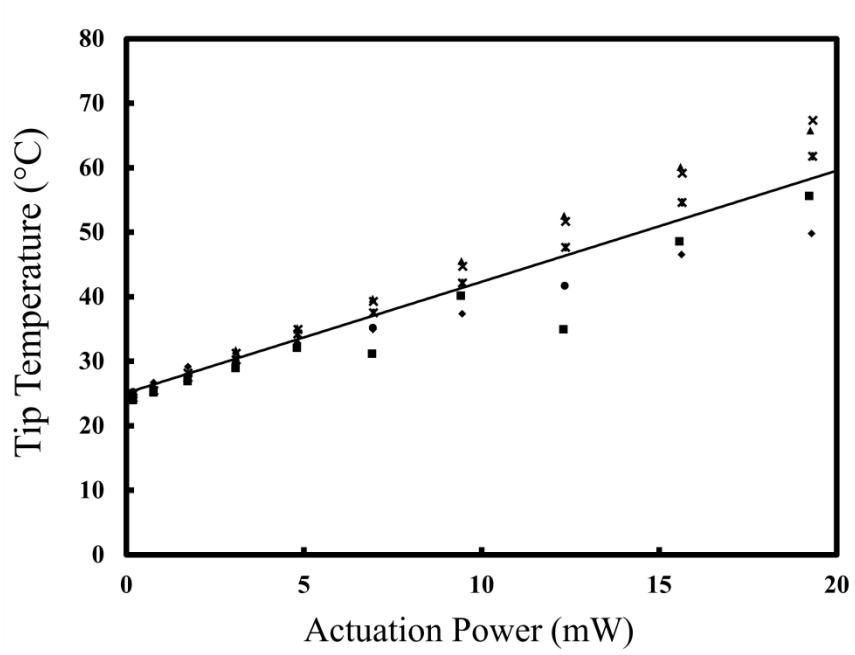

Figure 6.10 Maximum temperature of the actuated beam tip measured during a pulse versus actuation power for 6 different TD microcantilever beams: TD-1750 P (×); TD-1430 P (▲); TD-1750 A (*); TD-1430 A (■); TD-1150 A (◆) and TD-1150 P (●) where A stands for the active beam (that had been actuated previously) and P for the normally passive beam. Error bars on the individual points are too small to see clearly. Linear best to all points fit plotted.

Preliminary measurements suggested that there was no damage to the sensor at the power range tested; however there is certainly more variation between different chips in the beam tip temperature as the power is increased. This could be because of variations in the beam stiffness or level of stiction in the different beams mean that some beams are more deflected than others and the application of the calibration is inaccurate. Alternatively, some beams may be reaching higher temperatures than others depending on the deflection, stiction and consequent level of thermal isolation of the beam.

Each TD chip consists of two cantilever beams 100 μm apart as discussed in section 5.2.3. The cantilever that is being actuated is known as the 'active' beam with the other beam (used to complete the Wheatstone bridge) is known as the passive beam. It was also noted that the passive beam was heated during actuation, with the beam tip reaching up to 35 °C on the side closest to the active beam when actuated at 20 mW. The temperature of the tip of the passive beam increases by 25% of the active beam

temperature increase. When the response signal is recorded in the Wheatstone bridge circuit, the heating of the reference beam will serve to reduce the measured signal.

For an application in blood clot-time measurements, the sensor must not heat the sample above 37 °C, since temperature affects the kinetics of the clotting cascade. Due to the higher heat capacity and thermal conductivity of blood compared to air, it was expected that the temperature reached by the sample in blood would be much lower than the values recorded in *figure 6.10*. An attempt was made to measure the temperature of 10 µl clotting reagent pipetted onto a sensor while it is actuated. As only a few sensors had been expensively wire bonded into the ceramic holders, preliminary measurements were made using SmartStrip sensors. Less than 5 °C increase in temperature was recorded even at 30 mW. An additional test was conducted spotting 10 µl of raw egg-white onto the beam and observing the sample under a microscope after actuation. Egg white is known to increase in opacity sharply as the temperature increases beyond 61 °C, the coagulation temperature of albumin. No changes in the sample were observed up to 30 mW at which point a very small (approximately 10 µm) speck of opaque sample was noted near the beam tip. This indicates that at higher powers there may be hot-spots on the beam where the temperature exceeds 61 °C even though the majority of the sample is much cooler. It was concluded that the maximum pulse power to ensure that clinical samples won't be overly heated is 30 mW when a long pulse is used.

Pulse Duration

The variation in maximum beam temperature for pulses of less than 100 ms duration *(figure 6.11)* is indicative of the time taken to reach thermal equilibrium for 5 mW actuation power.

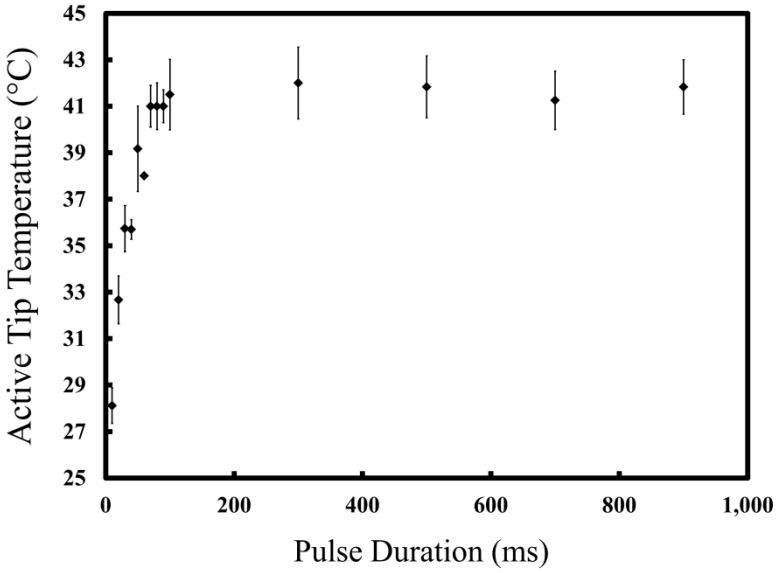

Figure 6.11 Variation in maximum beam temperature with pulse length for a 5mW pulse, error bars are 1 standard deviation of measurements from six beams.

In the shortest pulses measured (e.g. 10 ms), equilibrium is not reached, so the temperature is below the calibration line in *figure 6.10*. Therefore short pulses might be used to deliver high power with relatively low heating effect on the liquid. Likewise, for the longest pulse, 990 ms, the recorded temperature does not return to ambient. However there is no cumulative heating (i.e. the temperature does not drift over multiple pulses) which suggests that the time resolution is limited by the camera: if the beams were not cooling down between pulses there would be drift.

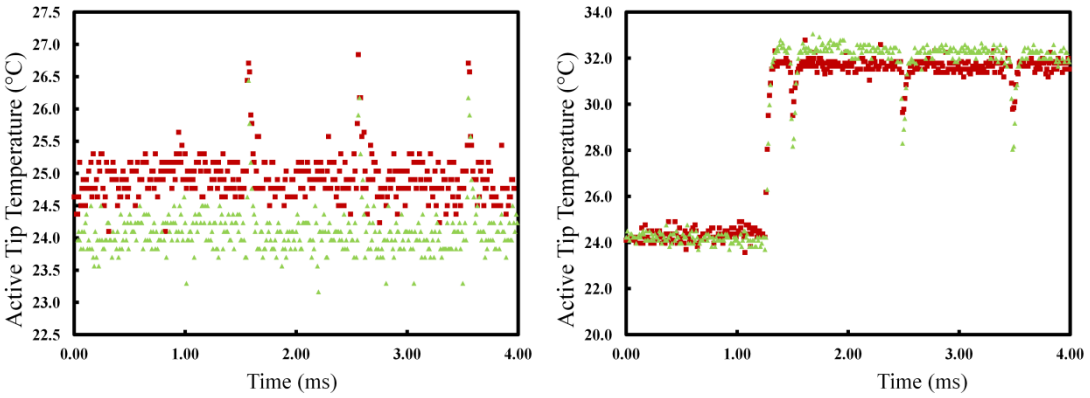

Figure 6.12 Example pulse profiles for 10ms 5mW pulse (left) and 990 ms 5 mW pulse (right) from the tips of two different beams (red and green).

Individual pulse train data were analysed to find the overall thermal decay constant of the beam by fitting to Newton's exponential cooling equation: $Ae^{-t/\tau}$. The results are presented in *table 6.2*, below. Data from 800 mV pulses were used because data from all six beams is available at this level and there is a favourably high signal to noise ratio.

Beam Reference	τ_{COOL} (ms)	95% CI of τ_{COOL} (ms)	A (°C)	95% CI of A (°C)
11-50 HL	26.30	24.95 - 27.80	10.47	9.98 - 10.96
14-30 HL	25.55	23.95 - 27.38	10.03	9.45 - 10.61
17-50 HL	27.78	26.37 - 29.36	15.50	14.79 - 16.21
11-50 HR	30.77	27.59 - 34.78	37.66	34.02 - 41.30
14-30 HR	14.89	13.30 - 16.91	36.93	32.43 - 41.42
17-50 HR	18.98	18.55 - 19.42	37.41	36.61 - 38.22

Table 6.2 Thermal profile of signal from different TD microcantilever sensors.

The same process was used to find the thermal rise time for the microcantilever tips.

Beam Reference	τ_{HOT} (ms)	95% CI of τ_{HOT} (ms)	A (°C)	95% CI of A (°C)
11-50 HL	29.83	28.25 – 31.59	11.44	10.98 – 11.98
14-30 HL	25.18	23.77 – 26.76	11.35	10.77 – 11.94
17-50 HL	29.80	28.32 – 31.45	16.70	15.96 – 17.44
11-50 HR	22.07	21.20 – 23.02	38.70	37.27 – 40.14
14-30 HR	20.99	20.49 – 21.52	36.89	36.07 – 37.72
17-50 HR	22.86	21.79 – 24.04	55.47	53.02 – 57.91

Table 6.3 Thermal profile of signal from different TD microcantilever sensors with values based on an exponential fit to the 'heating up' part of the curve.

It is interesting to compare the values for the thermal rise time with the predictions made in *chapter 5*. Comparison of the beam design and material properties of the microcantilevers discussed in this work and the previous work of Li and Uttamchandani [195] led to the prediction that the thermal design (TD) sensors would have a thermal rise time significantly shorter than 17 ms. In fact we find that it is longer at 20 – 30 ms. The discrepancy between these results and the earlier predictions could be due to the fact that the predictions are only based on approximations of the material properties of the polyimides, such as the polyimide thermal conductivity, which is not well established. There also seems to be a significant amount of variability between the individual cantilever beams. The fact that this variability is just as high between two

beams on the same chip as between beams on different chips indicates that actuation history is more likely than any problems related to the microfabrication process to be the main source of the variability. It is also possible that small deviations in the alignment of different beams under the thermal imaging camera contribute to the observed variability in results.

6.3.2 Characterising the long pulse in air

Experimental Set Up

Experiments to characterise sensor signal were conducted at STFC using the experimental set up shown in *figure 6.13.* LabView (Version 8, National Instruments) was used to control actuation of the sensor and data acquisition. The data collection program was designed by the author to operate on a fixed power basis, to account for the small differences in sensor resistance. Output from each test was stored automatically as .lvm (LabView measurement) files. The associated meta-data was recorded automatically in a notepad file. A data acquisition card (M-Series, NI PCI-6221) was routed through a shielded terminal black (NI SCXI 1314) via an 8 channel universal strain gauge (NI SCXI 1520) set to half bridge, and the signal generator (Agilent, 33220A). The metal box discussed in *Chapter 5, Section 5.3.4* was used to interface the chips with the electronics. Shielded coaxial cables of minimal length were used wherever possible, and unused channels from the 9 core cable were removed from within the cladding to reduce electrical interference.

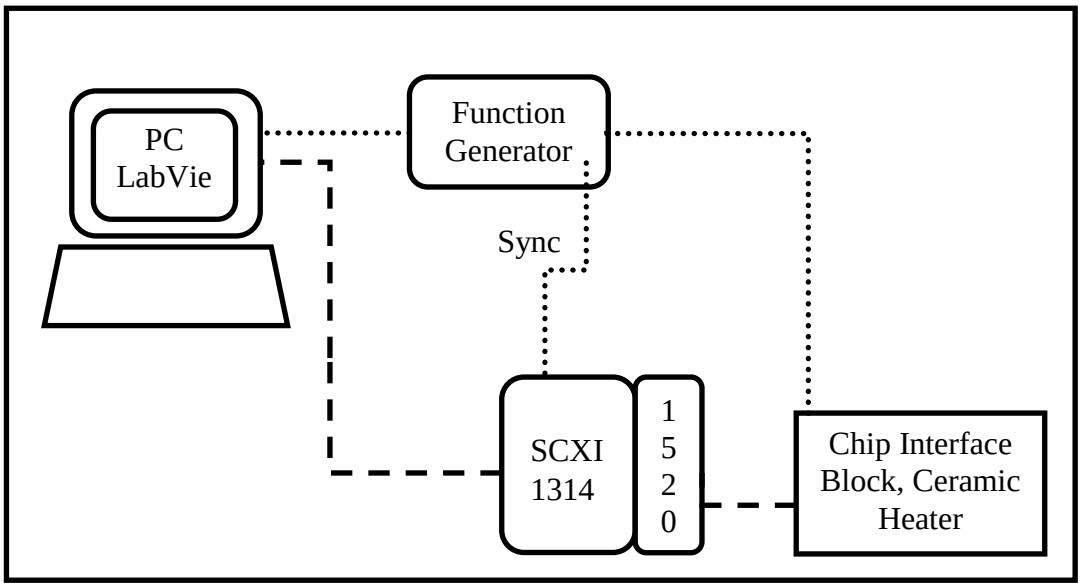

Figure 6.13 Block diagram of STFC set up: dotted lines are for shielded coaxial cables, dashed lines for shielded 9 core cable.

Shunt calibration

A shunt calibration was performed to calibrate the relationship between the Wheatstone output voltage and the corresponding change in sensor resistance dR brought about by movement of the cantilever. A high precision resistor is incorporated in the 'Sensor' arm of the bridge. Resistors R1 and R2 are set within the module to be equal to R_X, to balance the bridge, and the change in output voltage is measured when the switch position is changed to incorporate the shunt resistor R_S in series with the test resistor *(figure 6.14, left)*. The calibration was verified to be linear with the relative change in resistance, by use of various test resistors, and five repeat measurements were taken at each level; error bars in *figure 6.14, right*, show one standard deviation.

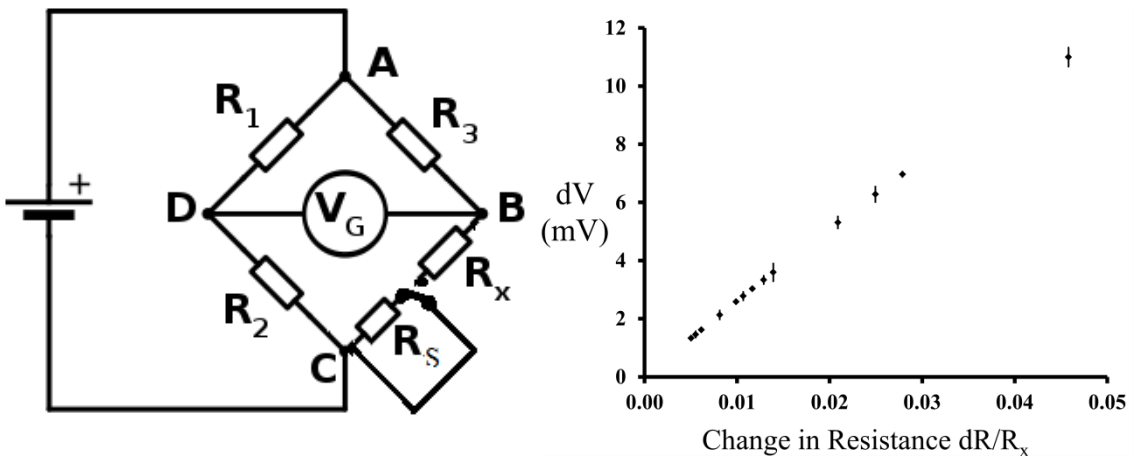

Figure 6.14 Bridge configuration for series shunt calibration (left), and results (right).

The temperature of the sensor can be found using the gradient of the shunt calibration in the following equation:

$$dT = \frac{dV}{TCR} . \left(\frac{{}^{dR}/_{R_x}}{dV} \right)_{SHUNT} \tag{6.1}$$

For typical gate voltages recorded during a pulse peak of 0.001V, the corresponding error in the change in temperature experienced by the beam (as calculated from the relative errors in shunt calibration fit and TCR) is 10%, with the majority of the error arising from the uncertainty in the TCR.

Determining instantaneous temperature from the long pulse signal

The sensor signal was collected in air for a series of 400 ms pulses of increasing power to enable direct comparison between the signal and the temperature of the beam found from the thermal imaging experiments. Unfortunately the very same beams were not used for both experiments because the testing was conducted concurrently. By using the same actuation power for both tests (instead of the same actuation voltage), the results are made comparable. *Figure 6.15* shows the average sensor signal from six measurement sets plotted against the average beam tip temperature for six pulses of the same power and duration recorded by thermal imaging.

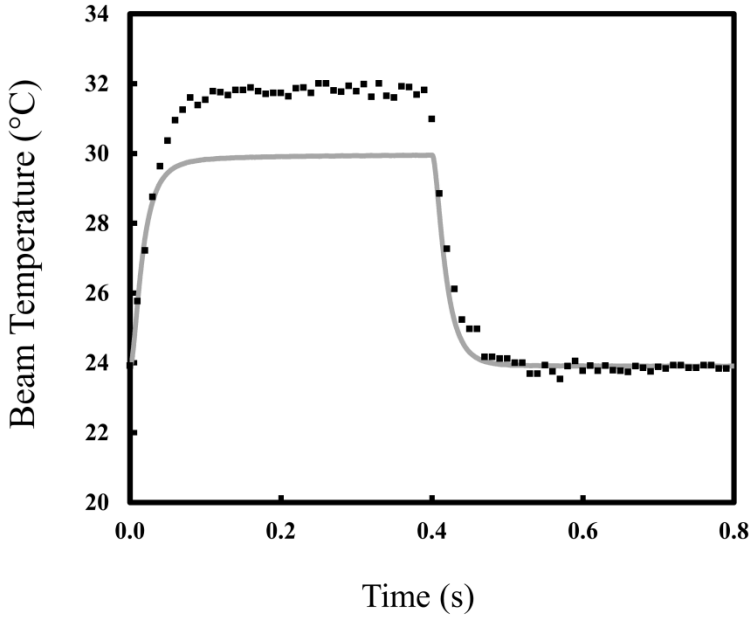

Figure 6.15 Comparison of microcantilever sensor signal (grey) with the temperature of the beam measured by thermal imaging (black) during a 400 ms pulse at 3.1 mW in air.

There are several important points to note:

1. The temperature increase sensed by the microcantilever is 24% smaller than that detected by thermal imaging. There are two principle reasons for this: the temperature rise of the reference sensor reduces efficiency of Wheatstone bridge; and the thermal image measurements are only recorded at the tip of the beam, which includes the heater tracks. The resistivity of the sensor tracks at all points on the cantilever contribute to the relative change in resistance as the beam is heated, so the base of the beam, which has a smaller temperature increase than the tip, dilutes the signal.

2. An exact thermal equilibrium is not reached. Both the temperature and the sensor signal do not tend towards a zero gradient over the duration of the pulse, rather they continue to increase at a linear rate after a certain point (approximately 0.15 seconds for the pulse shown in *figure 6.15*). This phenomenon was verified for pulse lengths up to 1.2 seconds. We can understand this as being due to incomplete thermal isolation of the cantilever from the substrate, which is a large heat sink.

3. The thermal time constant for the sensor signal is faster for the sensor than for the beam temperature. T90 for the sensor signal is 16 ms and for the beam tip

temperature is 30 ms. This could be because the thermal time constant of the microbolometer (on the order of 10 ms) is a limiting factor in the thermal imaging experiments or it could be due to variability in the different beams used in the experiments.

Comparison of the Wheatstone signal with the thermal imaging measured temperature between 0.2 and 0.4 seconds (the 'quasi-equilibrium' part of the signal) gives the temperature efficiency of the signal. *Figure 6.16* shows the correlation between temperature and sensor signal for three beams that were un-actuated prior to the thermal analysis. It was noted that beams that had previously been actuated reached higher temperatures per unit actuation power as observed previously in *figure 6.10*. This cannot be due to the gold becoming annealed upon actuation, as the cure of the subsequently deposited polyimide layer at 350 °C would have been at a sufficiently high temperature to thermally anneal the gold [201]. It could be that the heater resistance is increased due to agglomeration in the metal tracks occurring at very high temperatures when the cantilevers are actuated with a short, high power pulse; however at 150 nm thick, the heaters may be too thick for agglomeration to be significant. Alternatively, the thermal shock could have bent the tracks beyond their elastic limit and caused micro-fractures that increase the resistance even when it does not lead to a complete electrical short. Micro-fractures in gold can occur after bending and reduce the grain size by breaking up larger grains, and decrease the stiffness of gold as shown previously for gold films on PDMS [212].

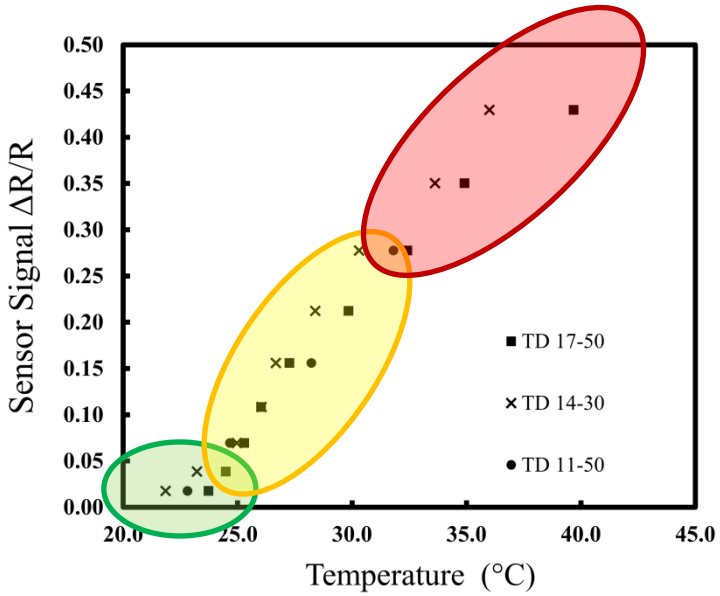

Figure 6.16 Correlation between microcantilever sensor signal and maximum beam tip temperature for 400 ms actuation pulses between 1 and 20 mW in air. Three regions are identified where the sensing efficiency is very low (green), medium (red) and highest (yellow).

From *figure 6.16* it appears that the sensing efficiency (i.e. the change in sensor signal per unit temperature change) is highest when the temperature change is around 5 °C. This corresponds to actuation powers of between 5 mW and 10 mW in air and 30 mW in an aqueous liquid. One possible reason for there to be regions of different efficiency in *figure 6.16* could be because at low temperature, much of the output from the heater has dissipated before it reaches the sensor and the inner passes of the serpentine section of the sensor are barely heated, as the temperature increases, more heat can build up on the sensor, but this is partially offset by the beam deflecting towards the substrate.

Thermal Decay Time in Air

It is interesting to observe whether the thermal decay time (i.e. the time required for the signal to decay to $1/e$ of its maximal value after the actuation heating is switched off) depends on the pulse duration. During the actuation pulse, the beam is heated, and some of this heat is transferred to the surrounding fluid. The longer the pulse, the more fluid can be heated. When the actuation pulse is switched off, heat continues to be transferred to the fluid. By Newton's law of cooling, the rate of cooling of the beam should be proportional to the difference in temperature between the beam and the

surrounding fluid, therefore the rate of cooling will be slower, and the thermal decay time (τ) longer, following a long pulse than following a short pulse.

Measurements of the Wheatstone bridge output signal were made upon actuating a microcantilever in air with a power of 5 mW for the following pulse durations: 10 ms, 20 ms, 30 ms, 50 ms, 70 ms, 90 ms, 100 ms, 300 ms, 500 ms and 700 ms. A frequency of 1 Hz was used throughout. Data from twenty pulses was acquired for each pulse type and the average pulse profile was calculated. The average pulse profiles were normalised such that the average of the final 100 ms of data is set equal to zero. The maximum value of the average pulse profile after the actuation was found from a linear fit to the gradient of the average pulse profiles. The thermal decay time was then measured as the time required for the signal to fall to $^1/_e$ of the maximum value of the average pulse profile. The error in the thermal decay time calculated using this method is less than 0.1 ms. Average pulse profiles relative to the maximum value are shown in *figure 6.17*, for different pulse durations. It can be seen that average pulse profiles following actuation pulses of shorter durations do indeed decay slightly faster than when longer pulse durations are used.

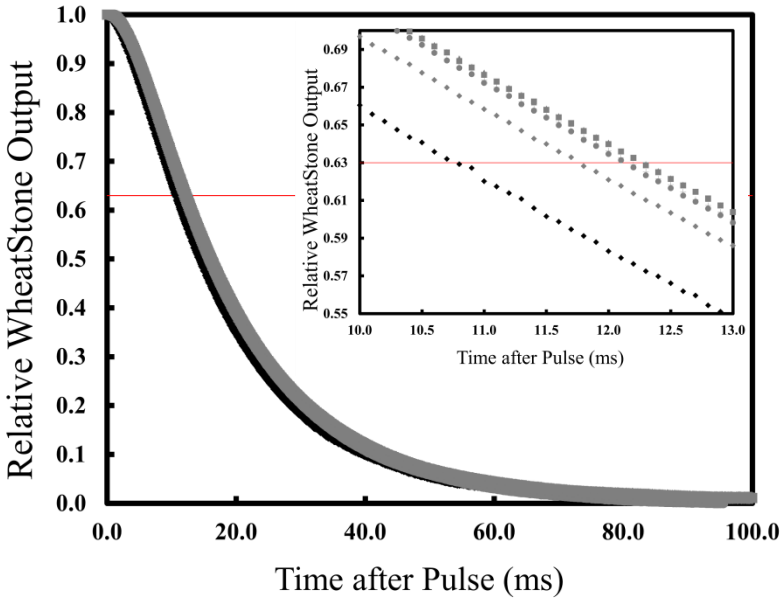

Figure 6.17 Measurements of the thermal decay time for different pulse lengths in air. Main picture shows the exponential decay for all pulse lengths. The 10 ms pulse is depicted in black and is distinct from the 50 ms, 100 ms, 300 ms, 500 ms, and 700 ms pulses (grey) which are indistinguishable at this scale. Inset shows the same graph at a higher resolution. The thermal decay time (τ) can be found as the point at which each curve crosses the line. At this resolution, grey diamonds (50 ms pulse), circles (700 ms) and squares (500 ms) are distinct. Red horizontal line denotes the point at which the signal has reduced to 63% of its maximum initial value.

The thermal decay time does not increase linearly with the $\sqrt{pulse\ duration}$ as claimed in [185]. In fact, the experimental data presented in [185] do not support this either as it is only linear with $\sqrt{pulse\ duration}$ over a limited range where the pulse duration is short. Instead the data follow a sigmoidal function with ln(pulse duration) both in [185] and in *figure 6.18*, which shows the results from the present study. A full theoretical account of these results would require simulation of the build-up of heat around the cantilever during the actuation pulse (inhomogeneous form of the heat equation) coupled to the cooling of the cooling of the beam following the actuation and would be a useful exercise in a theoretical study.

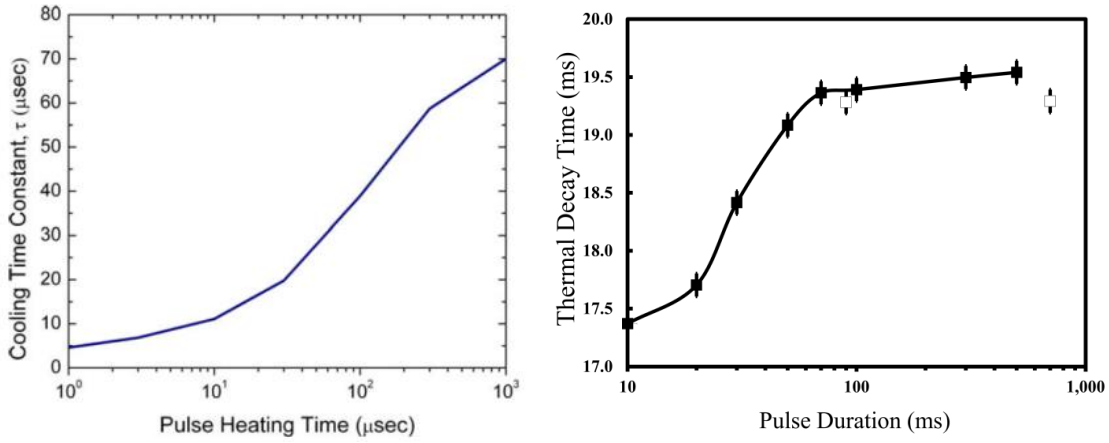

Figure 6.18 Comparison of cooling time for different pulse lengths, reproduced with permission [185] *(left). Sigmoidal relationship between the pulse duration and the thermal decay time from experimental data in this study (right). Two data points are slightly off-trend, and these are plotted as empty squares.*

It is notable that the thermal decay time varies by only a relatively small amount: around 10%; when the pulse duration varies by two orders of magnitude. In contrast, the thermal decay time presented in [185] doubles when the pulse duration varies by two orders of magnitude. The reason for this difference is that the absolute temperature increases of the microcantilever beam in this study are up to 10 °C, whereas in [185], temperature increases up to 400 °C are recorded.

Note that ideally this experiment would have been performed using thermal imaging data instead of the Wheatstone bridge output signal as the raw data, because the thermal imaging data is not affected by thermal crosstalk between the microcantilevers. However, the relatively poor temporal resolution of the thermal imaging equipment meant that it would be difficult to observe the small changes in thermal decay time using thermal imaging.

6.4 Thermal Conductivity Calibration

As a final characterisation, the response of the TD microcantilever sensors in liquids with varying thermal properties was measured. Because thermal conduction to the

surrounding liquid is one mechanism of heat loss from the cantilever beam, and because the signal from the sensor within that beam is temperature dependent, a simple hypothesis may be made that if the thermal conductivity of the liquid is higher, the time taken for the beam to reach thermal equilibrium will be longer, the equilibrium or maximum signal will be lower, and the signal will decrease more slowly. As discussed within the context of the literature and theory of *chapter 5*, it is difficult to estimate how much effect a change in liquid thermal conductivity will have, since there are competing thermal loss mechanisms through the beam to the substrate. These characterisations are therefore exploratory in nature.

6.4.1 Experimental Set Up

Silicone oils (Polydimethylsiloxane, of various average polymer chain lengths) were purchased from Clearco Products, USA for use as calibration standards for thermal conductivity measurements. They were chosen because they were supplied with a data sheet detailing important physical properties including viscosity, specific heat, coefficient of thermal expansion and thermal conductivity at 25 ºC. These properties are summarised in *table 6.4*.

Product	**Kinematic Viscosity (cSt)**	**Specific Gravity**	**Specific Heat@25°C (Cal/g/°C)**	**Thermal Conductivity @25°C ($Wm^{-1}K^{-1}$)**	**Surface Tension (mN/m)**	**Molecular Weight (Da)**
PSF-0.65	0.65	0.761	0.410	0.1008	15.9	162
PSF-1	1.0	0.818	0.410	0.1008	17.4	237
PSF-5	5.0	0.918	0.39	0.1176	19.7	770
PSF-10	10	0.935	0.36	0.1344	20.1	1250
PSF-20	20	0.950	0.36	0.1428	20.6	2000
PSF-100	100	0.966	0.36	0.1554	20.9	5970
PSF-200	200	0.968	0.36	0.1554	21.0	9430
PSF-350	350	0.970	0.36	0.1554	21.1	13650

Table 6.4 Properties of silicone oils as detailed in the datasheet from Clearco Products, USA.

Due to the extremely low surface tension of silicone oils compared to water (72 mN/m); the liquid readily wets the surface of the chip. Additional containment was needed around the cantilever sensors to make sure they remain fully immersed throughout the test. This was achieved via adhesion of a small well to the surface of the chip using a two part epoxy *(figure 6.19).*

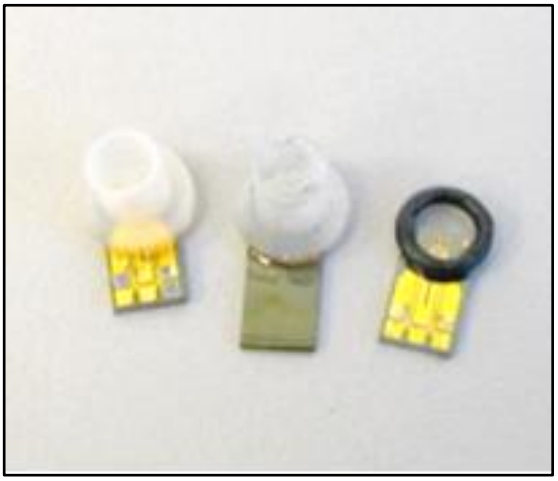

Figure 6.19 Three designs for containment of the silicone oils on the microcantilever sensor. Damaged chips were used to try out the different sample containment techniques. Left: sample fluidic well; Centre: Fluidic well mounted on top of an O-ring; Right: O-ring. It was found that the fluid well without the O-ring (left) was the best method as it incurred least losses in assembly.

Each well holds 30 µl of liquid so this volume was used as a fixed sample size. This is somewhat larger than the volume of 5 - 10 µl that would be required for a clinical application, but it is necessary to fill the fluidic wells for two reasons: a very small volume may not fully immerse the cantilevers due to the diameter of the well; and the larger the test volume, the smaller the influence of the finite heat capacity of the test liquid on the result. The 'reverse pipetting' technique was used throughout testing to prevent air bubbles from entering the small sample well.

6.4.2 Preliminary Experiment 1: Effect of Viscosity

Before using the silicone oils to characterise the TD cantilever response to liquids based on their thermal conductivity, it was first necessary to be sure that the sensor is

insensitive to viscosity because it was not possible to choose test liquids with uniform viscosity *and* varying thermal properties. To do this, the responses of both TD and MD chips immersed in silicone oils of the same thermal conductivity but different viscosity were compared under the hypothesis that there would be a difference in the MD signal between the two fluids that is greater than the chip-to-chip variation within the same fluid, while the response from the TD chips would be indistinguishable between the two fluids.

The silicones chosen for this part of the characterisation were PSF-0.65cP and PSF-1cP. An alternative test pair (PSF-200cP and PSF-350cP) was also tried, but without success, because of the limited sensitivity of the MD sensors to changes in viscosity at high viscosity. The experiments were performed using a square pulse 800 ms in duration, with a power of 20 mW, and at a frequency of 0.5 Hz. A sampling rate of 5000 Hz was used to acquire data. The bridge completion resistor (bridge excitation) was 364.80 Ω (0.65V) when testing the TD design, and 7.688 kΩ (2.5V) when testing the MD.

The results shown in *figure 6.20* are from three TD chips in 0.65 cP silicone oil (black), three TD chips in 1 cP silicone oil (blue), three MD chips in 0.65 cP silicone oil (green), and two MD chips in 1 cP silicone oil (red). *Figure 6.20* is scaled to view only the very start of the pulse, because as we have already seen, the mechanical signal operates on the time scale of a few milliseconds. The mechanical signal clearly differs between the two liquids whereas the thermal signal is identical.

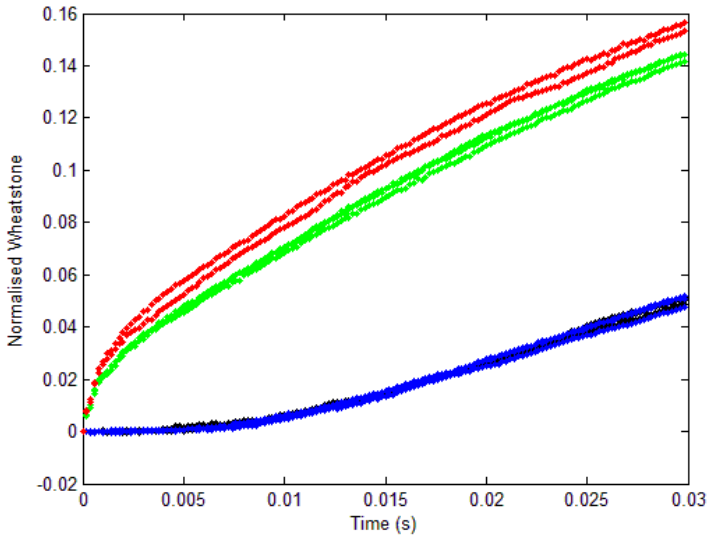

Figure 6.20 Comparison of thermal and mechanical sensors in liquids where only viscosity changes between measurements. 3 × TD chips in 0.65cP silicone oil (black), 3 × TD chips in 1cP silicone oil (blue), 3 × MD chips in 0.65cP silicone oil (green), and 2 × MD chips in 1cP silicone oil (red).

The results in *figure 6.20* are slightly unexpected because although the MD chips distinguish between different viscosities, it was expected that the rise time in the 0.65 cP liquid to be faster than in 1 cP. However it appears that the 1 cP liquid offered less resistance to motion of the cantilever. It is possible that difference in viscosity is too small to be accurately measured using the MD sensor.

To verify that the difference in mechanical signal is real, Microvisk SmartStrips were also tested using the same test liquids. The experimental set up used was the same as described in *section 4.5* (Microsystems set up). Results from the ac signal component *(figure 6.21)* show that the signal generated in the 1 cP liquid is more damped than the 0.65 cP liquid.

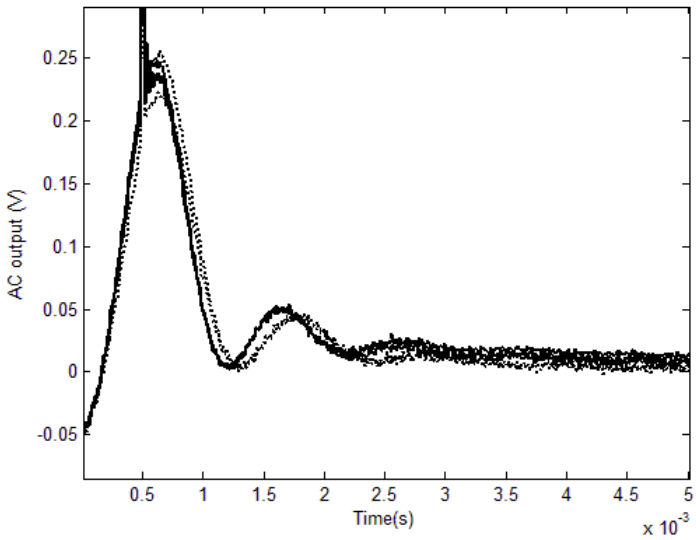

Figure 6.21 AC signal from 3× SmartStrips tested in 0.65 cP silicone oil (solid lines) and 1 cP silicone oil (dotted lines).

6.4.3 Preliminary Experiment 2: Determining suitable pulse parameters

The criteria for choosing test pulses that may be useful for measuring the heat flow out of the cantilever in liquids are:

1. Need to obtain sufficient signal to distinguish from the noise but not so much that the sensor is overheated and permanently deformed.
2. It would be useful to look at a pulse the same length as that used to actuate Microvisk sensors. This would tell us more about the "thermal background" of the Microvisk DC signal. However a thermal signal would approach equilibrium given a sufficiently long pulse. Samples of different thermal conductivity should be distinguishable based on time taken to reach thermal equilibrium. The higher the thermal conductivity of the sample, the longer it would take to reach equilibrium, but the quicker the beam would lose heat after the pulse.
3. The pulse frequency should be sufficiently low that the signal returns to equilibrium between pulses to be sure that heat does not build in the system and change the physical properties of the sample.
4. Data collection rate must be sufficiently fast to obtain good resolution during actuation, without requiring an excessive amount of data to be captured.

In order to determine the ideal pulse length to reach a 'quasi-equilibrium', i.e. obtain a flat response profile during the actuation pulse, a series of pulses from 50 ms to 1.2 s were tested with 30 µl of PSF-1 (0.1008$Wm^{-1}K^{-1}$) as the test liquid. The average raw signals (n = 5) that has been normalised by subtraction of the mean of the final 50 ms of data are plotted in *figure 6.22*.

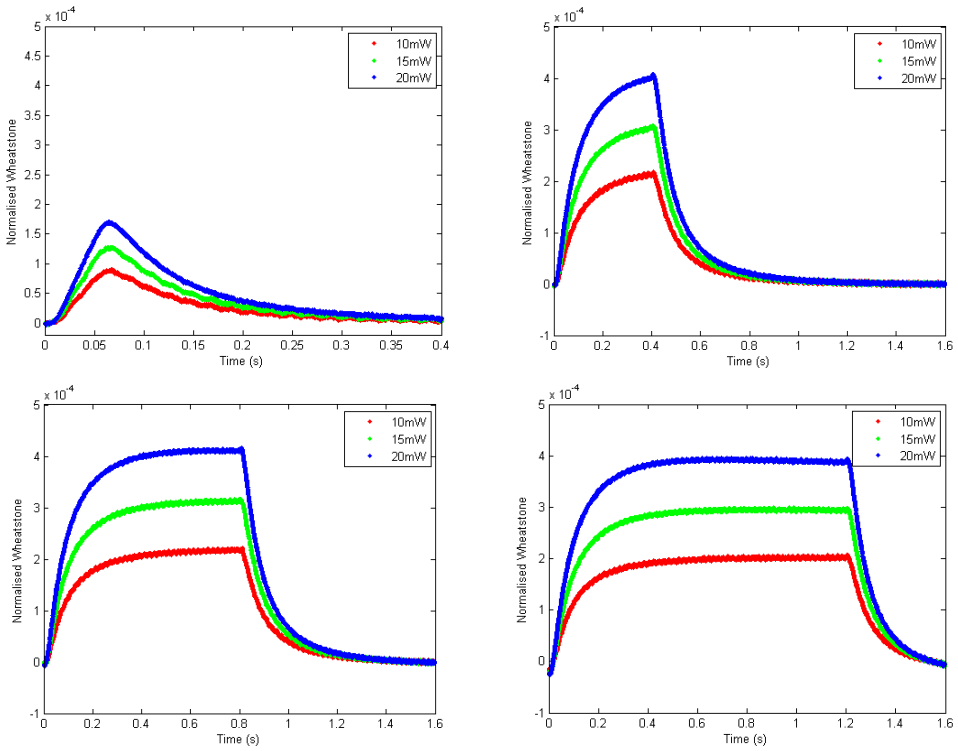

Figure 6.22 Trial pulse widths for a long pulse to bring cantilever and surrounding fluid into quasi-equilibrium. Pulse widths are 50ms (top left), 400ms (top right), 800ms (bottom left) and 1200ms (bottom right). Pulse powers are 10mW (red), 15mW (green) and 20mW (blue).

At the highest pulse power tested (20 mW), the signal approaches equilibrium as the pulse length is increased. For a pulse length of 1200 ms, the equilibrium has been reached. However after only 400 ms the position of the equilibrium can be extrapolated. A pulse width of 400 ms at 20mW was selected as the longest pulse length, as this is sufficiently long to indicate the equilibrium position whilst enabling a duty cycle of less than 50% on for a pulse rate of 1 Hz.

The 50 ms pulse width is also interesting because the Wheatstone signal increases at a near constant rate during the pulse before peaking just after the actuation pulse has

finished. This is very similar in form to the pulse encountered in *chapter 3* where we were looking at the mechanical signal, but the thermal signal occurs over a much longer time scale. For this reason, a pulse of 50 ms, 20 mW was also included in the testing.

Another series of actuation pulses ranging from 0.5 ms to 50 ms were tested to observe the change in pulse shape. Two relatively low powers (15 mW and 20 mW) were tested. The test liquid was PSF-1 ($0.1008 Wm^{-1}K^{-1}$). This quick test shows that 20 mW would be insufficient energy to achieve reasonable signal to noise for the shortest 0.5 ms pulse (*figure 6.23*). The aim for the shortest pulse is to be as close as possible to the pulse delivered to the MV sensor in the SmartStrip (approximately 130 mW). The data plotted in *figure 6.23* are the raw signal (mean of 5) that has been normalised by subtraction of the last mean of the final 25 ms of data. Due to the high level of interference in the raw signal, it was not possible to use such a low power setting. Instead, 200 mW was used, as this the absolute minimum power to achieve 3× signal to noise. *Table 6.5* shows the pulse conditions that were selected for the final experiment.

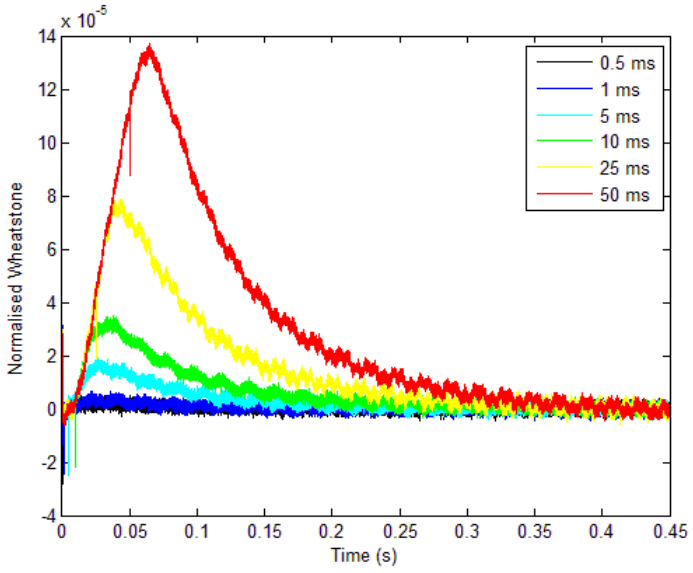

Figure 6.23 20 mW pulse with various pulse widths for actuations in PSF-1 silicone oil. Poor signal to noise for 0.5 ms pulse with 20 mW actuation means that a higher power must be used for this pulse than for the 50 ms or 400 ms pulses.

Pulse Width (ms)	Pulse Power (mW)	Pulse Energy (µJ)	Pulse Period (s)	Sampling Rate (kS/s)	Number Samples per file	Number pulses
0.5	200	100	0.5	No Data Acquired	6000	50
0.5	200	100	0.5	20	6000	42
50	20	1000	1		16000	35
400	20	8000	1		16000	35
ADD LIQUID SAMPLE						
0.5	200	100	0.5	20	6000	42
50	20	1000	1		16000	35
400	20	8000	1		16000	35

Table 6.5 Pulse Conditions for silicone oil measurements

As detailed in *table 6.5*, each microcantilever chip was actuated 50 times before data acquisition started. Data from three pulse types was acquired in air before the LabView data acquisition prompts the user to add the liquid sample. The actuation continues while the user adds the liquid sample, but data acquisition does not resume until the user notifies the program that liquid has been added. Data for the same three pulse types are then acquired in the liquid sample.

6.4.4 Data Analysis Methods

To simplify data analysis, four salient features of the Wheatstone bridge output voltage signal were identified: the gradient during the actuation pulse; the maximum voltage; time of the maximum voltage; and the thermal time constant for cooling of the beam. Given that in *section 6.2*, the piezoresistive component of the sensor was found to be negligible, and following from the results of Preliminary Experiment 2 *(section 6.4.3)*; it is assumed that the viscosity of the surrounding fluid does not have a significant impact on any part of the signal.

The process used to analyse the raw data is outlined in *figure 6.24*. The segmented gradient analysis was conducted using Matlab script and the transient hot wire and thermal decay time analyses were conducted using Microsoft Excel 2010 spreadsheets.

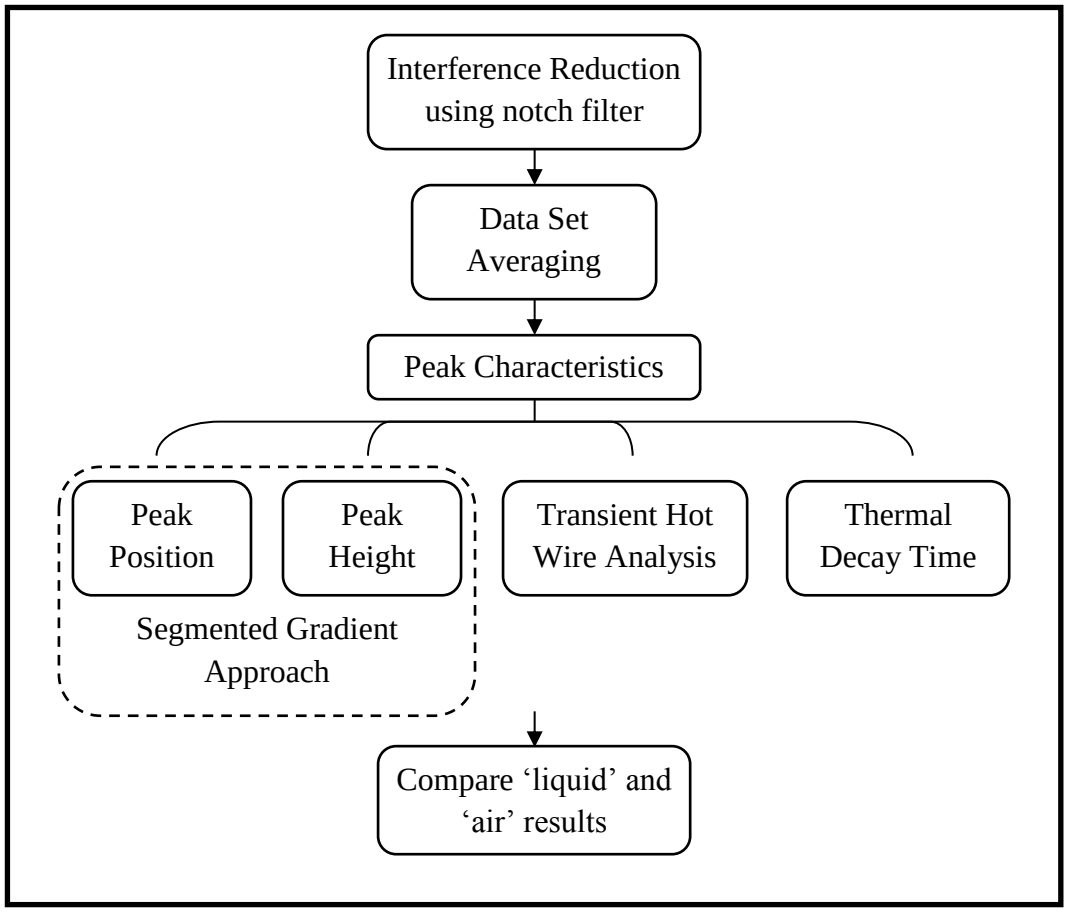

Figure 6.24 Schematic showing the approach to data analysis.

Interference Reduction

Efforts were made to reduce the noise and electrical interference in the signal before performing the experiment (insulating all cables, grounding the whole set up, operation away from strong electromagnetic interference sources such as fridges and heaters), yet there remains a significant amount of electrical interference at 50 Hz, and 150 Hz in the data. Some of this was shown to be due to interference from the sub-miniature heater used in the experiment. Placing a piece of copper tape over the heater (and re-calibrating the temperature) mitigated this source but it was not possible to completely smooth out the signal. The interference and noise affect the output of subsequent steps in the data analysis program, particularly the segmented gradient approach. This is because the length of each interference cycle is approximately 0.025 seconds, and when using the segmented gradient approach, each segment must incorporate at least one full interference cycle in order that the gradient of that segment is representative of the data. Thus the interference places a limit on the accuracy with which the peak position and peak height can be identified.

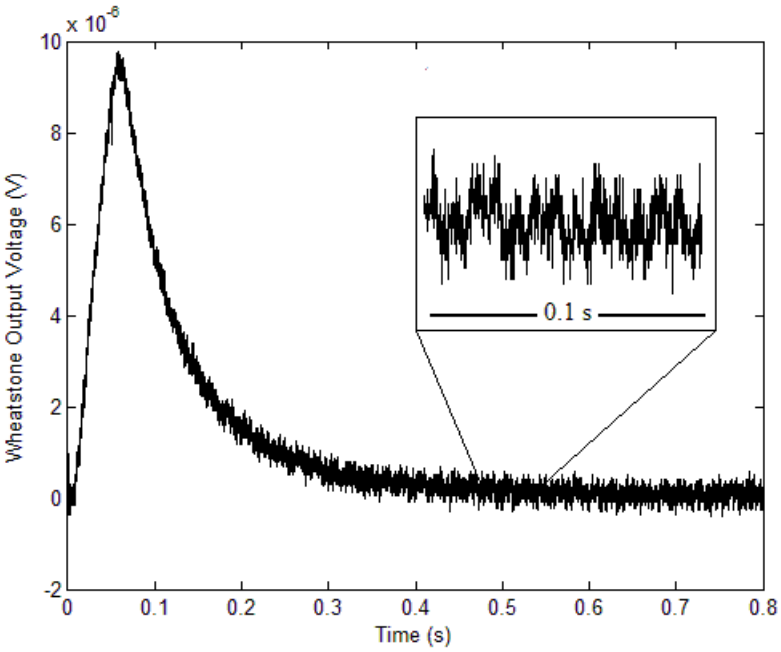

Figure 6.25 Example of the interference in the TD microcantilever sensor signal. The interference can clearly be seen (inset).

Data Averaging

Each set of data (i.e. measurements taken on one chip for one of the three pulse durations, in either silicone oil or in air) consists of the Wheatstone bridge output from the sensor for at least 35 actuation pulses in a single pulse train. Obtaining a single averaged pulse profile from all the pulses in the pulse train reduces the amount of data for further analysis, and averages out the noise and any residual interference not removed by the notch filter. Before the data were averaged, a sample of the raw data was inspected visually for signs of drift over the repeated pulse train. It was found that only the voltage offset trended over the pulse train: the pulse responses did not change shape. The magnitude of the offset was recorded and each pulse was normalised to the average signal over the last 25 ms. The average of each set of normalised results was used for further analysis of the peak characteristics.

Segmented gradient

To accurately identify the maximum of the average response voltage and the time at which this occurs, the averaged data was split into segments of sufficiently short duration to each approximate to a straight line. The gradient of each segment was calculated from a linear best fit using the method of least squares. The gradient values

were then plotted against time values corresponding to the midpoint of each segment in a 'gradient plot'. The time of the maximum of the average response was found by the zero intercept of a linear fit to the gradient data between the end of the actuation pulse and the time of minimum (most negative) gradient. The value for the maximum of the average response could then be found from the average response data. Because the averaged data contains spikes at the beginning and end of the heater actuation, gradient segments were only calculated on data acquired after the actuation.

The duration used for the segments was chosen carefully to avoid errors in identification of the peak due to noise or residual interference (segment too short) without relying too heavily on interpolation to identify the point of zero gradients. It was found that a segment length of 2.5 ms was a good compromise to smooth out the remaining noise whilst maintaining accuracy (*figure 6.26).*

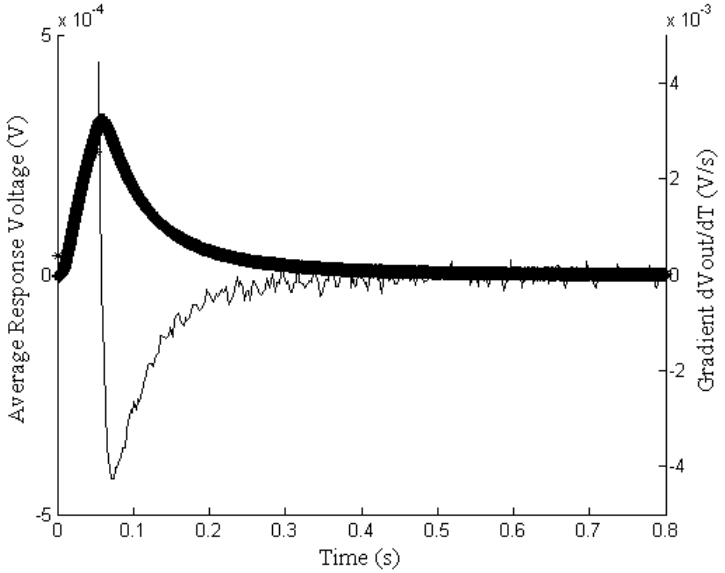

Figure 6.26 Example result set for 50 ms pulse showing mean pulse profile (thick black line) and calculated pulse gradient (thin black line).

Transient Hot Wire Analysis

The microcantilever sensor used in this work is of a very different design to a traditional hot wire sensor. In the hot wire technique, the temperature is measured both on the central heating element and on the outer cylinder: in the cantilever there is only one temperature sensing element along the centre of the beam, and the geometry is not cylindrical. In addition, the motion of the beam is a significant departure from the hot

wire approach. Therefore the full equation for traditional hot wire analysis as defined in *chapter 5* could not be used to verify the thermal conductivity of the test liquid. However because the microcantilever TD sensor works on a similar principle to the hot wire sensor, it was supposed that any region of the average response voltage that was linear with the natural log of time might correspond to the thermal conductivity of the materials for all thermal pathways between the heater and sensor tracks within the cantilever, including the test fluid. In the analysis of traditional hot wire pulse profiles, the analysis is conducted when a constant power is being dissipated by the hot wire. Therefore, for the two longest pulse durations (50 ms and 400 ms), hot wire analysis is restricted to the data acquired during the actuation pulse. In data acquired from 0.5 ms actuation pulses, the signal does not respond during the pulse, but peaks approximately 7 ms later; therefore hot wire analysis is not presented for data generated using this pulse.

In each case, data analysis was conducted using Microsoft Excel as follows. The linear region of the average response voltage data *vs*. ln(time) was located and a linear fit obtained using the least squares method. The correlation coefficient (R^2) was used to judge whether the linear region had been chosen correctly, but an assessment of the residuals was also needed in some cases. For example, an R^2 value may be low in comparison to the R^2 values from the same cantilever-type and fluid combination because the data is actually a shallow curve (in which case the length of data selected for a linear fit should be reduced), or because there is more noise in the data, in which case the region selected for a linear fit may be representative. For 50 ms pulses obtained in liquid, a typical R^2 value is 0.9990 with a linear region of 400 data points, and for 400 ms pulses obtained in liquid, a typical R^2 value is 0.9995 with a linear region of 800 data points.

Thermal Decay Time

Two different methods were applied to try and extract the thermal time constant from the 'cooling down' part of the average signal voltage.

- An exponential fit to the average signal voltage between the time of the most negative gradient (found using the segmented gradient approach) and the end of acquisition. A single exponential term $V = V_0 e^{-t/\tau}$ did not always provide a good fit for the average signal voltage curves using a non-linear least squares

method. Various methods were tried to improve the fit, such as choosing realistic start values and limits for V_0 and $1/\tau$, trying different algorithms (Trust Region was generally found to work better than Levenberg-Marquardt) and using a two term exponential; but these were met with only limited success. There seemed to be little pattern to quality of fit using this approach. Values for τ generated using this approach are therefore not reported in the results section. It is thought that the exponential fitting did not work well because in reality multiple exponential terms would be needed to describe all the modes by which heat is transferred away from the sensor: through the gold heater and sensor tracks; through the polyimide in the heater and sensor arms to the substrate; through the polyimide to the liquid on the top and bottom surfaces of the beam. The six modes by which heat is transferred away from the sensor just described would generate 12 fitting parameters, and this is too many from which to extract meaningful data.

- A first order approximation to the overall rate of heat loss was made by a direct measurement of the time taken for the average signal voltage to decay by a factor of $1/e$ from its maximum value.

Comparison to Air Measurements

The segmented gradient, transient hot wire, and thermal decay analyses were conducted on both the data acquired while the cantilever sensor chip was actuated in air and when it was immersed in liquid. The peak characteristics in liquid were then divided by the same measurement in air for each chip in order to reduce the impact of chip-to-chip variability.

6.4.5 Results Part I: Segmented Gradient

The time taken to reach the maximum signal following an actuation pulse in liquid was determined as a fraction of the time taken to reach the maximum signal following an actuation pulse in air and will henceforth be referred to as the fractional peak time (FPT). Similarly, the maximum value from the Wheatstone bridge output in liquid divided by the maximum value from the Wheatstone bridge output in air is referred to as the fractional peak height (FPH). Of all the pulse characteristics analysed, the pulse height is the most directly related to the maximum temperature reached by the sensor following actuation as shown by the thermal imaging measurements in *section 6.3.2*.

0.5 ms pulse duration

It should be noted that for the 0.5 ms pulse, the actuation is over before any significant change in signal occurs on the cantilever sensor. In this case, the time to reach maximum signal can be considered as the modal time taken for heat to be conveyed (conducted, convected, and radiated over a continuum of available pathways) from the heater to the sensor, and the shape of the peak can be regarded as the distribution of these times, analogous to the point spread function used to describe optical systems. On average, the time taken to reach the maximum signal was 6.5 ± 0.4 ms in air.

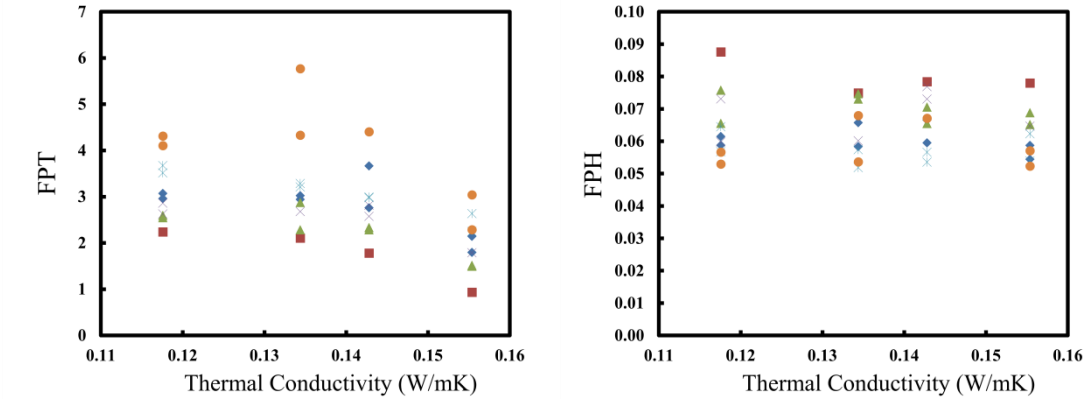

Figure 6.27 Individual value plot of fractional peak time (FPT, left), and fractional peak height (FPH, right) as a function of liquid thermal conductivity for the 0.5 ms pulse duration. The different chip designs are denoted thus: red square = TD 20; green triangle = TD 30; purple cross = TD 40; blue diamond = TD EH; cyan cross = TD 50; orange circles = TD 60.

The following points may be noted from *figure 6.27*:

1. The FPT decreases with increasing thermal conductivity, indicating that conduction between the heater and the sensor tracks via the intervening liquid is a significant thermal pathway. It also suggests that convection of the liquid is not significant, i.e. a low Rayleigh number. The liquids with higher thermal conductivity also had much higher viscosity and would therefore be expected to offer much slower heat transport if convection was the primary means of heat flow in the liquids.
2. All values of the FPT are greater than 1, indicating that the thermal conduction through the liquid is slower than the thermal conduction through air. The

thermal conductivity of air is 0.0257 W/mK at 20 °C, about 5 times lower than that of the silicone oils, so it might be expected that conduction would take longer in air. However, the thermal diffusivity of air is 1.9×10^{-5} m^2/s, compared to 7.1×10^{-8} m^2/s for PSF-5 silicone oil, primarily due to the higher density of the liquid. Therefore a greater amount of heat is dissipated in the liquid and does not reach the sensor, as confirmed by the fractional peak height (FPH), which is less than 0.1 in all cases.

3. As the gap between heater and sensor legs of the cantilever gets wider, the FPT increases and the FPH decreases because of the increased overall distance between heater and sensor.

Although some of the chip-chip variation is removed when taking into account the different chip designs, there is still significant variability, particularly for the fractional peak height. Regression analysis of the plots in *figure 6.27* is shown in *table 6.6.* Results where the slope of the fractional peak time or fractional peak height changes significantly with thermal conductivity are highlighted.

Parameter	Chip Design	Slope	95% Confidence Interval		R^2	F-val
			Low	High		
Fractional Peak Height	EH	-0.07	-0.34	0.19	0.07	0.44
	20	-0.24	-1.00	0.52	0.48	1.83
	30	-0.12	-0.39	0.15	0.16	1.16
	40	0.09	-0.58	0.75	0.03	0.14
	50	-0.07	-0.36	0.21	0.06	0.39
	60	0.03	-0.45	0.51	0.00	0.02
Fractional Peak Time	EH	-23.20	-55.14	8.74	0.34	3.16
	20	-33.46	-80.89	13.97	0.82	9.21
	30	-27.03	-47.14	-6.91	0.64	10.81
	40	-17.52	-44.06	9.02	0.46	3.36
	50	-30.11	-39.86	-20.35	0.90	57.06
	60	-40.85	-106.96	25.26	0.34	2.52

Table 6.6 Regression analysis results for changes in fractional peak height and fractional peak time with thermal conductivity for the 0.5 ms pulse duration. Highlighted cells indicate a statistically significant variation in slope indicating confidence that the parameter does vary with thermal conductivity at the 95% confidence level.

50 ms pulse duration

In the longer pulses, heat continues to be transferred out of the heater long after the 6 ms it takes to reach the sensor. Heat can therefore build on the sensor until the actuation is turned off. In air, the maximum values reached on the 50 ms pulse are similar to the maximum values reached on the 400 ms pulse (0.0026 ± 0.0005 and 0.0032 ± 0.0007 respectively) indicating that after 50 ms, the sensor track is approaching thermal saturation. In the 50 ms pulse in liquid, it is noted that for the majority of beams, the peak overshoots the pulse – i.e. there is a net inflow of heat onto the sensor for a few ms after the actuator is turned off indicating that thermal saturation of the sensor beam had not been achieved during the pulse because the liquid has a greater heat capacity than air does. Note that the difference between the liquid and the air results is not as pronounced as in the 0.5 ms pulses: for 50 ms pulses the sensor response maximum is at most 30% later in liquid than in air whereas for a 0.5 ms pulse that figure was approximately 500%. This is because the time taken when the peak overshoots the actuation pulse (3-10 ms depending on chip design) is very short compared to the duration of the pulse.

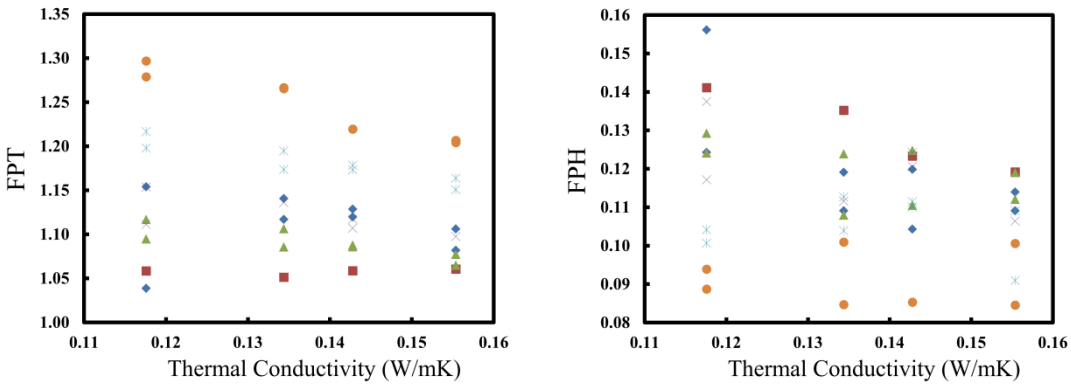

Figure 6.28 Individual value plot of fractional peak time (FPT, left), and fractional peak height (FPH, right) as a function of liquid thermal conductivity for the 50 ms pulse duration. The different chip designs are denoted thus: red square = TD 20; green triangle = TD 30; purple cross = TD 40; blue diamond = TD EH; cyan cross = TD 50; orange circles = TD 60.

The following points may be noted from *figure 6.28:*

1. As the gap between heater and sensor legs of the cantilever gets wider, the FPT increases because of the increased overall distance between heater and sensor.
2. As the gap between heater and sensor legs of the cantilever is increased, the thermal conductivity of the liquid has a greater effect on FPT and a smaller effect on the FPH. The effect is not noticeable on the shorter 0.5 ms pulse where the gradients for each subset on *figure 6.28* are similar for every chip design.

An atypical result can be noticed in *figure 6.28*: the result for TD-18 tested at PSF-5 is out of trend with the other results from the TD sensors. *Figure 6.29* shows the average sensor output from two the chips of the TD-EH design actuated in PSF-5 silicone oil.

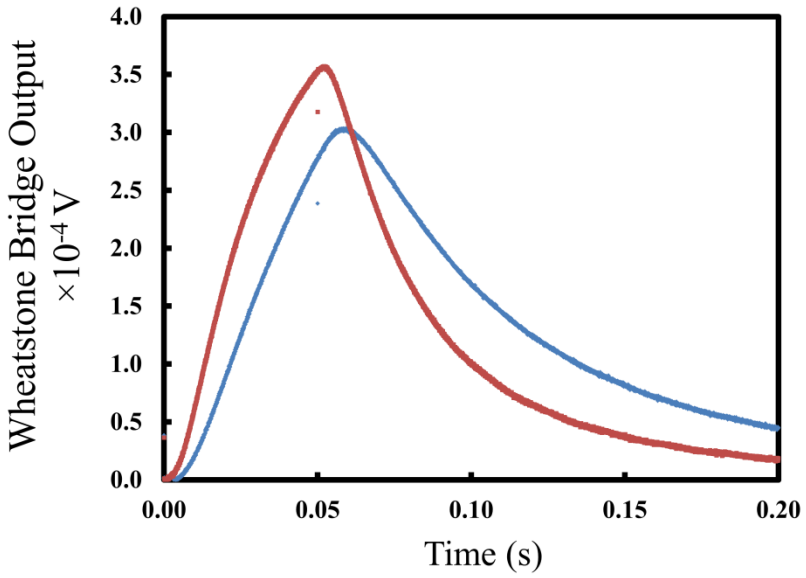

Figure 6.29 Average Wheatstone bridge output showing the sensor response to a 50 ms actuation pulse in liquid for the atypical result, chip 18-EH (red), and, for comparison chip 02-EH (blue).

From *figure 6.29* it can be seen that the signal that chip 18-EH is approaching saturation by the decrease in gradient after 20 ms, whereas the signal from 02-EH increases steadily.

Regression analysis of the plots in *figure 6.28* (including the outlier) is shown in *table 6.7.* Results where the slope of the fractional peak time or fractional peak height changes significantly with thermal conductivity are highlighted.

Parameter	Chip Design	Slope	95% Confidence Interval		R2	F-val
			Low	High		
Fractional Peak Height	EH	-0.77	-1.56	0.03	0.48	5.53
	20	-0.62	-1.16	-0.08	0.92	24.08
	30	-0.28	-0.73	0.17	0.28	2.30
	40	-0.43	-1.23	0.37	0.36	2.22
	50	-0.02	-0.51	0.46	0.00	0.01
	60	0.00	-0.53	0.54	0.00	0.00
Fractional Peak Time	EH	0.00	-2.47	2.47	0.00	0.00
	20	0.08	-0.65	0.82	0.11	0.24
	30	-0.91	-1.54	-0.29	0.68	12.74
	40	-0.90	-2.34	0.55	0.43	2.98
	50	-1.31	-1.88	-0.73	0.84	30.75
	60	-2.28	-3.09	-1.47	0.91	52.53

Table 6.7 Regression analysis results for changes in fractional peak height and fractional peak time with thermal conductivity for the 50 ms pulse duration. Highlighted cells indicate a statistically significant variation in slope indicating confidence that the parameter varies with thermal conductivity at the 95% confidence level.

400 ms pulse duration

With the longest pulse duration, 400 ms, the FPT is very close to 1 in all cases. Greater distance between the heater and sensor arms still correlates to higher values of FPT, but the variability is much higher. The trend to decreasing FPT with increasing thermal conductivity is inconsistent.

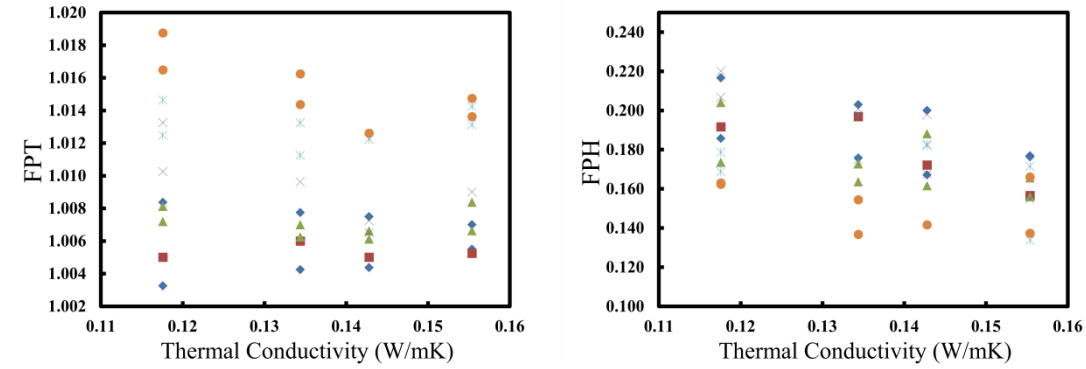

Figure 6.30 Individual value plot of fractional peak time (FPT, left), and fractional peak height (FPH, right) as a function of liquid thermal conductivity for the 400 ms pulse duration. The different chip designs are denoted thus: red square = TD 20; green triangle = TD 30; purple cross = TD 40; blue diamond = TD EH; cyan cross = TD 50; orange circles = TD 60.

The high variability in the results for FPT is at least partly due to the fact that by 400 ms, the beam approaches thermal equilibrium even in fluid; because the peak time in fluid is approximately the same as in air, measurement error in either will affect FPT. Regression analysis of the plots in *figure 6.30* is shown in *table 6.8.* Results where the slope of the fractional peak time or fractional peak height changes significantly with thermal conductivity are highlighted.

Parameter	Chip Design	Slope	95% Confidence Interval		R^2	F-val
			Low	High		
Fractional Peak Height	EH	-0.66	-1.61	0.30	0.32	2.79
	20	-0.99	-2.88	0.90	0.72	5.05
	30	-0.67	-1.52	0.17	0.39	3.83
	40	-1.45	-2.53	-0.36	0.77	13.62
	50	-0.49	-1.65	0.67	0.15	1.08
	60	-0.31	-1.18	0.56	0.14	0.82
Fractional Peak Time	EH	0.01	-0.12	0.14	0.01	0.04
	20	0.00	-0.09	0.09	0.00	0.01
	30	-0.01	-0.06	0.05	0.02	0.14
	40	-0.11	-0.27	0.04	0.51	4.15
	50	0.00	-0.08	0.08	0.00	0.00
	60	-0.10	-0.20	0.00	0.57	6.76

Table 6.8 Regression analysis results for changes in fractional peak height and fractional peak time with thermal conductivity for the 400 ms pulse duration. Highlighted cells indicate a statistically significant variation in slope indicating confidence that the parameter varies with thermal conductivity at the 95% confidence level.

6.4.6 Results Part II: Thermal Decay Time

The thermal decay time in liquid divided by the thermal decay time in air is denoted $F\tau$, the fractional thermal decay time in the following presentation of results and accompanying regression analyses *(table 6.9).*

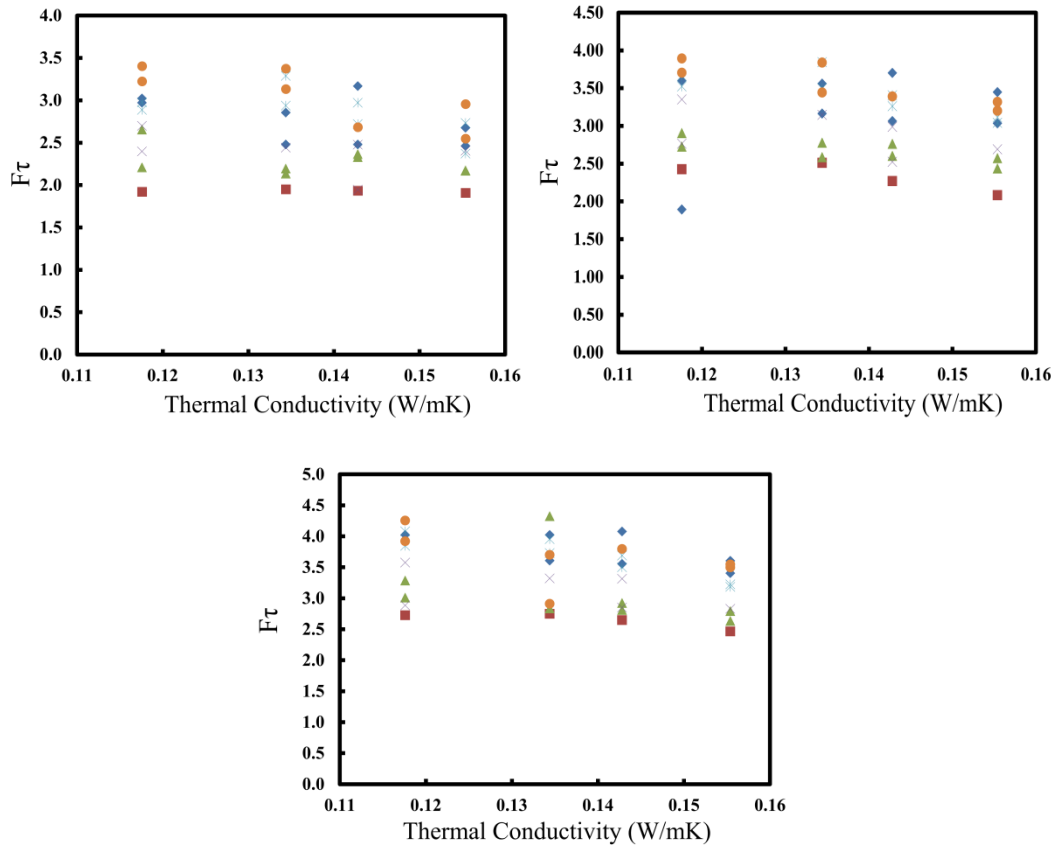

Figure 6.31 Individual value plots of the fractional thermal decay time vs. liquid thermal conductivity. Data from 0.5 ms (top left), 50 ms (top right) and 400 ms (bottom) pulse durations are included with chip designs denoted thus: red = TD 20; green = TD 30; purple = TD 40; blue = TD EH; cyan = TD 50; orange = TD 60.

Parameter	Chip Design	Slope	95% Confidence Interval		R^2	F-val
			Low	High		
0.5 ms pulse Fractional Thermal Decay Time	EH	-9.97	-26.06	6.13	0.28	2.29
	20	-0.37	-3.70	2.96	0.10	0.23
	30	-5.67	-15.94	4.59	0.23	1.83
	40	-6.95	-27.38	13.48	0.18	0.89
	50	-10.33	-25.11	4.44	0.33	2.93
	60	-16.50	-31.71	-1.28	0.61	7.77
50 ms pulse Fractional Thermal Decay Time	EH	13.58	-23.49	50.65	0.12	0.80
	20	-9.61	-31.00	11.79	0.65	3.73
	30	-7.69	-14.22	-1.16	0.58	8.30
	40	-10.65	-34.79	13.49	0.27	1.50
	50	-14.33	-26.06	-2.60	0.60	8.93
	60	-14.70	-24.91	-4.49	0.73	13.69
400 ms pulse Fractional Thermal Decay Time	EH	22.34	-33.43	78.11	0.14	0.96
	20	-6.81	-20.23	6.61	0.70	4.76
	30	-14.06	-47.98	19.87	0.15	1.03
	40	-9.17	-35.19	16.85	0.19	0.96
	50	-19.99	-29.58	-10.41	0.81	26.04
	60	-12.95	-39.61	13.71	0.24	1.56

Table 6.9 Regression analysis results for changes in fractional thermal decay time for all pulse durations. Highlighted cells indicate a statistically significant variation in slope indicating confidence that the parameter does vary with thermal conductivity at the 95% confidence level.

The thermal time constant in liquid has also been appraised without normalising to the thermal time constant in air, in order to see whether the sigmoidal relationship between pulse duration and thermal time constant discussed *section 6.3.2 (figure 6.18)* is also observed with actuation in liquid, shown in *figure 6.32*.

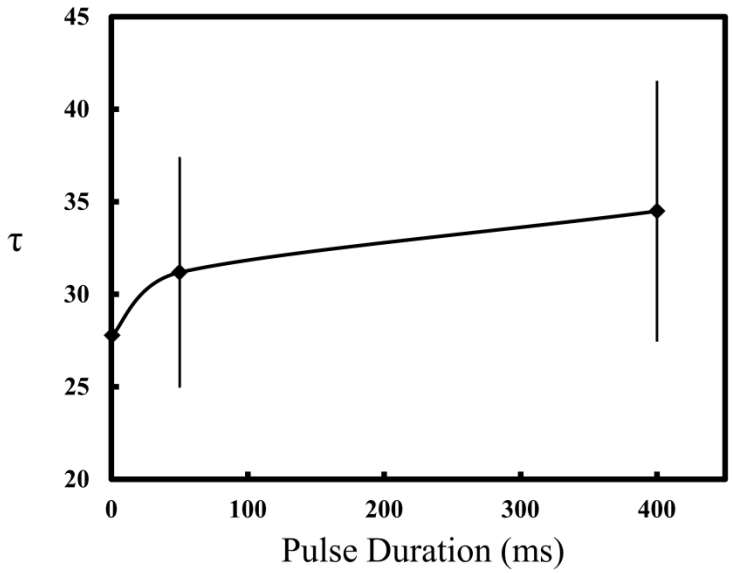

Figure 6.32 Thermal time constant versus pulse duration. Average results for all chips tested in all liquids. Error bars are 1 standard deviation and the line connecting the data points is a smoothed interpolation.

The limited number of data points and variation in the individual results mean that the relationship between pulse duration and τ (if any) cannot be determined with confidence from this data.

6.4.7 Results Part III: Transient Hot Wire Analysis

Both the gradient and intercept from the transient hot wire (THW) analysis were measured in the average signal response to actuation pulses in air and liquid. The results presented in this section are the gradient (or intercept) in liquid divided by the gradient (or intercept) in air and are referred to as FTHWG (fractional transient hot wire gradient) and FTHWI (fractional transient hot wire intercept) respectively. FTHWG is plotted against thermal conductivity of the test liquid, and FTHWI is plotted against the composite parameter of $\ln(D_{Th})/\lambda$ (where thermal diffusivity D_{Th} and thermal conductivity λ are properties for the liquid sample). The composite parameter is chosen to match the fluid property relationship in the ideal transient hot wire intercept given in equation (5.5).

50 ms pulse duration

The gradient of the transient hot wire plot should be inversely proportional to the thermal conductivity of the cantilever environment. The thermal conductivity of air is 0.0257 W/mK at 20 °C, about 5 times lower than that of the silicone oils, and would therefore be expected to have a transient hot wire gradient five times as great. *Figure 6.33* shows that the transient hot wire gradient in liquid is approximately 15 – 20% of the transient hot wire gradient in air and gives confidence that the sensor is functioning in a similar manner to a transient hot wire sensor. Furthermore, as the thermal conductivity of the liquid increases, the FTHWG decreases slightly, though the chip-to-chip variability is so great that it would not be possible to make absolute measurements of thermal conductivity using this technique.

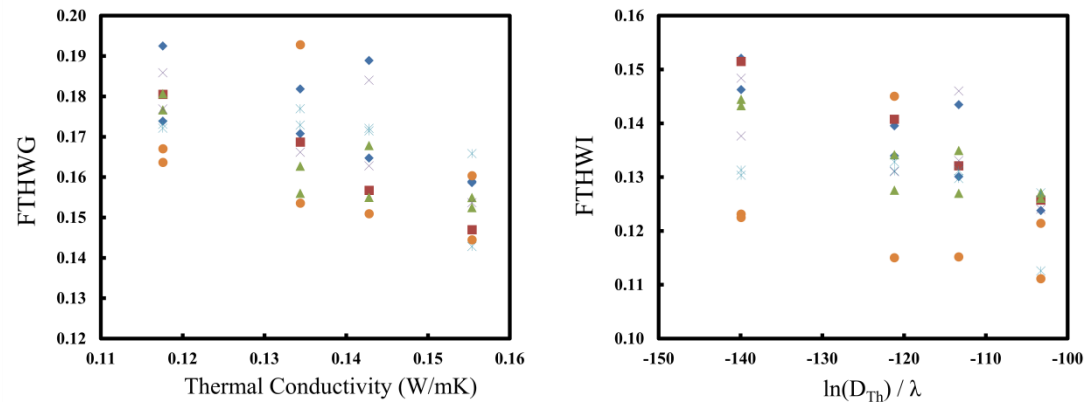

Figure 6.33 Individual value plots of the fractional THW gradient (left) and intercept (right) plotted against liquid thermal conductivity and a function of thermal conductivity and thermal diffusivity, for 50 ms pulse durations. The different chip designs are denoted thus: red square = TD 20; green triangle = TD 30; purple cross = TD 40; blue diamond = TD EH; cyan cross = TD 50; orange circles = TD 60.

The intercept of the transient hot wire plot should be inversely proportional to the thermal conductivity of the cantilever environment, and also proportional to $\ln(D_{Th})$, where D_{Th} is the thermal diffusivity of the cantilever environment. A trend in the data is observed that as the composite parameter $\ln(D_{Th})/\lambda$ increases, FTHWI decreases, but again the chip-to-chip variability makes it difficult to quantify the result.

400 ms pulse duration

The individual value plots for FTHWG and FTHWI for 400 ms pulses *(figure 6.34)* are somewhat similar to those obtained for the 50 ms pulses and discussed in the previous section. This is not surprising, given the findings from the trial of different pulse widths discussed in the Preliminary Experiment 2 of this section *(figure 6.23)* where it was observed that increasing the pulse length between 50 and 200 ms merely prolongs the signal as it tends towards equilibrium.

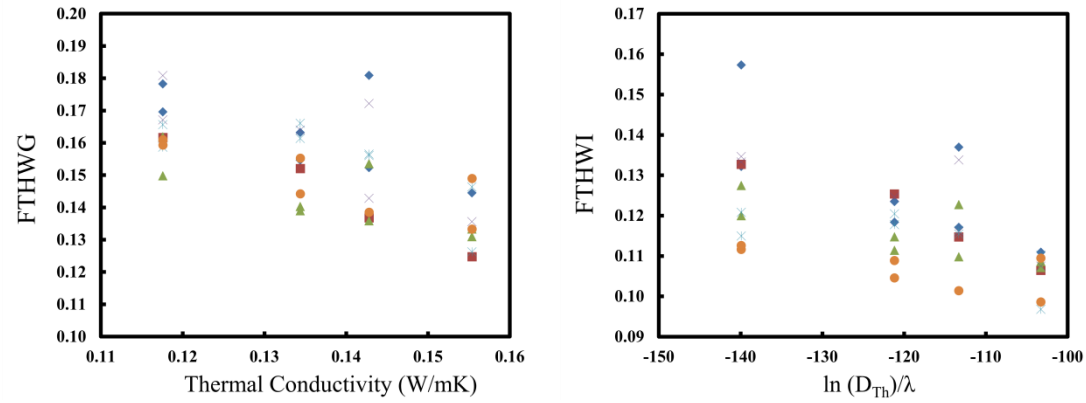

Figure 6.34 Individual value plots of the fractional THW gradient (left) and intercept (right) plotted against liquid thermal conductivity and a function of thermal conductivity and thermal diffusivity, for 400 ms pulse durations. The different chip designs are denoted thus: red square = TD 20; green triangle = TD 30; purple cross = TD 40; blue diamond = TD EH; cyan cross = TD 50; orange circles = TD 60.

The results from linear regression analysis of the graphs presented in figure 6.33 and 6.34 are shown below in *table 6.10.*

Parameter	Chip Design	Slope	95% Confidence Interval		R^2	F-val
			Low	High		
50 ms pulse Fractional Transient Hot Wire Gradient	EH	-0.59	-1.25	0.06	0.45	4.88
	20	-0.91	-1.27	-0.55	0.98	120.24
	30	-0.63	-1.00	-0.26	0.74	17.01
	40	-0.59	-1.43	0.25	0.49	3.83
	50	-0.45	-1.03	0.13	0.37	3.57
	60	-0.41	-1.46	0.64	0.17	1.00
400 ms pulse Fractional Transient Hot Wire Gradient	EH	-0.61	-1.51	0.29	0.38	3.03
	20	-1.01	-1.66	-0.35	0.96	43.71
	30	-0.57	-1.04	-0.10	0.59	8.79
	40	-0.90	-1.92	0.12	0.60	5.96
	50	-0.66	-1.26	-0.06	0.55	7.32
	60	-0.53	-1.00	-0.06	0.63	8.42
50 ms pulse Fractional Transient Hot Wire Intercept	EH	-0.0006	-0.0009	-0.0003	0.77	21.78
	20	-0.0007	-0.0009	-0.0005	0.99	160.39
	30	-0.0005	-0.0008	-0.0002	0.80	19.35
	40	-0.0004	-0.0011	0.0003	0.36	2.42
	50	-0.0003	-0.0007	0.0001	0.30	3.36
	60	-0.0002	-0.0009	0.0005	0.08	0.53
400 ms pulse Fractional Transient Hot Wire Intercept	EH	-0.0008	-0.0017	0.0001	0.53	5.40
	20	-0.0007	-0.0011	-0.0003	0.94	52.19
	30	-0.0004	-0.0007	-0.0001	0.58	8.22
	40	-0.0006	-0.0012	0.0000	0.59	6.73
	50	-0.0003	-0.0006	0.0000	0.40	5.16
	60	-0.0002	-0.0004	0.0000	0.49	4.24

Table 6.10 Regression analysis results for changes in fractional transient hot wire gradient versus thermal conductivity and fractional transient hot wire intercept versus $\ln(D_{Th})/\lambda$. Highlighted cells indicate a statistically significant variation in slope indicating confidence that the parameter does vary with the thermal property at the 95% confidence level.

6.4.8 Discussion of the Thermal Conductivity Calibrations

The thermal conductivity calibrations were an exploratory study because it was not known exactly which type of actuation pulse would produce a signal that was sensitive to changes in the liquid thermal properties, nor was it known for sure what form these changes would take. Therefore a total of 15 analysis combinations (3 pulses × 5 peak

features) were tried, each using 6 different cantilever designs, making a total of 90 pulse response calibrations that were analysed. *Table 6.11* shows the few calibrations where the sensor signal changed significantly with the thermal conductivity of the test fluid. The definition of significant used here is that both the gradient and the upper confidence limit of the gradient are negative.

Pulse Duration (ms)	Chip Design	Dependent Variable	Slope	Low Interval	High Interval	R^2	F-val	p-val
0.5	50	FPT	-30.1	-39.9	-20.4	0.90	57.06	0.0003
400	50	Fτ	-20.0	-29.6	-10.4	0.81	26.04	0.0022
0.5	30	FPT	-27.0	-47.1	-6.9	0.64	10.81	0.0167
50	60	Fτ	-14.7	-24.9	-4.5	0.73	13.69	0.0140
50	50	Fτ	-14.3	-26.1	-2.6	0.60	8.93	0.0244
50	60	FPT	-2.3	-3.1	-1.5	0.91	52.53	0.0008
0.5	60	Fτ	-16.5	-31.7	-1.3	0.61	7.77	0.0386
50	30	Fτ	-7.7	-14.2	-1.2	0.58	8.30	0.0280
50	50	FPT	-1.3	-1.9	-0.7	0.84	30.75	0.0015
50	20	FTHWG	-0.9	-1.3	-0.6	0.98	120.24	0.0082

Table 6.11 Results where the change in the signal property was found to be significant with change in sample thermal conductivity.

The range between the lower and upper confidence intervals is on average, 60% of the value for the slope, indicating low precision of the cantilevers for sensing thermal conductivity. However, for the results in table 6.11, the correlation coefficients are reasonable high, indicating that to a first approximation, linear fitting to the results was appropriate. Therefore the confidence interval could be narrowed with further testing.

The fractional thermal decay time and fractional peak time are the two best techniques for identifying changes in the TD sensor response with respect to changing thermal conductivity of the sample when viewed by confidence interval. When F-value, p-value and R^2 are also considered, the fractional peak time is evaluated to be a better overall technique than the fractional thermal decay time. Transient hot wire techniques typically have high correlation coefficients and F-values (the ratio between variance explained by the fit line and unexplained variance) but very small gradients, indicating that they could prove to be more reliable techniques if the range of fluid properties was

larger, provided the relationship remains linear. If the liquid values for the transient hot wire gradient and intercept are used instead of the fractional values, the regression gradients are larger, but the chip to chip variability is re-introduced, thus reducing the fit.

From the peak time measurements at 0.5 ms we know that it takes around 20 ms for a heat impulse to travel from heater to sensor. Therefore for pulses less than 20 ms will be attenuated primarily by the fluid interaction. The peak height recorded in each plot of *figure 6.23* varies linearly with the duration of the actuation pulse from 0.5ms to 50 ms. As the pulse length is increased, heat can start to build on the beam and other loss mechanisms such as conduction through the beam to the substrate become increasingly important. In *figure 6.22*, it is seen that the linear relationship does not continue: pulse lengths over ~400 ms reach the same height, as thermal equilibrium is reached. From this perspective it might be thought that the best results would be for 400 ms pulses, as these are least attenuated. In this calibration we see that pulse durations of 0.5 ms give a better level of sensitivity to thermal properties of the liquid than either 50 ms pulses or 400 ms pulses (higher slope for the FPT) but the 50 ms pulses have much lower variability.

Most of the results in *table 6.11* are from chips with either 50 µm or 60 µm wide holes. When the beam has wider holes, the heat reaching the sensor read out tracks is more attenuated than if smaller holes are used, which would decrease sensitivity, particularly for FPH. However because the thermal pulse has to travel further through the liquid when the holes in the beam are larger it would be expected to be more sensitive to the sample. In addition, and perhaps overriding the other considerations, the precision of the hole dimension is improved with the larger holes, as shown in *Chapter 5, table 5.6.*

The high levels of variability between different chips preclude the possibility of using these chips as miniaturised thermal property measurement systems for the present. Data have been further analysed to find out whether any of the parameters recorded at the time of testing such as the resistance of heater and sensor tracks are the cause of the variability and could be controlled for, but this was found not to be the case. The most likely cause of the variability between chips is the variations in the beam height under

ambient conditions between different cantilevers and that itself may be due to the 'air jet' technique used to dry the cantilever chips once they have been released from the substrate. It is noted that early prototypes of the Microvisk sensor for blood clot measurement were viewed as being capable of measuring small differential changes in viscosity only, and it was not until the fourth generation prototype (where among other improvements a dry release technique replaced liquid aluminium etch) that the sensor was sufficiently reproducible to make absolute measurements.

As noted throughout the discussion sections, the chip design has a significant influence on the results obtained in particular to the fractional peak time and fractional peak position obtained using a 0.5 ms pulse. This has implications for the design of the SmartStrip sensor, which also uses the short pulse in operation. Increasing the distance between the heater and sensor decreases fractional peak position and increases the fractional peak time, both of which reduce the chance that the thermal background signal will interfere with correct measurement of the oscillatory signal that is the intended measurement in the SmartStrip sensor. Increasing the width of the holes does not significantly decrease the surface area to volume ratio of the beam, as shown in *table 6.12*. Neither has the heat loss by conduction through the anchor points changed with the different chip designs.

Chip Design	Surface Area, S μm^2	Volume, V μm^3	S/V (% of Design 40)	Cross Sectional Area of Anchor, X, μm^2
20	341020	1089200	100.07	1400
30	347040	1108800	100.03	1400
40	353060	1128400	100.00	1400
50	359080	1148000	99.97	1400
60	365100	1167600	99.93	1400
TD	356630	1128400	101.01	1400

Table 6.12 Surface area and volume for the different TD design variations.

To improve the data generated in this study (i.e. within *section 6.3.3*), given the constraints of the TD sensor in its current form, two improvements to the experiment are suggested. The first is to increase the number of chips tested under in each liquid. It was originally intended that many more chips would be used in this study, but large number of chips were destroyed in attempts to find a working fluidic well before the

study commenced. The second improvement would be to widen the range of fluid thermal properties tested by including, water and other solvents as test liquids.

No information could be obtained from Clearco Products about the measurement method used to obtain the data sheet values for thermal conductivity, or the expected error in the quoted values. An independent test method was used to determine the thermal conductivity of the silicone oils. Testing was contracted to Gearing Scientific Ltd., Ashwell, UK and performed by J. W. E Gearing and the author using a Lasercomp FOX50 Thermal Conductivity Meter with liquid cell. At the time these measurements were made, it was thought that all testing would be performed at 37°C to make the results directly comparable with blood measurements. Therefore the measurements taken using the FOX50 were made around a set point of 37°C, which means that the values obtained may not be exactly the same as those encountered during the microcantilever testing. The set-up of the FOX50 liquid cell is shown in *figure 6.35*.

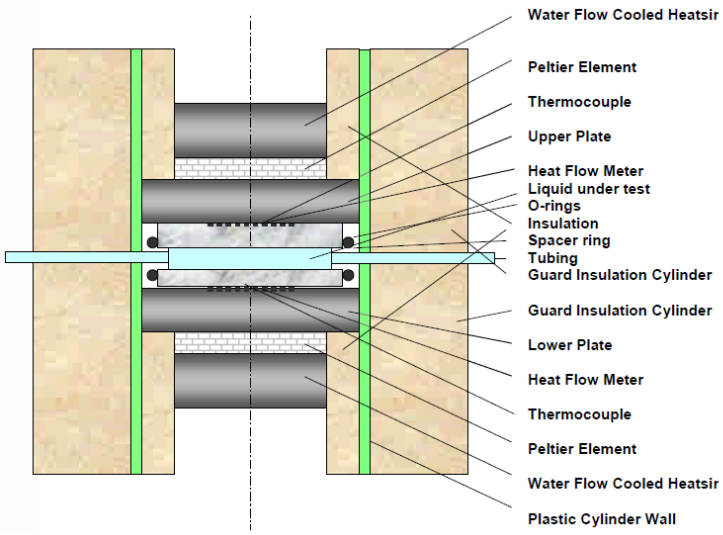

Figure 6.35 Schematic of liquid cell in FOX50 thermal conductivity meter supplied by Lasercomp and used to verify silicone oil thermal conductivities. Reproduced with permission from Lasercomp Inc., Saugus, USA.

Each sample was syringed in turn into the liquid cell of the FOX50 at an average ambient temperature of 23°C and relative humidity of 36%. The copper plates either side of the sample are held at 47°C (upper) and 27 °C (lower) using Peltier elements and thermocouples to maintain the plate temperatures to within 0.01°C of their set points

and generate conditions of constant heat flow through the sample whilst minimising the chance of convection cells forming in the liquid. The dimensions and thermal properties of the liquid cell are known, and the liquid thickness within the cell (Δl) is 2.06 mm. In the centre of each 62 mm diameter plate is a 25 mm^2 heat flux transducer and matched thermocouple and these are monitored every half second. The heat flux transducer signal Q is measured in μV and is linearly related to the total heat flux between the two plates, q, where the constant of proportionality, S, is determined by calibration of the instrument. After one hour of equilibration an average of 1820 results is taken to give the thermal conductivity at an average temperature of 37°C. The equation used by the software to calculate the liquid thermal conductivity is:

$$\lambda = \frac{\Delta l}{\frac{\Delta T}{Q\,S} - 2\psi_c - 2R\psi_g} \tag{6.2}$$

In equation (6.2), ΔT is the temperature difference measured between the two plates, ψ_c is the thermal resistance due to the surface roughness of the outside of the glass cell and ψ_g is the thermal resistance of the glass cell. It is important that the pressure used to hold the liquid cell in place is controlled in order to be able to obtain values for ψ_c and ψ_g from the calibrations. The accuracy claimed by Lasercomp for this type of test is 5% of the reported value. Results are shown in *table 6.13* and compared to the values quoted on the Clearco Data sheet.

Product	Thermal Conductivity ($Wm^{-1}K^{-1}$)			
	Clearco Data Sheet (@ 25 °C)	Range ± 5%	Independent Test Result (@ 37 °C)	Range ± 5%
PSF-0.65	0.1008	0.0958 – 0.1058	-	-
PSF-1	0.1008	0.0958 – 0.1058	-	-
PSF-5	0.1176	0.1117 – 0.1235	0.139	0.132 - 0.146
PSF-10	0.1344	0.1277 – 0.1411	0.145	0.138 - 0.152
PSF-20	0.1428	0.1357 – 0.1499	-	-
PSF-100	0.1554	0.1476 – 0.1632	0.170	0.162 – 0.179
PSF-200	0.1554	0.1476 – 0.1632	0.175	0.166 – 0.184
PSF-350	0.1554	0.1476 – 0.1632	0.181	0.172 – 0.190

Table 6.13 Thermal conductivity of silicone oils measured using FOX50 thermal conductivity meter compared to values quoted on the Clearco data sheet.

The range of results presented in *table 6.13* suggests that the differences in thermal conductivities between the different silicone oils are not as significant as first thought when it was decided to use them to characterize the microcantilever response to liquids of different thermal conductivity. The results presented in *figures 6.27 and 6.28* and *table 6.12* shows that the microcantilever sensor response is not sufficiently sensitive to changes in liquid thermal conductivity smaller than 0.05 $Wm^{-1}K^{-1}$ over the range 0.1 – 0.15 $Wm^{-1}K^{-1}$ to be able to be used to determine liquid thermal conductivity within that range.

6.5 Clinical Study

The aim of this section is to determine whether the coagulation process affects the Wheatstone bridge output response from the TD microcantilever following an actuation pulse, i.e. the thermal pulse profile. If it does, then it is possible that the thermal background signal is also affecting clot detection in the Microvisk SmartStrip sensor when used with the CoagMax device. Clot formation could affect the thermal pulse

profile by changing the physical properties of the blood sample, such as the thermal conductivity and heat capacity.

The calibrations with silicone oils *(section 6.4)* revealed that the thermal pulse profile is affected by changes in the thermal conductivity between 0.10 and 0.15 $Wm^{-1}K^{-1}$. Changes in the thermal properties of whole blood, plasma or serum during coagulation are not well explored in the literature. However a range of thermal conductivities for fresh and clotted human blood samples have been measured and are presented in *table 6.14*.

Sample	Thermal Conductivity ($Wm^{-1}K^{-1}$)	Heat Capacity ($Jkg^{-1}K^{-1}$)	Density (kg/m^3)	Thermal Diffusivity (10^{-7} m^2/s)	Ref.	Notes
Fresh whole blood	0.5082	-	-	-	[213]	Mean of 4
Clotted whole blood	0.59	3500	-	-	[214]	Mean of 9
Blood Plasma	0.60	3935	1030	1.48	[215]	
Whole blood*	0.54	3615	1037	1.44	[215]	Weighted mean of plasma and RBC

Table 6.14 Thermal properties of whole and clotted blood samples from the literature. **Based on average male haematocrit of 45%*

The difference in thermal conductivity between fresh and clotted blood as reported in the literature is 0.08 $Wm^{-1}K^{-1}$, slightly larger than the range of thermal conductivities of the silicone oils. However, it has been noted by [213] and others that the thermal conductivity correlated with water content of the sample. In the clotted blood studies by Nahirnyak *et al* [214] the clot samples were refrigerated several days between preparation and analysis which could lead to greater water loss than will be observed in 'in-situ' clot formation measurements using a microcantilever sensor.

6.5.1 Experiment design decisions

Testing was carried out at the Microvisk Clinical Laboratory in February 2012 using reconstituted blood plasma samples. It was decided not to use whole blood because the motion of the red blood cells is an additional source of noise and already it has been shown in *section 6.4* that the signal from the TD microcantilevers can carry a high level of interference and noise. The design variation '40' (with 40 µm wide holes) was used exclusively because in this study there was no wish to vary the sensor design and there was not enough chips of the '50' or '60' design variations available. All chips were taken from the same wafer.

The ideal pulse to use for the TD cantilevers in this study would be the 0.5 ms 200mW pulse as used for the silicone oil characterisations. Unlike the silicone oil experiments, where it was possible increase the signal to noise by averaging over 35 pulse trains, the clinical study requires examination of the response to each individual reaction pulse to see how this changes over time. In addition, the thermal diffusivity of blood plasma is an order of magnitude greater than the thermal diffusivity typical for silicone oil, so a lower sensor signal is expected. Trials of the short pulse in water confirmed that the signal-to-noise of individual pulse responses was unacceptably low, and that increasing the pulse power resulted in an electrical short in the heater tracks within the beam. Therefore the pulse length was increased to 5 ms at 200 mW. Data collection was conducted at a rate of 50 kHz for 100 ms from the start of actuation. Actuation occurred at a rate of 1 pulse every 2.5 second. Due to the high surface tension of blood plasma (similar to water), fluidic attachments to the microcantilever sensors were not necessary. It was decided to spot the plasma directly onto the sensor area of the chip.

6.5.2 Test Method and Data Analysis

In this experiment, the SmartStrip used in conjunction with the CoagMax is used as a comparator test to identify the time of formation of the incipient plasma clot. All testing was conducted at ambient room temperature. Twenty results were obtained on each sensor system.

25 µl reconstituted normal-type blood plasma (Hemosil) and 50 µl prepared thromboplastin reagent (Hemosil Recombiplastin 2G) were mixed together using a Gilson autopipette immediately prior to being dispensed onto first the TD chip and then the SmartStrip/EPR. Stopwatches were used to record the time between mixing and the start of data collection on both systems.

Data collection for the TD sensors was conducted using the test rig and LabView program outlined in *Chapter 5*. Results were analysed using Matlab. In *section 6.4*, the segmented gradient and approach was identified as being the best method to characterise the response to short actuation pulses, therefore these method was chosen to analyse the results from the TD sensor. The time of any shift in these parameters was noted, and compared to the clot time measured using the CoagMax software.

6.5.3 Results and Discussion

An example of how the peak position and peak time vary over time following the application of clotting plasma to the TD cantilever chip is shown in *figure 6.36.*

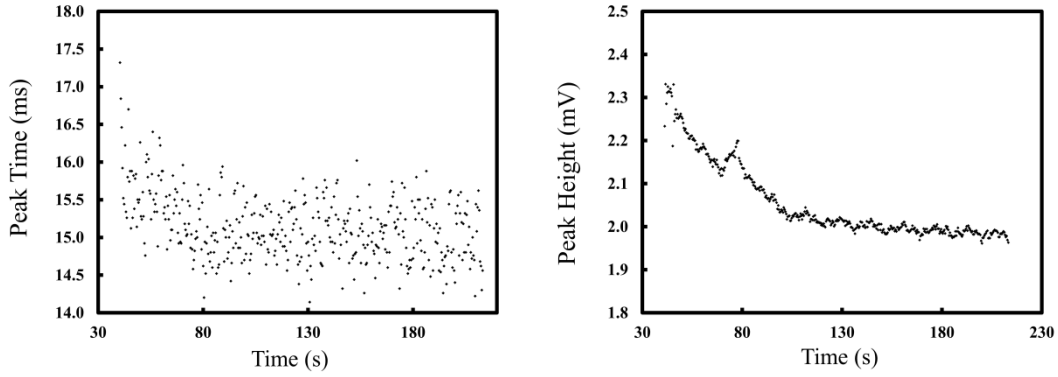

Figure 6.36 Example results of how peak time (left) and peak height (right) vary over time after the addition of clotting blood plasma to the TD chip.

It is seen that the peak time does decrease while the clot is forming and then levels-off, as shown in *figure 6.36.* There is a lot of noise in the peak times observed using the segmented gradient approach in blood plasma compared to the decrease in peak time during clot formation, making the inflection point difficult to identify. A clearer signal was found from analysis of the peak height. A feature similar to that occurring at 80

seconds in *figure 6.36* was identified in 15 out of 20 analyses from the TD chips. Note that the time on the horizontal axis of both plots of *figure 6.36* is the time from the start of actuation of the TD chip but only the data acquired after the liquid is added is shown. For each TD chip, the time between sample mixing and the start of the feature in the peak height was calculated and plotted against the time between sample mixing and the clot time measured using the CoagMax to make a linearity plot *(figure 6.37).*

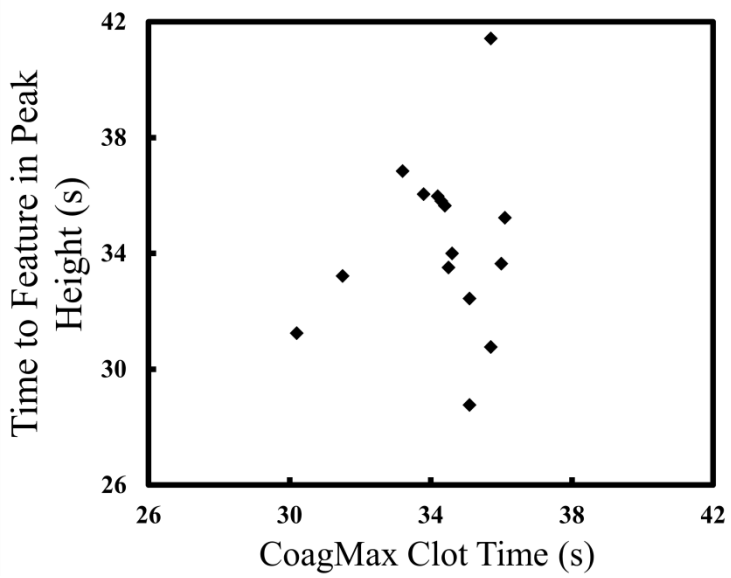

Figure 6.37 Linearity plot comparing the time taken from mixing of plasma with the clotting reagent the 'feature' identified in the TD peak height data with the clot time determined with using the Microvisk CoagMax.

Figure 6.37 shows that the feature identified in the signal from the TD cantilevers is consistently within the same time window (27 – 38 seconds) as the clot time determined using CoagMax, with only one exception, occurring slightly later at 42 seconds. The correlation coefficient from a linear fit by the method of least squares is 0.2. However it may be that this 'clot feature' is not sufficiently precise to pick up the small variations in clot time from one sample type and that abnormally slow and fast clotting plasma samples would be required in addition to the normal sample to demonstrate linearity. In an ideal plot, the gradient of a linear fit would indicate the activity of the thromboplastin used in the experiment, and the intercept would show the bias of the TD method compared to the CoagMax method. However, in this case it is possible that the feature identified in the TD peak height is not caused by the formation of a clot in the sample. An alternative explanation for the cause of the feature in the TD peak height is that the

sample is evaporating on the chip during the analysis and the feature arises when the surface of the droplet interacts with the moving cantilever. Further control experiments (such as substituting buffer for thromboplastin to provide a non-clotting control) are recommended to validate these results.

6.6 Conclusions

The TD sensor was developed with the aim of suppressing the piezoresistive component of the sensor signal to enable an assessment of the thermal background signal when the microcantilever is thermally actuated. In *section 6.2* a combination of characterisation measurements are made that provide evidence that contribution of motion of the beam to the TD sensor signal is effectively zero. In addition, measurements of the deflection in *sections 6.2.2* and *6.2.3* show that the TD sensor is has much higher curvature than the comparator MD beams as a result of having both heater and sensor read-out tracks at the neutral axis.

In *section 6.3*, the idea of the beam as a thermal sensor was developed. Thermal imaging studies of TD microcantilever actuation in air revealed that even when a duty cycle of 99% is used, heat does not build on the cantilever between consecutive pulses. In all cases of practical use of the sensor, the duty cycle is much lower (less than 70%), and the temperature of the beam returns fully to the ambient temperature between pulses. The equilibrium beam tip temperature reached during a pulse of 100 ms or longer scaled linearly with pulse power at a rate of 1.7 ± 0.5 °C/mW. For actuation pulses of shorter duration than 100 ms, the temperature increase is attenuated because the cantilever beam does not have enough time to reach thermal equilibrium. A maximum power of 30 mW was recommended for operation in liquid when using long pulses in order to avoid excessive heating or denaturation of the sample in a biological application of the sensor. The thermal imaging study also revealed that there is significant thermal crosstalk between the actuated and reference microcantilevers, with the reference cantilever incurring a temperature increase of 25% as much as the increase in temperature of the actuated beam. The thermal crosstalk decreases the sensitivity of the Wheatstone bridge output signal and this is evident when the Wheatstone bridge output signal is mapped onto the temperature domain and compared with the actual change in temperature of the beam observed with thermal imaging. The thermal

imaging data revealed that the temperature reached by beams that have previously been actuated is 1.1 – 1.5 times as great as the temperature reached by previously unactuated beams. This hysteresis is not of immediate concern for a single use disposable sensor application, but would non-the-less be interesting to study further.

It was not possible to obtain detailed measurements of the beam temperature during actuation in liquid using the thermal imaging equipment because liquid absorption and surface reflectivity obscure the measurement. However, by calculating the relative maximum signal compared to actuation in air the beam temperature may be deduced from the Wheatstone bridge output. Calibrations in silicone oils investigated the best data analysis techniques to quantify changes in the sensor read-out signal with thermal conductivity of the test liquid. Dividing parameters found in liquid for the same parameter in air was found to be an effective way of reducing the impact of chip-to-chip variability, though high variability and low number of results still posed a significant challenge in interpreting the results. Out of the 90 parameters investigated, 10 were found to vary significantly as the thermal conductivity of the sample was changed. The most sensitive parameter was found to be the fractional peak time for a 0.5 ms pulse, which had a slope of -30.1 (-39.9, -20.4) per $Wm^{-1}K^{-1}$. However this is only sufficient to give a thermal conductivity resolution of 0.3 $Wm^{-1}K^{-1}$ at 95% confidence.

The change in thermal conductivity of blood as it clots is found from the literature to be 0.08 $Wm^{-1}K^{-1}$, which is much less than the resolution afforded by the sensor. In *section 6.5*, a decrease in peak time was observed during clotting, but high levels of noise made it difficult to precisely identify the point at which the decrease levels off (the elbow). A feature was identified in the peak height that coincided with the elbow and was sharper and therefore easier to identify. This feature was coincident with the clot time measured by the CoagMax to within 6 seconds for 15 out of 20 samples, and is evidence that the blood clot does affect the thermal profile of the microcantilever sensor. However a linearity calibration and further control testing are required to determine whether the changing thermal properties of clotting blood are another mechanism through which the coagulation status could be monitored.

Thermal conductivity calibrations also showed that increasing the width of the holes in the cantilever beams could be useful in reducing the thermal crosstalk between the heater and sensor tracks within the same cantilever beam.

Before further studies with the TD microcantilever chips can be undertaken an attempt should be made to understand the root causes of the chip-to-chip variability, since this has prevented a quantitative assessment on the effect of thermal properties of the environment surrounding the microcantilever on the sensor signal. The first avenue of investigation recommended is to measure the tip displacement of a large number of beams prior to actuation in air and in liquid to see if a correlation exists between the tip displacement and any of the pulse response characteristics that were monitored in the thermal conductivity calibrations in *section 6.4.* As an alternative approach, the effects of chip-to-chip variability in thermal conductivity calibrations could be avoided if a single chip could be re-used in various environments. In the present work this has not been addressed due to the difficulty in cleaning and drying the chips between immersion in different liquid samples, a process which is likely to increase rather than decrease variability in the results. However, an alternative test could be designed whereby the sample is enclosed within a sealed chamber that could be filled with different gasses: variation of the composition of a gas mixture could be used to obtain sample environments with different thermal properties.

A difficulty encountered in the liquid characterisations (as well as in the viscosity calibrations in *Chapter 4*) was identification of suitable test liquids to measure how viscosity and the liquid thermal properties respectively affect the cantilever signal. *Figure 6.38* compares the thermal conductivity and viscosity of glycerol solutions and silicone oils side by side. In both silicone oils and glycerol solutions the thermal and rheological properties change together. Because the origins of thermal conductivity and viscosity both reside in the intermolecular forces between molecules in the liquid, it is difficult to find a set of fluids in which one property varies and the other remains constant. In general, thermal conductivity is slower-varying than viscosity for changes in temperature and pressure [216]. However it is clear from *figure 6.38,* that in the glycerol solutions, the change in viscosity for a given change in thermal conductivity is smaller than for the silicone oils, suggesting that they might have been a better choice for thermal conductivity calibrations.

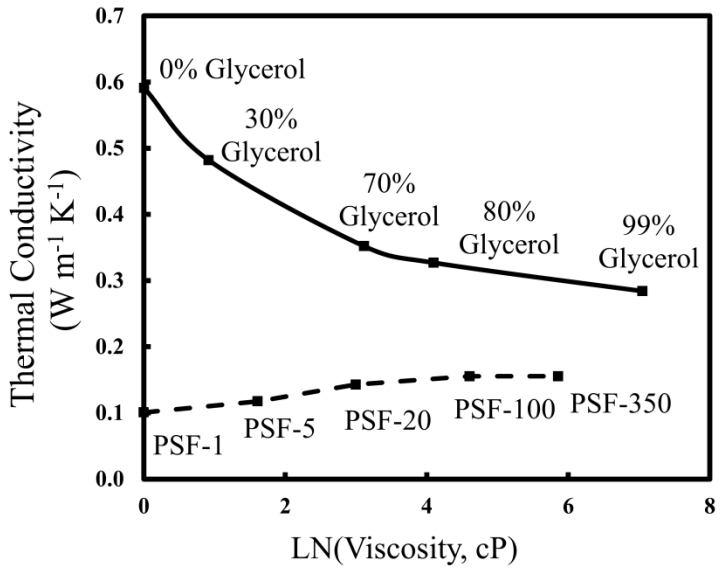

Figure 6.38 Rheological and thermal properties of glycerol solutions in water at 20 °C and of silicone oils at 25 °C.

In a retrospective consideration of how the silicone oil calibrations for the thermal design microcantilevers could have been better performed, electrolytic solutions, particularly potassium chloride, have been identified as possible test fluids. *Figure 6.39a* shows how the viscosity of different salt solutions changes with concentration in water. Both caesium chloride and potassium chloride change very little. In these solutions, the viscosity changes minimally with changes in thermal conductivity as the salt concentration is increased *(figure 6.39b)*. This phenomenon arises because for as the size of the cation increases, it becomes increasingly chaotrophic, disrupting the hydrogen bonds between water molecules so that they exert less 'pull' on one another when subject to shear.

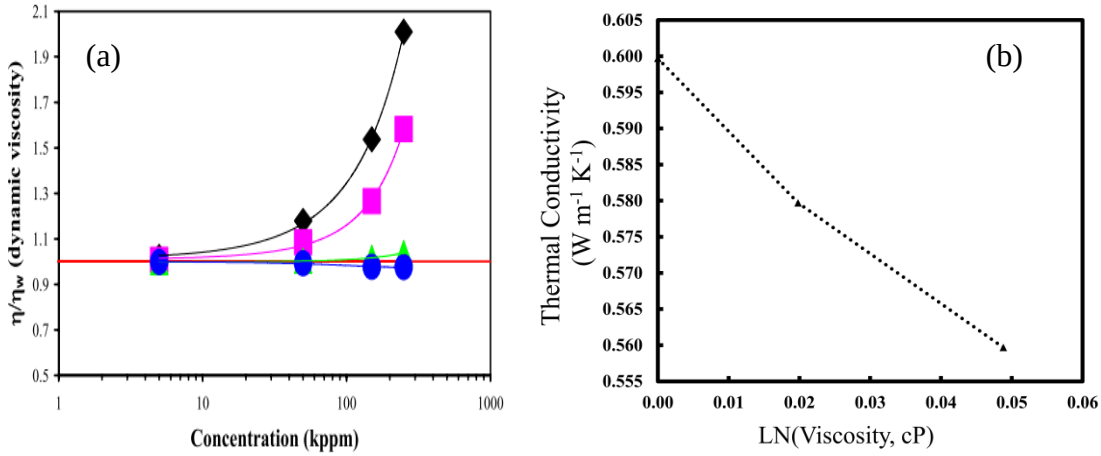

Figure 6.39 (a) Rheological properties of different salt solutions. Lithium chloride (black), sodium chloride (magenta), potassium chloride (green) and caesium chloride (blue). Reproduced with permission from [217]. *(b) Rheological and thermal properties of potassium chloride in water at 20 - 25°C. Data adapted from* [217, 218].

An additional benefit of using aqueous liquids is that they may not have needed sample containment, thus reducing the time required to prepare chips for experiments and avoiding the wastage of a large number of chips in fluidics development. The drawback to potassium chloride salt solutions is that it has a saturation of 360 g/kg, which is not high enough to change the thermal conductivity by more than 0.05 $Wm^{-1}K^{-1}$, about the same change as seen with the silicone oils. In the end the salt solutions technique was not attempted for the pragmatic reasons that the possibility to use them was encountered too late in the project: after the silicone oils had been purchased for the purpose and the number of functional devices had been significantly reduced through wastage during the fluidics development. Project funding for the development of the thermal sensor was supplied by STFC using the 'end of year spend.' This meant that there was very little time between commencement of the project and the deadline for consumables spending, and the majority of this time was taken up with mask design for the sensor with limited time available to research alternative test fluids. However if there was more time available for further chip manufacture and testing, both potassium chloride solutions and glycerol solutions would have been interesting test fluids to try.

Chapter 7
Conclusions and Outlook

7.1 Conclusions

In this thesis, potential sources of cross-sensitivity for an electrothermally actuated polymer bi-material microcantilever biosensor were evaluated. Investigations have focused on the blood coagulometer developed by the industrial partner to this project, Microvisk, but the methods and conclusions are applicable to other forms of polymer microcantilevers. For example, where microcantilevers are proposed as breath analysers to be used in static mode with various functional coatings, it would be useful to know whether moisture in the breath could give rise to a false positive result [219]. The technology is already expanding to new applications such as endotoxin detection and immunoassay diagnostics, and there is further potential to apply it in the fields of viscosity sensing in synovial fluid and pancreatic fluid. Incorporation of the microcantilever sensor technology into more complicated microfluidic analysis systems is also of interest [220]. Outside the healthcare industry, the use of microcantilever sensors for monitoring viscosity of oils and lubricants, fuels [221] and paints also show promise.

The literature review asked "Why are not a greater proportion of academic research prototypes for microcantilever biosensors finding commercial applications?" and identified a number of difficulties in commercialising the technologies, one of which was cross-sensitivity. In the case of the coagulometer application, change in beam response to any factor other than the clotting of blood around the microcantilever (with its associated effect on viscosity) could lead to an incorrect result and consequently to incorrect dosage of anti-coagulant being prescribed to the patient. In this thesis, studies

of the effect of the relative humidity of the storage and test environment, and also the thermal conductivity of the sample on the microcantilever signal were presented. It was shown that neither the relative humidity that the cantilever is exposed to before testing, nor the thermal conductivity of the test sample have an effect on the aspect of the microcantilever signal that arises from changing sample viscosity during a blood clot.

Table 7.1 summarises the effects that various fluid properties have on the microcantilever signal.

Physical Property	**Range in whole blood and clotted blood**	**Microcantilever Sensitivity**
Viscosity	2 – 70 cP	4 ± 1% shift in peak position of LPF from the SmartStrip. 8% ± 1% shift in resonant frequency (linear average) per cP.
Relative humidity	N/A but potential range prior to test is 2% to 100% RH.	$\frac{d\omega}{dRH} = 0.0\% \pm 0.1\%$ per 1% change in RH when actuated in air.
Thermal Conductivity	0.5 – 0.6 W/mK	$\frac{d\,PT}{d\lambda} = -0.18 \pm 0.07$ smK/W when calibrated in silicone oils. Peak position changes gradually from 17 ms to 15 ms during blood plasma clot.

Table 7.1 Comparison of the effects of different physical properties of the sample and the test environment on the microcantilever signal.

The change in peak time with thermal conductivity reported in the silicone oil calibrations in *section 6.4.8* would be sufficient to decrease the peak position by 20 ms during a blood clot. However, in the clinical study in *section 6.5* the peak position changed from 17 ms to 15 ms over the course of the experiment, i.e. 10 times less than indicated by the calibrations. This could be because the calibrations were conducted over a limited range that does not coincide with the thermal conductivity of blood. The region of interest in the mechanical signal that is used in the SmartStrip sensor occurs at

1.7ms and increases by 5% during incipient clot formation. Therefore although the calibrations do not cover the clinical range of thermal conductivity, the clinical study demonstrates that the thermal signal will not overlap the mechanical signal due to blood clotting.

The following aspects of this thesis have been identified by the author as novel:

1. The realisation, characterisation and calibration of the TD sensor specifically designed to identify whether the thermal conductivity of a liquid sample has a significant effect on the thermal crosstalk of heater and sensor tracks embedded within the same beam. (Chapter 5 – 6)
2. Positioning the read out sensor tracks at the neutral axis of the beam to reduce the mechanical component of the signal in the TD sensor. (Chapter 5)
3. Consideration of the combined effects of temperature and humidity acting on the beam simultaneously through use of the Buck equation is novel in a model of cantilever tip deflection and can be used to explain why experimental results generated in this work as well as in other studies exhibits a curved temperature versus deflection profile when the cantilever is heated through the substrate. (Chapter 3)
4. Although autofocus equipment is commercially available, the home build apparatus, that was developed and characterised in the course of this thesis, provides a cheaper, more flexible alternative for use in research laboratories. The contribution of the author to this part of the thesis is the linearity characterisation. (Chapter 3)
5. Demonstration of the viscosity sensitivity of the SmartStrip microcantilevers encompassing the chip-to-chip variability. (Chapter 4)

Characterisation of the sensor deflection was performed using both commercially available and home built profilometers, and the sensor signal was controlled and collected using LabView (National Instruments). In order to study the "thermal" component of the signal in greater depth, a new microcantilever sensor was designed and built. To fabricate this sensor, standard MEMS photolithography techniques were applied to pattern polymer layers. Characterisations were used to show that repositioning the sensor layer had reduced the piezoresistive signal component by an order of magnitude to enable measurement of the thermal signal. A clinical

demonstration of the new sensor was also performed, using the Microvisk SmartStrip as a comparator. The major contribution of this thesis to the field of polymer microcantilever sensors is the first demonstration of a microcantilever that is sensitive to the thermal conductivity of a liquid sample.

The main achievements and findings from each chapter are summarised section 7.2. In section 7.3 recommendations for further work arising from this thesis are proposed: the section is divided between proposals that might be of particular interest to Microvisk, and those that are more academically orientated.

7.2 Chapter Summaries

The deflection and operation of the polymer microcantilever under conditions of varying relative humidity and temperature were studied in the third chapter. Characterisation of the deflection of a polymer microcantilever versus temperature under ambient conditions gives a curved profile. The thermal bi-material effect equations typically used to describe deflection as a function of temperature do not work well with polymer cantilevers due to the high levels of moisture uptake; the changes in beam stress due to moisture absorption from the atmosphere can be as high as the thermally induced stresses. The thermal bi-material effect equations were modified and compared with experimental results to enable the change in deflection due to moisture to be separated from the change in deflection due to temperature. A value for the deflection sensitivity to moisture of 1.1 ± 0.4 µm per 1% RH was found for the Microvisk SmartStrip cantilevers, which is as high as the deflection sensitivity to temperature. The moisture sensitivity is sufficient to explain differences in beam tip height measured at the Semefab chip manufacturing facility and in the Microvisk assembly clean room. Humidifying the atmosphere did not affect the resonance frequency of cantilevers actuated in air, possibly because the temperature of the beam could reach as much as 850 °C when subject to 6 V (from extrapolation of *figure 6.10*) so the actuation of the beam quickly removes absorbed moisture. It was further demonstrated that blood clot measurements are unaffected by the beam being exposed to different levels of moisture prior to testing.

In the fourth chapter it was shown that the latest design of Microvisk SmartStrip cantilever sensor has a viscosity sensitivity of 2 cP and that the influence of inertial effects is negligible in comparison to the viscosity, possibly due to the epsilon shape of the beam. Such viscosity sensitivity is sufficient to detect the onset of clot formation.

The design and fabrication of a 'Thermal' (TD) microcantilever sensor were presented in *chapter 5*. This is the first demonstration of a cantilever designed specifically to observe the thermal background. Simulations of the microcantilevers were not possible during this study so similar devices from the literature were evaluated and there was found to be no clear consensus as to whether or not there would be a measurable change in the temperature profile of the microcantilever signal over a homologous series of silicone oils with thermal conductivity ranging from 0.1008 – 0.1554 W/mK. A TD sensor was designed, with the read out sensor tracks positioned at the neutral axis of the beam to avoid the thermal profile being drowned out by mechanical oscillations. Sensors were successfully fabricated using photolithographic processes.

In *chapter 6*, characterisation experiments showed that the peak position in response to a short pulse (0.5 ms) is sensitive to changes in thermal conductivity of the test fluid with a resolution of 0.3 $Wm^{-1}K^{-1}$ and demonstrated the impact of this when during clot formation. The temperature sensitivity of the signal was explored using thermal imaging to find that the temperature of the beam tip changes with actuation power by 1.7 ± 0.5 °C/mW, but significant (25%) thermal crosstalk between the active and reference cantilevers limited the temperature-sensitivity of the sensor.

7.3 Recommendations for further research

This section is divided into research that primarily concerns Microvisk, since it details further characterisation studies that should be performed, and further research identified in relation to the work in this thesis that would be of interest to the wider academic community.

7.3.1 Recommendations to academia

Micro and nano scale materials research

During the course of this research it became clear that further basic materials characterisation experiments on the polymer films would be beneficial to aid in modelling future design iterations or new polymer MEMS devices [44]. Spin deposited thin film polyimides exhibit anisotropy in their thermal and mechanical properties due to partial alignment of the polymer molecular chains parallel to the substrate [222], an effect that increases with spin speed and the datasheet quotes single values of a single thickness (10 μm) for the Young's Modulus, E, thermal conductivity, k, and coefficient of thermal expansion α, with no indication of which orientation the value applies to or what technique was used to determine the property or the uncertainty associated with the quoted value. Preliminary wafer curvature measurements were made using Tencor Flexus FLX- 2320 at Oxford Instruments Plasma Technology Lab indicate that more realistic values for the CTE and E of PI-2562 and PI-2610.

Property	**Data-sheet value**	**Flexus FLX 2320 measurement**
Young's Modulus PI-2562	1.3 GPa	8.0 ± 0.4 GPa
Young's Modulus PI-2610	8.5 GPa	82 ± 4 GPa
CTE PI-2562	60 ppm/°C	14.4 ± 0.7 ppm/°C
CTE PI-2610	3 ppm/°C	2.4 ± 0.1 ppm/°C

Table 7.2 Preliminary results for CTE and Young's Modulus obtained experimentally compared to data sheet values for the polyimides used in this research. Measurements made using the Flexus FLX 2320 give values for the plane of the wafer.

The measurements reported are based on measurements from a single set of four wafers (two different substrates are required for each polymer) and it would be cautious to repeat the measurements on further wafer sets before accepting the measurement value. However if correct these results indicate that the difference in thermal expansion coefficient between the polymers is not as great as predicted and efforts to model the

cantilever deflection using the datasheet values will consequently over-estimate the change in deflection with temperature.

Large Deflection

There is some controversy within the literature as to whether the large deflections of a cantilever beam become increasingly non-linear. As discussed in chapter 3, both circular and linear approximations to the beam profile can be used to predict the beam deflection. However in their authoritative text on thermal bi-material cantilevers, Lammell *et al* state that to fully account for large deflections, the problem should be re-cast as the elastica equation and solved using elliptic integrals [223].

As shown by Rhode et al, for the case of a uniformly loaded beam, the small deflection theory approximations over-estimate the tip deflection on a tip loaded beam by at least 10% for deflections above 18° [223]. There are several methods proposed in the literature for the solution of the elastica for end-loaded beams but as far as the author is aware, no consideration of the case of a beam where the change in curvature arises from expansion of the film material itself. Most microcantilever sensors operate within the region of small curvature where the linear approximation works well. Previous work in the field of polymer microcantilevers is divided as to whether the circular approximation can be used [163] or whether the beam curvature is non-linear [18]. It is the opinion of the author that the curvature of the beam should remain constant even at large deflections because

1) The experimental work supporting the non-linear deflection hypothesis was conducted using thermal bi-material strips with multiple layers of integrated metal tracks, and the tracks would introduce non-linearity in the deflection through varying the stiffness of the beam along its length

2) Experimental work that supports the use of the circular approximation also had metal tracks but these ran the length of the beam.

3) The physical cause of the non-linear curvature for large deflections under end-load conditions is that as the beam becomes more bent, the direction of the bending moment acting on the beam changes and therefore the moment, and consequently the curvature vary down the length of the beam. In the thermal bi-material beam, the bending moment arises from an expansion that is being driven throughout the length of

the beam and is therefore uniform along the length of the beam and constant curvature should be expected.

7.3.2 Recommendations for ongoing research at Microvisk

Beam deflection at low temperature

The beam deflections recorded in *Chapter 3* at 10°C were lower than anticipated and require further explanation: it was proposed that the deflection is reduced by condensation on the beam leading to stiction and consequent decrease in deflection. This hypothesis could be tested by observing whether the results are repeatable when the temperature order is changed, or when the humidity range used is not so large. In addition, a water spray could be used to mist the cantilevers with a fine droplet spray without changing the temperature or humidity of the environment and see if a decrease in deflection is observed.

Alternative single polymer structure

The research of Li and Uttamchandani [195] shows that the difference in heating of the central and outer beams in the epsilon beam design can drive the microcantilever vertical deflection in addition to the bi-material effect. This aspect of the cantilever motion has not, to the best knowledge of the author, been considered by Microvisk, and presents an opportunity for further investigation. If the effect of the temperature difference between the different parts of the beam predominates over the bi-material effect, there may be no need to employ two different polymers in the beam construction. Use of a single polymer layer offers many benefits because the design is no longer dependent on the use of a polymer with low CTE thus increasing the number of polymers that could be used and reducing the bill of materials, cost of fabrication, and consequent risk to manufacturing the sensors. The experimental characterisations using silicone oils in *section 6.3.3* already show that there is a temperature difference between the outer and inner arms of the cantilever during operation in liquid, which in the Li and Uttamchandani interpretation would contribute to the beam deflection. As noted in *section 7.3.1*, the difference in CTE of the two polyimides may not be as large as was assumed in this work and previously, therefore the bi-material effect may not be the dominant deflection mechanism. A recommendation of further experimental work to follow up on this lead would be to fabricate a variation of the current microcantilever

design but using a the high CTE polymer for all polymer layers and use a video-microscope or high speed imaging to record the cantilever response to actuation pulses of sub-millisecond duration. In this way, the extent of reduction in the amplitude of oscillation of the beam tip could be measured.

Further sources of cross sensitivity in the SmartStrip sensor

This thesis has looked at the relative humidity of the test environment before sample addition and the thermal conductivity of the sample as potential sources of cross-sensitivity that could potentially degrade sensor performance. There are other potential physical sources of cross sensitivity that have not been addressed in the thesis but are proposed as further research on the subject. For example, in chapter 3, surface tension of the test liquid was identified linked to test-error rate because it affects the way the meniscus of the sample interacts with the microcantilever and therefore could alter the reference signal against which all subsequent signals are compared to identify the time of the blood clot. Surface tension in a blood finger-stick sample could be reduced if the patient did not adequately clean the hands prior to lancing their finger for the blood sample which may then become contaminated with, for example, moisturisers that would lower the surface tension of the sample.

Another potential source of cross sensitivity is the haematocrit. Determining the impact of haematocrit is part of the product validation process undertaken by Microvisk. It was found that there was a measurable difference in the peak height profile over time for bloods of differing haematocrit and this was attributed to the effect of red blood cells settling on the beam over a period of up to 10 minutes. Given that the coagulation process typically takes around two minutes, the cell settling was not found to be significant source of interference on the test, but the concept that the concentration of suspended particulates could be measured with the sensor gave rise to the idea for a new application of the sensor: measuring agglutination reactions using the cantilever. In the literature survey it was noted that the vast majority of biosensor research involves capture of a target protein biomarker by a specific binding receptor immobilised on the cantilever surface. It was noted that the academic literature lacks demonstration of the same sensing platform being used with a variety of different biomarker chemistries to create a modular, generic biosensor platform. If such a platform could be created by

adapting the existing CoagMax point of care device, the technology could reach an extremely large number of markets.

The most common example of an agglutination immunoassay is for blood typing where the antigen is part of the outer membrane of the red blood cells. If the complimentary antibody is present in the sample matrix, this will bind the cells together, thus separating the cells from the rest of the matrix. The size of the cells amplifies the effect of the binding reaction to the point where its effect can be seen with the naked eye. To determine whether it was possible to differentiate between agglutinating and non-agglutinating samples, experiments were performed with 1 μm diameter streptavidin coated magnetic beads. The positive sample contained biotinylated immunoglobulin-G (b-IgG) and the control sample was contained normal IgG. In the positive sample, there was an average of 8 biotin binding sites per molecule as supplied by GE Healthcare, UK, meaning that it should be possible to bind more than one bead (Invitrogen, Life Sciences, UK). Initial test results are pictured in *figure 7.1* for different percentages of beads.

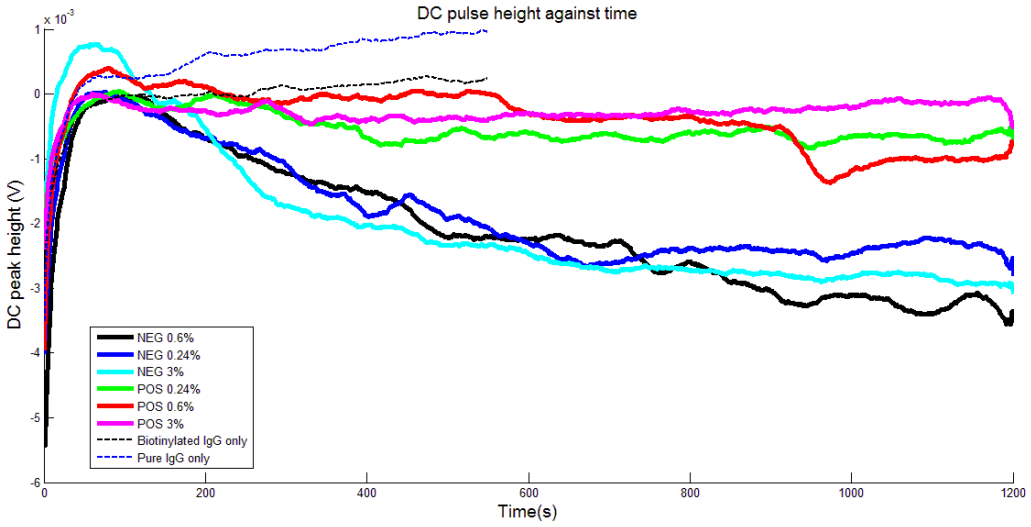

Figure 7.1 Initial results showing the effect of agglutination of magnetic bead particles local to the Microvisk SmartStrip sensor. Negative controls used streptavidin-coated beads suspended in IgG at concentrations of 0.24%v/v (blue), 0.6%v/v (black), and 3%v/v (cyan). 'Positive' samples contained coated beads suspended in polyvalent biotinylated-IgG at the same concentrations (green, red and magenta respectively). For comparison, traces from solutions without the magnetic beads are also shown for biotinylated-IgG and IgG in dashed black and blue traces respectively.

After 200 seconds, the DC peak response decreases in the control samples, not the agglutinating sample, however there is no discrimination between different concentrations of magnetic beads. The 'agglutinated' samples behave much more like the samples in which no beads were present, perhaps indicating that they have indeed 'stuck together' and fallen out of suspension. Observation of the 'agglutinating' and 'non- agglutinating' sample mixtures under a microscope revealed a similar distribution of beads in each, leaving the preliminary results inconclusive this stage. At the time this work was undertaken, the term of the EngD was drawing to a close, and managerial focus of the company was shifting towards the first product launch, so it was not possible to investigate these intriguing results any further.

7.4 Future Directions for bioMEMS

We still have a long way to go in demonstrating the effectiveness of MEMS for medical applications before Feynman's cell repair microbots are licenced to course our blood vessels, but the progress within the last few decades has been significant. BioMEMS

has moved from being a purely academic field in the late 1990's to a largely commercial field today. In pure research, it is being superseded by a smaller generation of devices, NEMS [224]. As *in vitro* diagnostic devices become more widely accepted, long term research projects look increasingly towards theranostics and implanted devices.

MEMS technology borrowed from other industries is already having an impact in healthcare. Mobile phones have proved a particularly fruitful industry from which to adapt technology as the requirements for portability and low power consumption are similar to that for modern diagnostics. It is probable that future healthcare devices, such as diagnostics, will be mobile based: the technology is available for a microfluidic chip the size of a Micro-SD to deliver a diagnostic test result to be read and displayed with a corresponding 'app' on the phone. The reason why we don't all already have one now is that the phone itself would be classed as a 'Medical Device' requiring FDA approval for licence in the US and similar approval elsewhere. Once this regulatory hurdle is overcome, it is likely that there will be a proliferation of mobile based sensing technology [225].

The polymer sensors that are the topic of this thesis are the first of their kind to be used in a medical diagnostic device and have not had extensive validation in other industries. They had not been as extensively characterised as other bioMEMS products at the start of the product development cycle. Three aspects of the sensor signal that required further investigations: the impact of humidity, thermal crosstalk and viscosity resolution are addressed in this thesis. Once this technology is accepted onto the market, the next step to be considered is integration of the results into an information management system (IMS) that will allow doctors and patients to monitor the test results over the long term and integrate them with other bio-stasis information which is currently limited to medical records but in future could comprehensively include genetic fingerprinting for personalised medicine, and streamed information on lifestyle from motion sensors.

The use of polymers in bioMEMS is not limited to large deflection thermally actuated microcantilevers. Polymers are attractive materials for *in-vivo* devices as unlike silicon

they can be biocompatible. The problems of rejection and of bio-fouling were recognised during the first flourish of biosensor research in the 1990's [226] and are still not solved today. In addition, the possibility of integrated polymer circuitry and optics increases the usefulness of the technology [227]. As the number of *in-vivo* bioMEMS applications increases, understanding how polymer components operate at the micro and nanoscale will become increasingly important.

References

1. Feynman, R. (1960). There's plenty of room at the bottom. *Caltech Engineering and Science*, *23*, 22–36.

2. Nathanson, H. C., Newell, W. E., Wickstrom, R. A., & Ransford Davis, J. (1967). The Resonant Gate Transistor. *IEEE Transactions on Electron Devices*, *14*(3), 117–133.

3. Hope, P., Bamford, S.-M., Beales, S., Brett, K., Kneale, D., Macdonnell, M., & McKeon, A. (2012). Creating sustainable health and care systems in aging societies: Report of the Aging Societies Working Group 2012. *Published Online (https://workspace.imperial.ac.uk/global-health-innovation/Public/GHPS_2012_Summit_Report.pdf). Last accessed 11 April 2014.*

4. Kissinger, P. T. (2005). Biosensors – A perspective. *Biosensors and Bioelectronics*, *20*, 2512–2516.

5. Orme, M. (2007). Is this the investment trend of the decade? *MoneyWeek, Published online (http://moneyweek.com/is-this-the-investment-trend-of-the-decade/). Last accessed 11 April 2014*, (3rd April).

6. Bashir, R. (2004). BioMEMS : state-of-the-art in detection , opportunities and prospects. *Advanced Drug Delivery Reviews*, *56*, 1565–1586. doi:10.1016/j.addr.2004.03.002

7. Herman, W. A., & Devey, G. B. (2008). Future Trends in Medical Device Technologies. *Published Online (http://www.fda.gov/downloads/AboutFDA/CentersOffices/CDRH/CDRHReports/UCM238527.pdf). Last accessed 11 April 2014*.

8. MHRA Press Office. (2001). PIP breast implants - UK medical devices regulator says no evidence to support routine removal. *Press Release Published Online (http://www.mhra.gov.uk/NewsCentre/Pressreleases/CON137935). Last accessed 11 April 2014*.

9. O'Dwyer, T., & Berney, H. (2011). MEMs devices in heathcare. In *Biosensors & Bioelectronics Conference Presentation*.

10. Pelesko, J. A., & Bernstein, D. H. (2003). Modeling MEMS and NEMS. *Chapman and Hall/CRC, Chapter 1*, 1–3.

11. Beck, H., Boden, W. E., Patibandla, S., Kireyev, D., Gupta, V., Campagna, F., Cain, M. E., Marine, J. E. (2010). 50th Anniversary of the First Successful Permanent Pacemaker Implantation in the United States: Historical Review and future directions. *The American Journal of Cardiology*, *106*(6), 810–818.

12. Garofalo, P. (2012). Healthcare applications based on MEMS technology. *Advancing Microelectronics*, *39*(2), 24–28.

13. Ruska, E., Binnig, G., & Rohrer, H. (1986). 1986 Nobel Prize for Physics. *Published Online (http://www.nobelprize.org/nobel_prizes/physics/laureates/1986/press.html). Accessed 11 Dec 2013*.

14. De Souza, N. (2012). Pulling on single molecules. *Nature methods*, *9*, 873–877.

15. Hunt, H. K., & Armani, A. M. (2010). Label-free biological and chemical sensors. *Nanoscale*, *2*(9), 1544–1559. doi:10.1039/c0nr00201a

16. Joint Press Release – London Centre for Nanotechnology and Imperial College London and University College London. (2009). Point of care nanosensors for HIV and monitoring to be developed with £2 million award. *Published Online (www3.imperial.ac.uk). Accessed 12 Decemeber 2013.*

17. Timurdogan, E., Alaca, B. E., Kavakli, I. H., & Urey, H. (2011). MEMS biosensor for detection of Hepatitis A and C viruses in serum. *Biosensors & bioelectronics*, *28*(1), 189–194. doi:10.1016/j.bios.2011.07.014

18. Dunn, R. J. (2010). Integrated Microcantilever Sensor as a Blood Coagulometer,. *EngD Thesis, Heriot Watt University*.

19. D'Angelo, A., Della Valle, P., Crippa, L., Pattarini, E., & Vigano D'Angelo, S. . (1996). Critical aspects in routine coagulation testing. *Pure and Applied Chemistry*, *68*(10), 1867–1871.

20. Heneghan, C., Ward, A., Perera, R., Bankhead, C., Fuller, A., Stevens, R., Bradford, K., Tyndel, S., Alonso-Coello, P., Ansell, J., Beyth, R., Bernardo, A., Christensen, T. D., Cromheecke, M. E., Edson, R. G., Fitzmaurice, D., Gadisseur, A. P.,Garcia-Alamino, J M., Gardiner, C., Hasenkam, J M., Jacobson, A., Kaatz, S., Kamali, F., Khan, T. I., Knight, E., Körtke, H., Levi, M., Matchar, D., Menéndez-Jándula, B., Rakovac, I., Schaefer, C., Siebenhofer, A., Souto, J. C., Sunderji, R., Gin, K., Shalansky, K., Völler, H., Wagner, O., Zittermann, A. (2012). Self-monitoring of oral anticoagulation: systematic review and meta-analysis of individual patient data. *Lancet*, *379*(9813), 322–334. doi:10.1016/S0140-6736(11)61294-4

21. Ansell, J. E. (1999). Empowering Patients to Monitor and Manage Oral Anticoagulation Therapy. *JAMA*, *281*(2), 182–183.

22. Fitzmaurice, D. A., Gardiner, C., Kitchen, S., Mackie, I., Murray, E. T., & Machin, S. J. (2005). An evidence-based review and guidelines for patient self-testing and management of oral anticoagulation. *British Journal of Hematology*, *131*, 156–165. doi:10.1111/j.1365-2141.2005.05739.x

23. Unkrig, V., Marquant, M., Hindelang, F., Kotzan, H., Horn, C., & Nortmeyer, C. (2003). Electrochemical sensor for determining blood clotting, corresponding system for measuring blood clotting and method for determining blood clotting (Patent No. US 2003/0146113 A1).

24. Abbott Point of Care. (2013). Prothrombin time (PT/INR). *Customer Information Article 715236-00R*, 1–8. Retrieved from http://www.abbottpointofcare.com/Customer-Info-Center/Cartridge-and-Test-Info-Sheets.aspx

25. Sharma, P. (2013). Evidence Assessment and Analysis Report: The clinical and cost-effectiveness of point of care tests (CoaguChek system, INRatio2 PT/INR monitor and ProTime Microcoagulation system). *Commissioned by the NIHR HTA Programme on behalf of the National Institute for Health and Care Excellence. HTA Reference Number: 13/06/01*, (June), 1–20. Retrieved from http://www.nice.org.uk/nicemedia/live/14091/64106/64106.pdf

26. ITC (Edison NJ). (2012). Hemochron® Signature Elite. *Published Online (http://www.itcmed.com/products/hemochron-signature-elite-whole-blood-microcoagulation-system). Accessed 11 April 2014*. Retrieved from http://www.itcmed.com/products/hemochron-signature-elite-whole-blood-microcoagulation-system

27. Christensen, T. D., & Larsen, T. B. (2012). Precision and accuracy of point-of-care testing coagulometers used for self-testing and self-management of oral anticoagulation therapy. *Journal of thrombosis and haemostasis*, *10*(2), 251–260. doi:10.1111/j.1538-7836.2011.04568.x

28. Gosselina, R. C., Owings, J. T., Larkin, E., White, R. H., Hutchinson, R., & Branch, J. (1997). Monitoring Oral Anticoagulant Therapy with Point-of-Care Devices: Correlations and Caveats. *Clinical Chemistry*, *43*, 1785–1786.

29. Djakov, V., Huq, E., & Vernon, P. (2008). Fluid Probe (Patent US2008/0028837). *Unit*.

30. Djakov, V., Huq, E., & Vernon, P. (2012). Fluid Probe (Patent No. US 8,210,030 B2).

31. Djakov, V., Huq, E., & Dunn, R. J. (2012). Fluid Probe (Patent No. US 8,297,110 B2).

32. Datar, R., Kim, S., Jeon, S., Hesketh, P., Manalis, S., Boisen, A., & Thundat, T. (2009). Cantilever Sensors : Nanomechanical Tools for Diagnostics. *MRS Bulletin*, *34*(June), 449–454.

33. Boisen, A., Dohn, S., Keller, S. S., Schmid, S., & Tenje, M. (2011). Cantilever-like micromechanical sensors. *Reports on Progress in Physics*, *74*(3), 036101, 1–30. doi:10.1088/0034-4885/74/3/036101

34. Larsen, T., Keller, S., Schmid, S., Dohn, S., & Boisen, A. (2011). Fabrication and characterization of SRN/SU-8 bimorph cantilevers for temperature sensing. *Microelectronic Engineering*, *88*(8), 2311–2313. doi:10.1016/j.mee.2010.12.015

35. Thundat, T., & Doktycz, M. J. (2000). Micromechanical Calorimetric Sensor (Patent No. US 6,096,559 A).

36. Lim, S., Choi, J., Horowitz, R., & Majumdar, A. (2005). Design and Fabrication of a Novel Bimorph Micro-Opto-Mechanical Sensor. *Journal of Micromechanical Systems*, *14*(4), 1–7.

37. Fragakis, J., Chatzandroulis, S., Papadimitriou, D., & Tsamis, C. (2005). Simulation of capacitive type bimorph humidity sensors. *Journal of Physics: Conference Series*, *10*, 305–308. doi:10.1088/1742-6596/10/1/075

38. Gunter, R. L., Delinger, W. D., Porter, T. L., Stewart, R., & Reed, J. (2005). Hydration level monitoring using embedded piezoresistive microcantilever sensors. *Medical Engineering and Physics*, *27*, 215–220.

39. Norris, A., Saafi, M., & Romine, P. (2008). Temperature and moisture monitoring in concrete structures using embedded nanotechnology mems sensors. *Construction and Building Materials*, *22*, 111–120.

40. Baller, M. K., Lang, H. P., Fritz, J., Gerber, C., Gimzewski, J. K., Drechsler, U., Rothuizen, H., Despont, M., Vettiger, P., Battiston, F M., Ramseyer, J P., Fornaro, P., Meyer, E., Gu, H. (2000). A cantilever array-based artificial nose. *Ultramicroscopy*, *82*, 1–9.

41. Berger, R., Delamarche, E., Lang, H. P., Gerber, C., Gimzewski, J. K., Meyer, E., & Guntherodt, H.-J. (1997). Surface Stress in the Self-Assembly of Alkanethiols on Gold. *Science*, *276*(5321), 2021–2024. doi:10.1126/science.276.5321.2021

42. Fritz, J., Baller, M. K., Lang, H. P., Strunz, T., Meyer, E., & Gu, H. (2000). Stress at the Solid - Liquid Interface of Self-Assembled Monolayers on Gold Investigated with a Nanomechanical Sensor, (15), 9694–9696.

43. McKendry, R. A., Zhang, J., Arntz, Y., Strunz, T., Hegner, M., Lang, H. P., Gerber, C., Baller, M. K., Certa, U., Meyer, E., Gu, H. (2002). Multiple label-free biodetection and quantitative DNA-binding assays on a nanomechanical cantilever array. *Proceedings of the National Academy of Sciences*, *99*(15), 9783–9788.

44. Liu, Y., Schweizer, L. M., Wang, W., Reuben, R. L., Schweizer, M., & Shu, W. (2013). Label-free and real-time monitoring of yeast cell growth by the bending of polymer microcantilever biosensors. *Sensors & Actuators: B. Chemical*, *178*, 621–626. doi:10.1016/j.snb.2012.12.111

45. Shekhawat, G., Tark, S.-H., & Dravid, V. P. (2006). MOSFET-Embedded microcantilevers for measuring deflection in biomolecular sensors. *Science (New York, N.Y.)*, *311*(5767), 1592–1595. doi:10.1126/science.1122588

46. Tseng, Y.-C., Chang, J.-S., Lin, S., Chao, S. D., & Liu, C.-H. (2012). 3,4-Methylenedioxymethylamphetamine detection using a microcantilever-based biosensor. *Sensors and Actuators A: Physical*, *182*, 163–167. doi:10.1016/j.sna.2012.05.036

47. Watari, M., Galbraith, J., Lang, H., Sousa, M., Hegner, M., Gerber, C., Horton, M. A, Mckendry, R. A. (2007). Investigating the Molecular Mechanisms of In-Plane Investigating the Molecular Mechanisms of In-Plane Mechanochemistry on Cantilever Arrays. *Journal of the American Chemical Society*, *129*(3), 601–609.

48. Ndieyira, J. W., Watari, M., Barrera, A. D., Zhou, D., Vögtli, M., Batchelor, M., Cooper, M. A., Strunz, T., Horton, M. A., Abell, C., Rayment, T., Aeppli, G., Mckendry, R. A. (2008). Nanomechanical detection of antibiotic- mucopeptide binding in a model for superbug drug resistance. *Nature Nanotechnology*, *3*, 691–696.

49. Ilic, B., Czaplewski, D., Craighead, H. G., Neuzil, P., Campagnolo, C., & Batt, C. (2000). Mechanical resonant immunospecific biological detector. *Applied Physics Letters*, *77*(3), 450–452. doi:10.1063/1.127006

50. Sungkanak, U., Sappat, A., Wisitsoraat, A., Promptmas, C., & Tuantranont, A. (2010). Ultrasensitive detection of Vibrio cholerae O1 using microcantilever-based biosensor with dynamic force microscopy. *Biosensors & bioelectronics*, *26*(2), 784–789. doi:10.1016/j.bios.2010.06.024

51. Lee, S., Cho, J., Lee, Y., Jeon, S., Cha, H. J., & Moon, W. (2012). Measurement of Hepatitis B Surface Antigen Concentrations Using a Piezoelectric Microcantilever as a Mass Sensor. *Journal of Sensors*, *2012*(217958), 1–6. doi:10.1155/2012/217958

52. Mcfarland, A. W., & Colton, J. S. (2005). Role of material microstructure in plate stiffness with relevance to microcantilever sensors. *J. Micromech. Microeng.*, *15*, 1060–1067. doi:10.1088/0960-1317/15/5/024

53. Mcfarland, A. W. (2004). Production and analysis of microcantilever parts. *PhD. Thesis, Georgia Institute of Technology, USA*, (November).

54. Tamayo, J., Ramos, D., Mertens, J., & Calleja, M. (2006). Effect of the adsorbate stiffness on the resonance response of microcantilever sensors. *Applied Physics Letters*, *89*(224104), 1–3. doi:10.1063/1.2388925

55. Grüter, R. R., Khan, Z., Paxman, R., Ndieyira, J. W., Dueck, B., Bircher, B. A., Yang, J. L., Drechsler, U., Despont, M., McKendry, R. A., Hoogenboom, B. W. (2010). Disentangling mechanical and mass effects on nanomechanical resonators. *Applied Physics Letters*, *96*(023113), 1–3. doi:10.1063/1.3285169

56. Vančura, C., Dufour, I., Heinrich, S. M., Josse, F., & Hierlemann, A. (2008). Analysis of resonating microcantilevers operating in a viscous liquid environment. *Sensors and Actuators A: Physical*, *141*(1), 43–51. doi:10.1016/j.sna.2007.07.010

57. Youssry, M., Belmiloud, N., Caillard, B., Ayela, C., Pellet, C., & Dufour, I. (2011). A straightforward determination of fluid viscosity and density using microcantilevers: From experimental data to analytical expressions. *Sensors and Actuators A: Physical*, *172*(1), 40–46. doi:10.1016/j.sna.2011.02.025

58. Heinisch, M., Reichel, E. K., & Jakoby, B. (2013). U-shaped, wire-based oscillators for rheological applications bridging the gap between100 Hz and 100 kHz. *Transducers 2013, Barcelona, Spain, 16-20 June 2013*, 90–93.

59. Lee, J., Shen, W., Payer, K., Burg, T. P., & Manalis, S. R. (2010). Toward Attogram Mass Measurements in Solution with Suspended Nanochannel Resonators. *Nano Lett.*, *10*(7), 2537–2542.

60. Weng, Y., Delgado, F. F., Son, S., Burg, T. P., Wasserman, S. C., & Manalis, S. R. (2011). Mass sensors with mechanical traps for weighing single cells in different fluids. *Lab on a chip*, *11*(24), 4174–80. doi:10.1039/c1lc20736a

61. Khan, M. F., Schmid, S., Larsen, P. E., Davis, Z. J., Yan, W., Stenby, E. H., & Boisen,A. (2013). Online measurement of mass density and viscosity of pL fluid samples with suspended microchannel resonator. *Sensors and Actuators B: Chemical*, *185*, 456–461. doi:10.1016/j.snb.2013.04.095

62. Burg, T., Sader, J., & Manalis, S. (2009). Nonmonotonic Energy Dissipation in Microfluidic Resonators. *Physical Review Letters*, *102*(228103), 1–4. doi:10.1103/PhysRevLett.102.228103

63. Cabal, A., Ross, D. S., Lebens, J. A., & Trauernicht, D. P. (2005). Thermal actuator with optimized heater for liquid drop ejectors. *Sensors and Actuators A: Physical*, *123-124*, 946–59. doi:10.1016/j.sna.2005.05.015

64. Han, L.-H., & Chen, S. (2005). Wireless bimorph micro-actuators by pulsed laser heating. *Sensors and Actuators A: Physical*, *121*(1), 35–43. doi:10.1016/j.sna.2004.12.012

65. Roy, P. K., & Ganesan, N. (1995). Transient response of a cantilever beam subjected to an impulse load. *Journal of Sound and Vibration*, *183*(5), 873–880.

66. Moulin, A. M., Stephenson, R. J., & Welland, M. E. (1997). Micromechanical thermal sensors : Comparison of experimental results and simulations. *J. Vac. Sci. Technol. B*, *15*(November 1996), 590–596.

67. Aioubi, M. Y. Al. (2004). Deflection and load characterisation of bimorph actuators for bioMEMS and other applications. *Microelectronic Engineering*, *73-74*, 898–903. doi:10.1016/j.mee.2004.03.072

68. Oguibe, C. N., & Webb, D. C. (2000). Large deflection analysis of multilayer cantilever beams subjected to impulse loading. *Computers and Structures*, *78*, 537–547.

69. Alexander, S., Hellemans, L., Marti, O., Schneir, J., Elings, V., Hansma, P. K., Longmire, M., Gurley, J. (1989). An atomic-resolution atomic-force microscope implemented using an optical lever. *Journal of Applied Physics*, *65*(1), 164–167. doi:10.1063/1.342563

70. Peng, W., Xiao, Z., & Farmer, K. R. (2003). Optimisation of Thermally Actuated Bimorph Cantilevers for Maximum Deflection. *Nanotechnology*, *1*, 376 – 379.

71. Fernando, S., Austin, M., & Chaffey, J. (2007). Improved cantilever profiles for sensor elements. *Journal of Physics D: Applied Physics*, *40*(24), 7652–7655. doi:10.1088/0022-3727/40/24/009

72. Kelling, S., Paoloni, F., Huang, J., Ostanin, V. P., & Elliott, S. R. (2009). Simultaneous readout of multiple microcantilever arrays with phase-shifting interferometric microscopy. *The Review of scientific instruments*, *80*(093101), 1–8. doi:10.1063/1.3212667

73. Nordström, M., Keller, S., Lillemose, M., Johansson, A., Dohn, S., Haefliger, D., Blagoi, G., Havsteen-Jakobsen, M., Boisen, A. (2008). SU-8 Cantilevers for Bio/chemical Sensing; Fabrication, Characterisation and Development of Novel Read-out Methods. *Sensors*, *8*, 1595–1612.

74. Zimmermann, M., Volden, T., Kirstein, K., Hafizovic, S., Lichtenberg, J., Brand, O., & Hierlemann, A. (2008). A CMOS-based integrated-system architecture for a static cantilever array. *Sensors and Actuators B: Chemical*, *131*, 254–264. doi:10.1016/j.snb.2007.11.016

75. Williamson Hodge, L. A., Dunn, R. J., Robert, H., & Huq, S. E. (2011). Polymer Microcantilevers for Thermal Sensing. *IEEE Sensors Conference Proceedings*, (28-31 Oct. 2011), 671–674.

76. Loui, A., Goericke, F. T., Ratto, T. V, Lee, J., Hart, B. R., & King, W. P. (2008). The effect of piezoresistive microcantilever geometry on cantilever sensitivity during surface stress chemical sensing. *Sensors and Actuators A Physical*, *147*, 516–521. doi:10.1016/j.sna.2008.06.016

77. Fragakis, J., Chatzandroulis, S., Papadimitriou, D., & Tsamis, C. (2005). Simulation of capacitive type bimorph humidity sensors. *Second Conference on Microelectronics, Microsystems and Nanotechnology*, 305–309.

78. Yi, J. W., Shih, W. Y., Mutharasan, R., & Shih, W.-H. (2003). In situ cell detection using piezoelectric lead zirconate titanate-stainless steel cantilevers. *Journal of Applied Physics*, *93*(1), 619–625. doi:10.1063/1.1524022

79. Kim, S., Kim, K. C., & Kihm, K. D. (2007). Near-Field thermometry Sensor based on the thermal resonance of a Microcantilever in Aqueous Medium. *Sensors & Actuators: B. Chemical*, *7*, 3156–3165.

80. Boisen, A., Thaysen, J., Jensenius, H., & Hansen, O. (2000). Environmental sensors based on micromachined cantilevers with integrated read-out. *Ultramicroscopy*, *82*(1-4), 11–6. Retrieved from http://www.ncbi.nlm.nih.gov/pubmed/10741646

81. Olmstead, M. A., Amer, N. M., & Kohn, S. (1983). Photothermal Displacement Spectroscopy: An Optical Probe for Solids and Surfaces. *Applied Physics A*, *32*, 141–154.

82. Lau, G. K., Duc, T. C., Goosen, J. F. L., Sarro, P. M., & Keulen, F. Van. (2007). An in-plane thermal unimorph using confined polymers. *Journal of Micromechanics and Microengineering*, *17*(7), S174–S183. doi:10.1088/0960-1317/17/7/S15

83. Li, Y., Vancura, C., Lichtenberg, C. H. J., & Baltes, B. H. (2003). Very high Q-factor in water achieved by monolithic resonant cantilever sensor with fully integrated feedback. *Sensors 2003*, 809–813.

84. Li, Y., Lichtenberg, J., Kirstein, K., Hierlemann, A., & Josse, F. (2007). Liquid-Phase Chemical and Biochemical Detection, *79*(4), 1646–1654.

85. Maraldo, D., Rijal, K., Campbell, G., & Mutharasan, R. (2007). Method for label-free detection of femtogram quantities of biologics in flowing liquid samples. *Analytical chemistry*, *79*(7), 2762–2770. doi:10.1021/ac0621726

86. Niezrecki, C., Brei, D., Balakrishnan, S., & Moskalik, A. (2001). Piezoelectric Actuation : State of the Art. *The Shock and Vibration Digest*, *33*, 269–280. doi:10.1177/058310240103300401

87. Seena, V., Rajorya, A., Pant, P., Mukherji, S., & Rao, V. R. (2009). Polymer microcantilever biochemical sensors with integrated polymer composites for electrical detection. *Solid State Sciences*, *11*(9), 1606–1611. doi:10.1016/j.solidstatesciences.2009.06.009

88. Ibbotson, R. H., Dunn, R. J., Djakov, V., Ferrigno, P. K., & Huq, S. E. (2008). Polyimide microcantilever surface stress sensor using low-cost, rapidly-interchangeable, spring-loaded microprobe connections. *Microelectronic Engineering*, *85*(5-6), 1314–1317. doi:10.1016/j.mee.2007.12.065

89. TOPAS Advanced Polymers GmbH. (2006). Cyclic Olefin Copolymer (COC) Manufacturers Data Sheet. *www.topas.com*.

90. Urwyler, P., Schift, H., Gobrecht, J., Häfeli, O., Altana, M., Battiston, F., & Müller, B. (2011). Surface patterned polymer micro-cantilever arrays for sensing. *Sensors and Actuators A: Physical*, *172*(1), 2–8. doi:10.1016/j.sna.2010.12.007

91. HD Microsystems GmbH. (2009). Product Bulletin PI-2600 Series – Low Stress Applications, (September), 1–4.

92. Mata, A., & Fleischman, A. J. (2005). Characterization of Polydimethylsiloxane (PDMS) Properties for Biomedical Micro / Nanosystems. *Biomedical Microdevices*, *7*(4), 281–293.

93. Joshi, M., Pinto, R., Rao, V. R., & Mukherji, S. (2007). Silanization and antibody immobilization on SU-8. *Applied Surface Science*, *253*, 3127–3132. doi:10.1016/j.apsusc.2006.07.017

94. Joshi, M., Kale, N., Lal, R., Ramgopal Rao, V., & Mukherji, S. (2007). A novel dry method for surface modification of SU-8 for immobilization of biomolecules in Bio-MEMS. *Biosensors & bioelectronics*, *22*(11), 2429–2435. doi:10.1016/j.bios.2006.08.045

95. Butt, H.-J. (1996). A Sensitive Method to Measure Changes in the Surface Stress of Solids. *Journal of Colloid and Interface Science*, *180*(1), 251–260. doi:10.1006/jcis.1996.0297

96. Zhang, Y., Kim, H. H., Kwon, B. H., & Go, J. S. (2013). Polymeric cantilever sensors functionalized with multiamine supramolecular hydrogel. *Sensors and Actuators B: Chemical*, *178*, 47–52. doi:10.1016/j.snb.2012.12.072

97. Ghatkesar, M. K., Barwich, V., Braun, T., Bredekamp, A. H., Drechsler, U., Despont, M., Lang, H. P., Hegner, M., Gerber, Ch Gerber, C. (2004). Real-Time Mass Sensing by Nanomechanical Resonators in Fluid. *Sensors Conference Proceedings*, *3*(5), 1060–1063.

98. Savran, C. A., Burg, T. P., Fritz, J., & Manalis, S. R. (2003). Microfabricated mechanical biosensor with inherently differential readout. *Applied Physics Letters*, *83*(8), 1659–1661. doi:10.1063/1.1605238

99. Butt, H.-J., Skladal, P., Raiteri, R., & Grattarola, M. (2001). Micromechanical cantilever-based biosensors. *Sensors and Actuators B: Chemical*, *79*, 115–126.

100. Shu, W., Laue, E. D., & Seshia, A. A. (2007). Investigation of biotin-streptavidin binding interactions using microcantilever sensors. *Biosensors & bioelectronics*, *22*(9-10), 2003–9. doi:10.1016/j.bios.2006.08.047

101. Gooding, J. J. (2006). Nanoscale biosensors: significant advantages over larger devices? *Small (Weinheim an der Bergstrasse, Germany)*, *2*(3), 313–5. doi:10.1002/smll.200500477

102. Thaysen, J., Marie, R., & Boisen, A. (2001). Cantilever-based bio-chemical sensor in a microliquid handling system. *Micro Electro Mechanical Systems, 2001. MEMS 2001. The 14th IEEE International Conference on 25-25 Jan. 2001*, 401–404.

103. Arlett, J. L., & Roukes, M. L. (2010). Ultimate and practical limits of fluid-based mass detection with suspended microchannel resonators. *Journal of Applied Physics*, *108*(084701), 1–12. doi:10.1063/1.3475151

104. Yan, D., Khajepour, A., & Mansour, R. (2003). Modeling of two-hot-arm horizontal. *J. Micromech. Microeng.*, *13*, 312–322.

105. Butler, J. T., Bright, V. M., & Cowan, W. D. (1999). Average power control and positioning of polysilicon thermal actuators. *Sensors and Actuators A: Physical*, *72*, 88–97.

106. Hosseinian, E., Theillet, P.-O., & Pierron, O. N. (2013). Temperature and humidity effects on the quality factor of a silicon lateral rotary micro-resonator in atmospheric air. *Sensors and Actuators A: Physical*, *189*, 380–389. doi:10.1016/j.sna.2012.09.020

107. Urwyler, P., Köser, J., Schift, H., Gobrecht, J., Battiston, F., & Müller, B. (2011). Injection Moulded Micro-Cantilever Arrays for Detecting DNA Sequences. In *17th Swiss Conference on Biomaterials, May 4th , 2011, Yverdon-les-Bains, Switzerland*.

108. Goeders, K. M., Colton, J. S., & Bottomley, L. A. (2008). Microcantilevers : Sensing Chemical Interactions via Mechanical Motion. *Chem. Rev.*, *108*, 522–542.

109. Mcfarland, A. W., & Colton, J. S. (2005). Chemical Sensing With Micromolded Plastic Microcantilevers. *Journal of Microelectromechanical Systems*, *14*(6), 1375–1385.

110. Nelson, B. J., Zhou, Y., & Vikramaditya, B. (1998). Sensor based microassembly of hybrid MEMS devices. *IEEE Control Systems*, (December 98), 35–45.

111. Piletsky, S. A., Piletskaya, E. V., Elgersma, A. V., Yano, K., Karube, I., Parhometz, Y. P., & El'skaya, A. V. (1995). Atrazine sensing by molecularly imprinted membranes. *Biosensors and Bioelectronics*, *10*, 959–964. doi:10.1016/0956-5663(95)99233-B

112. Bosco, F. G., Bache, M., Hwu, E.-T., Chen, C. H., Andersen, S. S., Nielsen, K. A., Keller, S.S., Jeppesen, J.O., Hwang, I.-S., Boisen, A. (2012). Statistical analysis of DNT detection using chemically functionalized microcantilever arrays. *Sensors and Actuators B: Chemical*, *171-172*, 1054–1059. doi:10.1016/j.snb.2012.06.033

113. Quan, X., Sun, Y., Heiskanen, A., Wolff, A., Grutter, P., & Boisen, A. (2012). Investigation of cleaning and regeneration methods for reliable construction of DNA cantilever biosensors. In *9th International Nanomechanical Sensing Workshop (6-8 June 2012)* (pp. 2–3).

114. Keller, S. S., Feidenhans, N., Fisker-bødker, N., Soulat, D., Greve, A., Plackett, D. V, & Boisen, A. (2011). Microelectronic Engineering Fabrication of biopolymer cantilevers using nanoimprint lithography. *Microelectronic Engineering*, *88*(8), 2294–2296. doi:10.1016/j.mee.2011.02.095

115. Park, K., Lee, J., Zhang, Z. M., & King, W. P. (2007). Topography imaging with a heated atomic force microscope cantilever in tapping mode. *The Review of scientific instruments*, *78*(043709), 1–7. doi:10.1063/1.2721422

116. Grimes, C. A., & Kouzoudis, D. (2000). Remote query measurement of pressure, fluid-flow velocity, and humidity using magnetoelastic thick-film sensors. *Sensors and actuators. A, Physical*, *84*(3), 205–212. Retrieved from http://www.ncbi.nlm.nih.gov/pubmed/12143886

117. Cakmak, O., Elbuken, C., Ermek, E., Mostafazadeh, A., Baris, I., Erdem Alaca, B., Kavakli, I. H., Urey, H. (2013). Microcantilever based disposable viscosity sensor for serum and blood plasma measurements. *Methods (San Diego, Calif.), IN PRESS*. doi:10.1016/j.ymeth.2013.07.009

118. Leis, J., Allman, S. L., & Mahmud, K. K. (2010). Estimating Gas Concentration using a Microcantilever-Based Electronic Nose. *Digital Signal Processing*, *24*(10), 1229–1237.

119. Gaster, R. S., Hall, D. A., & Wang, S. X. (2011). nanoLAB: an ultraportable, handheld diagnostic laboratory for global health. *Lab on a chip*, *11*(5), 950–956. doi:10.1039/c0lc00534g

120. Nanosurf®. EasyScan 2 AFM Portable atomic force microscope. *Web Page (http://www.nanoscience.com/products/afm/easyscan-2-afm/) Accessed 03 Feb 2014.*

121. Noeth, N., Keller, S. S., & Boisen, A. (2014). Integrated Cantilever-Based Flow Sensors with Tunable Sensitivity for In-Line Monitoring of Flow Fluctuations in Microfluidic Systems. *Sensors*, *14*, 229–244. doi:10.3390/s140100229

122. Tamayo, J., Humphris, A. D., Malloy, A. M., & Miles, M. J. (2001). Chemical sensors and biosensors in liquid environment based on microcantilevers with amplified quality factor. *Ultramicroscopy*, *86*, 167–173. Retrieved from http://www.ncbi.nlm.nih.gov/pubmed/11215620

123. Waggoner, P. S., Varshney, M., & Craighead, H. G. (2009). Detection of prostate specific antigen with nanomechanical resonators. *Lab on a chip*, *9*(21), 3095–3099. doi:10.1039/b907309b

124. Maloney, N., Lukacs, G., Nugaeva, N., Grange, W., Ramseyer, J. P., Jensen, J., & Hegner, M. (2012). Fibre Optic Readout of Microcantilever Arrays for Fast Microorganism Growth Detection. *Journal of Sensors*, *2012*(405281), 1–6. doi:10.1155/2012/405281

125. Capobianco, J., Shih, W.-H., Leu, J.-H., Lo, G. C.-F., & Shih, W. Y. (2012). Label Free Detection of White Spot Syndrome Virus Using Lead Magnesium Niobate-Lead Titanate Piezoelectric Microcantilever Sensors. *Biosensors & bioelectronics*, *26*(2), 964–969. doi:10.1016/j.bios.2010.08.004.Label

126. Bergese, P., Bontempi, E., Chiari, M., Colombi, P., Damin, F., Depero, L. E., Oliviero, G., Pirri, G., Zucca, M. (2007). Investigation of a biofunctional polymeric coating deposited onto silicon microcantilevers. *Applied Surface Science*, *253*(9), 4226–4231. doi:10.1016/j.apsusc.2006.09.036

127. Tabard-Cossa, V., Godin, M., Burgess, I. J., Monga, T., Lennox, R. B., & Grutter, P. (2007). Microcantilever-Based Sensors : Effect of Morphology , Adhesion , and Cleanliness of the Sensing Surface on Surface Stress. *Anal. Chem.*, *79*(21), 8136–8143.

128. Castelino, K., Kannan, B., & Majumdar, A. (2005). Characterization of Grafting Density and Binding Efficiency of DNA and Proteins on Gold Surfaces. *Langmuir*, *29*(15), 1956–1961.

129. Nair, P. R., & Alam, M. A. (2010). Theory of "Selectivity" of label-free nanobiosensors: A geometro-physical perspective. *Journal of Applied Physics*, *107*(064701), 1–6. doi:10.1063/1.3310531

130. National Cancer Institute. Prostate-Specific Antigen (PSA) Test. *(http://www.cancer.gov/cancertopics/factsheet/detection/PSA). Accessed 06 Feb 2014.*

131. Arlett, J. L., Myers, E. B., & Roukes, M. L. (2011). Comparative advantages of mechanical biosensors. *Nature nanotechnology*, *6*(4), 203–215. doi:10.1038/nnano.2011.44

132. Shu, W., Laurenson, S., Knowles, T. P. J., Ko Ferrigno, P., & Seshia, A. A. (2008). Highly specific label-free protein detection from lysed cells using internally

referenced microcantilever sensors. *Biosensors & bioelectronics*, *24*, 233–237. doi:10.1016/j.bios.2008.03.036

133. Gotszalk, T., Grabiec, P., & Rangelow, I. W. (2003). Calibration and examination of piezoresistive Wheatstone bridge cantilevers for scanning probe microscopy. *Ultramicroscopy*, *97*, 385–389. doi:10.1016/S0304-3991(03)00065-2

134. Pirri, G., Damin, F., Chiari, M., Bontempi, E., Depero, L. E., Molecolare, R., & Chimica, S. (2004). Characterization of A Polymeric Adsorbed Coating for DNA Microarray Glass Slides. *Anal. Chem.*, *76*(5), 1352–1358.

135. Cha, B. H., Lee, S.-M., Park, J. C., Hwang, K. S., Kim, S. K., Lee, Y.-S., Ju, B.-K., Kim, T. S. (2009). Detection of Hepatitis B Virus (HBV) DNA at femtomolar concentrations using a silica nanoparticle-enhanced microcantilever sensor. *Biosensors & bioelectronics*, *25*(1), 130–135. doi:10.1016/j.bios.2009.06.015

136. Hwang, K. S., Jeon, H. K., Lee, S.-M., Kim, S. K., & Kim, T. S. (2009). Quantification of disease marker in undiluted serum using an actuating layer-embedded microcantilever. *Journal of Applied Physics*, *105*(102017), 1–7. doi:10.1063/1.3116105

137. Von Muhlen, M. G., Brault, N. D., Knudsen, S. M., Jiang, S., & Manalis, S. R. (2010). Label-free biomarker sensing in undiluted serum with suspended microchannel resonators. *Analytical chemistry*, *82*(5), 1905–10. doi:10.1021/ac9027356

138. Capobianco, J. A, Shih, W. Y., Adams, G. P., & Shih, W.-H. (2011). Label-free Growth Receptor-2 Detection and Dissociation Constant Assessment in Diluted Human Serum Using a Longitudinal Extension Mode of a Piezoelectric Microcantilever Sensor. *Sensors and actuators. B, Chemical*, *160*(1), 349–356. doi:10.1016/j.snb.2011.07.060

139. Loo, L., Capobianco, J. A., Wu, W., Gao, X., Shih, W. Y., Pourrezaei, K., Robinson, M. K., Adams, G. P. (2011). Highly sensitive detection of HER2 extracellular domain (ECD) in the serum of breast cancer patients by piezoelectric microcantilevers (PEMS). *Anal. Chem.*, *83*(9), 3392–3397. doi:10.1021/ac103301r.Highly

140. Lee, J. H., Kim, T. S., & Yoon, K. H. (2004). Effect of mass and stress on resonant frequency shift of functionalized Pb(Zr[sub 0.52]Ti[sub 0.48])O[sub 3] thin film microcantilever for the detection of C-reactive protein. *Applied Physics Letters*, *84*(16), 3187–3189. doi:10.1063/1.1712028

141. Marie, R., Thaysen, J., & Voge, C. B. (2003). A cantilever-based sensor for thermal cycling in buffer solution. *Microelectronic Engineering*, *67 - 68*, 893 – 898.

142. Álvarez, M., Tamayo, J., Plaza, J. A., Zinoviev, K., Domínguez, C., & Lechuga, L. M. (2006). Dimension dependence of the thermomechanical noise of microcantilevers. *Journal of Applied Physics*, *99*(024910), 1–7. doi:10.1063/1.2164537

143. Lee, I., Park, K., & Lee, J. (2013). Precision density and volume contraction measurements of ethanol–water binary mixtures using suspended microchannel resonators. *Sensors and Actuators A: Physical*, *194*, 62–66. doi:10.1016/j.sna.2013.01.046

144. Ansari, M. Z., & Cho, C. (2011). Thermal Characteristics of Microcantilever Biosensors. *Biostec 2010*, 166–176.

145. Calleja, M., Tamayo, J., Nordström, M., & Boisen, A. (2006). Low-noise polymeric nanomechanical biosensors. *Applied Physics Letters*, *88*(113901), 1–3. doi:10.1063/1.2187437

146. Roozeboom, C. L., Hopcroft, M. A., Smith, W. S., Sim, J. Y., Wickeraad, D. A., Hartwell, P. G., & Pruitt, B. L. (2013). Integrated Multifunctional Environmental Sensors. *Journal of Microelectromechanical Systems*, *22*(3), 779–793.

147. Roozeboom, C. L., Salgado, J. F., Hopcroft, M. A., & Pruitt, B. L. (2013). Integrated sensor cross-sensitivity analysis. *Transducers Proceedings 2013*, (June), 30–34.

148. Cho, Y. H., Collard, D., Buchaillot, L., Conseil, F., & Kim, B. J. (2005). Fabrication and optimization of bimorph micro probes for the measurement of individual biocells. *Microsystem Technologies*, *12*(1-2), 30–37. doi:10.1007/s00542-005-0010-1

149. Ataka, M., Omodaka, A., Takeshima, N., & Fujita, H. (1993). Fabrication and Operation of Polyimide Bimorph Actuators for a Ciliary Motion System. *Journal of Microelectromechanical Systems*, *2*(4), 146–150.

150. Zhou, J. W. L., Chan, H., To, T. K. H., Lai, K. W. C., & Li, W. J. (2004). Polymer MEMS Actuators for Underwater Micromanipulation. *IEEE/ASME Transactions on Mechatronics*, *9*(2), 334–342.

151. Urbiztondo, M. A., Peralta, A., Pellejero, I., Sesé, J., Pina, M. P., Dufour, I., & Santamaría, J. (2012). Sensors and Actuators B : Chemical Detection of organic vapours with Si cantilevers coated with inorganic (zeolites) or organic (polymer) layers. *Sensors & Actuators: B. Chemical*, *171-172*, 822–831. doi:10.1016/j.snb.2012.05.078

152. Keller, S. S., Gammelgaard, L., Jensen, M. P., Schmid, S., Davis, Z. J., & Boisen, A. (2011). Deposition of biopolymer films on micromechanical sensors. *Microelectronic Engineering*, *88*(8), 2297–2299. doi:10.1016/j.mee.2011.02.093

153. Sager, K., Schroth, A., Nakladal, A., & Gerlach, G. (1996). Humidity-dependent mechanical properties of polyimide films and their use for IC-compatible humidity sensors. *Sensors and Actuators A: Physical*, *53*, 330–334.

154. Lammel, G., Schweizer, S., & Renaud, P. (2002). Chapter 2: Basics for a thermally actuated micromirror. *Optical Microscanners and Microspectrometers using Thermal Bimorph Actuators*, 27–64.

155. Timoshenko, S. (1925). Analysis of bi-metal thermostats. *Journal of the Optical Society of America*, *11*(3), 233–255.

156. Chu, W., Mehregany, M., & Mullen, R. L. (1993). Analysis of tip deflection and force of a bimetallic cantilever microactuator. *J. Micromech. Microeng.*, *4*, 3–7.

157. Buhler, J., Funk, J., Paul, O., Steiner, F.-P., & Baltes, H. (1995). Thermally actuated CMOS micromirrors. *Sensors and Actuators A: Physical*, *46*, 572 – 575.

158. Garcia, E., & Lobontiu, N. (2004). Induced-strain multimorphs for microscale sensory actuation design. *Smart Materials and Structures*, *13*(4), 725–732. doi:10.1088/0964-1726/13/4/010

159. Bhargava, P., Chuang, K. C., Chen, K., & Zehnder, A. (2006). Moisture Diffusion Properties of HFPE-II-52 Polyimide. *Journal of Applied Polymer Science*, *102*(4), 3471–3479.

160. Djakov, V., Huq, E., & Dunn, R. J. (2009). Fluid Probe (Patent No. US 2009/0084167 A1). *Fluid*.

161. Buchhold, R., Nakladal, A., Gerlach, G., Sahre, K., & Eichhorn, K.-J. (1998). Mechanical stress in micromachined components caused by humidity-induced in-plane expansion of thin polymer films. *Thin Solid Films*, *312*, 232 – 239.

162. Lahokallio, S., Saarinen, K., & Frisk, L.. Changes in Water Absorption and Modulus of Elasticity of Flexible Printed Circuit Board Materials in High Humidity Testing. Microelectronics and Packaging Conference (EMPC), 2011 18th European, IEEE, Print ISBN: 978-1-4673-0694-2

163. Alaioubi, M. Y., Djakov, V., Huq, S. E., & Prewett, P. D. (2004). Deflection and load characterisation of bimorph actuators for bioMEMS and other applications. *Microelectronic Engineering*, *73-74*, 898–903. doi:10.1016/j.mee.2004.03.072

164. Buck, A. L. (1981). New equations for computing vapour pressure and enhancement factor. *Journal of Applied Meteorology*, *20*, 1527 – 1532.

165. Hu, Z., Seeley, T., Kossek, S., & Thundat, T. (2004). Calibration of optical cantilever deflection readers. *Review of Scientific Instruments*, *75*(2), 400–404. doi:10.1063/1.1637457

166. Groen, F. C. A., Young, I. T., & Ligthart, G. (1985). A comprarison of different focus functions for use in autofocus algorithms. *Cytometry*, *6*, 81 – 91.

167. Sager, K., Schroth, A., Nakladal, A., & Gerlach, G. (1996). Humidity dependent mechanical properties of polyimide films and their use for IC compatible humidity sensors. *Sensors and Actuators A: Physical*, *53*, 330–334.

168. Tsilingiris, P. T. (2008). Thermophysical and transport properties of humid air at temperature range between 0 and 100°C. *Energy Conversion and Management*, *49*(5), 1098–1110. doi:10.1016/j.enconman.2007.09.015

169. Lemaire, E., Heinisch, M., Caillard, B., Jakoby, B., & Dufour, I. (2013). Comparison and experimental validation of two potential resonant viscosity sensors in the kilohertz range. *Measurement Science and Technology*, *24*(084005), 1–9. doi:10.1088/0957-0233/24/8/084005

170. Friedrich, D., Goetz, K., & Lindner, G. (2012). A PVDF-driven cantilever resonator for density and viscosity determination of fluids. *Proceedings of ICMS 2012 - The 14th International Meeting on Chemical Sensors*, 1429–1432. doi:10.5162/IMCS2012/P2.2.9

171. Baskurt, O. K., & Meiselman, H. J. (2003). Blood rheology and hemodynamics. *Seminars in thrombosis and hemostasis*, *29*(5), 435–450. doi:10.1055/s-2003-44551

172. Dintenfass, L. (1966). Effect of Velocity Gradient on the Clotting Time of Blood and on the Consistency of Clots Formed in Vitro. *Circulation Research*, *18*(4), 349–356. doi:10.1161/01.RES.18.4.349

173. Yesner, R., Hurwitz, A., Rich, S. R., Roth, W., & Gordon, M. E. (1951). Preliminary observations on blood coagulation utilizing ultrasonics for continuous measurement of viscosity. *Yale Journal of Biology and Medicine*, *24*(3), 231 – 235.

174. Evans, P. A., Hawkins, K., Lawrence, M., Williams, R. L., Barrow, M. S., Thirumalai, N., & Williams, P. R. (2008). Rheometry and associated techniques for blood coagulation studies. *Medical engineering & physics*, *30*(6), 671–679. doi:10.1016/j.medengphy.2007.08.005

175. Waigh, T. A. (2005). Microrheology of complex fluids. *Reports on Progress in Physics*, *68*(3), 685–742. doi:10.1088/0034-4885/68/3/R04

176. Evans, P. A., Hawkins, K., Williams, P. R., & Williams, R. L. (2008). Rheometrical detection of incipient blood clot formation by Fourier transform mechanical spectroscopy. *Journal of Non-Newtonian Fluid Mechanics*, *148*, 122–126. doi:10.1016/j.jnnfm.2007.04.020

177. Sader, J. E. (1998). Frequency response of cantilever beams immersed in viscous fluids with applications to the atomic force microscope. *Journal of Applied Physics*, *84*(1), 64–76.

178. Hennemeyer, M., Burghardt, S., & Stark, R. W. (2008). Cantilever Micro-rheometer for the Characterization of Sugar Solutions. *Sensors*, *8*, 10–22.

179. Sheely, M. (1931). Glycerol Viscosity Tables. *Industrial and Engineering Chemistry*, *24*(9), 1060 – 1064.

180. Dunn, R. J., Huq, S. E., Djakov, V., & Boothe, J. An Integrated Microactuator Fluid Probe. *Article in preparation*, 1–4.

181. Agoston, A., Keplinger, F., & Jakoby, B. (2005). Evaluation of a vibrating micromachined cantilever sensor for measuring the viscosity of complex organic liquids. *Sensors and Actuators A: Physical*, *123-124*, 82–86. doi:10.1016/j.sna.2005.02.020

182. HD Microsystems GmbH. (2008). Product Bulletin PI-2562 Polyimide. *Technical Information*, (September), 1–4.

183. Pamula, V. K., Jog, A., & Fair, R. B. (2001). Mechanical Property Measurement of Thin-Film Gold using Thermally Actuated Bimetallic Cantilever Beams. In *Technical Proceedings of the 2001 International Conference on Modeling and Simulation of Microsystems* (pp. 4–7).

184. Dufour, I., Maali, a., Amarouchene, Y., Ayela, C., Caillard, B., Darwiche, A., Guirardel, M., Kellay, H., Lemaire, E., Mathieu, F., Pellet, C., Saya, D., Youssry, M., Nicu, L., Colin, A. (2012). The Microcantilever: A Versatile Tool for Measuring the Rheological Properties of Complex Fluids. *Journal of Sensors*, *2012*(1), 1–9. doi:10.1155/2012/719898

185. Kim, K. J., & King, W. P. (2009). Thermal conduction between a heated microcantilever and a surrounding air environment. *Applied Thermal Engineering*, *29*, 1631–1641. doi:10.1016/j.applthermaleng.2008.07.019

186. Kim, K. J., Park, K., Lee, J., Zhang, Z. M., & King, W. P. (2007). Nanotopographical imaging using a heated atomic force microscope cantilever probe. *Sensors and Actuators A: Physical*, *136*(1), 95–103. doi:10.1016/j.sna.2006.10.052

187. Rangelow, I. W., Gotszalk, T., Abedinov, N., Grabiec, P., & Edinger, K. (2001). Thermal nano-probe. *Microelectronic Engineering*, *57*, 737–748.

188. Haeberle, W., Pantea, M., & Hoerber, J. K. H. (2006). Nanometer-scale heat-conductivity measurements on biological samples. *Ultramicroscopy*, *106*(8-9), 678–86. doi:10.1016/j.ultramic.2006.01.016

189. Sehr, H., Tomlin, I. S., Huang, B., Beeby, S. P., Evans, A. G. R., Brunnschweiler, A., Ensell, G. J., Schabmueller, C. G. J., Niblock, T. E. G. (2002). Time constant and lateral resonances of thermal vertical bimorph actuators. *J. Micromech. Microeng.*, *12*, 410–413.

190. Al Aioubi, M., Prewett, P. D., Huq, S. E., Djakov, V., & Michette, A. G. (2006). A novel MOEMS based adaptive optics for X-ray focusing. *Microelectronic Engineering*, *83*, 1321–1325. doi:10.1016/j.mee.2006.01.107

191. Al Aioubi, M., Prewett, P. D., Huq, S. E., Djakov, V., & Michette, A. G. (2007). Micro-opto-electro-mechanical system for X-ray focusing. *Microelectronic Engineering*, *84*, 1252–1255. doi:10.1016/j.mee.2007.01.167

192. Rangelow, I. W., Ivanov, T., Ivanova, K., Volland, B. E., Grabiec, P., Sarov, Y., Persaud, A., Gotszalk, T., Zawierucha, P., Zielony, M., Dontzov, D., Schmidt, B., Zier, M., Nikolov, N., Kostic, I., Engl, W., Sulzbach, T., Mielczarski, J., Kolb, S., Latimier, Du P., Pedreau, R., Djakov, V., Huq, S.E., Edinger, K., Fortagne, O., Almansa, A., Blom, H. O. (2007). Piezoresistive and self-actuated 128-cantilever arrays for nanotechnology applications. *Microelectronic Engineering*, *84*, 1260–1264. doi:10.1016/j.mee.2007.01.219

193. Schneider, A., Ibbotson, R. H., Dunn, R. J., & Huq, E. (2011). Arrays of SU-8 microcantilevers with integrated piezoresistive sensors for parallel AFM applications. *Microelectronic Engineering*, *88*(8), 2390–2393. doi:10.1016/j.mee.2010.11.047

194. Huq, E., Djakov, V., & Vernon, P. (2010). Fluid Probe (Patent No. US 7,775,084 B2).

195. Li, L., & Uttamchandani, D. (2009). Dynamic response modelling and characterization of a vertical electrothermal actuator. *Journal of Micromechanics and Microengineering*, *19*(7), 075014. doi:10.1088/0960-1317/19/7/075014

196. Kurabayashi, K., Asheghi, M., & Touzelbaev, M. (1999). Measurement of the Thermal Conductivity Anisotropy in Polyimide Films. *Journal of Microelectromechanical Systems*, *8*(2), 180–191.

197. Roder, H. M., Perkins, R. A., & Laesecke, A. (2000). Absolute Steady-State Thermal Conductivity Measurements by Use of a Transient Hot Wire System. *Journal of Research of the National Institue of Standards and Technology*, *105*(2), 221–253.

198. Perkins, R. A., & Roder, H. M. (1991). A High-Temperature Transient Hot-Wire Thermal Conductivity Apparatus for Fluids. *J. Res. Natl. Inst. Stand. Technol.*, *96*(3), 247–269.

199. Peng, W. (2004). Optimisation of Thermal Bimorph Cantilevers, Electrostatic Torsion Actuators and Variable Capacitors (Thesis). *PhD Thesis, New Jersey Institute of Technology*, (Chapter 2), 24 – 33.

200. Puente, D., Gracia, F. J., & Ayerdi, I. (2005). Thermal conductivity microsensor for determining the Methane Number of natural gas. *Sensors and Actuators B: Chemical*, *110*(2), 181–189. doi:10.1016/j.snb.2005.01.026

201. Belser, R. B., & Hicklin, W. H. (1959). Temperature Coefficients of Resistance of Metallic Films in the Temperature Range 25° to 600°C. *Journal of Applied Physics*, *30*(3), 313. doi:10.1063/1.1735158

202. Djugum, R., & Jolic, K. I. (2006). A fabrication process for vacuum-deposited strain gauges on thermally sprayed Al 2 O 3. *Journal of Micromechanics and Microengineering*, *16*(2), 457–462. doi:10.1088/0960-1317/16/2/032

203. Kazi, I. H., Wild, P. M., Moore, T. N., & Sayer, M. (2003). The electromechanical behavior of nichrome (80/20 wt.%) film. *Thin Solid Films*, *433*, 337–343. doi:10.1016/S0040-6090(03)00390-0

204. HD Microsystems GmbH. (2009). Product Bulletin HD-4100 Series. *Technical information*, (September), 1–4.

205. HD Microsystems GmbH. (2008). HD-7010 Polyimide. *Technical Information*, (April), 1–4.

206. Lee, J., & King, W. P. (2007). Microcantilever hotplates: Design, fabrication, and characterization. *Sensors and Actuators A: Physical*, *136*(1), 291–298. doi:10.1016/j.sna.2006.10.051

207. White, R. C., Paranjape, M., & Currie, J. F. (2003). A dry release technique for polymer µ-TAS integration. *Proceedings of 7th International Conference on Miniaturized Chemical and Biochemical Analysis Systems*, (October5-9), 191–194.

208. Sami Franssila. (2004). Chapter 13: Thermal Oxidation. *Introduction to Microfabrication, John Wiley & Sons, Ltd.*, 143–180.

209. Duffy, D. C., McDonald, J. C., Schueller, O. J., & Whitesides, G. M. (1998). Rapid Prototyping of Microfluidic Systems in Poly(dimethylsiloxane). *Analytical chemistry*, *70*(23), 4974–84. doi:10.1021/ac980656z

210. Angadi, M. A., & Whiting, R. (1990). Longitudinal and transverse strain sensitivity of nichrome films. *Materials Science and Engineering: B*, *7*, L1–L4. doi:10.1016/0921-5107(90)90020-C

211. Kazi, I. H., Wild, P. M., Moore, T. N., & Sayer, M. (2006). Characterization of sputtered nichrome (Ni–Cr 80/20 wt.%) films for strain gauge applications. *Thin Solid Films*, *515*(4), 2602–2606. doi:10.1016/j.tsf.2005.10.077

212. Midturi, S. (2010). Stress-strain behaviour of nano/micro thin film materials. *ARPN Journal of Engineering and Applied Sciences*, *5*(3), 72–76.

213. Spells, K. E. (1960). The Thermal Conductivities of some Biological Fluids. *Phys. Med. Miol.*, *5*, 139 – 153.

214. Nahirnyak, V. M., Yoon, S. W., & Holland, C. K. (2007). Acousto-mechanical and thermal properties of clotted blood. *J. Acoust. Soc. Am.*, *119*(2005), 3766–3772.

215. Ahuja, A. S., & Hendee, W. R. (1978). Thermal design of a heat exchanger for heating or cooling blood. *Physics in medicine and biology*, *23*(5), 937–51. Retrieved from http://www.ncbi.nlm.nih.gov/pubmed/715008

216. Bridgman, P. W. (1923). The Thermal Conductivity of Liquids. *Proceedings of the National Academy of Sciences*, *9*, 341–345.

217. Kwak, H. T., Zhang, G., Chen, S., & Atlas, B. (2005). The effects of salt type and salinity on formation water viscosity and NMR responses. *Proceedings of the International Symposium of the. Society of Core Analysts, Toronto, 21-25 August 2005*, 1–13.

218. Ramires, M. L. V, & Castro, C. A. N. De. (2000). Thermal Conductivity of Aqueous Potassium Chloride Solutions. *International Journal of Thermophysics*, *21*(3), 671 – 679.

219. Kelling, S., Huang, J., Capener, M. J., & Elliott, S. R. (2011). Breath analysis system based on phase-shifting interferometric microscopy readout of microcantilever arrays. *Journal of Breath Research*, *5*(3), 7106.

220. ST Micro showed interest in persuing a collaboration of this nature with STFC in 2009, but this was never initiated.

221. Infinium Ltd. showed interest in collaboration with STFC in 2011 to use microcantilever sensors to monitor the viscosity changes in fuel using different additives. This project was never initiated.

222. Ree, M., Chen, K., Kirby, D. P., Katzenellenbogen, N., & Grischkowsky, G. (1992). Anisotropic properties of high-temperature polyimide thin films - Dielectric and thermal-expansion behaviors. *J. Appl. Phys*, *5*, 2014–2021.

223. Lammel, G., Schweizer, S., & Renaud, P. (2002). Appendix A3: Large Deflections. In *Optical Microscanners and Microspectrometers Using Thermal Bimorph Actuators* (pp. 225 – 228). Kluwer Academic Publishers.

224. Craighead, H. G. (2000). Nanoelectromechanical systems. *Science (New York, N.Y.)*, *290*, 1532–1535.

225. Van den Berg, N., Schumann, M., Kraft, K., & Hoffmann, W. (2012). Telemedicine and telecare for older patients-A systematic review. *Maturitas*, *73*(2), 94–114. doi:10.1016/j.maturitas.2012.06.010

226. Rechnitz, G. A. (1991). Biosensors into the 1990's. *Electroanalysis*, *3*, 73–76.

227. Liu, C. (2007). Recent Developments in Polymer MEMS. *Advanced Materials*, *19*(22), 3783–3790. Retrieved from http://onlinelibrary.wiley.com/doi/10.1002/adma.200701709/abstract